A New Spin on Top-Quark Physics

Using angular distributions to probe top-quark properties, and make the first observation of entanglement between quarks

Ethan Lewis Simpson

A thesis presented for the partial fulfilment of the degree of
Doctor of Philosophy

University of Glasgow

School of Physics and Astronomy,
College of Science and Engineering,
University of Glasgow.

To three friends I lost over the duration of this PhD:
Granny Eileen, Papa Andy, and Leo.

Abstract

Measurements of angular properties of top-quarks constitute stringent tests of the Standard Model, probe physics beyond it, and even reveal underlying quantum information phenomena. This thesis discusses angular top-quark properties in two new contexts. A study of $t\bar{t}$ spin correlations and top-quark polarisations in associated $t\bar{t}Z$ production presents theoretical predictions for these parameters at $\sqrt{s} = 13\,\text{TeV}$. A measurement strategy for observation of spin correlations in $t\bar{t}Z$ production at the Large Hadron Collider is proposed, and the constraint on effective field theory models provided by angular observables investigated. Related angular observables are used to make the first ever observation of quantum entanglement between quarks, in the di-leptonic $t\bar{t}$-production channel. An entanglement marker D is extracted from an angular differential cross-section measured in ATLAS $\sqrt{s} = 13\,\text{TeV}$ proton-proton collision data, and corrected to a fiducial particle-level phase-space. This observed entanglement marker is found to be -0.547 ± 0.022, corresponding to an exclusion of the *no-entanglement* hypothesis well in excess of five standard deviations. Short studies on novel methods to emulate the ATLAS detector response are also presented.

Declaration

I certify that the thesis presented here for examination for PhD degree of the University of Glasgow is solely my own work other than where I have clearly indicated that it is the work of others and that the thesis has not been edited by a third party beyond what is permitted by the University's PGR Code of Practice.

I declare that the thesis does not include work forming part of a thesis presented successfully for another degree.

I declare that this thesis has been produced in accordance with the University of Glasgow's Code of Good Practice in Research.

I acknowledge that if any issues are raised regarding good research practice based on review of the thesis, the examination may be postponed pending the outcome of any investigation of the issues.

Ethan Lewis Simpson
30-09-2023

Acknowledgements

First and foremost, I would like to acknowledge my first supervisor Jay Howarth for paying my stipend until it ran out. I have found Jay's expertise in experimental particle physics, love of the top-quark, willingness to answer my many questions, and tenacity to always be himself, both helpful and inspiring. I must also acknowledge the post-doctoral staff who I have worked with directly, namely Baptiste Ravina and Federica Fabbri. I wish to acknowledge Mark Owen's contributions to the Glasgow Top Quark group, and the Glasgow Experimental Particle Physics group at large. I should like to thank Jonathan Jamieson for helping with many points of clarification I had in writing this thesis. Finally, I would like to thank my colleagues in Glasgow and beyond for their support and continual willingness to provide assistance.

I would like to thank my family for their continual support, freely offered despite my lack of permanent job, house or Help-to-Buy ISA. In particular, I would like to thank my parents for putting up with me for extended stays in Hawick during the pandemic and after my return from Geneva.

I haven't ever liked that trend in thesis acknowledgements of listing friends: the line between who gets listed and who doesn't seems impossibly hard to draw. I therefore simply acknowledge my friends outside physics, and the friends and colleagues I made over the course of this PhD, both at Glasgow, in Geneva, and elsewhere. In particular, my Long-Term Attachment at CERN was the highlight of this PhD experience, so it seems fitting to acknowledge the large company of fellow LTA-ers who made that experience memorable, and participated in occasional Simpsom's Holidays. The PhD experience was a great learning experience, but that friendship aspect is, for me, the key take-away.

Finally, I would like to thank Roger the Ski Instructor. "Et bon weekend"...

Preface

Sometime during the course of this PhD, possibly in a rainy Glasgow tenement flat, I was struck by a conversation I was having with a non-physicist. I had mentioned the phrase "New Physics".

"How can there be New Physics?," came the reply.

It seems that the distinction between old physics, or known physics, and new physics, or undiscovered physics, was not clear. It was an incident which brought home a realisation: the idea that original scientific research is perhaps more subtle than those in the community realise. But on closer reflection, I realised there is more than one way to think about New Physics.

Perhaps a general definition of New Physics would be something like, "as-yet undiscovered mechanisms for describing the physical world". Understanding that our description of the universe is incomplete and that physics is not a solved problem, New Physics is what remains to be discovered, the missing pieces of the puzzle.

New Physics could mean something different. It could mean physics which has not been performed before: an experimental study of a known physics process using new techniques to drive finer precision; a new calculation of a known aspect of some theory; a novel interpretation of an existing result; the measurement of some phenomenon conjectured to exist, but never validated before. In this context, New Physics is simply physics research. This New Physics is something we do every day.

In a particle physics context, New Physics can mean something much more specific. It can mean particular models which extend our current understanding of particle physics. These models are unverified conjectures, designed to solve plot holes in existing theories or suggest as-yet unmeasured phenomena. This New Physics is something we specifically and studiously search for.

This thesis presents some Old Physics and some New Physics.

"The effort to understand the universe is one of the very few things that lifts human life a little above the level of farce, and gives it some of the grace of tragedy."

— Steven Weinberg

"I am beyond reproach."

— Jay Howarth

Contents

List of tables

List of figures

Chapter 1

Introduction

1.1 The State of Particle Physics

The narrative begins with the Standard Model of Elementary Particle Physics, or the Standard Model, or SM. It is a beautiful and miraculous construction: a model that tells physicists which fundamental objects exist in the universe, how they behave, how they interact, and how they combine to make the ink on this page, the pixels on this screen, and rainy Glasgow tenement flats. Crucially for our purposes, it describes how particular particles behave when smashed together at ludicrously high energies.

If the Standard Model is one great product of human endeavour, then the Large Hadron Collider (LHC) is surely another [1]. Nestled between the Jura mountains and Lac Leman, hidden under fields and woods and Meyrin kebab shops and French supermarkets, the LHC squats, a particle collider of unseen size and energy, capable of throwing protons together at basically the speed of light. Its main purpose is to square off with the SM, a curiously un-Swiss-like state of conflict. Over the course of the last half century, the SM has battled many foes in many guises. The LHC is just the newest and biggest and most expensive of them, and its purpose is to test the SM to breaking point.

Let us be clear. We need the LHC, because we know the Standard Model cannot be all there is[1]. The shortcomings of the Standard Model are numerous and well-documented. The large number of free parameters suggests that it is too arbitrary to be a complete description of nature. Issues like the hierarchy problem [2], predominance of dark matter in the universe [3], or absence of description of the gravitational interaction [4], all indicate that New Physics must exist beyond the Standard Model.

Experimental evidence in tension with the Standard Model is, however, relatively thin on the ground. Three specific, controversial measurements which garnered much attention over the course of this PhD were irregularities in B-meson decays [5], anomalies in the magnetic moment of the muon [6], and tension in the mass of the W boson [7], [8]. Perhaps one of these results indicates a crack in the Standard Model's facade.

[1]The Standard Model is considered to be an effective description, in the spirit of Section 2.7.1, of the universe at the energy scales we can probe.

Experimental particle physicists are determined to keep searching for those cracks, all the while measuring the Standard Model to ever-greater precision.

A key object of study in this regard, and a most distinguished member of the Standard Model, is the top-quark. Heaviest of all fundamental particles, the top-quark provides us with a fascinating playground to study the Standard Model in great detail, and test for theories beyond it. The study of spin properties of the top-quarks form a central theme of this thesis. These properties can be measured in collider experiments through observables which encode information about the spatial-direction of the top-quarks' decay products. Such observables can even probe the quantum mechanical foundations of the Standard Model itself.

The Standard Model is introduced, and its phenomenology in hadron colliders described, in Chapter 2. The top-quark is the star of the show in Chapter 3, where its history, production, decay and spin are discussed. One of the LHC's chief weapons in its war against the Standard Model, the ATLAS detector, is revealed in its 7,000 tonne glory in Chapter 4.

1.2 Experimental and Modelling Techniques

Experimentally-verifying the Standard Model requires a powerful toolkit. Chapter 5 presents the myriad procedures, methods and algorithms we use to turn a deluge of electrical signals in the ATLAS detector into precise measurements of particle interactions. Simulation is the compliment of measurement, and in Chapter 6, the techniques used to model proton collisions are discussed.

Simulating a particle 'burrowing' its way through the ATLAS detector is hard work, and many tools have been developed to expedite this simulation process. One highly-efficient technique is to emulate the effects of the simulation process on particles' kinematics, without doing any expensive simulation at all. In Chapter 7, two such methods are proposed and tested. Both use existing simulation to derive mappings which emulate the detector response: the first sampling kinematic distributions, and the second learning a mapping through deep learning methods. Both methods are compared to existing simulation tools, and future research directions are proposed.

1.3 Spin Properties in $t\bar{t}Z$ Production

The spin properties of top-quarks in the production of a top-antitop-quark pair, $t\bar{t}$, are measured to high precision. When the $t\bar{t}$ pair is produced with additional vector bosons, the spin properties are relatively unexplored. Chapter 8 presents predictions for these properties in the production of a $t\bar{t}$ pair accompanied by a Z-boson, and outlines how precise a measurement at the LHC could be. The same spin observables are studied to see if their measurement could indicate directions of possible New Physics.

1.4 Quantum Information in Particle Colliders

Of the many strange and counter-intuitive physics ideas which leak out into the public's collective imagination, perhaps none is more thought-provoking and downright weird than quantum entanglement. Einstein is famously alleged to have termed it "spooky action at a distance", and spooky it is. If two particles exist in an entangled quantum state, it is impossible to describe one of those particles independently from the other. The notion of quantum entanglement is central to one of the most important results in quantum mechanics, the celebrated Bell inequalities [9]. Further, the 2022 Nobel Prize in Physics was awarded to Aspect, Clauser and Zeilinger for pioneering experimental work in measuring quantum entanglement [10].

A top-quark and anti-top-quark are conjectured to form an entangled state in certain conditions. Chapter 9 introduces a formal notion of entanglement which can be applied to a pair of spin-1/2 particles in a collider context. Chapter 10 describes the measurement of quantum entanglement made in ATLAS data at the LHC [11]. A set of selections are imposed on collision events to isolate $t\bar{t}$ pairs at low invariant mass, and an entanglement marker is extracted from a particular angular distribution of the top-quarks' decay products. Simulation is used to 'correct' the measured result for distortions caused by the detector, and the measured result is compared to predictions from simulation. The chapter points out several challenges faced, and speculates on areas where improvements could be made.

Chapter 11 summarises the scope of this thesis, highlighting the findings of the original research and making a definitive statement about quantum entanglement at the LHC.

Chapter 2

The Standard Model and its Phenomenology

"The SM: a quick explanation:
Fields exist as group representations;
The S-matrix lets scatter,
Both bosons and matter.
But it's not without its limitations."
—

What is the greatest work of the human mind? The Complete Works of Shakespeare? The nine symphonies of Beethoven? ABBA Gold? Surely the Standard Model of Elementary Particle Physics constitutes a worthy contender? It represents the culmination of a half-century's intellectual endeavour: a fantastical construction, equal parts elegant and enigmatic, able to describe why the most fundamental objects discovered behave as they do, wielding enormous predictive power, and inspiring experimental particle physicists to try their damnedest to tear it apart. And yet despite its tremendous success, the shortcomings of the Standard Model, both in its construction, and in its failure to provide a complete microscopic description of nature, are well known.

In this chapter, the Standard Model is described as a four-dimensional, non-Abelian, chiral, gauge quantum field theory, with a partially spontaneously-broken gauge sector, coupled to three generations of matter possessing a particular flavour structure and mass hierarchy. Its basic principles, underlying group-theoretic structure, matter content and mass-generation mechanism are outlined. The phenomenology of the model and its application in computing scattering cross-sections at the LHC are discussed. The chapter concludes with a discussion on the Standard Model Effective Field Theory, a framework for searching for extensions to the Standard Model.

2.1 The Structure and Symmetries of the Standard Model

A sensible theory of particle dynamics and interactions should meet several key requirements. To be of any utility, the theory must have predictive power, and its predictions be testable in experiments. Further, those predictions must agree with observations of nature: *"it doesn't make a difference how beautiful your guess is... if it disagrees with experiment, it's wrong"* [12]. Several other requirements are chosen to form the base of this description of nature. The theory is constructed to exhibit locality — events which are space-like separated cannot affect one another — and conserve probabilities — the probabilities of all possible outcomes should sum to unity.

The Standard Model (SM) [13], [14] is a particular Quantum Field Theory (QFT) [15] which meets these requirements. As a QFT, the dramatis personæ are quantum fields: operator-valued distributions that map positions in spacetime to linear operators in a Hilbert space. Locality is ensured by stipulating that these fields transform under the Poincaré group, discussed below, and that the interactions between the fields are local: this can be achieved through a Lagrangian prescription [13]. Interacting QFTs are characterised by a scattering matrix, or S-matrix,

$$S_{fi} = \langle f|\hat{S}|i\rangle, \tag{2.1.1}$$

where i and f are asymptotic initial and final states, respectively, and $\hat{S}$ a scattering operator. The S-matrix is required to be unitary [16]: this condition forces probabilities to be conserved. Furthermore, the SM is a renormalisable QFT, which means there exists a prescription for dealing with divergences that arise in calculations, such that finite results can be obtained. This ultimately saves the predictive power of the SM, and renormalisation is discussed further in Section 2.5.

Having understood that locality, unitarity and renormalisability are key characteristics of the SM, its structure can be elucidated. The fundamental idea is that quantum fields exist as representations of a specific set of Lie groups which together constitute the symmetry group of the S-matrix. The "physics" of how each field behaves and interacts is then given by how its representation transforms under the action of these specific Lie groups. Several classes of Lie group are defined. The first is the group of spacetime symmetries. The base manifold of the SM is four-dimensional Minkowski spacetime, as characterised by the Minkowski metric $\eta_{\mu\nu}$. This is the arena in which physical reality plays out. The Poincaré group $\mathcal{P}$ is the group of transformations which leave the spacetime interval ds^2 invariant: the semi-direct product of the group of translations, and the Lorentz group containing rotations and boosts:

$$\mathcal{P} = \mathbb{R}^{1,3} \rtimes \mathrm{O}(1,3). \tag{2.1.2}$$

In addition to the symmetry structure of the Poincaré group, the SM fields are charged under the internal gauge group

$$G_{SM} = SU(3)_C \otimes SU(2)_L \otimes U(1)_Y. \tag{2.1.3}$$

Identifying this particular gauge structure, perhaps the most defining feature of the SM, as the product of quantum chromodynamics ($SU(3)_C$) [17]–[19] with the Glashow-Weinberg-Salam electroweak model ($SU(2)_L \otimes U(1)_Y$) [20]–[22] constituted the birth of the SM as we recognise it today. The fields' representations under G_{SM} define a set of quantum numbers, or generalised charges, which characterises each field. Equivalently, the gauge structure can be said to define the interactions between the fields of the SM, with the various Lie sub-groups corresponding to particular interactions, or "forces". The subscripts in equation 2.1.3 denote the names of each subgroup's quantum numbers: colour, left-handed weak isospin, and weak hypercharge, respectively.

The product of these two symmetry groups, $\mathcal{P} \times G_{SM}$, is then the maximal symmetry group of the SM S-matrix, in accordance with the Coleman-Mandula theorem [23]. This is the statement that all generators of $\mathcal{P}$ commute with those of G_{SM} , $\left[\mathcal{P}, G_{SM}\right] = 0$, and that any extension of $\mathcal{P}$ over-constrains scattering amplitudes[1] [24].

In addition to considering a field's charges under G_{SM}, the associated quantum numbers for positive-energy irreducible representations of the Poincaré group $\mathcal{P}$ are mass m and spin s, with $2s + 1$ linearly independent polarisation states for $m > 0$ and two states for $m = 0$. SM fields are classified by their spins: as spin-0 "scalars", spin-1/2 "spinors" or spin-1 "vectors". There are no fundamental objects in the SM with higher spin[2]; any experimental evidence for such a field would indicate some extension of the SM, and no such evidence has ever been found.

The restricted Lorentz group $SO^+(1,3)$ is the subgroup of the full Lorentz group $O(1,3)$ whose transformations preserve the direction of time and the orientation of space. The following isomorphism holds true for the restricted Lorentz group[3] :

$$SO(1,3) \simeq SL(2,\mathbb{C}) \simeq SU(2)_L \otimes SU(2)_R. \tag{2.1.4}$$

Any field can thus be decomposed into left- and right-handed components and characterised by its representations in these sub-groups (L, R). A spinor element of either of these SU(2) subgroups constitutes a Weyl spinor ψ, and their direct sum forms the Lorentz-invariant Dirac bispinor $\Psi = \psi_L \oplus \psi_R$. It was realised in the 1950s that left-handed particles participate in weak decays whilst their right-handed counterparts do not [26], [27]. This behaviour is built in to the SM by specifying that right-handed

[1] Famously, there are several ways to circumvent the Coleman-Mandula theorem and extend the group of spacetime symmetries: introducing conformal transformations for massless particles, or extending to supersymmetric algebras.

[2] Composite hadrons can exist in spin states greater than spin-1

[3] The property actually stems from the nature of odd-dimensional Clifford algebras [25]

fields do not transform under the $\mathrm{SU}(2)_\mathrm{L}$ group: the SM is thus viewed as a chiral theory.

The full Lorentz group $\mathrm{O}(1,3)$ contains the additional discrete unitary operations of parity P and time-reversal T, which act on a field to reverse the spatial and temporal coordinates respectively. A final discrete group operation, charge conjugation C, maps a particle to its anti-particle, and flips its spin. Weak interactions in the SM are shown to violate C-, P- and T-symmetries [28]–[30]. Nevertheless, Lorentz invariance and unitarity stipulate that the SM Lagrangian is invariant under the combined action of CPT, a result known as the CPT Theorem [31]. In addition, there exist so-called "accidental" global $\mathrm{U}(1)$ symmetries such as baryon-number and lepton-family-number symmetries, which place additional constraints on the type of permissible SM interactions. These symmetries arise only because one cannot write down a four-dimensional term in the SM Lagrangian which violates the symmetry yet maintains renormalisability; for this reason are these symmetries seen as accidental, and BSM theories frequently do not contain them.

2.2 The Cast

Having understood that the SM concerns quantum fields and their representation under a particular symmetry structures, the natural question arises: which quantum fields actually makes up the SM?

2.2.1 Gauge Fields

The gauge sector brings with it a set of gauge fields which exist in the adjoint representation of the gauge subgroups:

$$\begin{aligned} \mathrm{SU}(3) &: G^a_\mu,\ {}_{a=1,\ldots,8,} \\ \mathrm{SU}(2)\otimes\mathrm{U}(1) &: W^J_\mu,\ {}_{J=1,2,3;}\ \ B_\mu. \end{aligned} \tag{2.2.1}$$

with a and J indexing the group charge of $\mathrm{SU}(3)$ and $\mathrm{SU}(2)$ groups, respectively. These are bosonic fields of spin-1[4] which are said to facilitate the gauge interactions of the SM. The dynamics of the gauge fields are captured in Lagrangian Yang-Mills[5] terms of the form

$$\mathcal{L}_\text{gauge} = -\frac{1}{4}F^{a\mu\nu}F^a_{\mu\nu}, \tag{2.2.2}$$

[4] All spin-1 fields in renormalisable 4D QFTs are associated with a gauge symmetry [15].

[5] There are no interacting, renormalisable theories of massless vector bosons other than Yang-Mills [32].

where $F^a_{\mu\nu}$ is the field strength tensor. Defining $A_\mu = A^a_\mu T_a$and $F_{\mu\nu} = F^a_{\mu\nu} T_a$, the field strength tensor is related to the commutator of the gauge covariant derivatives D_μ:

$$F_{\mu\nu} = \frac{i}{g}[D_\mu, D_\nu], \tag{2.2.3}$$

$$= \partial_\mu A_\nu - \partial_\nu A_\mu - ig\left[A_\mu, A_\nu\right] \tag{2.2.4}$$

which follows from the definition of the gauge covariant derivative,

$$D_\mu = \partial_\mu - igA_\mu. \tag{2.2.5}$$

Throughout, g is the coupling strength of the interaction facilitated by the gauge group, T_a the generators of the corresponding Lie algebra, and A^a_μ the gauge field [33]. The non-Abelian groups $\mathrm{SU(3)_C}$ and $\mathrm{SU(2)_L}$ have by definition non-vanishing commutators of the gauge fields , $[A_\mu, A_\nu] \neq 0$, representing the self-interaction of the gauge bosons. The fully gauge covariant derivative of the SM reads,

$$D_\mu = \partial_\mu - ig_1\frac{Y}{2}B_\mu - ig_2\frac{\tau_j}{2}W^j_\mu - ig_3\frac{\lambda_a}{2}G^a_\mu, \tag{2.2.6}$$

and operates on the matter fields discussed next. The terms contain the gauge coupling, generators and gauge fields for the $\mathrm{U(1)_Y}, \mathrm{SU(2)_L}$ and $\mathrm{SU(3)_C}$ groups respectively.

2.2.2 Fermions

The gauge fields are coupled to a set of spin-half matter fields, $\Psi = \{\psi\}$. These fermions are the quarks and leptons which constitute the very stuff our universe is made out of. Gauge interactions between the fermions can be introduced through kinetic Lagrangian terms of the form,

$$\mathcal{L}_{\text{kinetic}} = i\bar{\Psi}D_\mu\Psi, \tag{2.2.7}$$

with D_μ the gauge covariant derivative 2.2.6. The SM fermions can be summarised in the tuple,

$$\Psi_i = \left\{Q_L, l_L, u_R, d_R, e_R\right\}_i \ , \ i = 1, 2, 3, \tag{2.2.8}$$

representing the five representations of $\mathrm{G_{SM}}$ which exist per *generation*, with three generations of matter observed, as denoted by the index i. Why there exists exactly three generations of matter, and not more or less, is one of the great mysteries of the SM [34]. The subscript L denotes left-handed SU(2) quark and lepton doublets:

$$Q^a_{L_i} = \begin{pmatrix} u^a_{L_i} \\ d^a_{L_i} \end{pmatrix} \quad \text{and} \quad l_{L_i} = \begin{pmatrix} \nu_{L_i} \\ e_{L_i} \end{pmatrix}, \tag{2.2.9}$$

with the subscript R denoting right-handed $\mathrm{SU}(2)_L$ singlets[6]:

$$u_R^a \ , \ d_R^a \ , \ e_R. \tag{2.2.10}$$

The index a, suppressed in equation 2.2.8, represents the three $\mathrm{SU}(3)_C$ colour charges the quarks can possess: $a = 1, 2, 3$. Right-handed neutrinos are omitted, as though theoretically well-motivated, they have no direct experimental detection to date and as such are considered extensions of the SM.

Any one of the fermions in 2.2.8 is characterised by its quantum numbers, which are identical across generations, with the distinguishing exception of mass. The masses of fermions are free parameters in the theory; why the fermions adopt the mass hierarchy observed by experiment is a further mystery. This thesis is primarily interested in the top-quark which sits at the apex of that mass hierarchy.

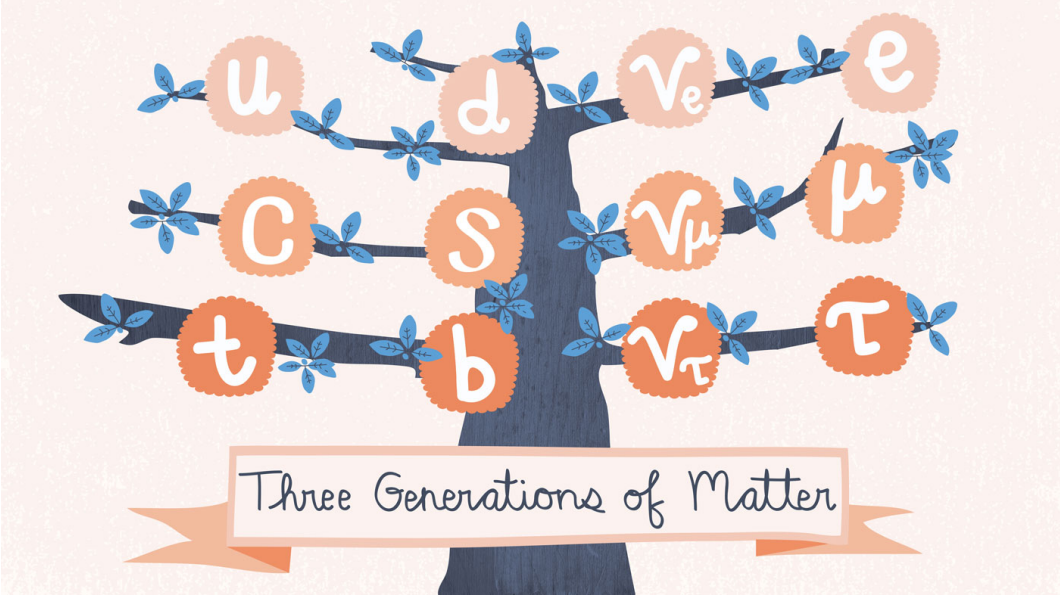

Figure 2.1: An illustration of the three generations of fermions. Artwork by Sandbox Studios, Chicago; taken from a Symmetry magazine [35]. The mystery of why is there is three-fold repetition of matter fields within the SM (differentiated by mass) is not explained by the theory, and thus constitutes one of many strong motivators for BSM physics.

[6]The Latin prefixes "singlet" , "doublet" etc. are a nomenclature for how a field behaves under a particular Lie group action: how many independent states exist. By way of example, representations invariant under group action have only one value they can take and so are termed singlets; representations which transform in the fundamental representation of $\mathrm{SU}(2)_L$ are doublets; and so on far larger groups.

2.3 The Higgs Sector and Electroweak Symmetry Breaking

The SM must possess a mechanism for generating the measured masses of the SM particles observed in nature, but this mechanism must respect the symmetries of the theory. For example, naively inserting mass terms of the form $mf_L\bar{f}_R$ for fermions is seen to break the $SU(2)_L$ gauge symmetry. Electroweak symmetry breaking (EWSB) is therefore introduced to provide a mechanism for dynamical mass generation whilst maintaining gauge invariance. The first thing to note is that EWSB is an example of spontaneous symmetry breaking (SSB), a scenario in which the Lagrangian of a theory is invariant under some group action, but the ground state of the theory is not. The SSB mechanism in question is the Higgs mechanism, which explains how the non-Abelian gauge symmetries of the SM are spontaneously broken[7]. The Higgs mechanism is therefore another defining characteristic of the SM, and responsible for symmetry breaking of the electroweak group down to the familiar electromagnetism group:

$$SU(2)_L \otimes U(1)_Y \rightarrow U(1)_Q. \tag{2.3.1}$$

The mechanism was proposed by a number of authors in the mid-1960s [36]–[38], with the term "Higgs" mechanism perhaps inappropriately singling out one of those authors. It received final validation in 2012 with experimental observation of the Higgs boson [39], [40], the final member of the SM cast, which arises out of the 'ruins' of electroweak symmetry breaking.

In general, SSB is achieved through introducing some scalar field which then acquires some non-zero vacuum expectation value. In the SM, this field is the Higgs field ϕ, a complex scalar SU(2) doublet with non-zero hypercharge:

$$\phi = \begin{pmatrix} \phi^+ \\ \phi^0 \end{pmatrix}, \tag{2.3.2}$$

whose Lagrangian takes the form

$$\mathcal{L} = \left(D_\mu\phi\right)^\dagger \left(D_\mu\phi\right) + \mu^2\phi^\dagger\phi - \lambda\left(\phi^\dagger\phi\right)^2. \tag{2.3.3}$$

The left-most term describes the Higgs field's kinematics, however the field is not charged under the $SU(3)_C$ group, and as such the covariant derivatives in the kinetic terms contain no SU(3) term. The remaining two terms define the Higgs potential, with $\lambda\left(\phi^\dagger\phi\right)^2$ introducing quartic self-interactions amongst the scalar fields ϕ, and with $\lambda > 0$ required for vacuum stability. For $\mu^2 > 0$, the Higgs field acquires a non-zero

[7] A similar, though Abelian, mechanism is responsible for providing an effective description of superconductivity as a second-order phase transition in the Landau-Ginzburg theory. The full microscopic theory is the BCS theory [13].

vacuum expectation value, which can be written [41]:

$$\langle\phi\rangle = \phi_0 = \frac{1}{\sqrt{2}}\begin{pmatrix} 0 \\ v \end{pmatrix}, \tag{2.3.4}$$

with $v^2 = \mu^2/\lambda$ defining the electroweak scale. Expanding the Higgs field around this minimum $\phi \to \phi_0 + h$,

$$\phi = \frac{1}{\sqrt{2}}\begin{pmatrix} 0 \\ v + h \end{pmatrix}, \tag{2.3.5}$$

introduces physical Higgs field h. The kinetic terms in 2.3.3 contain the vacuum expectation values v, along with the electroweak vector fields, and as such give rise to the following mass terms for the gauge bosons:

$$\left(D_\mu\phi\right)^\dagger\left(D_\mu\phi\right) = \frac{v^2}{8}\left[g_2^2\left(\left(W_\mu^1\right)^2 + \left(W_\mu^2\right)^2\right) + \left(g_2 W_\mu^3 - g_1 B_\mu\right)^2\right]. \tag{2.3.6}$$

The charged W-bosons of the broken phase are defined as

$$W_\mu^\pm \equiv \frac{1}{\sqrt{2}}\left(W_\mu^1 \mp i W_\mu^2\right), \tag{2.3.7}$$

with masses $m_W = g_2 v/2$. The neutral bosons can be defined from diagonalisation: a rotation through the weak mixing angle, θ_W:

$$\begin{pmatrix} A_\mu \\ Z_\mu \end{pmatrix} = \begin{pmatrix} \cos\theta_\mathrm{W} & \sin\theta_\mathrm{W} \\ -\sin\theta_\mathrm{W} & \cos\theta_\mathrm{W} \end{pmatrix}\begin{pmatrix} B_\mu \\ W_\mu^3 \end{pmatrix}, \tag{2.3.8}$$

where $\tan\theta_\mathrm{W} = g_1/g_2$, with $m_Z = v/2\sqrt{g_1^2 + g_2^2}$ and the photon massless. The fact that the Higgs field is a singlet under $\mathrm{SU(3)_c}$ leads directly to a massless gluon. The origin of electric charge Q is also made clear under EWSB:

$$Q = T_3 + \frac{Y}{2}, \tag{2.3.9}$$

with T_3 and Y the gauge charges of the $\mathrm{SU(2)_C}$ and U(1) groups. These are termed third component of weak isospin and weak hypercharge, respectively. The resultant $\mathrm{U(1)_{em}}$ group has coupling

$$e = g_2 \sin\theta_\mathrm{W} = g_1 \cos\theta_\mathrm{W} = \frac{g_1 g_2}{\sqrt{g_1^2 + g_2^2}}. \tag{2.3.10}$$

The remaining task is endowing the fermions, with the exception of neutrinos, with mass. This is achieved through so-called Yukawa interaction terms in the Lagrangian which facilitate the mixing of left- and right-handed fermionic fields in a gauge-invariant way:

$$\mathcal{L}_{\text{Yukawa}} = \bar{\psi}_L y \psi_R \phi, \tag{2.3.11}$$

where y denotes the *Yukawa coupling* quantifying the strength of the fermion's interaction with the Higgs field. Expanding over the SM quark and lepton multiplets whilst omitting neutrino Yukawa terms yields

$$\mathcal{L}_{\text{Yukawa}} = \bar{q}_L Y_u u_R \tilde{\phi} + \bar{q}_L Y_d d_R \phi + \bar{l}_L Y_e e_R \phi + \text{h.c.}, \tag{2.3.12}$$

where h.c. denotes the hermitian conjugates of the preceding three terms, $\tilde{\phi} = i\sigma_2 \phi$, and the Y are general complex 3×3 Yukawa matrices containing the individual Yukawa couplings. These terms correspond to mass terms when the Higgs field ϕ obtains its vacuum expectation value.

Focusing on the quark sector, the Yukawa matrices can be diagonalised to achieve physical mass parameters through applying a bi-unitary transformation, rendering the fermions in a *mass eigenstate*, in contrast to the original *flavour eigenstate*. In the flavour basis, flavour eigenstates by definition do not mix in charged-current interactions. The flavour $\rightarrow$ mass transformation induces a flavour mixing through the complex, unitary *CKM matrix*, V_{CKM}:

$$\begin{aligned} J^{+\mu} &= \bar{u}^i_L \gamma^\mu V^{ij}_{\text{CKM}} d^j_L \\ J^{-\mu} &= \bar{d}^i_L \gamma^\mu (V^\dagger_{\text{CKM}})^{ij} u^j_L \end{aligned} \tag{2.3.13}$$

with J the charged currents facilitated by the charged W-bosons, and i, j flavour indices. Experimentally-measured deviations from unitarity in V_{CKM} could indicate the presence of additional fermion generations [42], [43]. Neutral currents are unaffected: flavour-changing neutral currents (FCNCs) are forbidden at tree-level in the SM, and suppressed at higher orders [44]. A similar PMNS matrix exists for the mixing between charged leptons and neutrinos, though it requires massive neutrinos and as such might only be thought of as an extension of the SM.

2.4 The Standard Model, Complete

Let the full SM Lagrangian, pre-EWSB, be the final word in this exposition of SM structure:

$$\begin{aligned}\mathcal{L}^{(4)}_{\text{SM}} = &-\frac{1}{4}G^a_{\mu\nu}G^{a\mu\nu} - \frac{1}{4}W^J_{\mu\nu}W^{J\mu\nu} - \frac{1}{4}B_{\mu\nu}B^{\mu\nu} + \left(D_\mu\phi\right)^\dagger\left(D^\mu\phi\right) + \mu^2\phi^\dagger\phi - \lambda\left(\phi^\dagger\phi\right)^2 \\ &+ i(\bar{l}\not{D}l + \bar{e}\not{D}e + \bar{q}\not{D}q + \bar{u}\not{D}u + \bar{d}\not{D}d) - \left(\bar{l}Y_e e\phi + \bar{q}Y_u u\widetilde{\phi} + \bar{q}Y_d d\phi + \text{ h.c. }\right),\end{aligned} \tag{2.4.1}$$

where the notation $\not{D}$ is shorthand for $\gamma^\mu D_\mu$. Here the gauge, Higgs, kinematic and Yukawa sectors are laid bare. To recapitulate, they represent respectively:

- the interaction of the gauge bosons with themselves;
- the interaction of the Higgs field with itself and the gauge bosons;
- the interactions of the fermions with the gauge bosons;
- the interactions of the fermions with the Higgs field.

Interactions involving gauge bosons constitute the "forces" of the SM, and interactions with the Higgs field generate masses after electroweak symmetry breaking. The representations of the SM fermions are summarised in Table 2.1. The three generations of matter fields and the bosons are tabulated along with their masses, charges and spins in Figure 2.2.

Table 2.1: Each SM fermion can be classified by its various representations under the gauge and spacetime symmetry groups of the SM. The $\text{SU}(3)_\text{c}$, $\text{SU}(2)_\text{L}$ and $\text{U}(1)_\text{Y}$ columns list the gauge charges of five fermion SM field representations. All three generations are shown in each representation.

Field	$\text{SU}(3)_\text{c}$	$\text{SU}(2)_\text{L}$	$\text{U}(1)_\text{Y}$	$\text{SO}^+(3,1)$
$\text{q}_L = \left\{\begin{pmatrix} u_L \\ d_L \end{pmatrix}, \begin{pmatrix} c_L \\ s_L \end{pmatrix}, \begin{pmatrix} t_L \\ b_L \end{pmatrix}\right\}$	**3**	**2**	$\frac{1}{6}$	$(\mathbf{1/2}, \mathbf{0})$
$\text{u}_R = \{u_R\,,\, c_R\,,\, t_R\}$	**3**	**1**	$\frac{2}{3}$	$(\mathbf{0}, \mathbf{1/2})$
$\text{d}_R = \{d_R\,,\, s_R\,,\, b_R\}$	**3**	**1**	$-\frac{1}{3}$	$(\mathbf{0}, \mathbf{1/2})$
$\ell_L = \left\{\begin{pmatrix} \nu_{eL} \\ e_L \end{pmatrix}, \begin{pmatrix} \nu_{\mu L} \\ \mu_L \end{pmatrix}, \begin{pmatrix} \nu_{\tau L} \\ \tau_L \end{pmatrix}\right\}$	**1**	**2**	$-\frac{1}{2}$	$(\mathbf{1/2}, \mathbf{0})$
$\text{e}_R = \{e_R\,,\, \mu_R\,,\, \tau_R\}$	**1**	**1**	-1	$(\mathbf{0}, \mathbf{1/2})$

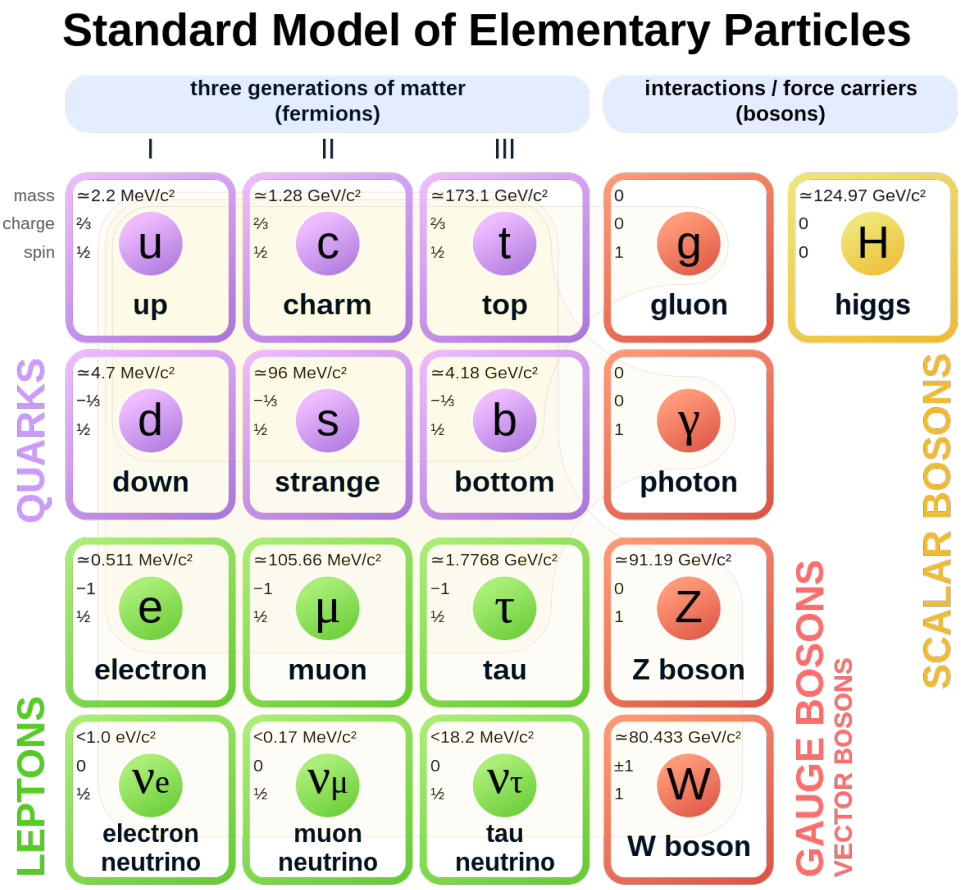

Figure 2.2: A summary of all the particles which feature in the SM, with the three generations of fermions plus the scalar and vector bosons. Taken from [45].

2.5 Scattering Calculations in the Standard Model

Some SM enthusiasts may be drawn to its underlying mathematical structure, or to conjecturing extensions of it which solve outstanding physics problems. For SM phenomenologists, experimentalists, and readers of this thesis, the power of the SM lies in its ability to predict the outcomes of practical collider experiments. Scattering amplitudes are fundamental observables of the SM, and important aspects of their computation are summarised below.

Scattering cross-sections are measured at collider experiments such as the LHC. The SM can then be tested by comparing the measured results to theoretical cross-section predictions. These predictions are calculated by integrating probability amplitudes $|\mathcal{A}|^2$ describing the scattering over the appropriate (Lorentz-invariant) phase-space

$\mathrm{d}\Pi_{\mathrm{LIPS}}$:

$$\mathrm{d}\hat{\sigma}_n = \frac{1}{2\hat{s}}\mathrm{d}\Pi_{\mathrm{LIPS}}\,|\mathcal{A}|^2\,. \tag{2.5.1}$$

The probability amplitudes are derived from the interacting part of the S-matrix:

$$S_{fi} = \langle f|\hat{S}|i\rangle = \mathbb{1} + i\mathbb{T} = \delta_{fi} + i(2\pi)^4\delta^4(p_f - p_i)\mathcal{A} \tag{2.5.2}$$

with p_f and p_i the total momenta of the final and initial states, respectively. Computation of these S-matrix elements is achieved through the Lehmann-Symanzik-Zimmerman (LSZ) reduction formula, which links the scattering amplitudes $\mathcal{A}$ to vacuum expectation values of time-ordered products of quantum fields [46]. The vacuum expectation values, or correlators, are evaluated through a perturbative expansion in the coupling parameter g of the interaction — or the related $\alpha = g^2/4\pi$ — for domains where this parameter is sufficiently small: $\mathcal{A} = \mathcal{A}_0(\alpha) + \mathcal{A}_1(\alpha^2) + \ldots$. This expansion can be expressed as a series of Feynman diagrams, loved by both the amateur particle physics enthusiast and the down-trodden professional. Figure 2.3 shows three Feynman diagrams for the production of a top-anti-top-quark pair, $t\bar{t}$, from the annihilation of a quark-anti-quark pair, mediated by the gluon. The first diagram, Figure 2.3a, shows the corresponding process for the leading-order term in α_s expansion, referred to as LO-QCD[8]. The next term in the expansion, proportional to α_s^2, is represented by a set of next-to-leading-order (NLO) diagrams, one of which is shown in Figure 2.3b; similarly, an example next-to-next-to-leading-order (NNLO) diagram is shown in Figure 2.3c. Higher-order terms correspond to sets of diagrams with either additional real emissions in the final state, or "virtual" loops. Such loop are sometimes referred to as "quantum corrections", as they alter the scattering amplitude but not the composition of the final state.

Terms beyond Leading-Order in the expansion of $\mathcal{A}$ can lead to UV-divergent integrals. The SM is however a renormalisable theory [48]: any UV-divergences can be cancelled in a finite number of counter-terms. A key technique is regularisation, which isolates divergent pieces of the problematic integrals. Renormalisation is a general prescription for then linking the regularised theory to a physical one, by absorbing the divergent terms into the parameters of the theory. A key consequence of these procedures is the unavoidable introduction of a renormalisation scale μ_F into the calculation, a phenomena known as dimensional transmutation. There is therefore a creative decision to be made about which energy scale to perform some scattering calculation. The parameters of the theory are also functions of energy scale; their

[8] Frequently the 'QCD' part is dropped in this thesis, as it focuses on top-quark states generated through QCD processes. If electroweak (EW) terms are included, the accuracy of both the QCD and EW parts is specified e.g. NLO-QCD + NLO-EW.

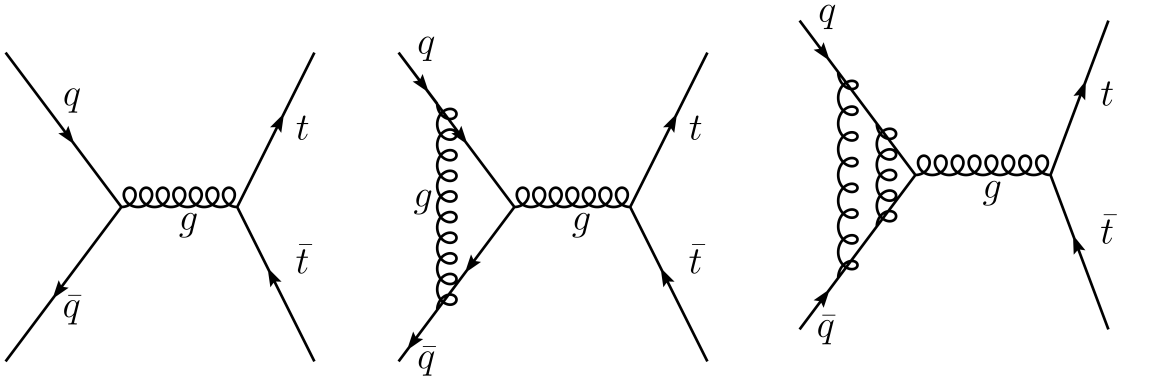

(**a**) Leading0order (LO) (**b**) Next-to-leading-order (NLO) (**c**) Next-to-next-to-leading-order (NNLO)

Figure 2.3: Sets of Feynman diagrams correspond to terms in the perturbative expansion of a scattering amplitude calculation. In the figure, the production of a top-anti-top-quark pair through the annihilation of two quarks, $q\bar{q} \to t\bar{t}$ is shown. The amplitude is evaluated as an expansion in the strong coupling α_s: 2.3a represents the leading-order (LO) term; 2.3b represents one additional next-to-leading-order (NLO) term which features a virtual correction; 2.3c represents an additional term at next-to-next-to-leading-order (NNLO), featuring two virtual corrections.

evolution with that scale is given the beta function,

$$\beta(g) = \frac{\partial g}{\partial \log(\mu)}. \tag{2.5.3}$$

The beta functions for the SM gauge groups in the broken phase (post-EWSB when the $\mathrm{SU}(3)_C$ and $\mathrm{U}(1)_{\mathrm{em}}$ groups remaining), are given at one-loop order as:

$$\beta(e) = \frac{e^3}{12\pi^2}, \tag{2.5.4}$$

$$\beta(g_s) = -\frac{9g_s^3}{16\pi^2}. \tag{2.5.5}$$

The different behaviour of these interactions at differing energy scales is immediately apparent. Whilst the electromagnetic interaction becomes stronger at high scales, the QCD coupling decreases, and this has important phenomenological implications. The running of several SM parameters — the gauge couplings, Higgs potential parameters, and third-generation Yukawa couplings — are shown to three-loop order in Figure 2.4.

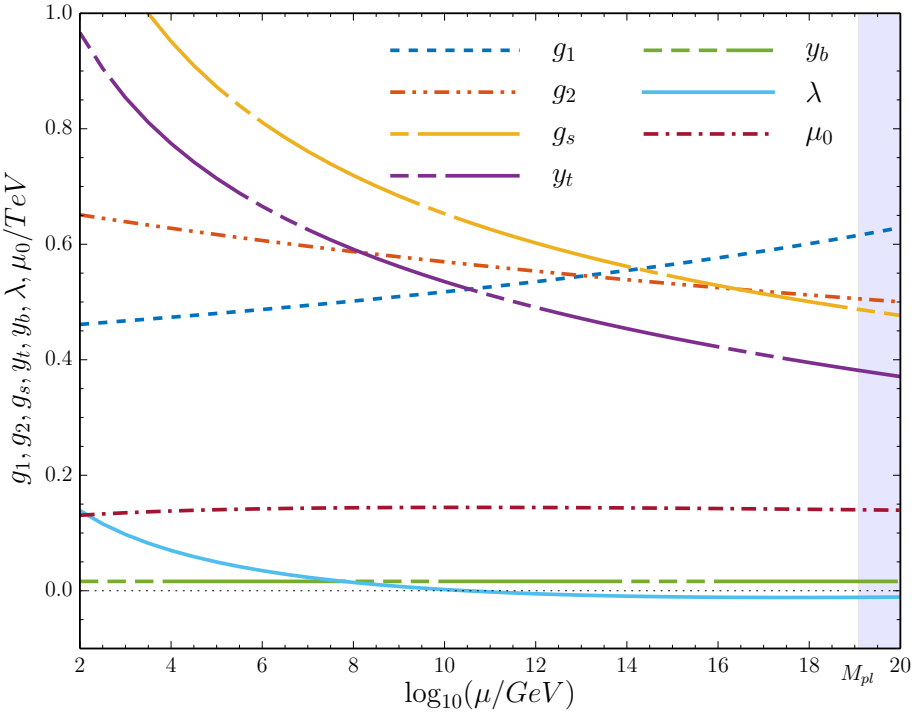

Figure 2.4: The running of the SM couplings, specifically the gauge couplings, third-generation Yukawa couplings and Higgs potential parameters, evaluated to three-loop order using the `mr:Matching and Running` tool up to the Planck scale [47]. The monotonically-decreasing behaviour of the strong coupling g_s leads to asymptotic freedom as high scales.

2.6 QCD Phenomenology

Quantum chromodynamics (QCD) is the sub-sector of the SM commonly referred to as the strong interaction, concerning the dynamics of all fields charged under the $SU(3)_C$ colour group. Quarks are the sole fermionic participants in the strong interaction, which is mediated by the gluon. The non-Abelian nature of QCD means that gluons interact with one another in triple and quartic gauge interactions. The features of QCD are hidden from sight in the SM Lagrangian, but given that the LHC is a hadron collider, it is crucial to understand the behaviour of coloured particles in scattering experiments.

QCD possesses several interesting features with important phenomenological consequences. These features are rooted in the monotonically-decreasing behaviour of the beta-function 2.5.5, and relevant in different energy regimes. *Asymptotic freedom* [49], [50] is a property of QCD (and other gauge theories with particular RGE flow) where the interaction strength decreases at higher energy scales. Without asymptotic

freedom, perturbative calculations in QCD would be impossible. A second property is *colour confinement*. At some low energy scale, commonly denoted Λ_{QCD}, the coupling strength α_s becomes sufficiently large that coloured objects are always contained in bound states [51]. Below Λ_{QCD}, free quarks and gluons are unobservable, trapped inside the colour-neutral hadrons which are observed in particle detectors.

The phenomenology of QCD is particularly apparent when considering the behaviour of a coloured particle in the final state of a scattering process. This coloured particle will undergo QCD brehmsstralung, with the single high-energy *parton* radiating quarks and gluons, and so evolving into to a high-multiplicity state of collimated, lower energy particles. Once the threshold Λ_{QCD} is crossed, confinement demands that hadronisation occurs. In the ATLAS detector, these colour-neutral final states are detected, with confinement shielding the bare coloured partons from ever being observable. The techniques used to simulate this process — the hard scatter of the parton, the showering into many coloured particles, and the binding into hadrons — are critically important to measurements at the LHC and are discussed in Chapter 6. It is useful here to introduce the *jet*: the collimated collection of colour-neutral final states which show up in the detector, and which serve as a proxy for the original hard, coloured parton [52]. Jets are really the dynamical objects of practical collider QCD, but defining exactly what a constitutes a jet requires a certain creativity: it requires a jet algorithm and a jet radius. Since the LHC is a hadron collider, almost all hard proton-proton interactions produce jets. They are ubiquitous at collider experiments. A technical discussion on the jet algorithms used in ATLAS is presented in Section 5.5.1.

2.6.1 Factorisation Theorems and Parton Density Functions

Section 2.5 introduced scattering amplitudes as a key deliverable of interacting QFTs. These are entities which can only be computed perturbatively in regimes where such an expansion is valid. A possible problem arises when we consider hadronic collisions: how can the techniques of perturbative QCD still be useful in scattering amplitude calculations when the initial states are composite? The keys to unlocking this problem are the celebrated factorisation theorems, a cornerstone of hadronic collider phenomenology [53]. Factorisation theorems involve a separation of scales, a decoupling of the short-distance effects, which are described perturbatively, from the non-perturbative long-distance effects. This allows the cross-section to be factorised into two parts, a valid approximation because of the high-momenta of the colliding protons. The cross-section for the process $a, b \to Z$ can be written as the convolution of the partonic cross-section $\hat{\sigma}$, the cross-section of each partonic process, with particular pre-factors f_a, f_b which effectively contain the long-distance effects attributed to the composite

proton structure:

$$\sigma(P_a, P_b)_{a,b\to Z} = \sum_{a,b} \int_0^1 dx_1 dx_2 f_a\left(x_1, \mu_F^2\right) f_b\left(x_2, \mu_F^2\right) \times \hat{\sigma}_{ab\to Z}\left(x_1, x_2, \alpha_s, \frac{Q^2}{\mu_F^2}, \frac{Q^2}{\mu_R^2}\right), \tag{2.6.1}$$

where P_a, P_b are the momenta of the incoming hadrons, Q^2 the square of the transferred momentum, and x the fraction of incoming hadron momentum carried by a particular parton: $p_i = x_i P_i$, $0 \leq x_i \leq 1$. The scales μ_F and μ_R are, respectively, the factorisation scale and the renormalisation scale discussed in Section 2.5. The partonic cross-section is calculated using equation 2.5.1 with the matrix elements computed perturbatively. The strong coupling α_s is also a function of the renormalisation scale.

The pre-factors f_a, f_b are called *parton distribution functions* (PDFs), and give the probability of finding a particular parton at a particular value of x_i. Describing a bound QCD system and therefore not computable perturbatively, the PDFs are instead derived from global fits to relevant data[9]. Traditionally, deep inelastic scatter (DIS) and fixed-target Drell-Yan (DY) data from SLAC [56], CERN and HERA [57] were used in PDF fits. Over time, increased use of collider data from the Tevatron and LHC has become prevalent, and the state-of-the-art now includes inclusive and differential electroweak, top-quark and jet production data, as well as novel fitting techniques and increased accuracy theory calculations [58]–[60]. The evolution of the PDFs with energy scales are given by the celebrated DGLAP equations [61]–[63]. Note that the PDFs as defined above consider only the longitudinal momentum of the incoming hadrons; information about the transverse structure and in particular orbital angular momentum is only contained in so-called generalised parton distributions [64]. One set of PDFs at $Q = 100\,\text{Gev}$ are shown in Figure 2.5.

2.7 Beyond the Standard Model

The introductory chapter discussed how one of the primary motivators of current, and future, particle physics research is the incompleteness of the SM. Since the maturation of the SM in the 1970s, models for new physics have taken flight in a variety of directions. A summary of such models, even those relevant to the top-quark, is beyond the scope of this thesis. There are, however, a number of generic descriptions of BSM physics which prove useful in probing NP models in an agnostic manner. The remainder of this chapter discusses the most popular of these descriptions, the *Standard Model Effective Field Theory*.

[9] In recent years, excitement has built around attempts to compute parton distribution functions on the lattice [54], [55].

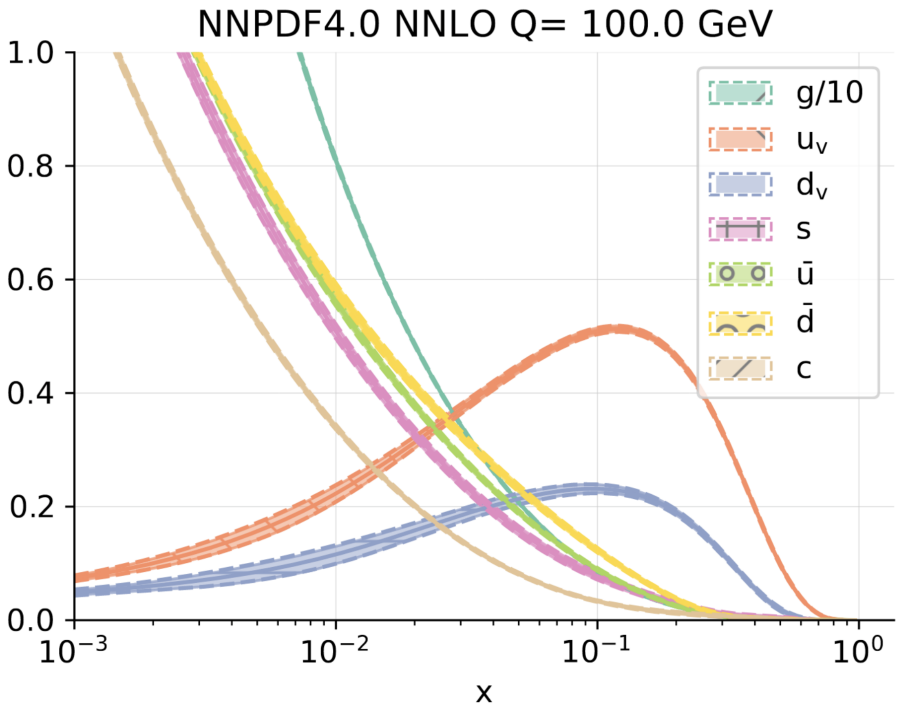

Figure 2.5: The NNPDF Collaboration's state-of-the-art NNPDF4.0 NNLO proton PDFs, at $Q = 100\,\text{Gev}$ [59]. The Bjorken scaling variable x runs along the horizontal, whilst the relative proportion of each type of parton in the PDF is given on the vertical.

2.7.1 Effective Field Theories

The word "effective" brings with it connotations of utility and practicality, despite perhaps not explaining the full picture. This is what *effective field theories* (EFT) are: field theories which do not provide a full description of the physical system to arbitrarily-high energy scales, but offer great utility by providing a simplified explanation [65]. EFTs are motivated in cases where a clear separation, or hierarchy, of scales exist; situations where it is possible to separate the full theory into high-scale behaviour above some cut-off Λ_{UV}, and low-scale behaviour below it. They are a low-energy approximation of some larger, UV-complete theory, containing a set of parameters which describe well the low-scale physical behaviour, with the higher-energy behaviour "integrated out". The utility of EFTs lies in the fact that they are completely legitimate QFTs, and so can be used to calculate scattering amplitudes without possessing exact knowledge of the UV-complete theory.

Numerous examples of EFTs exist across the physics literature, from particle physics [66] to condensed matter physics [67], and from general relativity [68] to hydrodynamics [69]. The canonical example of an EFT in particle physics is the Fermi model of weak decays, which approximates the weak interaction as a four-point *contact interaction* by integrating out the degrees of freedom of the W-boson [70]. The Fermi model proved

exceedingly effective because of a large separation of scales, of around three orders of magnitude, between the β-decay experiments of the time and the electroweak scale.

One of the big players in the particle physics EFT domain is the Standard Model Effective Field Theory, or SMEFT [71]. The SMEFT introduces a set of contact interactions analogous to that of the 4-Fermi theory. It can be constructed through two approaches, a statement which is true of EFTs in general. The first considers a "top-down" approach, beginning with some UV-complete theory, and systematically integrating out the heavy states to yield higher-dimensional 'effective operators' [72]. Alternatively, one can arrive at an equivalent set of operators by adopting a 'bottom-up' approach, and viewing the SMEFT as a deformation of the SM. Here, the SM Lagrangian is generalised to contain all permissible operators of a particular mass dimension d which obey the SM symmetries: $\mathcal{L}_{\text{SM}} \rightarrow \mathcal{L}_{\text{SM}} + \mathcal{L}_{\text{BSM}}$. In this case, the BSM physics is viewed as a perturbation around the SM, and the Lagrangian is expressed as a series expansion in $\frac{1}{\Lambda}$:

$$\mathcal{L}_{\text{SMEFT}} = \mathcal{L}_{SM} + \sum \frac{c_i^d}{\Lambda^{d-4}} Q_i^d, \tag{2.7.1}$$

for mass-dimension $d > 4$. New interactions are contained in the EFT operators Q which are solely functions of the SM fields. Crucially, these operators obey the same symmetry laws as the SM operators themselves: each operator is invariant under G_{SM}, but new Lorentz structures are introduced. The coefficients c_i^d in 2.7.1 are called *Wilson coefficients*.The dependence of some generic observable O is given as an expansion in the Wilson coefficients suppressed by powers of Λ:

$$O = O_{\text{SM}} + \sum_i \frac{c_i^{(6)}}{\Lambda^2} O_i^{(6)} + \sum_{ij} \frac{c_i^{(6)} c_j^{(6)}}{\Lambda^4} O_{ij}^{(6)} + \sum_k \frac{c_k^{(8)}}{\Lambda^4} O_k^{(8)} + O\left(\Lambda^{-6}\right) + \ldots \tag{2.7.2}$$

and truncated according to taste.

By way of example, Figure 2.6 presents permissible dimension-6 diagrams for the scattering of $u\bar{u} \rightarrow t\bar{t}$ in the SMEFT.

The key advantage of the SMEFT lies in its sole use of SM fields: the SMEFT is BSM-model independent, and can therefore probe for NP in an agnostic manner. This comes at the expense of a large number of free parameters, the Wilson coefficients. Additionally, the SMEFT has a limited region of validity, as it is only defined for scales well below Λ. Phenomenologists and experimentalists have turned this large set of free parameters to their advantage, and work systematically to measure each and every Wilson coefficient using experimental data. Setting bounds on Wilson coefficients allows the HEP community to measure the impact of each EFT operator; this in turn indicates where deviations from the SM are arising, and in which sectors tensions with the SM exist. It is now vogue for ATLAS analyses to perform EFT interpretations individually, seeking to set bounds on the relevant Wilson coefficients

for their particular measurement. Experimental collaborations, in an effort to catch up with the phenomenological community, are moving towards large global fits using data from many SM sectors.

SMEFT operators of 'low' mass dimension, $d \leq 8$, are fully categorised [73]–[75], and prescriptions for obtaining higher mass operators exist [76]. At $d = 5$, a single operator and its Hermitian conjugate exist. These operators are known to violate lepton-number conservation and to give rise to neutrino masses. Since neutrino oscillation experiments require neutrino masses to be very small, these dimension-five operators are highly suppressed [77]. The first non-redundant parameterisation of all $\mathcal{L}^6$ operators is referred to as the *Warsaw basis* [73], which has 2499 dimension-six operators which conserve baryon- and lepton-number. This number can be reduced significantly through the introduction of some additional flavour structure [10] [78]. In this thesis, the effects of EFT operators on interesting top-quark spin observables are discussed in Chapter 3, on quantum information observables in the top-quark sector in Chapter 9, and projected limits on Wilson coefficients are derived from consideration of spin observables in the $t\bar{t}Z$ process in Chapter 8.

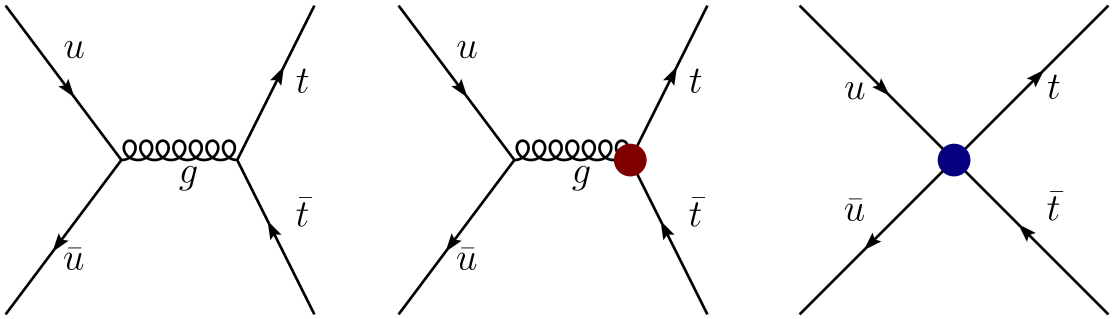

Figure 2.6: Permissible diagrams for the process $u\bar{u} \to t\bar{t}$ in the SMEFT. The coloured circles indicate effective interactions. The first diagram (**a**) is the SM process; the second diagram considers the presence of an enhanced top-quark-gluon coupling (**b**); the third is an effective four-quark contact interaction (**c**) [79].

[10] The SM flavour structure without Yukawa terms is $U(3)^5$. The SM flavour symmetry, once all Yukawa interactions are included, is $U(1)_B \times U(1)^3$.

Chapter 3

The Top-Quark

"Consider the top-quark, alas,
It outweighs all fermions in its class.
Its phenomenology,
As we shall soon see,
Is driven by that gigantic mass."
—

The top-quark is special. It is massive, unique, interesting, and downright troublesome. It is almost as heavy as an atom of gold. It spins, it rapidly decays, it affects other fundamental parameters of the SM. It is frequently cited as our strongest probe of New Physics. It has been my friend for the duration of this PhD, and is what most of this thesis is all about.

3.1 Top of the Quarks

3.1.1 History

The top-quark was a long time coming. A third generation of quarks was postulated by Kobayashi and Maskawa in 1973, as means of describing CP-violation in the weak sector [80]. The existence of third-generation fermions was confirmed, initially through the discovery of the tau lepton in 1975 by Perl et al. [81], and subsequently through the discovery of the b-quark in 1977 [82]. Determination of the b-quark's weak isospin quantum number as $I_3 = -1/2$, through measurement of a forward-backward asymmetry in $e^+e^- \to b\bar{b}$, implied the existence third-generation SU(2) doublet, for which the top-quark is the isospin partner [83]. The stage was set for the top-quark to make its entrance...

Searches for the top-quark began in earnest in the late 1970s, and were taken up at the various collider experiments around the world: first by SLAC and DESY, then the Super Proton Synchrotron (SPS) at CERN, and later by the CDF and D0 experiments at the Tevatron at Fermilab. Lower bounds for the top-quark mass were steadily increased in the late 1980s and early 1990s, including a limit of 91 GeV set in 1992 [84]. This was important as it precluded top-quark production through the channel $W^+ \to t\bar{b}$. In the spring of 1995, the CDF and D0 collaborations finally announced observation of the top-quark at $\sqrt{s} = 1.8\,\text{TeV}$ [85], [86]. The D0 result measured the top-quark mass to be 199 GeV from an integrated luminosity of $50\,\text{fb}^{-1}$; the CDF collaboration were closer to the current value in measuring a mass of 176 GeV from $67\,\text{fb}^{-1}$. Fast-forward to the present day, where nearly three decades of refined measurements place the top-quark mass at around around 172 GeV. The LHC has measured hundreds of millions of top-quarks, allowing for an ambitious and varied programme of top-quark physics to be pursued by the ATLAS and CMS Collaborations.

3.1.2 Significance

The top-quark is the third-generation, spin-1/2, charge-2/3 fermion, which transforms as a colour triplet under $\text{SU}(3)_\text{C}$ and forms one half of the the $\text{SU}(2)_\text{L}$ doublet with the bottom-quark. Every one of its quantum numbers is identical to those of the up and charm quarks, bar one. The top-quark's enormous mass — around 40 times that of the bottom-quark, and heavier than the nuclei of the first 75 elements in the periodic table — is what makes it so special. That large mass is a direct consequence of a large Yukawa coupling, yet the phenomenology driven by that mass makes the top-quark an extremely active area of research, in theoretical, phenomenological and experimental contexts.

Top-quark enthusiasts can study its production cross-section in scattering experiments, its mass or couplings or decay rates, and a myriad of derived properties. The production of top-quarks at the LHC almost always proceeds through gluon-mediation, so accurate measurements of top-quark cross-sections and properties provide stringent tests of QCD [87]. Precise knowledge of the top-quark mass is a crucial input for accurate modelling of both SM and BSM processes [88]. The top-quark may also have a special role within the electroweak (EW) sector. The question which dominates concerns that provocative mass: why is the top-quark Yukawa coupling so large? To phrase the question differently, consider that the top-quark is viewed as the only "natural" quark, of mass around the EW scale: why are the other quarks so unnaturally light? This indicates that the top-quark possesses some close and intimate connection to the Higgs sector and EWSB. A manifestation of this is the key role the top-quark mass plays in determining the RG evolution (refer to Section 2.5) and stability of the Higgs potential [89]. Precise measurements of the top-quark's properties seek to shine a light on the special coalition between the top-quark and the Higgs, and probe New Physics (NP) in the EW sector.

The top-quark may also be the best current candidate in the search for NP, likely playing a leading role above the EW scale. New heavy states will alter top-quark properties through loop corrections: the top-quark is conjectured to be the SM particle with the largest mixing with exotic states under certain scenarios [71], [90]. Heavy BSM resonances should decay preferentially through top-quark channels, leading to deviations from expected SM production rates [91], [92].

3.2 Top-Quark Phenomenology

3.2.1 Top-Quark Production in Hadron Colliders

The dominant mode in which top-quarks are produced at hadron colliders is through the production of top-anti-top-quark pairs, $hh \to t\bar{t}$, where h is generally p or $\bar{p}$. In the operational lifetime of the LHC to date, around 60 million $t\bar{t}$ pairs have been measured by ATLAS [93]. The processes of gluon-gluon fusion, $gg \to t\bar{t}$, are shown at leading order in α_s in Figure 3.1. The additional $t\bar{t}$ production mechanism is that of quark-anti-quark annihilation $q\bar{q} \to t\bar{t}$, for which the leading-order diagram, and two higher-order diagrams, were given in Figure 2.3. In proton-proton collisions evaluated to NLO-QCD for $\sqrt{s} = 13\,\text{TeV}$, around 90 % of $t\bar{t}$ production cross-section stems from gg fusion [94]. The Tevatron collided proton with anti-protons, allowing access to valence anti-quarks interactions which enhanced $q\bar{q}$ production rates.

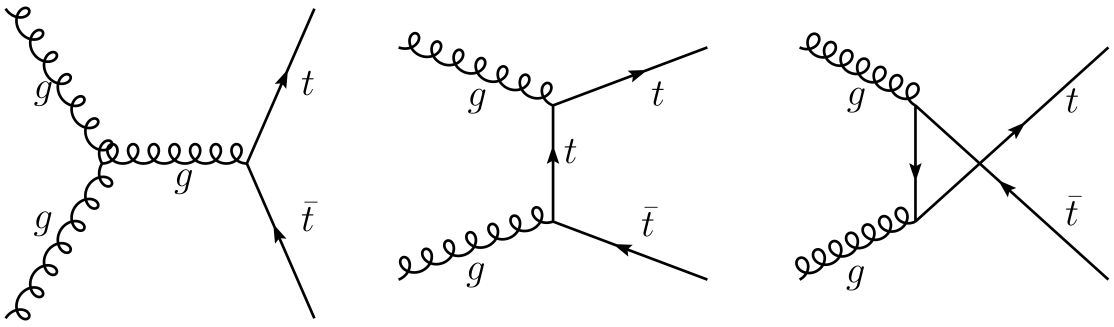

(**a**) s-channel (**b**) t-channel (**c**) u-channel

Figure 3.1: The production of $t\bar{t}$ pairs at the LHC can proceed through the fusion of two gluons, in three distinct channels at LO QCD.

The state-of-the-art theoretical predictions for the total $t\bar{t}$ cross-section is currently NNLO-accurate in QCD with NNLL soft-gluon resummation [95], [96]. (Refer to Section 6.2 for a discussion on these terms.) Predictions at NLO QCD with the inclusion of NLO EW corrections are also available [97]. A quoted value of $\sigma_{t\bar{t}} = 831.8^{+19.8+35.1}_{-29.2-35.1}\text{pb}$ at $\sqrt{s} = 13\,\text{TeV}$ in the Particle Data Group summary assumes a top-quark mass of

172.5 GeV [94]. The $t\bar{t}$ inclusive cross-section has been measured at the CDF, D0, ATLAS and CMS experiments at a variety of centre-of-mass energies. The latest LHC Top Working Group summary plot is presented in Figure 3.2, showing ATLAS and CMS results at 5.02, 7, 8, 13 and 13.6 TeV. The most recent ATLAS result of the inclusive $t\bar{t}$ cross-section at $\sqrt{s} = 13$ TeV is a remarkably precise measurement made in the di-leptonic channel, the first result of its kind at this centre-of-mass energy whose uncertainties fall entirely within the state-of-the-art theoretical prediction [98]. This measurement, along with a number of other ATLAS and CMS inclusive $t\bar{t}$ cross-section measurements, are shown in Figure 3.3.

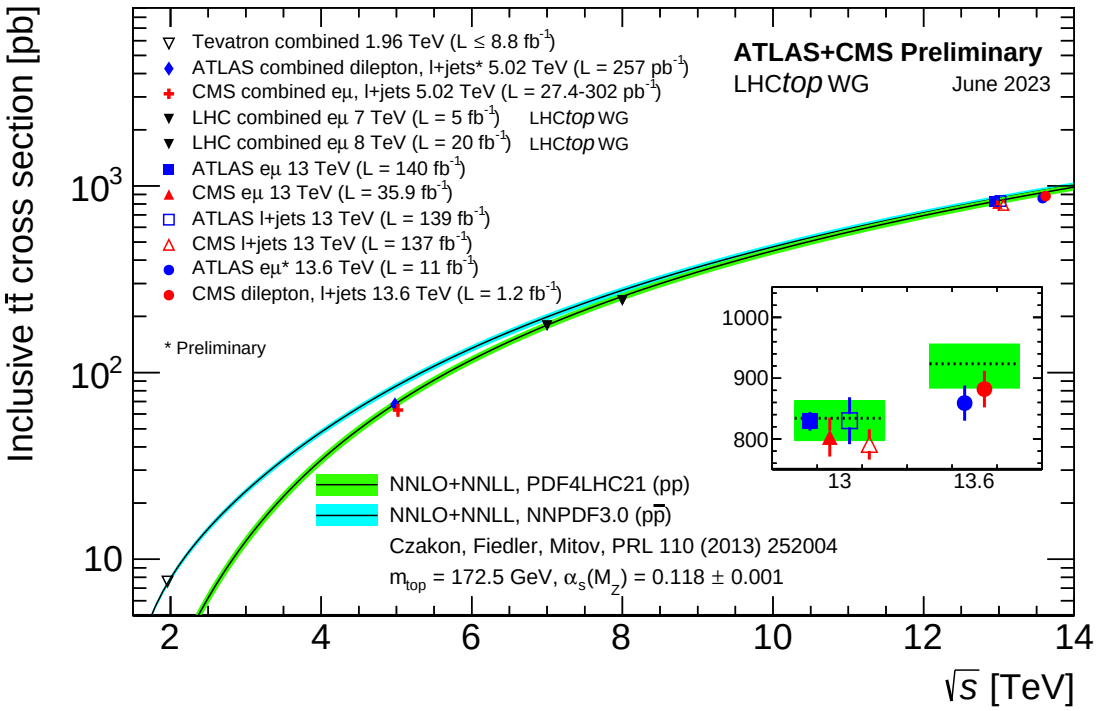

Figure 3.2: A summary of various measurements on the $t\bar{t}$ inclusive cross-section as measured by the ATLAS and CMS experiments [99]. Also shown are the NNLO + NNLL predictions for the processes $pp \to t\bar{t}$ and $p\bar{p} \to t\bar{t}$, with uncertainty bands corresponding to the renormalisation and factorisation scales, PDFs and uncertainty on the value of α_s. All results assume a top-quark mass of 172.5 GeV.

Additional measurements have probed a variety of single, and increasingly higher-dimensional, differential $t\bar{t}$ cross-sections [98], [100]–[103]. Such differential spectra can be presented at reconstruction-level, or unfolded back to parton- or particle-level (formal definitions of these terms are given in Section 6.1). Measuring differential cross-sections provides a rigorous test of the SM and perturbative QCD; they also provide comparisons to state-of-the-art theoretical predictions; constitute important tests of MC generators; are useful inputs for global PDF fits; and provide a probe of NP through

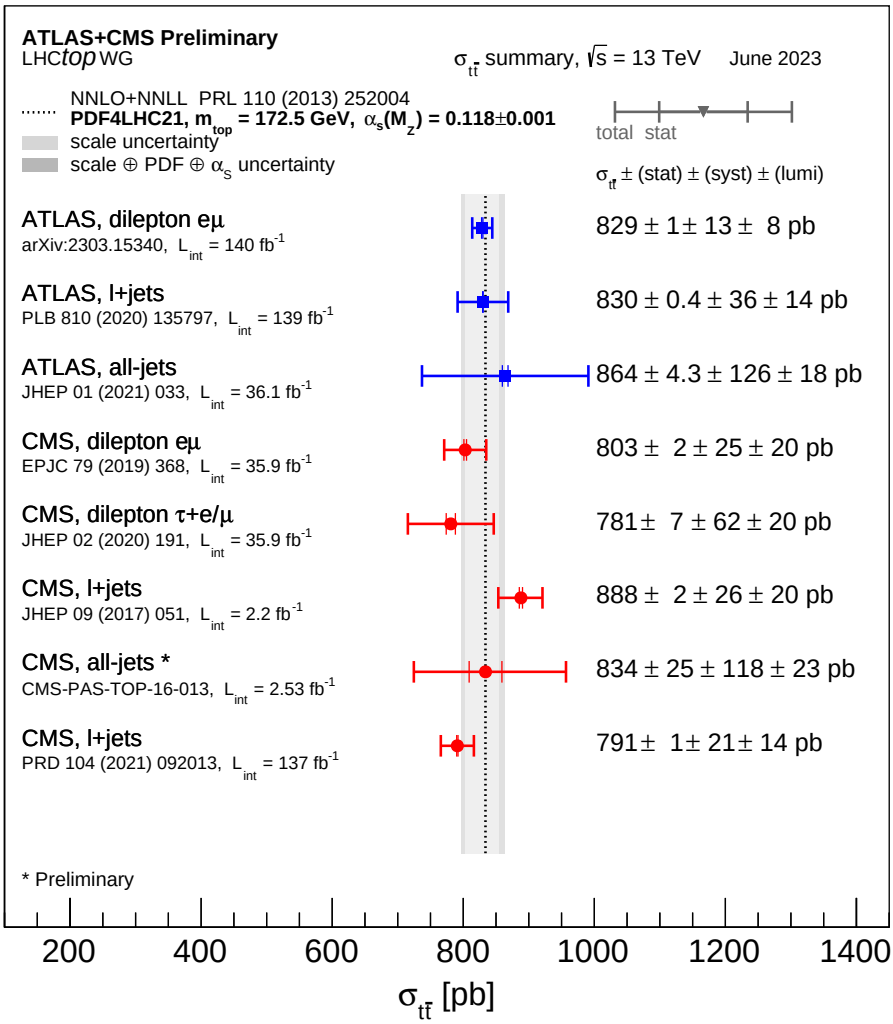

Figure 3.3: A detailed summary of inclusive $t\bar{t}$ cross-section measurements made by the ATLAS and CMS experiments [99]. The uncertainty band correspond to the same uncertainties as stated in Figure 3.2. The hierarchy of precision attainable through the various different $t\bar{t}$ decay channel is illustrated nicely.

EFT fits, or through searches for deviations in high-mass bins. Historical tensions remain between data and simulation some top-quark kinematics and properties.

Although $t\bar{t}$ pair production overshadows other top-quark production mechanisms in terms of total cross-section, many additional mechanisms exist. Chief amongst these is single-top production, a set of electroweak processes which are suppressed with respect to QCD pair production because of the magnitude of the weak coupling. The mechanisms in question are $q\bar{q}' \to t\bar{b}$, $qb \to q't$ and $gb \to tW^-$, along with the conjugate processes for producing $\bar{t}$. Single-top-quark production is an important background process in $t\bar{t}$ measurements such as the one presented in Chapter 10. One

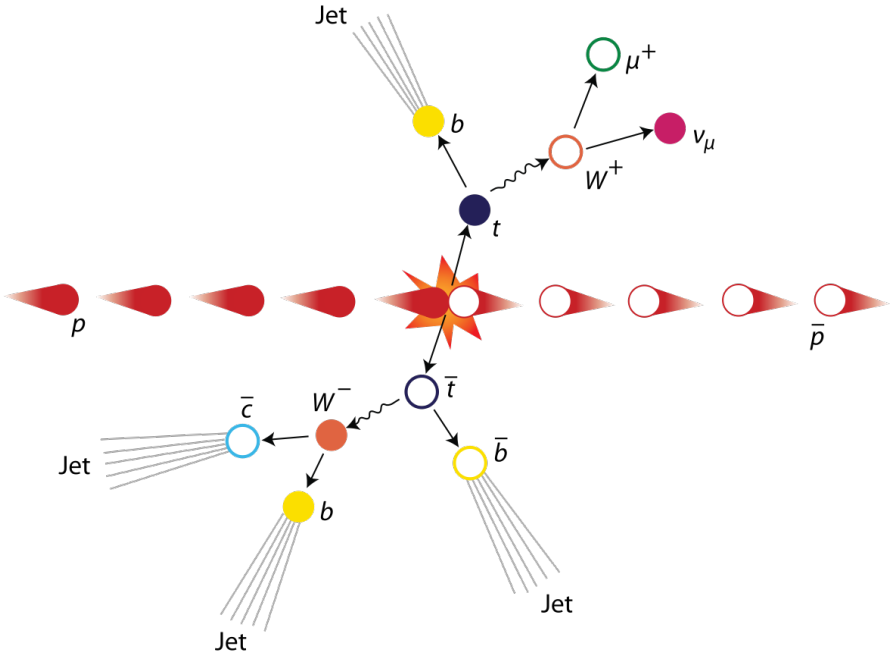

Figure 3.4: A cartoon of a $p\bar{p}$ collision creating a $t\bar{t}$ pair, where the top-quark decays leptonically into an anti-muon and muon neutrino, and the anti-top-quark decays into a b-quark and a $\bar{c}$-quark.

can also consider both $t\bar{t}$ and single-top production in association with additional final-states. Processes in which $t\bar{t}$ pairs are produced with an additional bosonic final-state are key probes of top-EW couplings and NP, and are discussed at greater length in Chapter 8.

3.2.2 Top-Quark Decays

Attention now turns to the decay of the top-quark. And it does not hang around. The SM states that the top-quark must experience a two-body decay into a down-type quark and an intermediate W-boson, which can exist on-shell due to the top-quark's large mass. The decay channel $t \to W^+b$ entirely dominates the branching fraction of the top-quark, a consequence of the CKM matrix structure, thus the total width of the top-quark, Γ_t, is essentially just the partial width $\Gamma_{t\to W^+b}$. The Particle Data Group Top-Quark Summary quotes a width of 1.35 GeV [104], for a top-quark mass of 173.3 GeV with a strong coupling value at the Z mass ($\alpha_s = 0.118$); ATLAS made a measurement of the decay width of 1.9 GeV ± 0.5 GeV in 2017 [105]. The large decay width drives an exceptionally short lifetime: $\tau_t = 0.5 \times 10^{-24}$. This is shorter than hadronisation time-scale $\tau_{had} \approx 1/\Lambda_{\text{QCD}} \approx 3 \times 10^{-24}$ [106], thus one does not observe colour-neutral $t\bar{q}$ mesons or tqq' baryons, including a $t\bar{t}$-quarkonium bound state.

The decay channels of the W-bosons determine the final state of the top-quark decay. Two classes of decays are possible: the hadronic decay, $W^+ \to q\bar{q}'$ into different flavours; and the leptonic decay, $W^+ \to l^+\bar{\nu}_l$, in which lepton flavour universality[1] (LFU) is assumed. This means that when considering $t\bar{t}$ pair decays, three channels can be defined:

- the *all-hadronic* channel, where both W-bosons decay hadronically,
- the *di-leptonic* channel, where both W-bosons decay into charged lepton-neutrino pairs,
- the *semi-leptonic* or *lepton + jets* channel, containing one hadronic and one leptonic W-boson decay.

The branching fractions of each channel, as a percentage of the total $t\bar{t}$ branching ratio, are listed in Table 3.1, and an cartoon $t\bar{t}$ decay is shown in Figure 3.4.

Table 3.1: The branching ratios for a $t\bar{t}$ pair as presented as percentages of the total branch ratio. In the di-leptonic category, the tau-lepton ratios ($e\tau + \mu\tau + \tau\tau$) are combined, as tau-leptons are reconstructed differently to electrons and muons in the ATLAS detector, and are not included in the measurement presented in Chapter 10. The total branching ratio for each category is given in the bottom row. The values are obtained from considering the branching ratios of W-boson as listed in "Gauge and Higgs Boson" summary table of [104].

Di-leptonic				Semi-leptonic			All-hadronic
ee	$e\mu$	$\mu\mu$	$l\tau$	qe	$q\mu$	$q\tau$	qq
1.15	2.28	1.15	6.15	14.4	14.3	15.3	45.4
	10.73				44.0		45.4

The most realistic means of modelling the production of these final states is to consider the general process $pp \to b\bar{b}f_1\bar{f}_1f_2\bar{f}_2$, where f_1 and f_2 are leptons or quarks, and which includes the case where either of both of the top-quarks can exist off-shell. The case where one top-quark is on-shell is called "resonant", and when both top-quarks are on-shell, the system is "doubly-resonant". The modelling of such general processes presents an extreme computational challenge beyond leading-order [107]. Whenever doubly-resonant production dominates, the *narrow-width approximation* (NWA) can be applied [108]. This is a means of reducing the complexity of scattering amplitudes for promptly-decaying resonances, replacing the Breit-Wigner term in the amplitude with a simpler delta function. This has the effect of neglecting non-resonant contributions, forcing the top-quarks on-shell [109]. In general, the NWA is applied

[1] The flavours of the lepton and the neutrino are identical e.g. $W^+ \to e^+\bar{\nu}_e$ is permitted, but $W^+ \to \mu^+\bar{\nu}_e$ is not.

when the total width is much smaller than the mass, $\Gamma << M^2$, and so is frequently utilised in calculations of $t\bar{t}$ production. Envoking the NWA effectively factorises the scattering amplitude into separate production and decay components, a fact which is key in defining a formalism for $t\bar{t}$ spin states, discussed below.

3.3 Taking the Top-Quark for a Spin

The property of spin was introduced as quantum number possessed by all fundamental particles, rooted in irreducible unitary representations of the Lorentz group. This thesis is concerned in large part with studies involving the spin properties of the top-quarks produced in $t\bar{t}$ and $t\bar{t}Z$ production. This section discusses the idea of spin in a top-quark context, paying particular attention to the spin density matrix formalism with which one may study spin properties in $t\bar{t}$ systems.

Composite systems like a $t\bar{t}$ pair may exist in a number of spin states, based on the individual spins of the constituents. When the spin of the individual quarks in the $t\bar{t}$ pair are anti-aligned (they point in opposite directions), they exist in a "spin singlet" state with total spin quantum number $s = 0$; when their spins align, a "spin triplet" of $s = 1$ is formed[3]. *Polarisation* is the degree to which the spin axis of a particle is aligned in a particular direction. An ensemble of unpolarised particles have no preferred spin direction. In the context of this chapter, the term *spin correlation* refers to the degree to which an ensemble of top-quarks' spin axes are correlated to those of the corresponding anti-top-quark. This is defined quantitatively in Section 3.3.2.

Several features of top-quark decays conspire to let its spin properties be studied, even though the top-quark itself decays long before direct measurement. These features are its short lifespan and the chiral nature of the weak interaction. The short lifespan protects the top-quark from spin state decoherence, which can occur through gluon emission. The likelihood of gluon-emission spin-flip transitions occurring before the top-quark decays is heavily suppressed by the large top-quark mass: $\tau_t << \tau_{flip} \propto m_t^2$, [106]. A large fraction of quark hadronisation results in spin-singlet mesons with the original quark spin information destroyed. That short lifetime also protects the top-quark from hadronising into such a state where the spin information would then lost. The $V - A$ structure of the weak decay restricts proceedings to involving left-chiral states, which has consequences for the polarisation of the W^+ boson and thus the directions in which the W^+-boson decay products are ultimately produced with respect to the original top-quarks' spins. [106], [111], [112]. The top-quark is truly unique amongst the quarks in that its dynamics are readily probed through its spin information.

[2]There are other conditions which are sometimes neglected [110].

[3]One would require an odd number of fermions to generate the spin doublet state. These are baryons.

3.3.1 Spin Analysing Power

Consider further the spin analyser used to probe the top-quark spins. The partial decay width of an unpolarised top-quark is given at LO by the differential distribution,

$$\frac{1}{\Gamma_i}\frac{d\Gamma_i}{d\cos\theta_i} = \frac{1+\alpha_i\cos\theta_i}{2}, \tag{3.3.1}$$

where $\cos\theta_i$ is the angular separation between the top-quark and decay product i in the 'parent' top-quark's rest frame. The parameter α_i is known as the *spin analysing power*, and quantifies the extent to which the decay product's spin information is correlated to that of its parent top [113]. It can be computed using perturbative QCD. Charged leptons and down-type quarks have spin analysing powers of unity at LO. This means that for an ensemble of 100% polarised top-quarks, the probability of leptons l^+ being emitted in the direction of the top-quark is maximal. Charged leptons and down-type quarks therefore constitute the best top-quark spin analysers. In contrast, up-type quarks and neutrinos possess $\alpha = -0.3$, whilst b-quarks and W bosons have $\alpha = -0.4$. It in an interesting quirk that charged-leptons have greater spin analysing power than their parent W-bosons. The reasoning is that charged-lepton distributions are generated by interfering W-boson amplitudes of differing helicities: these constructive interference terms push the charged-lepton α to its maximal value.

One can consider higher-order predictions of the spin analysing power, as well as possible deviations under the effects of NP. The consequence of higher-order QCD corrections are a shift in α, as computed in [113]. NP effects on α have been studied from both anomolous coupling [114] and effective field theory perspectives [115]. In particular, the EFT operator connecting the top-quark and W-boson, $Q_{uW,33}$, modifies the tWb vertex structure and therefore the spin analysing power. Remarkably, there is no linear correction to α arising from $Q_{uW,33}$ when considering the full on-shell decay $t \to bl\nu_l$; in other words, NP corrections to top quark decays are a second-order (Λ^{-4}) effect. The magnitude of this EFT correction is less than one part in a thousand.

Charged leptons and down-type quarks are excellent spin analysers, and as such constitute perfect candidates for top-quark spin studies. Experimental considerations now come in to play. The di-leptonic channel is considered an extremely clean channel for making precise measurements, largely due to an excellent signal-to-background ratio, and is thusly popular for $t\bar{t}$ spin studies. In contrast, hadronic channels have garnered less interest in spin contexts for several reasons. Branderburg, Si and Uwer [113] propose using the channel $W^+ \to c\bar{s}$, using c-tagging to capture the $\bar{s}$-jet, with $\bar{s}$ the spin-analyser. The performance of charm-taggers is limited, and as such, these decays suffer from poor reconstruction efficiencies. In short, it is simply much harder to identify a down-type jet than a charged lepton in practical experimental environments. Additionally, many top-quark spin studies require reconstruction of the top-quark kinematics to define particular spin observables — see Section 3.3.3. This can prove challenging in any of the $t\bar{t}$ decay channels, but the all-hadronic channel is plagued by

the issue of correctly matching final-state jets to the correct quark decays. New methods for all-hadronic kinematic reconstruction are becoming available on the market [116], [117], but spin measurements have almost exclusively been made in the di-leptonic channel.

3.3.2 The Spin Density Matrix Formalism in $t\bar{t}$ Production

Spin density is a general concept in the physical sciences, loosely representing the ratio or proportion of various spin states. Frequently such an idea can be captured in the *spin density matrix* (SDM) formalism. The SDM of a quantum system is a complete characterisation of that system in terms of its spins states, defined relative to some particular basis [118], and with matrix elements containing information on the polarisations of system constituents, and correlations between constituent spins. Applications of SDM techniques, or experimental measurements of SDM elements, is common in a number of physical systems: quantum dots [119], paramagnetic molecules [120], baryons [121], mesons [122], [123], gauge vector bosons [124], and quark-gluon plasmas [125]. The SDM formalism can also be applied to the study of top-quarks spins in $t\bar{t}$ production [126], [127]. The following sections discuss this application, in particular linking SDM elements to observables which can be readily measured at the LHC. The remainder of this chapter borrows heavily from [115], [127]–[130].

Under the approximation of on-shell $t\bar{t}$ production and decay, the general partonic reaction of

$$gg, q\bar{q} \to t\bar{t} + X \to b\bar{b} + 4f + X \tag{3.3.2}$$

represents the production of the $t\bar{t}$ pair from gg fusion or $q\bar{q}$ annihilation, with a possible unspecified, additional state X also produced, and where the top-quarks decay weakly to four fermions f in the manner described in Section 3.2.2. Invoking the NWA as a further approximation, the square of the leading-order matrix elements read,

$$\left|\mathcal{A}^{(\lambda)}\right|^2 \propto \mathrm{Tr}\left[\Gamma R^{(\lambda)}\bar{\Gamma}\right] \equiv \Gamma_{ab} R^{(\lambda)}_{ab,\bar{a}\bar{b}} \bar{\Gamma}_{\bar{a}\bar{b}}, \tag{3.3.3}$$

where $\lambda = gg, q\bar{q}$, $R^{(\lambda)}$ is the four-dimensional production SDM for either production process, and Γ represent the two-dimensional decay density matrices [111]. The NWA has allowed for the matrix elements to be written in a factorised form: separate production and decay. The indices span the spin spaces of individual top-quarks, parameterised in some basis, with the barred indices referring to the anti-top-quark spin space.

The production of a $t\bar{t}$ pair can be cast solely as a function of the invariant mass $m_{t\bar{t}}$ and some direction vector, generally taken to be that of the top-quark in $t\bar{t}$ centre-

of-mass frame, $\hat{\mathbf{k}}$[4]. The production SDM is therefore a function of these parameters, $R = R(m_{t\bar{t}}, \hat{\mathbf{k}})$, and the production matrix elements squared are given by [128]:

$$R^{(\lambda)}_{ab,\bar{a}\bar{b}} = \left(\frac{1}{3^2 \text{ or } 8^2}\sum_{\text{colors}}\right)\left(\frac{1}{2^2}\sum_{\text{initial spins}}\right)\mathcal{A}\left(q\bar{q}/gg \to t_a\bar{t}_{\bar{a}}\right)\mathcal{A}\left(q\bar{q}/gg \to t_b\bar{t}_{\bar{b}}\right)^*, \quad (3.3.4)$$

which can be decomposed into the individual spin spaces of t and $\bar{t}$:

$$R_{ab,\bar{a}\bar{b}} = M^{\mu\bar{\mu}}\sigma^{\mu}_{ab}\sigma^{\bar{\mu}}_{\bar{a}\bar{b}} \quad (3.3.5)$$

$$= M^{00}\delta_{ab}\delta_{\bar{a}\bar{b}} + M^{i0}\sigma^{i}_{ab}\delta_{\bar{a}\bar{b}} + M^{0\bar{i}}\delta_{ab}\sigma^{\bar{i}}_{\bar{a}\bar{b}} + M^{i\bar{i}}\sigma^{i}_{ab}\sigma^{\bar{i}}_{\bar{a}\bar{b}}, \quad (3.3.6)$$

where the $M^{\mu\bar{\mu}}$ coefficients are function of $m_{t\bar{t}}$ and $\hat{\mathbf{k}}$. The (λ) superscript has been dropped for clarity, though one should keep in mind always that there are two versions of R, one for gg-fusion and one for $q\bar{q}$-annihilation. Equation 3.3.6 can be written in a more recognised form:

$$R = A\mathbb{1}_2 \otimes \mathbb{1}_2 + B^{+}_i\sigma^i \otimes \mathbb{1}_2 + B^{-}_i\mathbb{1}_2 \otimes \sigma^i + C_{ij}\sigma^i \otimes \sigma^j, \quad (3.3.7)$$

with spin indices suppressed. The tensor product in equation 3.3.7 is applied between the top-quark (to the left) and anti-top-quark (to the right) spin spaces[5], with $\mathbb{1}_2$ the 2×2 identity matrix, and σ_i the Pauli matrices. The parameter A controls the $t\bar{t}$ cross-section and kinematics of the partons [130]:

$$\frac{\mathrm{d}^2\sigma}{\mathrm{d}\Omega \mathrm{d}m_{t\bar{t}}} = \frac{\alpha_s^2\beta}{m_{t\bar{t}}^2}A\left(m_{t\bar{t}}, \hat{k}\right), \quad (3.3.8)$$

where Ω is the solid-angle associated with $\hat{\mathbf{k}}$. The velocity of the top-quark in the $t\bar{t}$ centre-of-mass frame, β, is uniquely determined by the ratio of the top mass m_t to the invariant mass of the $t\bar{t}$ system:

$$\beta = \sqrt{1 - 4m_t^2/m_{t\bar{t}}^2}. \quad (3.3.9)$$

The other pre-factors in 3.3.7 encode the spin information of the system. The terms B_i are vectors encapsulating the polarisation information of the individual top-quark and anti-top-quark. The matrix C_{ij} quantifies the spin correlations between the two quarks. If the top-quark and anti-top-quark possess spin operators S and $\bar{S}$, respectively, these spin coefficients are expectation values of those spin operators: $B^{+}_i = \langle 2S_i \rangle$, $B^{-}_i = \langle 2\bar{S}_i \rangle$ and $C_{ij} = \langle 4S^i\bar{S}^j \rangle$.

[4] In the CoM frame, the top-quark and anti-top-quark are 'back-to-back' by definition, $\hat{k}_t + \hat{k}_{\bar{t}} = 0$

[5] For example, $\mathbb{1}_2 \otimes \sigma^i = \begin{pmatrix} \sigma^i & 0_2 \\ 0_2 & \sigma^i \end{pmatrix}$ with 0_2 a 2×2 matrix of zeros. The resulting matrix is of dimension 4×4.

3.3.3 Decay Products and Angular Observables

The decay spin density matrices are purely a function of the top decay kinematics, and can be written

$$\Gamma_{ab} \equiv \mathcal{M}\left(t_a \to f\bar{f}'b\right)\mathcal{M}\left(t_b \to f\bar{f}'b\right)^* \tag{3.3.10}$$

for the decay into a b-quark plus some $f\bar{f}$ final-state[6]. Each decay spin density matrix may be simplified by considering a particular decay product, defining its directional 3-vector in some basis related to the parent top quark, and integrating out all of the additional degrees of freedom [111]. Under these circumstances, the leptonic decay spin density matrix can be written as:

$$\Gamma_\ell \propto \frac{1}{2}\left(\mathbb{1}_2 + \alpha_\ell(\hat{\ell}_+ \cdot \sigma)\right), \tag{3.3.11}$$

where $\hat{\ell}_+$ is the direction of the leptonic decay product. Define the unit 3-vectors $\hat{\psi}$ and $\hat{\chi}$, corresponding to the direction of a particular decay product of the top- and anti-top-quarks respectively. An expression for the four-fold angular distributions can be obtained by contracting over the spin indices of 3.3.3 [128]:

$$\frac{1}{\sigma}\frac{\mathrm{d}^4\sigma}{\mathrm{d}\Omega_+\mathrm{d}\Omega_-} = \frac{1}{(4\pi)^2}\left(1 + \alpha_\psi \mathbf{B}^+ \cdot \hat{\psi}_+ + \alpha_\chi \mathbf{B}^- \cdot \hat{\chi}_+ - \alpha_\psi\alpha_\chi \hat{\psi}_+ \cdot C \cdot \hat{\chi}_-\right), \tag{3.3.12}$$

where $\mathrm{d}\Omega = \mathrm{d}\cos\theta\mathrm{d}\phi$, and α the spin analysing power discussed in Section 3.3.1. Defining:

$$\cos\theta_i^+ = \hat{\psi}^+ \cdot \hat{\mathbf{e}}_i^+, \tag{3.3.13}$$
$$\cos\theta_i^- = -\hat{\chi}^- \cdot \hat{\mathbf{e}}_i^-, \tag{3.3.14}$$

with $i = \{1, 2, 3\}$, a range of angular distributions can be obtained through partial integration of 3.3.12. The choice of basis with which to define $\hat{\mathbf{e}}^\pm$ is arbitrary. Several useful results are listed below:

- A direct handle on the polarisation with respect to a chosen direction is given by the polar angle single distribution,

$$\frac{1}{\sigma}\frac{\mathrm{d}\sigma}{\mathrm{d}\cos\theta_i^\pm} = \frac{1}{2}\left(1 + \alpha B_i^\pm \cos\theta_i^\pm\right). \tag{3.3.15}$$

[6] The full decay cross-section is given by Equation 4 of [131].

- The polar angle double distribution,

$$\frac{1}{\sigma}\frac{\mathrm{d}^2\sigma}{\mathrm{d}\cos\theta_i^+ d\cos\theta_j^-} = \frac{1}{4}\left(1 + B_i^+\cos\theta_i^+ + B_j^-\cos\theta_j^- - C_{ij}\cos\theta_i^+\cos\theta_j^-\right). \tag{3.3.16}$$

- The single differential distribution where the independent variable is the product of the two polar angle cosines:

$$\frac{1}{\sigma}\frac{\mathrm{d}\sigma}{\mathrm{d}\left(\cos\theta_i^+\cos\theta_j^-\right)} = -\frac{1 + C_{ij}\alpha_\psi\alpha_\chi\cos\theta_i^+\cos\theta_j^-}{2}\log\left|\cos\theta_i\cos\bar{\theta}_j\right|. \tag{3.3.17}$$

In all distributions, repeated indices do not imply summation, but indicate parameters defined with respect to the i^{th} basis vector. The C_{ij} coefficient, given by

$$C(\hat{\mathbf{e}}^+, \hat{\mathbf{e}}^-) = \alpha_\psi\alpha_\chi\frac{\sigma(\uparrow\uparrow) + \sigma(\downarrow\downarrow) - \sigma(\uparrow\downarrow) - \sigma(\downarrow\uparrow)}{\sigma(\uparrow\uparrow) + \sigma(\downarrow\downarrow) + \sigma(\uparrow\downarrow) + \sigma(\downarrow\uparrow)}, \tag{3.3.18}$$

is a useful expression for understanding the spin correlations. Relative to a set of basis vectors, $\hat{\mathbf{e}}^+, \hat{\mathbf{e}}^-$, the coefficient C_{ij} defines a spin asymmetry: it quantifies the asymmetry between spin-aligned and spin-anti-aligned states. Spin polarisations are a statement on the direction of spin of a single quark, whilst the correlations are the asymmetry in the spin-aligned vs spin-anti-aligned case.

The opening angle between the two decay products, φ, is defined by $\cos\varphi = \hat{\psi}_t \cdot \hat{\chi}_{\bar{t}}$, where the t and $\bar{t}$ subscripts indicate that the decay direction 3-vectors are defined in their parent top-quark's reference frame. This observable appears in the differential cross-section,

$$\frac{1}{\sigma}\frac{\mathrm{d}\sigma}{\mathrm{d}\cos\varphi} = \frac{1}{2}(1 - D\cos\varphi), \tag{3.3.19}$$

where D is the related to trace of the spin-correlation matrix through $3D = \mathrm{Tr}[C]$. This distribution is of central importance to the $t\bar{t}$ quantum entanglement measurement presented in Chapter 10.

Expectation values present a simple means of extracting the SDM elements from the distributions presented above. Define the expectation value $\langle s\rangle$ of an observable s in phase-space region Π through,

$$\langle s\rangle = \frac{\int s|\mathcal{A}|^2\mathrm{d}\Pi}{\int|\mathcal{A}|^2\mathrm{d}\Pi} \equiv \frac{1}{\sigma}\int s|\mathcal{A}|^2\mathrm{d}\Pi, \tag{3.3.20}$$

where $|\mathcal{A}|^2$ is the squared-matrix element. By way of example, Equation 3.3.20 is applied to the distribution 3.3.19 to give an expression for parameter D as a function

of the expectation value of 3.3.19. Realising that $|\mathcal{A}|^2 \mathrm{d}\Pi = \mathrm{d}\sigma$, and writing $\mathrm{d}\sigma = \frac{\mathrm{d}\sigma}{\mathrm{d}s}\mathrm{d}s$, Equation 3.3.20 can be written

$$\langle s \rangle = \int s \frac{1}{\sigma} \frac{\mathrm{d}\sigma}{\mathrm{d}s} \mathrm{d}s. \tag{3.3.21}$$

The independent variable in 3.3.19 is $\cos\varphi$. Performing the substitution $s = \cos\varphi$, equation 3.3.19 reads $\frac{1}{\sigma}\frac{\mathrm{d}\sigma}{\mathrm{d}s} = \frac{1}{2}(1 - Ds)$, the right-side of which can be substituted for the left in 3.3.21, and the integration performed:

$$\langle s \rangle = \frac{1}{2}\int_{-1}^{1} s(1 - Ds)\mathrm{d}s = \frac{1}{2}\left[\frac{s^2}{2} - \frac{Ds^3}{3}\right]_{-1}^{1} = -\frac{D}{3}. \tag{3.3.22}$$

The resultant expression

$$D = -3\langle \cos\varphi \rangle \tag{3.3.23}$$

is used to extract D from the measured differential cross-section 3.3.19 in Chapter **??**.

Applying similar treatment to the distributions 3.3.15 and 3.3.17, the following definitions are obtained:

$$B_i^{\pm} = 3\langle \cos\theta_i^{\pm} \rangle, \tag{3.3.24}$$
$$C_{ij} = -9\langle \cos\theta_i^{+} \cos\theta_j^{-} \rangle, \tag{3.3.25}$$

These expressions allow for easy extraction of the spin parameters once the relevant angular observables are defined in a particular basis, as in done for the $t\bar{t}Z$ production channel in Chapter 8.

3.3.4 A Suitable Choice of Basis

The terms $B_i^{\pm}$ and C_{ij} can be written explicitly after defining some orthonormal basis. In principle the choice of basis is arbitrary, but particular bases may be optimal for particular circumstances. A simple example is the beam basis, coincident with the beam axes described in Section 4.2.1, and used for early measurements of spin correlation at the Tevatron. A widely-used choice is the so-called *helicity basis*, defined with respect to the flight direction of one of the incoming partons $\hat{\mathbf{p}}$ and the flight direction of the top-quark $\hat{\mathbf{k}}$ [127]. The three unit vectors $\{\hat{\mathbf{r}}, \hat{\mathbf{k}}, \hat{\mathbf{n}}\}$ form a right-handed orthonormal basis defined by:

$$\begin{aligned} y &= \hat{\mathbf{p}} \cdot \hat{\mathbf{k}} = \cos\Theta \quad , \\ \hat{\mathbf{r}} &= \frac{\mathrm{sign}(y)}{\sin\Theta}(\hat{\mathbf{p}} - \cos\Theta\hat{\mathbf{k}}), \quad \hat{\mathbf{n}} = \frac{\mathrm{sign}(y)}{\sin\Theta}(\hat{\mathbf{p}} \times \hat{\mathbf{k}}). \end{aligned} \tag{3.3.26}$$

The factors of sign(y) are included to break the Bose symmetry of the gg initial state by identifying a specific forward direction, thus ensuring that the relevant spin parameters are non-zero. The helicity basis is sketched in Figure 3.5. The polarisation vectors can be written

$$B^{\pm} = B_r^{\pm}\hat{\mathbf{r}} + B_k^{\pm}\hat{\mathbf{k}} + B_n^{\pm}\hat{\mathbf{n}}. \tag{3.3.27}$$

Components B_r, B_k indicate longitudinal polarisations whilst B_n induces transverse polarisations. The C matrix is expressed under this basis decomposition as

$$\begin{aligned} C = C_{rr}\hat{\mathbf{r}}\hat{\mathbf{r}}^{\intercal} &+ C_{kk}\hat{\mathbf{k}}\hat{\mathbf{k}}^{\intercal} &+ C_{nn}\hat{\mathbf{n}}\hat{\mathbf{n}}^{\intercal} \\ + C_{rk}^{+}\left(\hat{\mathbf{r}}\hat{\mathbf{k}}^{\intercal} + \hat{\mathbf{k}}\hat{\mathbf{r}}^{\intercal}\right) &+ C_{kn}^{+}\left(\hat{\mathbf{k}}\hat{\mathbf{n}}^{\intercal} + \hat{\mathbf{n}}\hat{\mathbf{k}}^{\intercal}\right) &+ C_{rn}^{+}\left(\hat{\mathbf{r}}\hat{\mathbf{n}}^{\intercal} + \hat{\mathbf{n}}\hat{\mathbf{r}}^{\intercal}\right) \\ + C_{rk}^{-}\left(\hat{\mathbf{r}}\hat{\mathbf{k}}^{\intercal} - \hat{\mathbf{k}}\hat{\mathbf{r}}^{\intercal}\right) &+ C_{kn}^{-}\left(\hat{\mathbf{k}}\hat{\mathbf{n}}^{\intercal} - \hat{\mathbf{n}}\hat{\mathbf{k}}^{\intercal}\right) &+ C_{rn}^{-}\left(\hat{\mathbf{n}}\hat{\mathbf{r}}^{\intercal} - \hat{\mathbf{r}}\hat{\mathbf{n}}^{\intercal}\right), \end{aligned}$$

which contains six symmetric and three antisymmetric terms. Explicit forms of the $B_i^{\pm}$ and C_{ij} components, in terms of the kinematics of the $t\bar{t}$ production, can be found in [131]. [7].

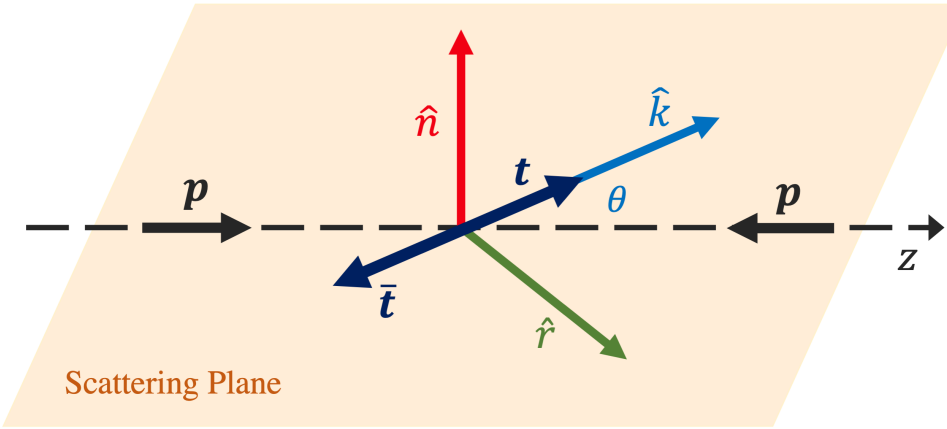

Figure 3.5: The helicity basis is an important basis for characterising spin density matrix elements. It is defined in the centre-of-mass frame, where the top-quarks are produced back-to-back. Incoming protons enter along the z-axis. The direction of the produced top-quark defines the $\hat{\mathbf{k}}$ basis vector, the plane defined by $\hat{\mathbf{k}}$ basis vector and the z-axis is termed the "scattering plane", with the angle between these two directions θ. The basis vector $\hat{\mathbf{n}}$ is the normal vector of the scattering plane, and the basis vector $\hat{\mathbf{r}}$ is that vector which is orthogonal to both $\hat{\mathbf{k}}$ and $\hat{\mathbf{n}}$. Together, $\{\hat{\mathbf{r}}, \hat{\mathbf{k}}, \hat{\mathbf{n}}\}$ define a right-handed orthonormal basis.

[7] Explicit forms in the presence of NP are given in the anomolous coupling framework in [127]

3.3.5 Phenomenology of the $t\bar{t}$ Spin Density Matrix

The SM predicts that the spins of $t\bar{t}$ pairs are unpolarised at Born-level QCD, due to the approximate time- and parity-invariance of QCD [132], $B_i^+ \approx B_i^- \approx 0$. Components of longitudinal polarisations arising from NLO EW corrections, and transverse polarisations arising from absorptive processes [133], [134], are of $(O(1\%))$. In contrast, single-top-quark production processes produce highly polarised top-quarks, once again a consequence of the chiral weak interaction at the Wtb vertex [112], and measurements of these polarisations have been made [135].

The spin states of top-quarks in $t\bar{t}$ production are predicted to be highly correlated [132], [136], [137], $C_{ii} \neq 0$. The helicity basis defined above is most frequently used to probe the elements of the spin correlation matrix C_{ij}. The diagonal elements are referred to as *spin correlations* and the off-diagonal elements as *cross-correlations*. All diagonal spin correlations are C- and CP-even, as is the term cross-correlation C_{rk}^+. All of these elements take on non-zero values in the SM, with the element C_{rr} being the smallest due to cancellations between gg-fusion and $q\bar{q}$-annihilation helicity states [127]. The other positive cross-correlations, C_{kn}^+, C_{rn}^+, arise from negligible mixed QCD-EW 1-loop corrections. The negative cross-correlations, $C_{rk}^-, C_{kn}^-, C_{rn}^-$, are sourced from CP-violating production mechanisms, so are suppressed in the SM, but constitute a useful probe of CP-violation in the QCD sector.

3.3.6 Measurements and Developments of the $t\bar{t}$ Spin Density Matrix

This chapter concludes with a short review of the history of theoretical predictions and experimental measurements of the $t\bar{t}$ SDM elements over the last three decades. First measurements of spin correlations in $t\bar{t}$ systems were made at the Tevatron in di-leptonic [138]–[140] and semi-leptonic channels [141], [142]. In the early career of the LHC, ATLAS studied the azimuthal opening angle between the decay leptons in the laboratory frame at $\sqrt{s} = 7$ TeV [143], applying a template fit using two dedicated MC-simulated samples, one with spin correlations preserved in the top-quark decays, and one with spin correlations set to zero. This method allowed for the first exclusion of the 'zero spin correlation hypothesis' at a certainty of over five standard deviations: unambiguous observation of spin correlations in $t\bar{t}$ production. An analogous methodology is applied in Chapter 8, where the study of spin correlations in the $t\bar{t}Z$ channel is presented. Subsequent measurements by the ATLAS and CMS experiments studied additional spin observables at $\sqrt{s} = 7$ TeV [144], [145] and $\sqrt{s} = 8$ TeV [146], [147], finding no significant deviations from SM expectations.

During the LHC Run-2 campaign, ATLAS re-studied the azimuthal opening angle at $\sqrt{s} = 13$ TeV [148], finding significant tension with SM predictions: the observed strength of spin correlations was higher than that predicted by leading theoretical predictions, and by NLO event generators. This measurement was also used to set bounds on supersymmetric top squark masses, highlighting the utility of such angular

and spin-observable measurements in constraining BSM model parameters spaces. The full SDM was measured at $\sqrt{s}$ = 13 TeV by the CMS experiment in 2019 [149]. In this measurement, a large number of angular differential cross-sections were unfolded back to parton- and particle-level, including the distribution $\frac{d\sigma}{d\cos\varphi}$, which is a critical observable in the measurement of quantum entanglement presented in Chapter 10. SDM elements were extracted from the relevant angular distributions, and compared to the latest fixed order and NLO-accurate event generator predictions. A selection of measured angular and spin coefficients are shown in Figure 3.6. Limits were set on a particular EFT operator, namely the chromomagnetic dipole moment operator Q_{tG} which controls the six-dimensional top-gluon effective coupling, and on several anomolous coupling parameters.

Theoretical predictions for spin correlations and polarisations have advanced significantly. NLO-accurate SDM elements have been available for a number of years [150]–[152], and have been surpassed in accuracy by NLO + Weak corrections [127], NLO + EW corrections [153], and most recently, full NNLO-accuracy predictions [154], [155]. The most recent predictions have reduced the tension present in the $\sqrt{s}$ = 13 TeV ATLAS and CMS measurements, whilst not entirely removing it.

This review has shown that $t\bar{t}$ spin correlations are experimentally-verified to high precision, and that the elements of the SDM have been measured and modelled at a number of centre-of-mass energies. This thesis presents novel uses of the SDM formalism: in considering the spin correlations and polarisation of top-quarks produced in $t\bar{t}Z$ production in Chapter 8; and in using the SDM to make statements regarding the underlying quantum entanglement of the $t\bar{t}$ system in Chapter 9. Future research will surely deliver new measurements of the SDM at $\sqrt{s}$ = 13 TeV and at higher energies, including higher-dimensional differential measurements of SDM observables which the phenomenological community is crying out for [115]. Such updated measurements will have great power in setting limits on a large number of EFT operators, and complimentary measurements could shine light on quantum information phenomena.

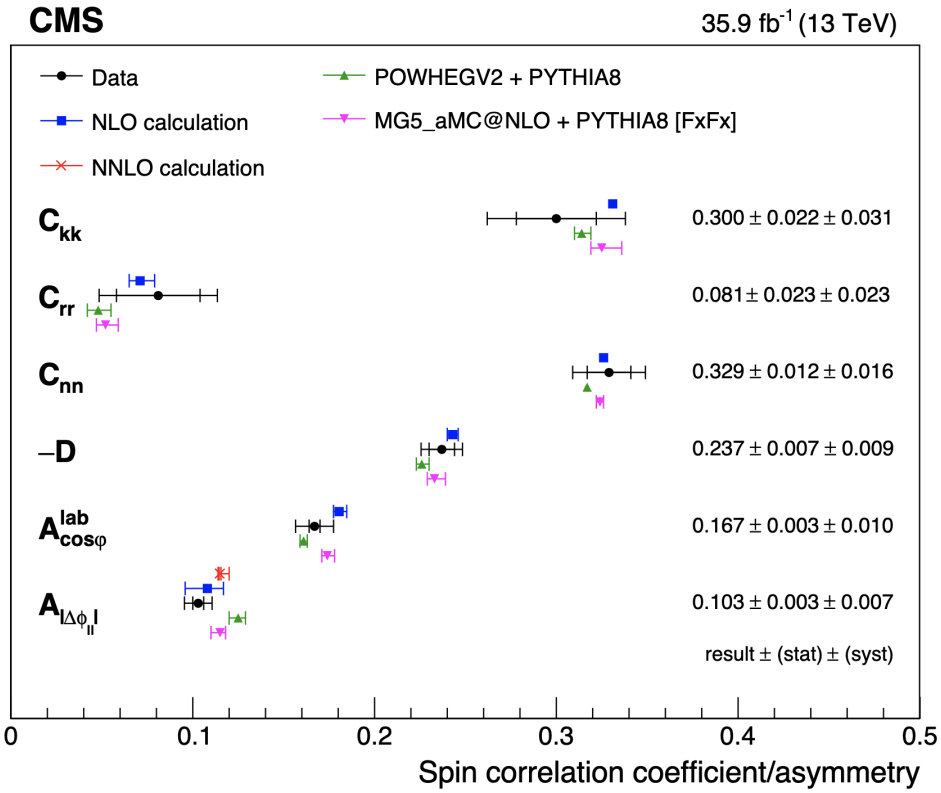

Figure 3.6: A comparison of CMS data to various fixed-order and MC-simulation-derived predictions for several key angular and spin coefficients, including the diagonal elements of the spin-correlation matrix and the negative of the D coefficient of 3.3.19 [149]. Coefficients $A_{\cos\varphi}^{\text{lab}}$ and $A_{|\Delta\phi_{ll}|}$ are defined as asymmetries in the distributions 3.3.19, where in this instance $\cos\varphi$ is defined in the laboratory frame, and $\Delta\phi_{ll}$, the opening angle of the leptons in the laboratory frame. Horizontal error bars give the statistical (inner) and total (outer) uncertainty on coefficient, and it can be seen that all SM predictions are essentially compatible with the data to within the quoted error. It should be noted for future reference that the measured value of $D = -0.237$ pertains to the $\cos\varphi$ observable as measured inclusively in $m_{t\bar{t}}$. These results represent the most up-to-date measurements of these coefficients at $\sqrt{s} = 13\,\text{TeV}$.

Chapter 4

The Large Hadron Collider and the ATLAS Detector

"For QCD results of high status,
(If you don't want to solve on the lattice)
Use that famous detector,
That great particle inspector,
A Toroidal LHC Apparatus"
—

The *Conseil Européen pour la Recherche Nucléaire*, or CERN, is by many accounts the largest particle physics laboratory on Earth. Since its inception in 1954, CERN has pursued a wide and varied programme of particle, nuclear, accelerator and high-energy physics research. The discoveries of neutral currents [156], electroweak bosons [157]–[160], direct CP-violation [161], quark-gluon plasma (QGP) [162], and the Higgs boson [39], [40] are all credited to CERN, to list but a few of its particle physics achievements.

The current golden child of CERN is the Large Hadron Collider (LHC) [1], the machine that made possible the last of those discoveries possible. The LHC facilitates the study of proton collisions and heavy-ion collisions at energies never attained before in particle colliders. Its physics programme is nothing if not diverse, investigating everything from the couplings of fundamental fermions and bosons, to searches for BSM candidates; from dedicated measurements of CP-violation in the B-sector, to the phenomenology of heavy-ion collisions; from the dynamics of QGPs, to diffractive proton scattering in forward regions. This enormous physics programme is undertaken by several experiments of varied size, design and scope. The largest of these are the ATLAS [163] and CMS [164] experiments, so-called "general-purpose detectors" with broad physics programmes, including the measurements of angular properties of top-quarks with which this thesis is chiefly concerned. The following chapter discusses how the LHC delivers a high luminosity of proton collisions to the ATLAS detector,

and the systems of the ATLAS detector which turn such collisions into groundbreaking physics results.

4.1 The Large Hadron Collider

The Large Hadron Collider (LHC) is exactly that: an extremely large collider of high-intensity hadron beams. The name LHC refers strictly to the 26.7 km circumference ring which constitutes the largest accelerator ring in the CERN accelerator complex. The circular tunnel it occupies was originally the home of the Large Electron-Positron collider (LEP) [165], the first collider experiment dedicated to searches for the Higgs boson.

The LHC is of synchrotron design, the successor in a long line of circular particle accelerators, in which injected beams of particles follow closed-loop trajectories [166]. Acceleration is achieved by passing particles through radio-frequency (RF) cavities, where oscillating electric fields transfer energy to particles in the beam-wise direction [167]. Cyclic accelerators deliver far higher particle energies than linear colliders because the particles can pass through the RF cavities many times as they circulate. The bending of the beam is achieved through a particular configuration of magnetic fields. The synchrotron is distinguished amongst its predecessors in holding particle beams in a constant radius orbit, achieving the appropriate acceleration and bending through phasing of the RF frequency and bending magnetic field[1]. The interplay between the oscillation frequency of the RF cavities and the revolution frequency of the beam create an integer number of "RF buckets" around the ring [168]. When operating at full energy, a particle at the centre of such a bucket is exactly synchronised with the RF frequency and sees zero accelerating voltage. Particles at other positions will experience varying amounts of acceleration: this has the effect of clumping particles together into confined "bunches".

Accelerating a beam of particles is only half the fun. To generate particle collisions at the LHC, two separate beams are accelerated to particular beam energies, then brought together at designated interaction points. The LHC has four collision points, and the various experiments, including ATLAS and CMS, are clustered around these points. The beam energies determine the centre-of-mass energy, $\sqrt{s}$: this is the energy available in collisions with which to generate new final states. Higher values of $\sqrt{s}$ correspond to larger collision energies and a probing of shorter distance scales.

[1] In contrast, older circular detector designs like the cyclotron held entire discs under constant electric and magnetic fields, with particles accelerating as they traced spiral trajectories outwards from the disc centre.

4.1.1 LHC Operation

Maximising the running time of the LHC maximises the number of proton-proton collisions. Of course, there are many factors — accelerator and detector performance, energy consumption, socio-economic pressures — which mean the LHC cannot be operated continuously. The LHC programme divides the lifetime of the LHC into periods of data-taking, known as "Runs", and periods of shut-down, during which maintenance and upgrading of the accelerator and detector infrastructures can be conducted. A particular run collides particles at set centre-of-mass energies. The *Run-1* period occurred between 2009 and 2013, operating at $\sqrt{s}$ = 900 GeV , 7 TeV and 8 TeV. *Long-Shutdown 1* followed, during which time upgrades were made to the magnet infrastructure to enable eventual collision energies of $\sqrt{s}$ =14 TeV. The *Run-2* campaign operated at $\sqrt{s}$ = 13 TeV from 2015 to 2018. The data used in the entanglement measurement presented in this thesis (Chapter 10) were collected by the ATLAS detector during this run. *Long-Shutdown 2* commenced in 2018, before the long-awaited *Run-3* campaign began in July of 2022 at $\sqrt{s}$ = 13.6 TeV. The target collision energy of 14 TeV is yet to be achieved, a consequence of long-running issues with magnet training [169].

4.1.2 Accelerator Chain

Proton beams of energy $\sqrt{s}/2$ are not attained in the LHC alone. A dedicated chain of pre-existing accelerators, both linear and synchrotron, were repurposed for operation alongside the LHC [170], [171]. Some of these accelerators are themselves retired collider experiments reborn in pursuit of higher collision energies. Figure 4.1 illustrates this complex setup. Protons are produced by a duoplasmatron source, in which hydrogen gas is dispossessed of its electrons to form a plasma, from which protons can be extracted [172]. The protons then process through a series of accelerators, each composed of radio-frequency (RF) cavities which provide electrical impulses through oscillating electric fields. Protons are first boosted up to 50 MeV in Linac2, a linear accelerator dating from the 1970s. Linac2 has been superseded by Linac4 for Run-3 onwards. The protons are passed to the Proton Synchrotron Booster (PSBooster) which further accelerates them up to 1.4 GeV, or 2 GeV from Run-3 onwards. Next comes the Proton Synchrotron (PS), which has been accelerating protons for over 60 years, and delivers 26 GeV protons to the Super Proton Synchrotron (SPS). The SPS accelerates the protons to 450 GeV before their injection into the main LHC ring, which brings them up to a final energy of 6.5 TeV over a period of 20 minutes. The beams are then held at this energy and brought together at the collision points, where the experiments record the outcomes of the collisions. Eventually, the beams are dumped into dedicated facilities known as Target Dump Externals (TDEs), designed to progressively absorb the beam energy and thus safely terminate the beams [173]. By the end of Run-2, the proton beams which circulated the LHC were composed of 2556 bunches of 1.15×10^{11} protons, with each bunch separated by 25 ns [174].

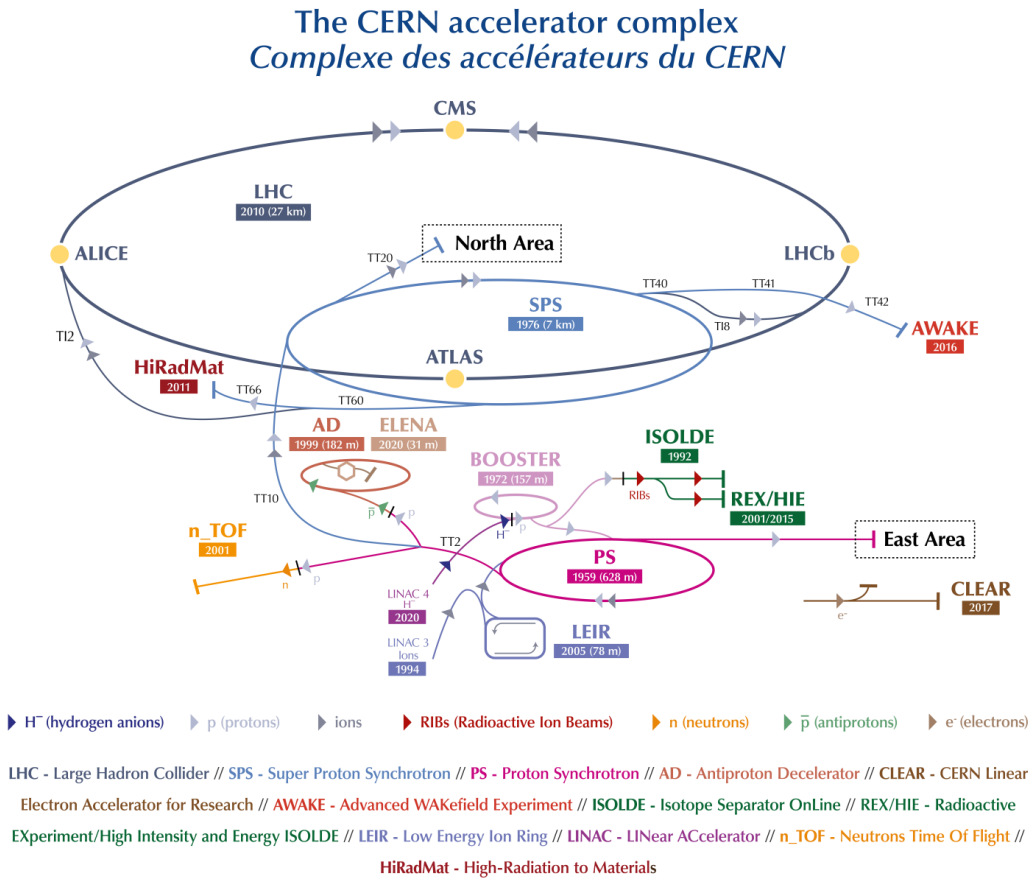

Figure 4.1: The CERN accelerator complex [175]. The specific LHC accelerator chain is composed of a series of linear and circular accelerators which collectively achieve proton beam energies of 6.5 TeV. LINAC4 has replaced LINAC2 from Run-3 onwards.

Whilst the other stages of the accelerator chain use room-temperature magnets, the LHC is the first CERN-based accelerator to employ superconducting magnets. It uses a niobium-titanium variety, cooled using liquid helium, to generate the intense magnetic fields required to manipulate the beams [176]. A total of 1232 dipole magnets (8.3T) are employed to generate magnetic fields perpendicular to the beam-line which bend the beam trajectories into the desired circular shape. Quadrupole magnets, of which there are 392, focus the beam in the plane perpendicular to the beam-line, and various higher-order multipole magnets provide additional beam corrections [177].

4.1.3 Beam Characteristics

Instantaneous luminosity $\mathcal{L}$ is a measure of the flux of colliding particles which can be achieved for given collider conditions. In scattering experiments like the proton beam

collisions of the LHC, the expected number of events N of some process X, observed over some time-window Δt, is given by the *integrated luminosity* L and the cross-section of process X:

$$N_X = \sigma_X \cdot L = \sigma_X \cdot \int_{\Delta t} \mathcal{L} \mathrm{d}t, \tag{4.1.1}$$

where the cross-section σ_X is a function of $\sqrt{s}$. It is readily seen from 4.1.1 that N_X grows with increasing $\mathcal{L}$, motivating careful tuning of the beam characteristics to maximise the integrated luminosity[2].

The instantaneous luminosity for the collision of two beams, composed of bunches with particle populations N_1 and N_2, and collided with a frequency f_{coll}, is given by [104] as:

$$\mathcal{L} = f_{\text{coll}} \frac{N_1 N_2}{4\pi \sigma_x^* \sigma_y^*} \mathcal{F}. \tag{4.1.2}$$

The geometric luminosity reduction factor $\mathcal{F}$, $\mathcal{F} \sim 1$, accounts for inefficiencies resulting from non-zero crossing angles between the beams, and finite bunch length [178]. The collision frequency of a circular collider is expressed as the product of the revolution frequency, f_0, and the number of bunches per beam, k_b. The σ_x^*, σ_y^* terms denote the root-mean-square beam dimensions in the x and y directions which span the plane transverse to the beam, with the star indicating evaluation at the interaction point. Consideration of the transverse beam dynamics allows the beam dimensions to be expressed as:

$$\sigma_x^2(s) = \frac{\epsilon_{nx} \beta_x(s)}{\beta\gamma}, \tag{4.1.3}$$

with $\gamma = (1-\beta)^{1/2}$, $\beta = v/c$, and an analogous expression for the y ordinate. Here, ϵ_{nx} is the normalised emittance, $\beta_x(s)$ the amplitude function or beta function, and s the beam path length [104], [179]. Precise control of these parameters is essential to achieving high luminosities: careful design of the magnet lattice is crucial in focusing the beams to minimise β_x at the collision point; techniques like beam cooling are invaluable in maintaining beam quality and therefore reducing emittance [180]. Table 4.1 lists the LHC operating parameters discussed above for two scenarios, namely the projected design running conditions and achieved Run-2 conditions. Figure 4.2 shows the total integrated luminosity provided by the LHC over the Run-2 campaign, and the smaller quantity which was recorded by the ATLAS detector.

[2] For any process X measured at the LHC, the statistical uncertainty scales as $1/\sqrt{N_X}$. Maximising the number of measured events naturally improves the statistical power of a measurement of X.

Table 4.1: LHC operating parameters, adapted from [181], based on [182]

Parameter	Design	Run-2	Units
Beam energy	7.0	6.5	TeV
Bunch population (N_b)	1.15	1.15	10^{11} protons
Bunch spacing	25	25	ns
Bunch multiplicity (k_b)	2808	2556	
Revolution frequency (f_0)	11.2	11.2	kHz
Normalised emittance (ϵ_n)	3.75	2.2	μm
Beta function (β^*)	55	25	cm
Crossing angle (θ_c)	285	260	μrad
Geometric reduction (F)	0.836	0.858	
Peak luminosity $(\mathcal{L})$	1.0	2.0	10^{34} cm^{-2} s^{-1}

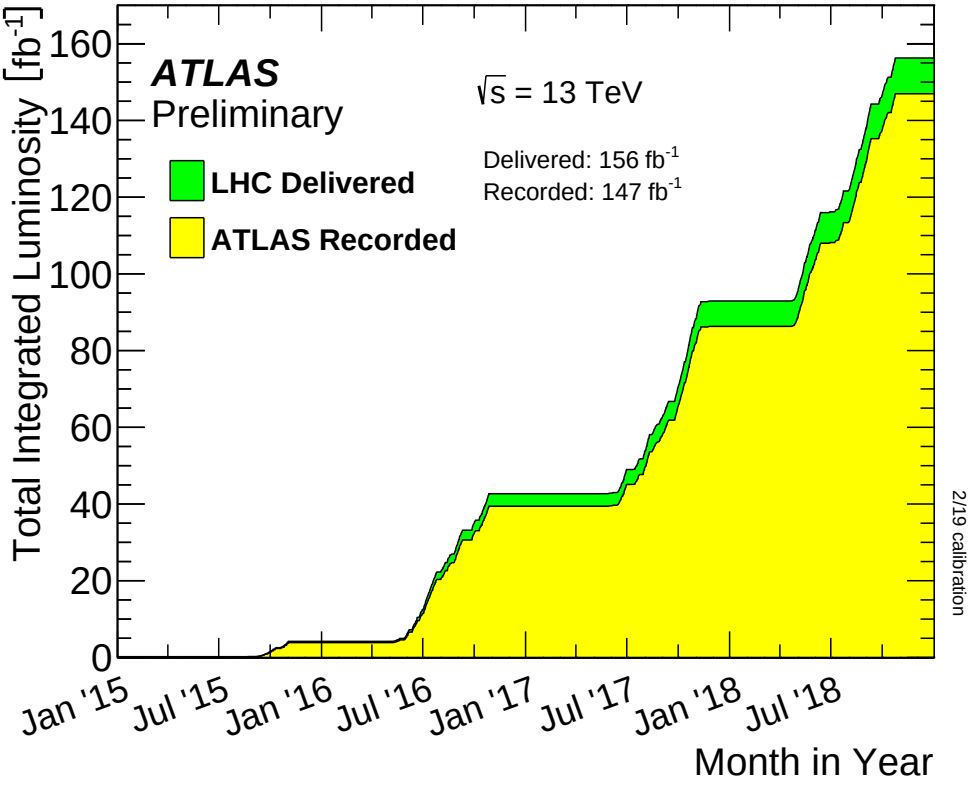

Figure 4.2: Total integrated luminosity from the Run-2 LHC campaign as delivered by the LHC and recorded by ATLAS [183].

4.2 Introduction to the ATLAS Detector

This chapter is one of superlatives. Not only is the LHC the largest and most powerful particle collider ever built, but the ATLAS detector [163] possesses the largest detector volume every constructed for a particle collider[3]. Located almost 100m underground at Point 1 on the LHC ring, the ATLAS detector is a general-purpose detector with a large experimental physics remit. This 25m wide, 44m long, 7000 tonne behemoth is composed of a superconducting magnet infrastructure and several detector sub-systems. These "sub-detectors" are arranged in a cylindrically-symmetric configuration around the collision point. A combination of barrel sub-detectors, which cover the central regions around the interaction point, and end-cap systems, which sit at either end of the cylindrical detector volume capturing emissions in the forward and backward directions, allow ATLAS to cover almost the entire 4π solid angle. A radial cross-section of the ATLAS detector is sketched in Figure 4.3. Proceeding outwards from the interaction point, the Inner Detector (ID) (Section 4.3) focuses on precision tracking of charged particles; the calorimeter systems (Section 4.4), capture and quantify energy deposits from electromagnetic and hadronic particles; the Muon Spectrometer (MS) (Section 4.5) provides additional tracking for muons, which in general permeate furthest through the detector volume. Additional critical components include the triggering and data acquisition systems (TDAQ) which filter and record useful event data from the millions of collisions happening each second, as discussed in Section 4.6.

4.2.1 Coordinate System

ATLAS employs a particular right-handed coordinate system, centred at the nominal interaction point within the detector, as shown in Figure 4.4. In this basis, the x-direction points towards the centre of the LHC ring, the z-axis points down the beam pipe, with the y-axis pointing almost vertically upwards. Particular kinematic quantities may appear with an appropriate subscript to denote their component in a particular direction: the four-momenta of a particle may be written in terms of its energy and components of three-momenta, $p^{\mu} = \left(E, p_x, p_y, p_z\right)$, defined with respect to this coordinate system. The transverse plane subtended by the x and y axes is characterised by the polar coordinates r, the distance from interaction point, and ϕ, the azimuthal angle aroud the beam pipe from the x-axis. The transverse momentum $p_{\mathrm{T}} = \sqrt{p_x^2 + p_y^2}$ is a ubiquitous kinematic observable in high-energy physics. The polar angle θ, measured from the beam axis, completes a cylindrical coordinate system set.

[3] Interestingly, despite being less than half the length and 3/5ths the diameter of ATLAS, CMS weighs nearly twice as much.

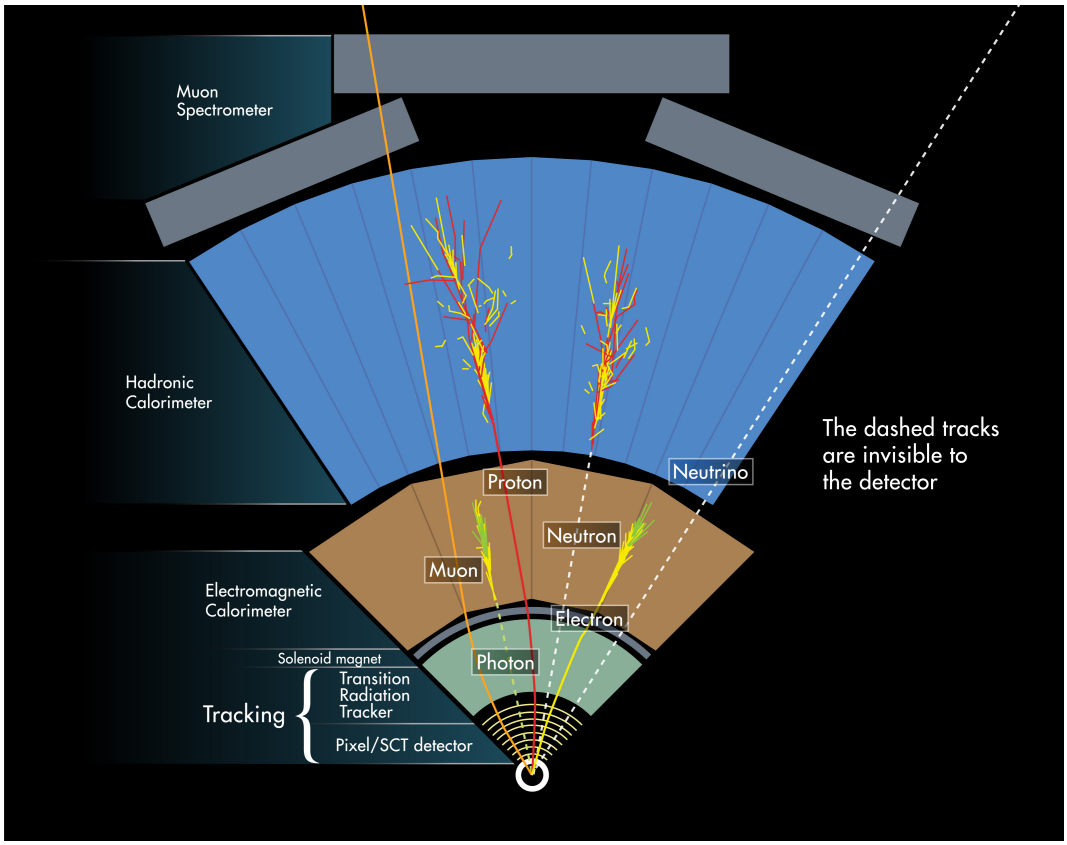

Figure 4.3: Cartoon radial cross-section of the ATLAS detector, with the paths of various particles shown. The *Tracking* section constitutes the Inner Detector. Hadrons, electrons and photons all form hadronic or hadronic electromagnetic showers in the calorimeters, which allows for measurements of their total energy. Muons propagate furthest, so the Muon Spectrometer components are placed furthest out from the interaction point. Some particles, like neutrinos, barely interact and so pass through essentially undetected. Taken from [184]

Rapidity, defined as

$$y = \frac{1}{2} \ln \left(\frac{E + p_z}{E - p_z} \right), \tag{4.2.1}$$

is useful because it is an additive quantity under Lorentz boosts. More commonly seen is pseudorapidity

$$\eta = -\ln \left(\tan \frac{\theta}{2} \right), \tag{4.2.2}$$

which is vanishing along the y-axis, with $\eta \to \infty$ as θ approaches the beamline direction. Finally, the parameter ΔR,

$$\Delta R = \sqrt{(\Delta\eta)^2 + (\Delta\phi)^2} \tag{4.2.3}$$

quantifies distances in the η-ϕ–plane.

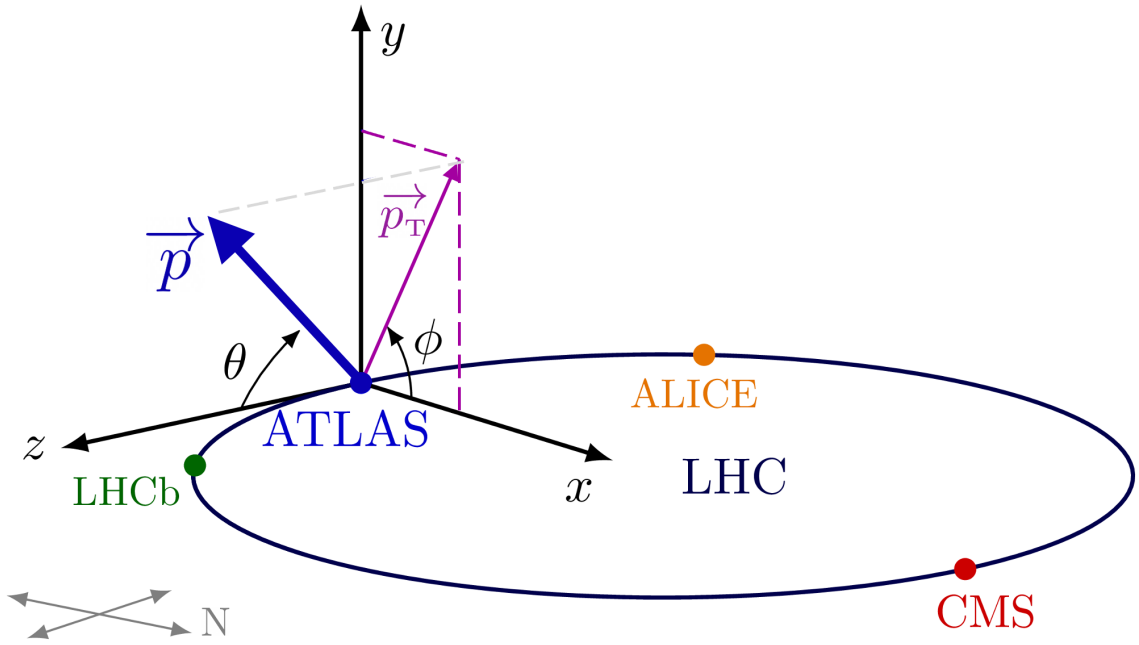

Figure 4.4: The ATLAS right-handed coordinate system, as defined with respect to the ring of the LHC. The angle ϕ is defined as that subtended by the x-axis and the three-momentum projection into the the x-y, or transverse, plane. Similarly, θ is the angle between the z-axis and the three-momentum projection into the the z-y–plane. These planes are demarcated by the purple dashed lines, and the three-momentum projections and corresponding angles are shown. CMS, LHCb and ALICE are other large LHC experiments.

4.2.2 Magnet System

Historically, a common feature of particle detectors has been their immersion in magnetic fields, which force charged particles to follow curved trajectories. The curvature of the trajectory informs the experimentalist about the momentum and charge of the particle. The ATLAS detector utilises several magnet systems which together constitute the largest superconducting magnet system in the world [185]. The Central Solenoid Magnet (CSM) surrounds the Inner Detector (ID), providing it with an axial 2T magnetic field [186]. The CSM was designed to be as thin as possible to avoid affecting detector systems located at larger radii, namely the calorimeter. A set of superconducting toroidal magnets provide a magnetic field for the Muon Spectrometer

(MS): the eight iconic barrel toroids provide a magnetic field of strength 0.5 T, and are complemented by two end-cap toroids which provide a 1 T magnetic field. All magnet systems use niobium-titanium superconducting wires. The magnet system is drawn in Figure 4.5, with the concentric coloured cylinders indicating the CSM, and the red components the toroids.

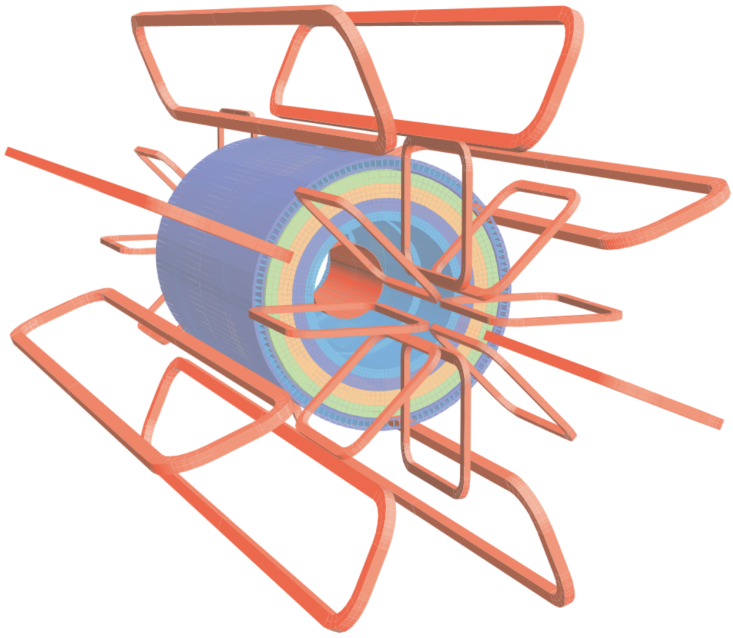

Figure 4.5: The ATLAS superconducting magnet system is comprised of a Central Solenoid magnet (CSM), shown by the coloured cylinders in the centre, eight barrel toroids, and two end-cap toroids. The toroids are indicated by the red components [163].

4.3 The Inner Detector

The Inner Detector (ID) is designed to provide high-granularity tracking information for charged particles within the range $\eta < 2.5$, and precision identification of interaction vertices [187]. The trajectories of charged particles are inferred from recorded interactions with the ID detector components. These recorded interactions are called *hits*, and the trajectories traced out are called *tracks*. The ID is made up of several different technologies, arranged in a nested cylindrical geometry, an exploded view of which is shown in Figure 4.6.

The two inner components of the ID utilise semiconductor tracking technologies [189], which work as follows. The energy of incident charged particles is directly correlated with the number of electron-hole pairs generated in the doped silicon substrate. The free charge carriers separate and collect at electrodes under the presence

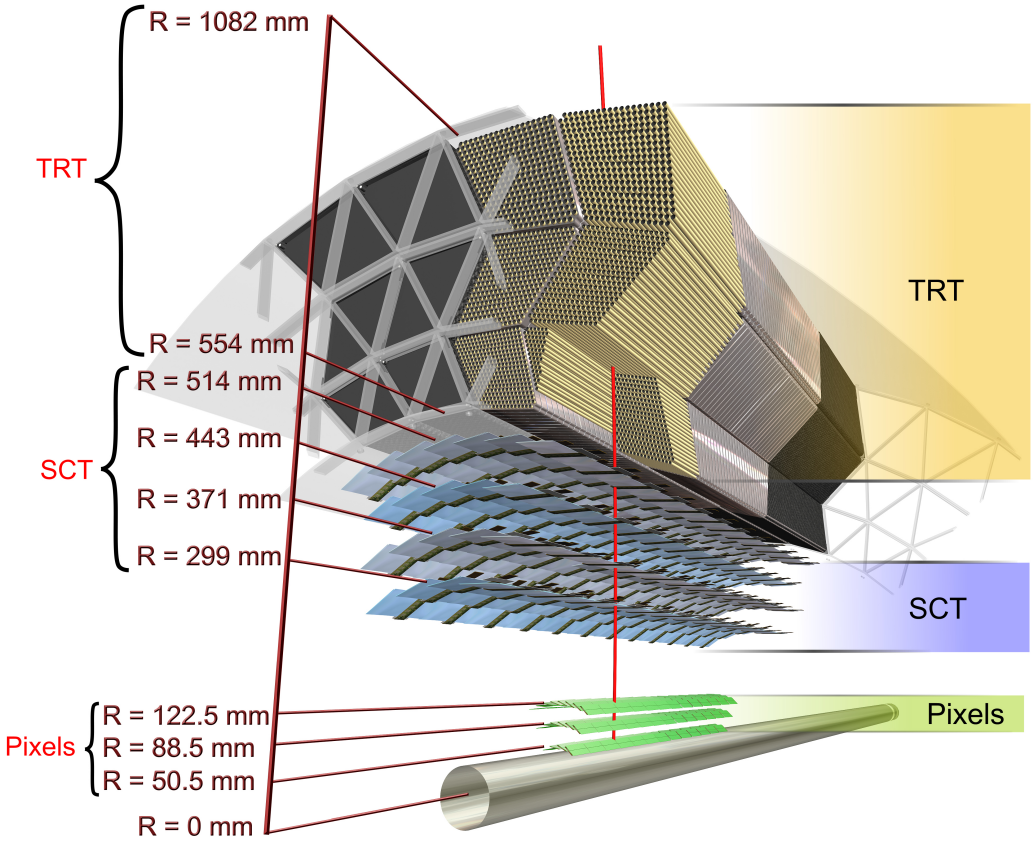

Figure 4.6: A cross-sectional view of part of the ATLAS Inner Detector [188], illustrating the various layers of silicon pixel detectors in the innermost Pixel Detector and Semiconductor Tracker. The gas-filled straw tubes form the outer Transition Radiation Tracker. These sub-detectors combine to give high-granularity tracking information for charged particles traversing the ID volume.

of an external electric field, yielding a signal which is passed to a Read-out Driver (RoD). This signal is processed as a *hit*, which is the basic unit from which all derived track objects are build — see Section 5.1.1 for details of this track construction process.

The **Pixel Detector** (PD) is the first detector encountered by particles rushing outwards from the interaction point [190]. It is designed to provide a minimum of three tracking points for each charged track emanating from the interaction point, and its superb spatial resolution allows for reconstruction of the primary vertex in three dimensions. Closest to the beampipe is the Insertable B-Layer, whose function is the identification of secondary vertices stemming from the decay of B-hadrons [191]. It

boasts a resolution of 50 µm × 250 µm. The remainder of the PD is composed of three barrel layers of silicon pixel detectors comprising 1736 modules, with a resolution of 50 µm × 400 µm. Three disks in each of the end-caps, comprising a total 288 modules, complete the set-up. A pixel module is a set of silicon sensors coupled to control circuits and front-end electronics, with a nominal pixel size in the barrel region of 50 µm in the azimuthal direction and 400 µm in the z-direction [192]. The total number of pixels in the PD is around 80 million.

The **Semi-Conductor Tracker** (SCT) surrounds the PD and is of similar design, with long pixel strips replacing individual pixels [193]. The SCT spans a radial distance of 299mm to 560mm, and comprises a total of 4088 modules — 6.3 million strips — arranged in four layers in the barrel, and nine discs in each end-cap. The coarse pixel structure compromises granularity at the expense of manufacturing complexity: the resolution achieved is 17 µm in the r-ϕ–plane and 580 µm in the z-direction. The layout of the modules is optimised such that each particle passes through at least four layers of silicon.

Covering radial distances from 563 mm out to 1082mm, the **Transition Radiation Tracker** (TRT) constitutes the outermost element of the ID [194]. It differs from the other ID subsystems in that it employs gas detectors rather than solid-state silicon. Around 300,000 gas-filled tubes — called straw tubes, or simply straws — are arranged in three cylindrical layers in the barrel, and in 80 wheel-like structures in the end-caps. The gas mixture is 70 % xenon, 27 % carbon dioxide, and 3% oxygen, chosen for stability and for tracking performance. Charged particles traversing the straws ionise the gas, liberating electrons; these travel to the straw ends, where the current is registered as a hit. The chosen geometry guarantees that particles in the kinematic range $0 < \eta < 2$ will cross over 30 straws, providing a similar number of space-points with a resolution of 0.12 – 0.15 mm [195]. Additionally, transition radiation photons are generated by charged particles moving through polypropylene fibres interleaved between the straws, and absorbed by the xenon gas. This mechanism provides a means of electron identification: differences in expected energy deposition between electrons and charged pions [4] manifest as differences in the hit strength and particle flight time [196].

[4] The probability of generating transition radiation is related to the velocity of the traversing charged particle. In ATLAS, electrons are generally the only particle light enough to attain the velocities required [195].

4.4 Calorimeter Systems

The calorimeter systems have a challenging remit. They are designed to absorb the energy of incoming particles, both charged and neutral, such that the total energy of these particles can be accurately ascertained [197]. To achieve this ambitious goal, ATLAS uses so-called "sampling calorimeters" which feature two distinct materials interleaved with one another in a sandwich-like substructure. Layers of high-density "absorber" alternate with "active" layers which measure shower energy[5] [198]. Incident charged particles interact with the dense absorber layers, giving rise to a slew of lower-energy particles. Repetition of this process across the cross-section of the calorimeter leads to the formation of electromagnetic and hadronic showers. The shape of the particle shower is regularly sampled to infer the original particle's energy.

ATLAS employs an electromagnetic calorimeter (ECAL) to detect and absorb electrons and photons. In the former case, energy is predominantly lost through bremsstrahlung, whereas for the latter, the dominant means of energy dissipation is through electron-position pair production. Hadrons, which may interact with calorimeters materials through the strong interaction as well as the electromagnetic, are targeted using a hadronic calorimeter (HCAL). The characteristic length-scale λ over which an interaction will occur is far smaller for electromagnetic interactions than hadronic interactions[6]. This necessitates placing the ECAL closer to the interaction point than the HCAL, as is shown in Figure 4.7. The forward calorimeters (FCAL), located at high values of $|\eta|$, complete the calorimeter infrastructure. The ECAL and FCAL are built entirely using liquid argon calorimeter technology, whilst the HCAL is composed of a liquid argon component surrounded by a tile calorimeter. Both technologies are discussed below.

4.4.1 Liquid Argon Sampling Calorimeters

Liquid argon (LAr) sampling calorimeters are used for the identification and characterisation of electrons, photons and charged hadrons [199]. The LAr calorimeters are located in three cryostats, one in the barrel and two in the end caps, all held at 89 K. The barrel LAr calorimeter constitutes part of the ECAL and covers the central region $0 < \eta < 1.4$ [200]. It is divided into three longitudinal layers and uses a characteristic accordion structure, with liquid argon "active" layers and lead absorber plates. Incident electrons and photons ionise the liquid argon, producing a characteristic ionisation pulse which is processed as a signal, and output to the trigger infrastructure (see Section 4.6) and to physics reconstruction. A liquid argon pre-sampler is also included upstream of the ECAL barrel to estimate energy losses which occurred at smaller radii.

[5] This is in contrast to homogeneous calorimeters where the entire volume is considered active

[6] This is equivalent to saying that, for a given length of detector material, the probability of an electromagnetic interaction occurring is higher than that of an hadronic interaction.

The ECAL is split into stacks of size $\Delta\eta \times \Delta\phi = 0.025 \times 0.025$, corresponding to the granularity of the second ECAL LAr layer, defining 200×256 ECAL *towers*.

The end-cap regions contain three separate LAr calorimeters. Inner-most is the electromagnetic end-cap (EMEC), the remaining part of the ECAL system which employs the same technology as the barrel. The EMEC is arranged in two separate wheel-like geometries covering $1.375 < \eta < 2.5$ and $2.5 < \eta < 3.2$ respectively, with an additional pre-sampler included in front, covering $1.5 < \eta < 1.8$. The hadronic end-cap constitutes the liquid argon part of HCAL, is divided into four longitudinal layers, and is distinct from the ECAL technology in using copper as the absorber, with coverage up to $\eta < 3.2$.

Finally, the forward calorimeter covers the pseudorapidity range $3.1 < \eta < 4.9$, in close proximity to the beampipe. The FCAL is split into three layers: an electromagnetic layer with copper used as the absorber; and two hadronic layers with tungsten as absorber. The physics remit of the FCAL focuses on detection and measurement of high-η jets, required to minimise mis-measurement of missing E_{T} [201].

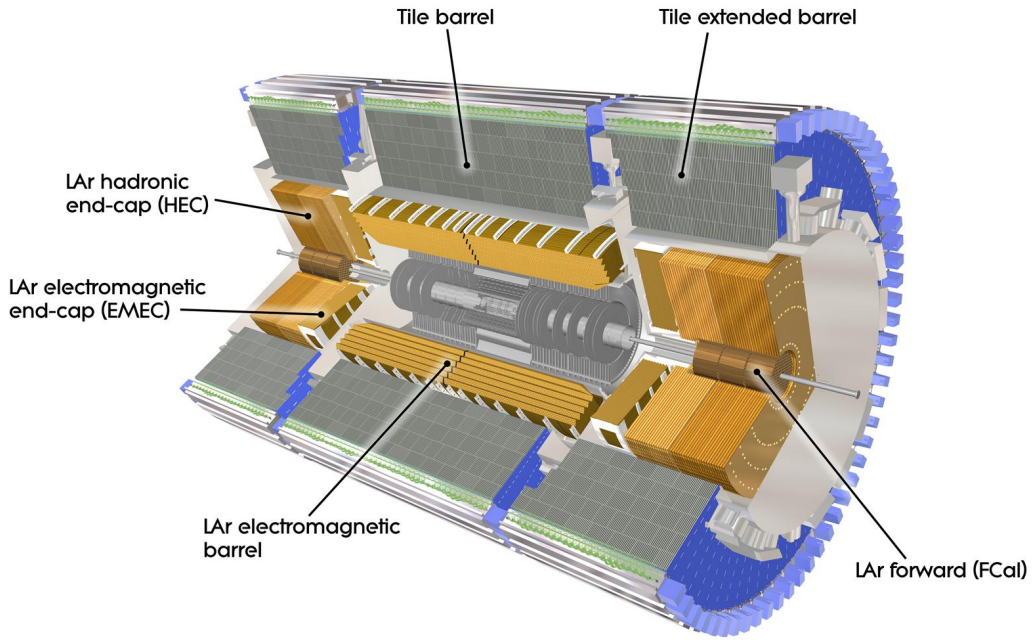

Figure 4.7: Illustration of the ATLAS calorimeter systems, with each tile and end-cap subsystem labelled [202]. Liquid argon calorimeters are located at smaller radii in the form of the ECAL and FCAL, and part of the HCAL. The tile calorimeter makes up the remainder of the HCAL.

4.4.2 Tile Calorimeter

The Tile Calorimeter (TileCal) is the part of the HCAL which covers the central region [203]. It uses steel as an absorber, with plastic scintillators acting as active mediums, with a ratio of steel-to-plastic of 4.7 : 1. The heaviest ATLAS component, the TileCal weighs in at around 2900 tonnes. Like many other sub-detectors, the TileCal is split into barrel (Long-Barrel $0 < \eta < 1.0$) and movable end-cap (Extended-Barrel $0.8 < \eta < 1.7$) components. The plastic scintillators are arranged in tiles perpendicular to the colliding beams, and the TileCal is made up of around 420,000 such plastic tiles. Scintillation light is collected at the edge of each tile by wavelength-shifting fibres (WSFs), and eventually fed to a pair of photomultiplier tubes (PMTs). The light collected by these PMTs forms a current pulse, with amplitude proportional to the energy of the traversing particle in the cell [204]. The electronic signals from the PMTs are measured and digitised every 25 ns. The HCAL has a coarser resolution than the ECAL: $\Delta\eta \times \Delta\phi = 0.1 \times 0.1$.

4.5 Muon Spectrometer

High-quality measurement of muons, over a large range of p_{T}, is a key physics requirement of the LHC general-purpose detectors [205]. The outermost ATLAS detector component is the Muon Spectrometer (MS), dedicated to tracking of muons, which make up the vast majority of detectable particles which make it this far out of the detector[7]. A schematic of the MS is shown in Figure 4.8. The principle of muon measurements within the MS relies on their bending through the magnetic fields generated by the superconducting toroidal magnets. A total of 4000 individual muon chambers use four different technologies to achieve precision tracking and triggering information for muons. The target precision is a p_{T} resolution of 10% for 1 TeV muon tracks.

Monitored Drift Tubes (MDT) and **Cathode Strip Chambers** (CSC) deal with precision muon tracking. The MDTs total around 350,000 aluminium tubes, each containing a mixture of argon and carbon dioxide gas; arranged in three concentric rings they form the barrel of the MS [206]. Traversing muons ionise the gas mixture, with the drifting electrons created providing an electrical signal. The combination of such signals over several MDTs allows for precision tracking down to below 50 µm. The CSCs are employed near the end-caps, in the range $2.0 < \eta < 2.7$, where their superior spatial resolution is necessitated by large background rates [207]. Each CSC contains four radially-orientated multi-wire proportional chambers which incorporate cathode strips and anode wires within a gas volume. The ionisation mechanism is similar to have to the MDTs but with shorter drift times. A resolution of 60 µm is achieved for reconstructed tracks in the bending plane [205].

[7] There may be other types of particle which also make it this far but are undetectable, namely neutrinos. Muons are able to propagate greater distances that electrons, photons or various hadrons because although they will interact with the calorimeters through brehmsstralung, the probability of such interactions is suppressed by the muon's large mass

The electron drift time in both MDTs and CSCs is larger than 25 ns, the standard time period between bunch crossings in the LHC. Whilst both are extremely adept at measuring muon momentum, they are not sufficiently fast for use with the trigger system which streamlines the throughput of events recorded for analysis (Section 4.6). Two subsystems with higher temporal resolution are therefore employed for muon triggering. **Resistive Plate Chambers** (RPCs) are used in the barrel [208], [209]. Each chamber houses two gas volumes, predominantly tetrafluoroethane ($C_2H_2F_4$), between Bakelite plates held in a very strong magnetic field. Incident charged muons ionise the gas, and the strength of the magnetic field is such that an electron "avalanche" is caused, providing a large signal quickly and so an immediate response. Two layers are dedicated to low p_T muon triggers, whilst a third deals with the high p_T case. They contribute to a trigger response of less than 3 ns, but have a spatial resolution of the order of 1 cm. **Thin Gap Plates** perform the analogous trigger job in the end-cap regions [210]. These are thinner, and achieve a similar time resolution whilst lowering the spatial resolution down to 2 - 7 mm.

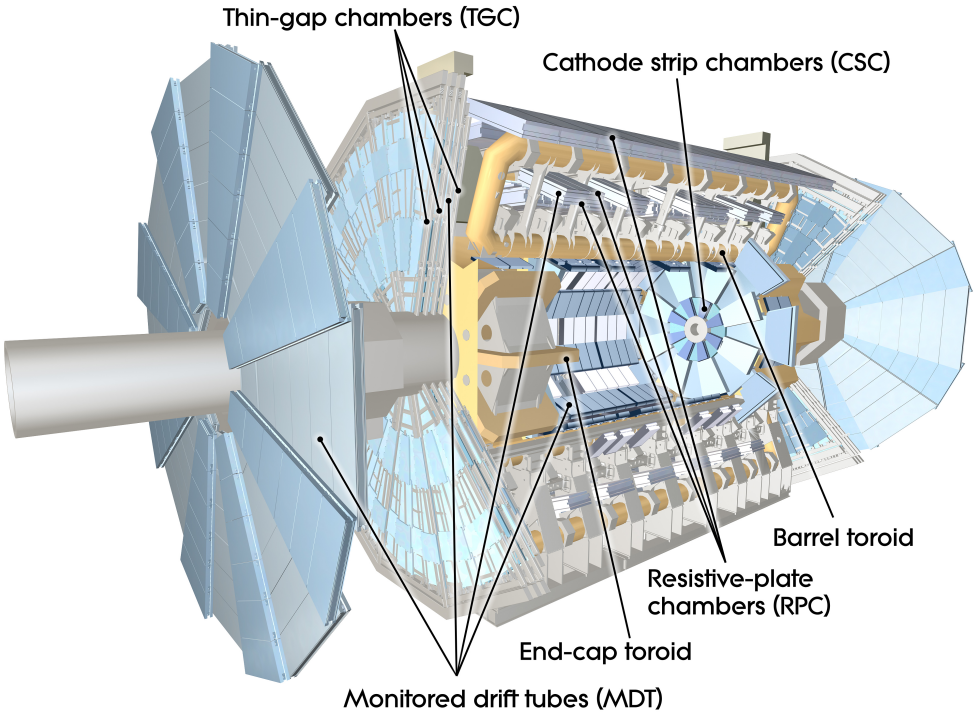

Figure 4.8: The ATLAS Muon Spectrometer comprises the outermost primary ATLAS detector component. The various MS sub-systems are labelled. From [211].

4.6 ATLAS Trigger and Data Acquisition

Up to 1.7 billion proton-proton collisions occur in the ATLAS detector every second. It does not have the ability to record each collision, nor is this desirable from a computational perspective: each event contains about 1 MB of information. Therefore, in addition to requiring an efficient data-acquisition system (DAQ), ATLAS requires a means of selecting particular event candidates. The "trigger" is an umbrella term referring to dedicated hardware and software designed to select interesting physics events based on distinguishing criteria. During Run-2, the ATLAS trigger was composed of two parts: the L1 trigger and the High-Level Trigger (HLT). A flow-chart of the combined TDAQ system [212], illustrating how the two triggers inform and interface with the DAQ, is shown in Figure 4.9

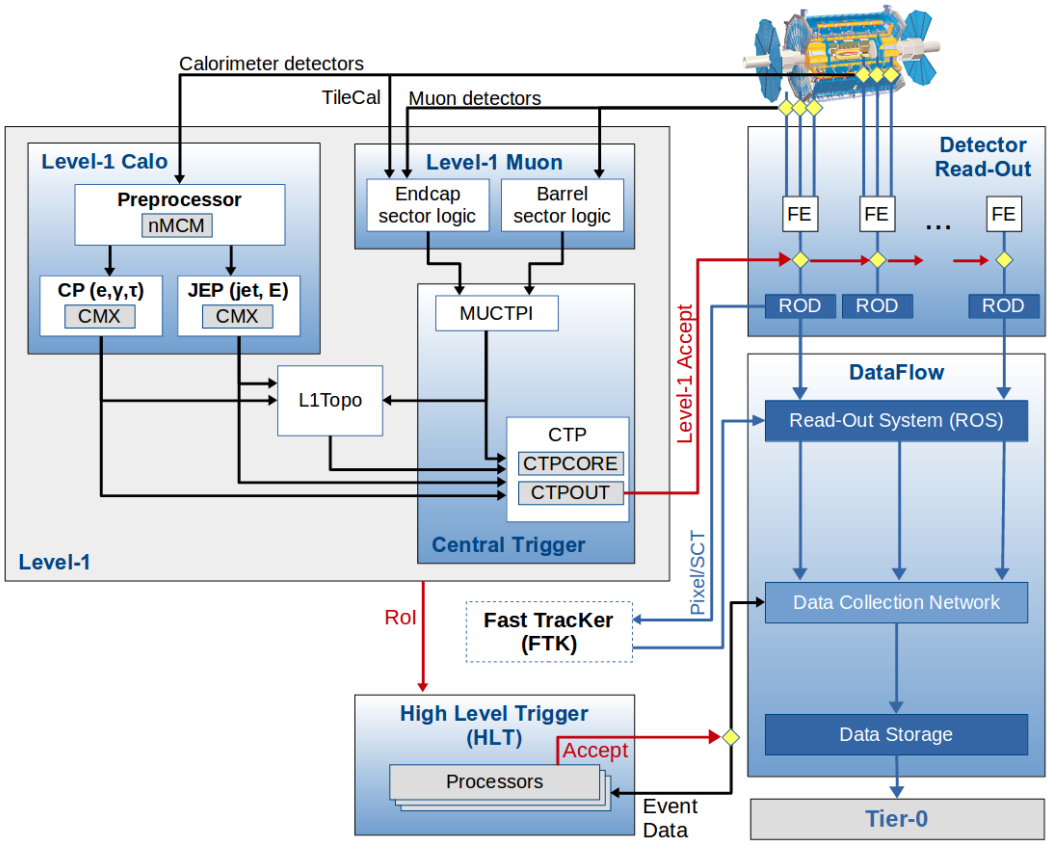

Figure 4.9: Schematic of the ATLAS TDAQ [212]. Dedicated trigger infrastructure builds coarse-grain information about each event, firstly in the L1 hardware trigger. The L1 Trigger's decision to accept or reject events is pass to the primary detector readout channels, and also to the High-Level Trigger (HLT) which further scrutinises the event. The HLT makes the final decision on whether a particular event is written to disk for possible future physical analysis. The combined trigger infrastructure streamlines the throughput of data from 40 MHz down to 1 kHz.

The L1 trigger is a hardware-based system, utilising custom electronics embedded in the calorimeters (L1Calo) and MS (L1Muon) to construct reduced-granularity event information [212], [213]. This information determines whether an event should be selected or discarded. The L1 trigger reduces the throughput from 40 MHz to 100 kHz[8]: first by demanding that bunch crossing are filled, corresponding to interacting protons; then by performing a fast analysis on detector signals. These decisions are made in real-time, meaning that L1 is referred to as an 'online' trigger. L1Calo searches for high-p_{T} electron, photon and τ-lepton candidates, as well as jet candidates and global MET objects. This is achieved by building coarse towers of energy deposits across both calorimeters, using a sliding-window algorithm (see Section 5.2.1) to identify maxima across groups of towers, and comparing these against trigger menu thresholds [214]. The L1Muon system searches for hits across multiple layers of trigger chambers, consistent with expected hits from a muon originating at the interaction point [215]. The L1 Topological (L1Topo) trigger accepts geometric or kinematic combinations of trigger objects from L1Calo and L1Muon, and selects events ("triggers") based on derived features like invariant masses and angular separations [216]. The output of the L1 trigger are so-called *Regions of Interest* (RoIs): regions in η-ϕ–space containing information about the type of object and the kinematic thresholds passed.

The RoIs are passed to the HLT for further scrutiny. The HLT is a software-based trigger, running offline on a dedicated processor farm, and responsible for streamlining the rate of saved events down to 1 kHz [212], [217]. The typical reconstruction process consists of fast trigger algorithms providing initial rejection, before more CPU-intensive reconstruction algorithms — similar to those used for full object reconstruction — perform the final selection [218]. These reconstruction methods typically extract features from particular RoIs to construct physics objects, then apply a hypothesis algorithm to determine whether the object satisfies the trigger condition. Information from the full detector can also be used to inform selection based on global kinematic properties.

A combination of L1 and HLT trigger algorithms collectively defines a "trigger". The selection and configuration of specific L1 and HLT triggers used is specified through a *trigger menu*, and different trigger menus can be designed for different scenarios. The measurement presented in Chapter 10 uses a combination of single-electron and single-muon triggers, which are specifically designed to select those collision events which produce electrons or muons which possess sufficiently large p_{T} [219], [220].

[8] This rate was 75 kHz in Run-1.

Chapter 5

Object Reconstruction

"Measuring particle collisions:
Hard to do with any precison...
So the tools that we muster,
Are tracks, towers and clusters,
And the anti-K_t algorithm"
—

Chapter 4 presented the ATLAS detector in all its glory, where it was shown that detector subsystems are designed to identify, track the passage of, and infer the kinematics of particular particles. The first section of this chapter describes the *low-level objects* which are built directly from these basic detector responses. From these low-level objects, *high-level physics objects* are constructed. These high-level objects capture the kinematic behaviour of particles or jets that traverse the detector: to an experimental particle physicist, these objects *are* the particles. Consideration is only given to high-level physics objects which are stable final-states of top-quark decays, that is charged leptons, jets and neutrinos. A rendering of a LHC Run-2 $t\bar{t}$ event is shown in Figure 5.8, along with a summary discussion of the present physics objects. Other stable objects which are detectable by the ATLAS detector include photons and various hadrons, principally charged pions. These have dedicated reconstruction techniques but, playing no part in the physics programme of this thesis, are not discussed further.

5.1 Tracks and Vertices

Tracks are the reconstructed paths of charged particles, built from spatial hits in the ID and MS. They are an essential part of the data analysis chain, as are the vertices subtended by these tracks.

5.1.1 Inner Detector Tracks

Primary-track reconstruction in the ID is derived from hits in the Pixel and SCT detectors [221]. The process begins with the building of *clusters* from raw measurements. In a sensor where the deposited energy yields a charge above a prescribed threshold, a connected component analysis (CCA) algorithm groups connected pixels and strips into a cluster [222], as illustrated in Figure 5.1a. A single cluster in the pixel detector defines a three-dimensional *space-point*; similarly, clusters from both sides of a strip layer constitute a space-point in the SCT.

A set of three space-points constitute a track seed, subject to a number of criteria included to maximise purity, where purity is defined as the fraction of seeds that result in good-quality tracks [223]. Track quality criteria are listed below. Track candidates are built from these initial track seeds using a combinatorial Kalman filter, a technique borrowed from control theory [224], [225]. For a given seed, the Kalman filter works progressively, first predicting the next point in the proposed track, then filtering prospective points by comparing them with space-points actually present in subsequent layers of the detector [226]. The output is a tree of possible track candidates, as shown in Figure 5.1b. These may arise from a single seed, or share space-points, or even be constructed from mis-assigned space-points.

A dedicated algorithm resolves the ambiguity of which track candidates correspond to actual charged particle trajectories. It achieves this by assigning a *track score* to all candidate tracks; this track score indicates the quality of each track based on a set of criteria. Factors which are detrimental to achieving a high track score include: cluster quality — penalising clusters with holes; tracks with too few clusters; and tracks with low p_{T}, which is seen to correlate with incorrect cluster assignment [223]. Further, clusters can be shared by no more than two tracks, and tracks can contain a maximum of two shared clusters.

When multiple incident charged particles create charge deposits in the same set of pixels or strips, "merged clusters" are formed. Clusters identified as merged can be used by competing tracks without penalty, thus accurate identification of merged clusters is crucial. A neural network is employed to identify such clusters in instances when they are featured in multiple track candidates [227]. The NN's accuracy exceeds 85 % for merged clusters created from up to three incident charged particles.

Candidate tracks which make it this far are subject to a set of basic selection criteria [223]:

- $p_{\mathrm{T}} > 400$ MeV .
- $\eta < 2.5$.
- The combined numbers of clusters from PD and SCT must be at least seven.
- A maximum of one shared space-point.
- A maximum of two holes, with a maximum of one hole in the PD.
- $\left|d_0^{\mathrm{BL}}\right| < 2.0$ mm, where d_0^{BL} is transverse impact parameter, defined as the track's distance of closest approach to the beamline, in the transverse plan.
- $\left|z_0^{\mathrm{BL}} \sin(\theta)\right| < 3.0$ mm, where z_0^{BL} is the longitudinal impact parameter: the distance along the z-direction from the primary interaction vertex; θ is defined as above.

Finally, a high-resolution fit is performed to yield the ultimate track candidates, with additional input from the same NN architecture described above to finalise cluster positions.

Track candidates are extended into the TRT by matching them with compatible TRT hits [228]. TRT-extended tracks are evaluated once more using the ambiguity-score method. In addition, "outside-in"reconstruction algorithms, which use TRT hits as seeds and extrapolate inwards, are a complimentary track-finding technique to the highly-efficient "inside-out" algorithm discussed.

5.1.2 Muon Spectrometer Tracks

Building tracks in the MS is analogous to the process employed in the ID. In this instance, a Hough transform is used to search for hits aligned on a trajectory in successive layers of the MDT and trigger chambers, and form segments. The Hough transform maps the problem of connecting hits into a parameter space. A search of this space returns the set of parameters corresponding to the most probably candidate track. For each layer of the MDT, a straight line fit to the hits in then performed. Hits in the RPC and TGC provide spatial resolution orthogonal to the bending plane of the toroidal magnets. Hits in the CSC are built into tracks using a separate combinatorial search in η-ϕ–space.

Track candidates are then built up from hits in different layers of the MS, starting with track seeds in the middle layers and moving both inwards and outwards using a combinatorial search. At least two matching segments are required to build a track, apart from in the barrel–end-cap transition region where a single high resolution segment suffices [229]. The same segment may feature in several candidate tracks, and an overlap removal algorithm is employed to either select the best track assignment or

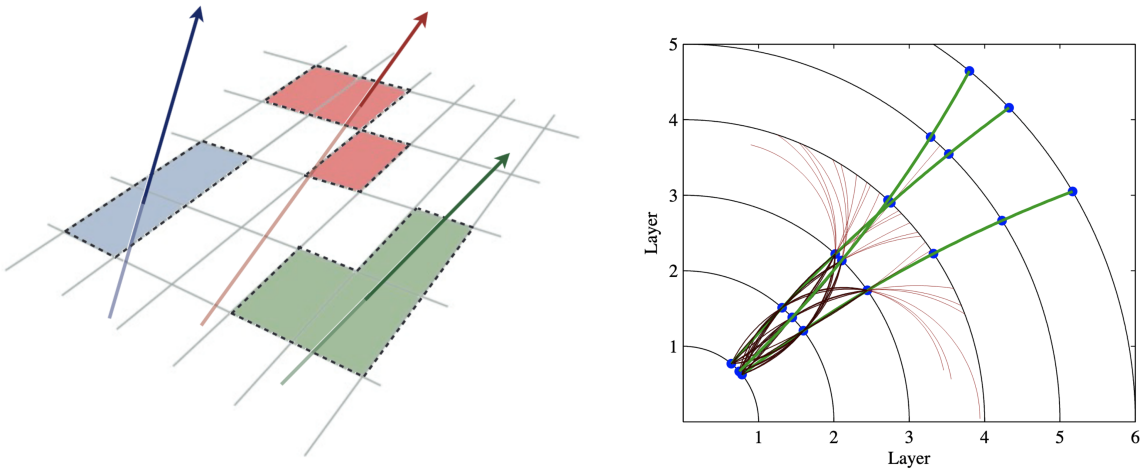

(**a**) (**b**)

Figure 5.1: Specifics of ATLAS track-fitting procedures: (**a**) Several single-particle pixel clusters. The incident charged particles deposit energy in pixels, and a connected component analysis clusters these pixels [223]. Several techniques have been implemented to solve ambiguities arising from problematic clusters. (**b**) The Kalman filter builds track by extrapolating track seeds (brown) outwards, and then matching the predicted track position to subsequent spatial hits (blue dots). Green curves represent matched tracks, whilst red tracks represent extrapolated tracks which did not match with spatial hits in the outer layers [225].

retain segment sharing between two tracks. In particular, tracks which share segments in the inner two layers but have distinct segments in the outermost layer are always retained, to ensure high efficiency for muons in close proximity.

5.1.3 Vertices

Tracks in the inner detector can be extrapolated back into the collision region. Points where tracks intersect constitute likely vertices where some interaction occured: the interaction of some multi-particle initial state, or the decay of some unstable particle. Each vertex can be assigned a track transverse momenta through the expression,

$$p_{\mathrm{T}}^{\mathrm{track}} = \sum_{i}^{N} \left(p_{\mathrm{T}}^{i} \right)^{2}, \tag{5.1.1}$$

the sum of the square of the p_{T} of all N tracks which converge at the vertex in question. The quantity $\max \left(p_{\mathrm{T}}^{\mathrm{track}} \right)$ defines the *primary vertex*, assumed to be the interaction point of the hard pp scatter. Other vertices are labelled *secondary vertices*. These arise from

interactions between other protons in the bunch (referred to as *pile-up*), or from the decay of long-lived particles like B-hadrons.

5.2 Clustering Algorithms

Particles traversing the calorimeters deposit their energy in the constituent cells, and in doing so induce a signal within those cells. Cell clustering is designed to group signal cells together to reconstruct electromagnetic or hadronic showers from single particles, with a desire for high precision in both the shower shape and its energy. This information is used for particle identification and reconstruction. *Clustering algorithms* are devised to group cells to form composite objects which capture the shower profile and from which the total deposited energy can be computed [230]. Two separate clustering algorithms are described below.

5.2.1 Sliding-Window Algorithm

Sliding-window algorithms [230] begin with the partition of the relevant calorimeter into longitudinal towers of specified size $\Delta\eta \times \Delta\phi$. These *CaloTowers* constitute an intermediate step between cells and clusters, and the energy of all cells in all tower layers is summed to yield the tower energy. A window of fixed size is defined, $\Delta\eta^{\text{window}} \times \Delta\phi^{\text{window}}$, with each dimension an integer multiple of the tower dimensions. This window moves across the tower grid to search for local maxima in transverse energy. A precluster is formed if the transverse energy exceeds a pre-defined threshold, with both window size and energy threshold optimised to maximise the chances of finding preclusters, whilst minimising those generated from noise. The position of the cluster is computed and duplicate clusters removed. Preclusters are filled with additional cells encompassed in the sliding window to form electromagnetic clusters in the ECAL. Electromagnetic clusters have been used as building blocks for electron and photon reconstruction.

5.2.2 Topological Clustering Algorithm

Clusters of topologically-connected calorimeter cell signals form *topo-clusters* [231]. These are the primary objects used in the reconstruction of hadronic final states absorbed in the HCAL, and now also represent the state-of-the-art in electron and photon reconstruction in the ECAL.

Traversing particles induce a signal, $E^{\text{EM}}_{\text{cell}}$, in a calorimeter cell. This signal is expected to be larger than the expected noise in the cell, $\sigma^{\text{EM}}_{\text{noise,cell}}$, and the ratio of the

two defines a cell signal significance:

$$\zeta_{\text{cell}}^{\text{EM}} = \frac{E_{\text{cell}}^{\text{EM}}}{\sigma_{\text{noise,cell}}^{\text{EM}}}. \tag{5.2.1}$$

The value $\sigma_{\text{noise,cell}}^{\text{EM}}$ is estimated from simulation for each Run-2 year separately, and the EM superscript indicates that these quantities are measured on the electromagnetic energy scale[1]. A hierarchy of numerical thresholds is introduced: $S > N > P$. These thresholds denote "seeding", "growth" and "boundary" significances respectively. Each cell is classified into one of these categories — or none of them — based on its significance, $|\zeta_{\text{cell}}^{\text{EM}}| > X$ with $X \in \{S, N, P\}$. This informs a volume-growing algorithm, which works by identifying a seed cell with $|\zeta_{\text{cell}}^{\text{EM}}| > S$ — the beginning of a proto-cluster — and sequentially adding significant neighbouring cells[2]. A proto-cluster is thus built from a seed cell, populated by growth cells and bounded by the boundary cells. The default values are $S = 4, N = 2$ and $P = 1$.

Topo-clusters can form from negative cell signals, which arise from pile-up conditions and electronic noise. Retaining such cells improves noise suppression, as there is a local cancellation of random positive noise fluctuations by the negative fluctuations. Proto-clusters which feature multiple local energy maxima are commonly the result of multiple particles. Such proto-clusters are split into separate proto-clusters, provided they exist inside specific layers, using a geometrical method with local signal maxima defined by $E_{\text{cell}}^{\text{EM}} > 500\,\text{MeV}$.

Each topo-cluster is interpreted as a massless pseudo-particle with particular cluster kinematics $(E_{\text{clus}}, \eta_{\text{clus}}, \phi_{\text{clus}})$, where each of these parameters is computed from a weighted sum of the kinematics of the individual cells. The three-momentum of the cluster is then computed through the projection of the cluster energy along Cartesian axes. The shape of topo-clusters and the distribution of the signal within provide additional utility in signal characterisation and cluster-based calibration. Topo-clusters go on to form the building blocks of several high-level physics objects.

5.3 Particle Flow Algorithm

The *particle flow* (PF) algorithm is a reconstruction procedure which combines tracking information from the ID with calorimeter information [234]. These reconstruction techniques were used in the construction of high-level hadronic jets during Run-2; in contrast, almost all Run-1 jet reconstruction relied solely on topo-clusters. The PF tech-

[1] The electromagnetic energy scale is a baseline calorimeter energy scale which quantifies energy depositions in electromagnetic showers. It was establish during test-beam runs during detector development [232], [233].

[2] Neighbouring cells are generally defined to be those adjacent to seed cells in the same sampling layer, or with partial overlap in (η, ϕ) in adjacent layers.

nique is also applied in the reconstruction of soft activity — below the threshold used for jet reconstruction — which constitutes an important input for missing transverse momentum construction.

Using a combination of ID tracking and calorimeter information has a number of advantages:

- The momentum resolution of the ID tracker is superior to the energy resolution of calorimeters for low-energy charged particles. The opposite is true for high-energy particles. The combination of ID tracker and calorimeters provides superior resolution across the phase-space to either technology's sole use.
- The lower energy threshold of the ID allows softer objects to be reconstructed than would be possible using solely calorimeter information.
- The angular resolution of single charged particles is also superior in the ID.
- Tracking information captures low-p_{T} charged particles which exit the jet cone before the calorimeter, and which would otherwise be lost.
- Precise tracking information allows signals deriving from pile-up vertices to be discarded.

It is critical to avoid double-counting a charged particle's energy when considering both ID tracker and calorimeter information. This is achieved by subtracting the energy of this particle from the calorimeter, whilst avoiding subtraction of energy deposits derived from other particles. The steps of the particle-flow algorithm are outlined:

1. High-quality tracks are selected according to stringent criteria concerning the number of silicon hits, lack of pixel holes, kinematics and isolation.
2. Each track is matched to one topo-cluster. A preliminary matching criterion is the ratio $E^{\mathrm{cluster}}/p^{\mathrm{track}} > 0.1$, with p the three-momentum of the track. Angular-matching is then applied using the distance metric

$$\Delta R' = \sqrt{\left(\frac{\Delta\phi}{\sigma_\phi}\right)^2 + \left(\frac{\Delta\eta}{\sigma_\eta}\right)^2}, \tag{5.3.1}$$

   where σ_ϕ, σ_η are the topo-cluster widths in the $\phi-$ and $\eta-$directions.
3. The expected energy deposition in the calorimeter $\left\langle E_{\mathrm{dep}} \right\rangle$ is calculated from the topo-cluster position and track momentum:

$$\left\langle E_{\mathrm{dep}} \right\rangle = p^{\mathrm{track}} \left\langle \frac{E_{\mathrm{ref}}^{\mathrm{clus}}}{p_{\mathrm{ref}}^{\mathrm{track}}} \right\rangle, \tag{5.3.2}$$

This informs how much energy must be subtracted from the calorimeter. The expectation value on the right of 5.3.2 is determined from simulated single-particle samples, by considering topo-cluster energies contained within a cone defined by $\Delta R = 0.4$ around track position.

4. For each track candidate, the possibility of the particle depositing energy in multiple topo-clusters is evaluated, based on a metric:

$$S\left(E^{\text{clus}}\right) = \frac{E^{\text{clus}} - \left\langle E_{\text{dep}} \right\rangle}{\sigma\left(E_{\text{dep}}\right)} \tag{5.3.3}$$

   Additional topo-clusters are added to the track if required.

5. The expected energy $\left\langle E_{\text{dep}} \right\rangle$ is subtracted from the set of matched topo-clusters, cell-by-cell.

6. The remnant energy in the set of topo-clusters is compared to $\left\langle E_{\text{dep}} \right\rangle$. If this remnant totals less than a set threshold, $1.5\sigma(E_{\text{dep}})$, it is assumed to have arisen from shower fluctuations, and the energy in the relevant cells is removed. Otherwise, the remnant topo-clusters are retained for likely incorporation into other particle-flow objects.

Any unmatched topo-clusters are assumed to represent energy deposits from neutral particles and are retained. The output are a set of particle-flow objects for use in the construction of high-level physics objects. These use of particle-flow algorithms for reconstructing jets has lead to improved energy and angular resolution of reconstructed jets, compared to older techniques which relied solely on calorimeter information.

5.4 Leptons

The tau-lepton gets an unfair deal. Although a prominent member of the charged lepton family, its large mass opens up hadronic decay channels, unlike its lighter siblings. This introduces complications: tau-leptons can also deposit significant energy in hadronic calorimeters. ATLAS measurements which utilise tau-leptons employ dedicated reconstruction techniques and so in the top-quark sector, the tau-lepton is seen as separate from its charged lepton compatriots, and of minimal relevance in this thesis. Tau-lepton reconstruction techniques are therefore not discussed.

Neutrinos present a different problem. Their weakly-interacting nature renders them undetectable by the puny ATLAS sub-detectors[3]. The effects of neutrinos are

[3]One would require a far larger detector, perhaps containing vast quantities absorber liquid, or dedicated detection devices buried far underground.

therefore inferred through reconstructing proxy objects called *missing transverse energy* (MET), discussed in Section 5.6. What remains is the reconstruction of electrons and muons, elucidated below.

5.4.1 Electrons

The bremsstrahlung process is extremely important for electrons, where its small mass drives a large bremsstrahlung probability. The radiated photon can decay into electron-positron pairs, which can themselves interact and bremsstrahlung with the detector materials. This process generates an electromagnetic shower, with multiple tracks appearing in the ID or multiple clusters generated in the ECAL. The reconstruction of electrons thus requires as input: clusters in the ECAL, charged particle tracks in the ID, and close matching of the two in $\eta \times \phi$ space to form final electron candidates. The journey of an electron through the various sub-detectors is sketched in Figure 5.2.

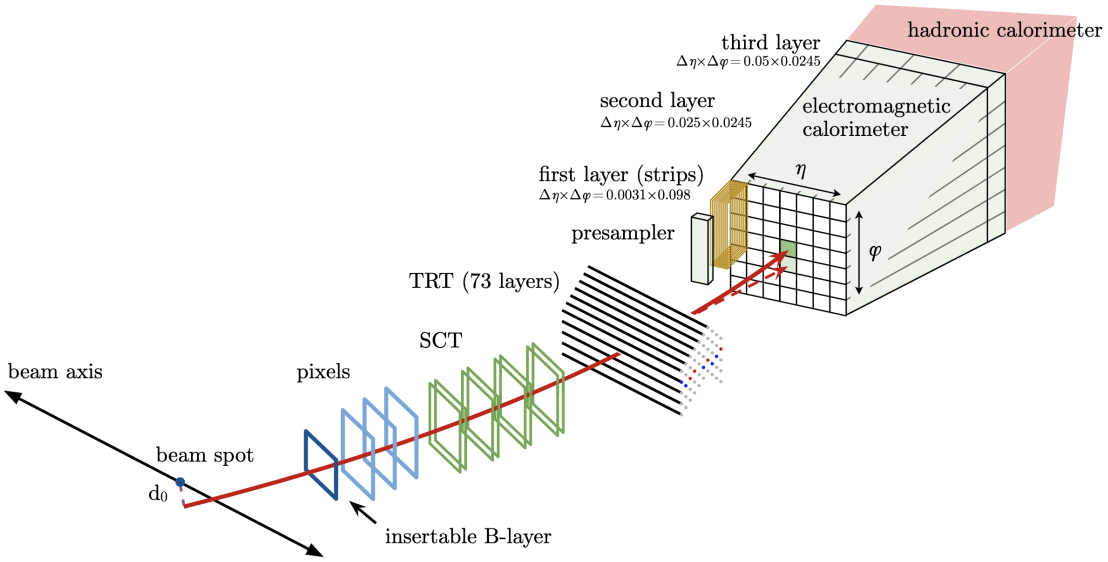

Figure 5.2: An electron emanating from the primary interaction point will leave a set of hits in the ID. It will then give rise to an electromagnetic shower, which will deposit the electrons energy in successive layers of the ECAL. Clustering algorithms define electron candidates based on depositions in the ECAL. These clusters are matched to track candidates to build reconstructed electrons. Taken from [235].

Electron reconstruction techniques evolved over the course of Run-2. Initially, sliding-window algorithms were used to construct electromagnetic-energy cluster seeds from towers in the ECAL [235]. These clustering methods were replaced by dynamical clustering in the form of topo-clusters, reaping improvements in reconstruction efficiency [236]. In both cases, analysis-level electrons are created by loosely matching

the cluster seeds to re-fitted tracks[4], then growing "superclusters" from cluster seeds by adding proximal clusters, matching the superclusters to tracks, and calibrating the final energy [237]. Candidate electrons in the entanglement measurement, Chapter 10, are then subject to the following requirements:

- $p_{\mathrm{T}} > 15\,\mathrm{GeV}$,
- $|\eta| < 1.37$ or $1.52 < |\eta| < 2.47$, avoiding the barrel–end-cap transition zone,
- $|d_0/\sigma(d_0)| < 5.0$,
- $\left|z_0 \sin(\theta)\right| < 0.5$ mm.

Prompt electrons are those which stem from the primary vertex. *Identification* criteria are applied to discriminate between prompt electrons, and photons, hadronic jets, or non-prompt electrons. A likelihood discriminant provides additional differentiation. ATLAS defines several "operating points" which specify the lower-bound of that likelihood discriminant; most commonly used are the `Loose`, `Medium` and `Tight` operating points [235]. Selecting a tighter operating point effectively enforces a stricter definition of a prompt electron[5]. Electron *isolation* concerns the proximity of prompt electron candidates to other objects in busy detector conditions, and good isolation is enforced by limiting the amount of activity in a prescribed cone around the electron. A series of analogous operating points are defined for electron isolation, allowing the experimentalist to choose the stringency of the isolation definition [236]. The entanglement measurement presented in Chapter 10 uses the `Tight` identification and `Tight` isolation operating points. Finally, multivariate methods are employed to suppress electron candidates with mis-identified charge.

The total electron efficiency (for a given selection of identification and isolation working points) is the product of the individual efficiencies associated with the reconstruction, identification, isolation, mis-identification and triggering of an electron candidate. These individual efficiencies are computed using a data-driven method known as the *tag-and-probe* method, which concerns the decay of known resonances. In the case of electrons, the decays $Z \to ee$ and $J/\Psi \to ee$ are used. One decay product is the probe, specified by loose selection criteria; the other decay product constitutes the tag, defined by tight selection criteria. The efficiency is defined as the fraction of probe decay particles which pass a particular selection criteria, where each event is triggered by the tag particle. Figure 5.3a presents the variation of the isolation efficiency component as a function of electron p_{T}, in data and as a ratio of data to simulation, for the $Z \to ee$ process. The figure illustrates how isolation efficiency is strongly-dependent on electron p_{T}, rising to close to unity for higher p_{T} electrons.

[4] Cluster seeds are considered matched to re-fitted tracks if they meet the following requirements: $|\eta_{\mathrm{cluster}} - \eta_{\mathrm{track}}| < 0.05$ and $-0.10 < \Delta\phi < 0.05$, with $\Delta\phi = -q \times (\phi_{\mathrm{cluster}} - \phi_{\mathrm{track}})$ and q the charge.

[5] In a sample of events, a tighter operating point will result in fewer "confirmed" electrons than a loose operating point, but one can be more confident that each of those confirmed electrons is actually an electron. The operating points reflect a trade-off between electron purity and efficiency.

Electron scale factors are defined as the ratio of the efficiency for a given working point in data, to that same efficiency as derived from simulation. These scale factors quantify the deviation in simulation from the real detector behaviour, and are used in physics measurements to correct the simulation to more closely match data. Uncertainties in the measurement of the scale factors will manifest as an uncertainty on the scale factors themselves. This uncertainty can be summarised as a set of experimental uncertainties on the various electron efficiencies, as well as variation in the electron energy scale and momentum resolution. These uncertainties can be propagated to ATLAS measurements through variation of the scale factors, as is done in Chapter 10.

5.4.2 Muons

Muon reconstruction is initiated separately with the construction of track candidates in the ID and the MS, through the techniques discussed in Sections 5.1.1 and 5.1.2 [229]. These two types of track candidate provide complimentary information, and five types of muons can be defined through their varied usage [238]:

- **Combined muons** (CBs) are built by combining muon track candidates in the ID and MS using a global refit. Hits in the MS may be included or neglected to improve the quality of the track fit. These are the primary type of reconstructed muon.
- **Inside-Out muons** (IOs) are reconstructed by starting with the ID track, and searching for complimentary hits in the MS.
- **Segment-tagged muons** (STs) are built from ID tracks with one associated local track segment in the MDT or CSC chambers. This occurs when the muon crosses only one layer of the MS chambers.
- **Calorimeter-tagged muons** (CTs). The probability of muons depositing energy in calorimeters is lower than electrons or hadrons, but not zero. CT muons are those built from matching an ID track to a calorimeter deposit from a minimum-ionising particle.
- **Extrapolated muons** (MEs) are those built from an MS track only, provided the track is loosely compatible with the nominal interaction point. MEs require two hits in the central regions but three in the forward regions. MEs are sometimes built with partial information from the PD and SCT of the ID.

Any overlap between different muon types is resolved by preferentially selecting CBs, then STs, then CTs.

Requirements are now placed on the quality of the reconstructed muons, defining three nominal working points, `Loose`, `Medium` and `Tight`, plus the `Low-pT` and `High-pT` working points for use in extreme phase-space regions. The defining criteria include the number of hits in the ID and MS, and particular properties of the fitted final track.

The `Medium` working-point muon is the default ATLAS selection and is used in the entanglement measurement presented in Chapter 10. For $0.1 < |\eta| < 2.5$, the `Medium` working-point accepts only CB and IO muons, and requires at least three hits each in two separate MS stations (the MS being split radially into three stations), as well as good compatibility between the MS and ID charge and momentum measurements[6]. The `Medium` identification criteria also include ME tracks with three MDT/CSC hits each in three separate MS stations in the $2.5 < \eta < 2.7$ range, extending acceptance beyond the pseudorapidity coverage of the ID. Muon isolation is also quantified using ID track information, calorimeter information, or the combination of the two through the particle-flow algorithm. Seven isolation working points are defined, and the Chapter 10 entanglement measurement uses the `PFlow_Loose` working point as defined in [238]. Muon candidates are also required to meet the baseline requirements:

- $p_{\mathrm{T}} > 15\,\mathrm{GeV}$,
- $|\eta| < 2.5$,
- $|d_0/\sigma(d_0)| < 3.0$,
- $\left|z_0 \sin(\theta)\right| < 0.5\,\mathrm{mm}$.

Similarly to the electron case, muon efficiencies concern reconstruction, identification, isolation and track-to-vertex association, and scale factors are derived from these efficiencies. Efficiencies are evaluated using the tag-and-probe method using $Z \to \mu\mu$ and $J/\Psi \to \mu\mu$ events. The reconstruction efficiency for muons defined using the `Medium` identification working point are shown for data and simulation for these two processes in Figure 5.3b. A muon uncertainty prescription is arrived at by variation of the scale factors, and propagated to the entanglement measurement, Chapter 10.

5.5 Jets

The jet was introduced in the discussion of QCD phenomenology in Section 2.6. Given the hadronic nature of LHC collisions, jets constitute the most common final-state objects that ATLAS detects, and are invaluable probes of the dynamics of QCD. In contrast to the charged leptons discussed above, a jet is not a single particle, but a collection of many, wrapped up into a single object acting as a proxy for the true, coloured partonic object. Whilst charged leptons produce a relatively clear, concentrated detector signal, the spray of collimated particles which is eventually labelled a jet register as a wide, conical collection of tracks and energy depositions. The procedure by which tracking and calorimetry information is combined into a jet object is the jet algorithm. Jets reconstructed through a particular algorithm are calibrated in several ways for use in ATLAS physics analyses.

[6] This is defined formally in Section 5.1.1 of [238]

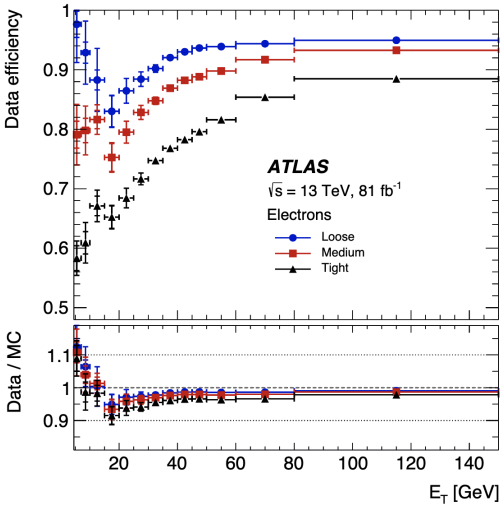

(**a**)

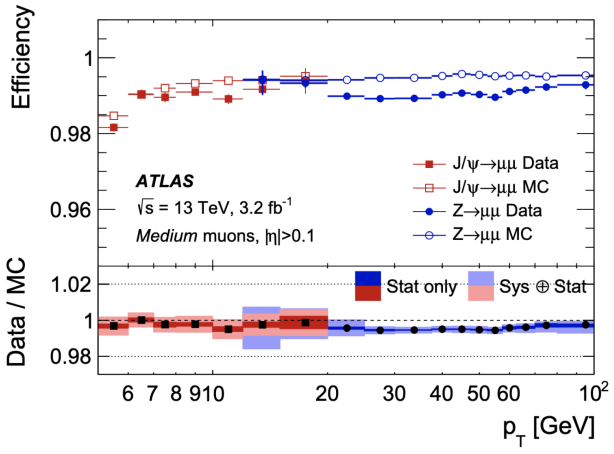

(**b**)

Figure 5.3: An illustration of two specific lepton efficiencies: (**a**) Electron isolation efficiency for $Z \rightarrow ee$ events, in bins of electron transverse energy, for Loose, Medium and Tight working points. Taken from [235]. (**b**) Reconstruction efficiency for Medium muons as a function of muon transverse momentum. Red points refer to $J/\Psi \rightarrow \mu\mu$ events whilst blue refer to $Z \rightarrow \mu\mu$ events. The bottom panel shows the ratio with respect to predicted efficiencies. Taken from [229].

5.5.1 Jet Algorithms

Any jet algorithm worth its salt should meet a set of criteria. One such criterion would be parton-jet correspondence: the final-state jets should closely correspond to kinematics of the high-energy partons and so capture the interesting QCD physics of the underlying interaction. Other infamous criteria include infra-red and collinear safety: these are conditions for using sensible observables in perturbative QCD [239].

Infra-red safety describes an insensitivity to soft radiation effects: a jet definition should be stable under the emission of a suitably low-p_{T} coloured particle. Observables which are collinear-safe are those unaffected by partonic splittings which are collinear i.e. the emission of a coloured particle in the direction of the original particle should have negligible effect. Collinear- or infra-red-unsafe (IRC-unsafe) algorithms will suffer from varying jet number and constituents. Jet algorithms should also be independent of detector technology and of hadronisation model. Finally, it is of practical merit to employ jet algorithms which are simple to implement, fast to run and stable in conditions characterised by heavy pile-up.

Jet algorithms have evolved significantly since the original work of Sterman and Weinberg in 1977 [240], and are now generally classed into two types. *Cone algorithms* cluster particles contained within rigid conical shapes [241], [242]. These algorithms were generally found to be IRC unsafe or suffer from poor scaling. More popular in current times are the *sequential clustering algorithms*, which group particles in momentum space. Their premise is that jet constituents will differ in transverse momenta by only small amounts, making p_{T} a suitable variable for identifying clusters [243]. Once suffering from poor computational performance, these algorithms are now used widely in experimental collaborations. This is a result of the FastJet programme [244], responsible for introducing vastly more efficient implementations of the sequential clustering algorithms.

Sequential clustering algorithms work by defining some notion of distance between input constituents [244]. These input constituents may be tracks, calorimeter clusters or particles. The closest pair of constituents are combined and the process is repeated, iteratively combining constituents into a jet until some stopping criterion is achieved. Two distance parameters, $\left(d_{ij}, d_{iB}\right)$, are defined as follows for particles i and j:

$$d_{ij} = \min\left(p_{\mathrm{T},i}^{2a}, p_{\mathrm{T},j}^{2a}\right)\frac{\Delta R_{ij}^2}{R^2}, \tag{5.5.1}$$

$$d_{iB} = p_{\mathrm{T},i}^{2a}, \tag{5.5.2}$$

with $R_{ij}^2 = \left(y_i - y_j\right)^2 + \left(\phi_i - \phi_j\right)^2$ and a an integer exponent.
The value of a, $a \in \{1, 0, -1\}$, defines three separate algorithms:

- $a = 1$ yields the K_t algorithm, in which low p_{T} particles dominate and are clustered first [245];
- $a = 0$ yields the Cambridge-Aachen algorithm which is independent of p_{T} and clusters closest particles first [246];
- $a = -1$ yields the anti-K_t algorithm in which high p_{T} particles dominate, meaning that hard particles are clustered first [247].

The anti-K_t algorithm is distinguished in producing round jets and being relatively insensitive to underlying event (UE) and pile-up (PU) conditions, unlike the K_t algorithm which is highly susceptible to such phenomena. Figure 5.4 provides a comparison of four different jet algorithms on a simulated event which features both hard and soft behaviour. It shows the robustness of the anti-K_t algorithm, which continues to generate circular jets in the face of the soft activity. In contrast, the K_t and Cambridge-Aachen algorithms produce jet shapes which are strongly dependent on this soft activity. ATLAS uses the anti-K_t algorithm almost exclusively [248]. The distance parameter R is clearly also influential, and different sizes of jet are defined as a function of R. Most commonly seen is $R = 0.4$, which is the definition used for all studies and measurements presented in this thesis, but large-radius jets with $R = 1$ are feature in the ATLAS top-quark physics programme.

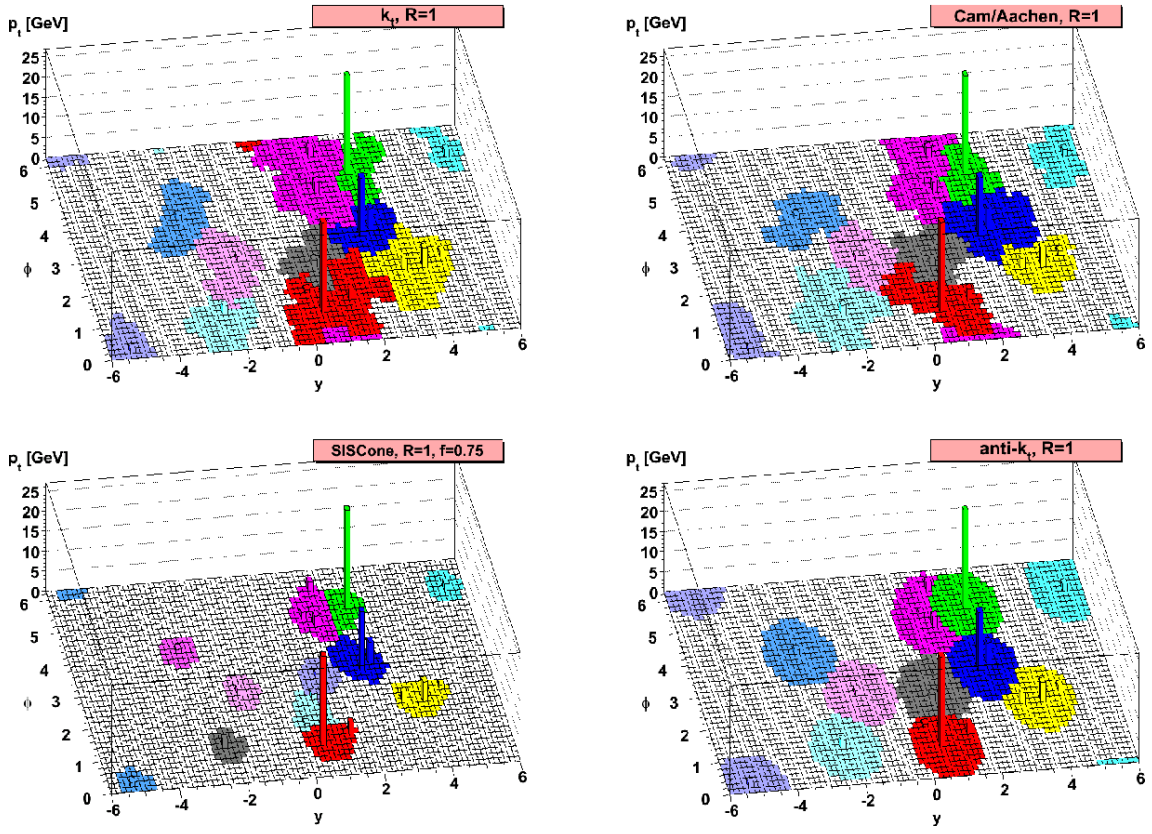

Figure 5.4: A celebrated example of the power of the anti-K_t algorithm, taken from [247]. A sample MC-simulated event, featuring some partonic hard scatter and some soft background, is clustered using four different jet algorithms. The anti-K_t algorithm is able to produce rounded jets, unlike the other algorithms whose resultant jet shapes strongly depend on soft background activity.

5.5.2 Jet Reconstruction

Pertinent to all physics studies in this thesis are small-radius jets with $R = 0.4$, reconstructed using the FastJet package. Two types of jets are defined, depending on the input objects used to construct them. EMTopo jets are built using topo-clusters as inputs; PFlow jets are built using particle-flow objects and exhibit improved energy and angular resolution, robustness to pile-up, and reconstruction efficiency compared to the EMTopo jets [234]. Both types of jet are reconstructed if they have $p_{\mathrm{T}} > 7\,\mathrm{GeV}$ and $|\eta| < 4.5$. Reconstructed ID tracks with $p_{\mathrm{T}} > 500\,\mathrm{MeV}$ are also used in the reconstruction of jets, subject to quality requirements on the number of ID hits. All jets used in studies in this thesis are PFlow jets.

The analogous truth-level object is the *truth jet*. Truth jets are reconstructed from stable final-state particles in simulation . Candidate particles have $c\tau > 10\,\mathrm{mm}$ with τ the particle lifetime. Muons, neutrinos and pile-up activity particles are not included. Truth-matching to reconstructed jets is done geometrically using the distance parameter ΔR.

The *jet energy scale* (JES) calibration is a procedure for correcting a jet's four-momentum after reconstruction, so as to better match a corresponding truth jet [232]. It is detailed in Figure 5.5, and summarised as follows. The procedure begins by moving the jet origin to the primary interaction vertex and correcting the kinematics accordingly. Two *pile-up correction* stages remove additional energy from pile-up effects. The jet four-momenta are calibrated using both corrections derived from di-jet simulation, and a global sequential calibration (GSC) which applies corrections based on detector-level information [249], [250]. Finally, an "in-situ" calibration is applied only to data, to account for differences in jet response between simulation and data. The JES procedure results in marked reduction in associated jet uncertainties for EMTopo and PFlow jets used in Run-2 ATLAS measurements. The set of procedures has since been improved, with corrections now derived from the entire Run-2 dataset, and modifications to particular algorithms, including a replacement of the GSC method with a deep learning approach. The updated JES calibrations are ready for deployment on Run-3 data [251].

The *jet energy resolution* (JER) quantifies how well the energy of a jet can be measured, subject to the limited accuracy of the detector, as a function of p_{T}. It is quantified as a function of various factors including electronic noise, pile-up effects, statistical fluctuations and detector hardware effects [232]. The JER is measured and calibrated using di-jet data events, and a smearing can be applied to simulated jets when the JER in simulation does not match that of data. Additionally, a *jet vertex tagger* (JVT) uses multivariate likelihood methods to discriminate between signal and pile-up jets based on tracking information [252]. In the entanglement measurement, Chapter 10, reconstructed jets are required to have $p_{\mathrm{T}} > 15\,\mathrm{GeV}$ and $|\eta| < 2.5$. Jets which meet the criteria $p_{\mathrm{T}} < 60\,\mathrm{GeV}$ and $|\eta| < 2.4$ are scrutinised by the JVT to suppress pile-up contributions.

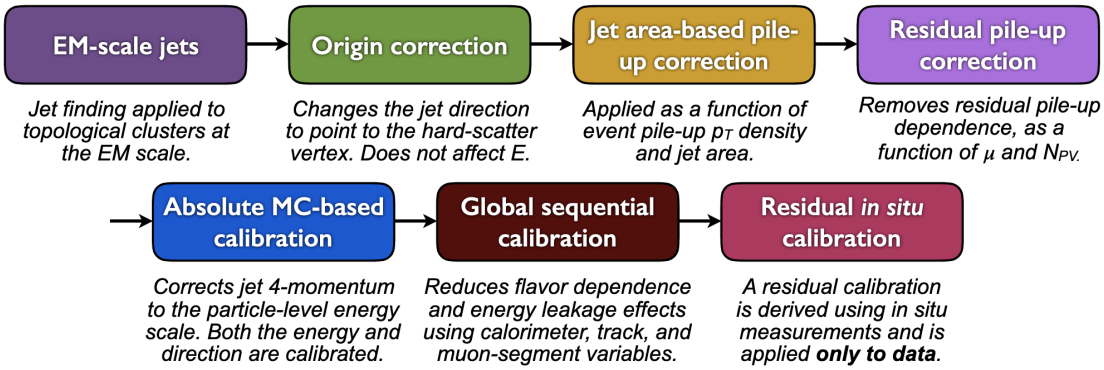

Figure 5.5: The Jet Energy Scale calibration procedure as applied to jets during Run-2 [232]. The corrections restore the jet energy to match that of reconstructed truth jets.

The JES calibration procedure is affected by a large set of systematic uncertainties, with most stemming from the in-situ correction step. The set is reduced by constructing a covariance matrix of all uncertainty sources, and performing an eigen-decomposition using the category reduction scheme, leaving 15 'summary' uncertainties which can be propagated to measurements [250]. Similarly, uncertainties defined for the JER procedure are propagated to the entanglement measurement in Chapter 10, as well as uncertainties relating to jet flavour, pile-up conditions and calibration of the jet pseudorapidity.

5.5.3 Jet Flavour Tagging

Flavour tagging asks the question,"what kind of parton seeded this jet?". The ability to identify whether a jet originated from a b-quark, a c-quark, a light quark, a gluon — or even a boosted t-quark — is extremely useful for categorising events [253]. In the context of this thesis, the ability to tag two b-jets is critical to identifying candidate $t\bar{t}$ events.

Flavour tagging is predicated on the idea that particular jet flavours will have particular characteristics. These could relate to the lifetime and mass of heavy hadrons, the properties of heavy-quark fragmentation, or even the substructure of the jet itself. Focusing specifically on identifying b-jets (*b-tagging*), a key feature of b-hadrons is their long lifetime. This gives an increased likelihood of a secondary vertex, displaced some distance from the hard-scatter collision point, and associated tracks with high impact parameters. ATLAS flavour-tagging algorithms begin by considering low-level objects. The IP2D and IP3D algorithms use impact parameters to generate a set of discriminants for b-, c- or light-hadrons [254]. The RNNIP algorithms utilises a recurrent neural network to learn correlations between tracks arising from the same b-hadron: this provides an additional flavour discriminant [255]. Additional approaches focus on reconstructing displaced vertices. The SV1 algorithm builds a single secondary vertex

[256]. The JetFitter algorithm seeks to reconstruct the full b- to c-hadron decay chain, using a modified Kalman filter to build a single track containing the b- and c-hadron decay vertices [257].

The discriminant outputs of the low-level flavour tagging algorithms are fed into a neural network (NN) which constitutes the DL1 algorithm family[7]. Selected outputs from the IP2D, IP3D, SV1 and JetFitter algorithms serve as inputs for the standard DL1 algorithm, whilst the DL1r algorithm also includes RNNIP outputs [253]. Both input sets are augmented by high-level jet kinematic properties. The NN output is a three-dimensional score $(p_b, p_c, p_{\text{light}})$, with the final b-tagging discriminant given by

$$D_{\text{DL1r}} = \ln\left(\frac{p_b}{f_c \cdot p_c + (1 - f_c) \cdot p_{\text{light}}}\right), \tag{5.5.3}$$

with f_c quantifying the c-jet fraction in the background hypothesis and being tailorable for a particular physics analysis. An analogous c-tagging discriminant also exists. The network is trained on a simulated sample consisting of $t\bar{t}$ and $Z' \to q\bar{q}$ events[8], giving a total of 22 million jets. The performance of the DL1r discriminator for b- and c-tagged jets is shown in Figure 5.6. ATLAS physics analyses can set an 'operating point' defined by the proportion of jets categorised as a b-jets in the baseline $t\bar{t}$ simulated sample. The '85% operating point' is the value of the DL1r discriminant for which 85% of the b-jets in the sample have the higher score: this operating point is used to define b-jets in the Chapter 10 entanglement measurement.

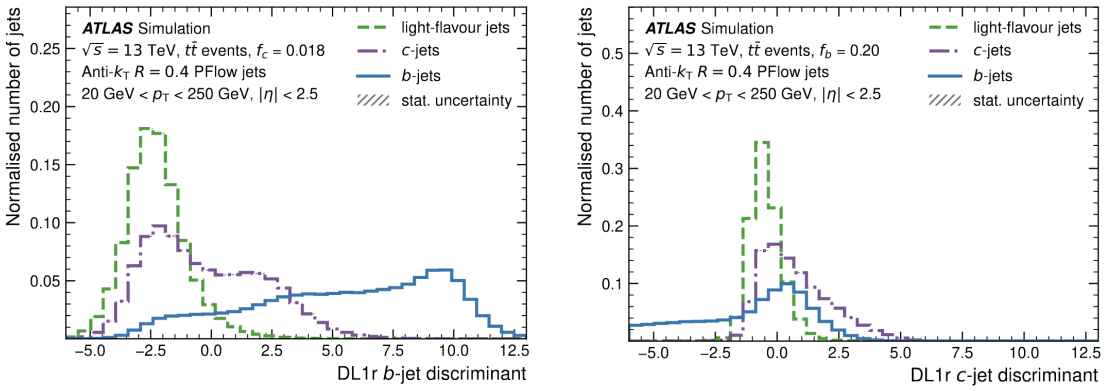

Figure 5.6: DL1r discriminants for b-jet and c-jet discrimination [253].

The performance of the b-tagging algorithm is assessed in data and simulation using di-leptonic $t\bar{t}$ events. Uncertainties in the calibration of the b-tagging algorithm

[7] The DL1 algorithm replaced the MV2c10 algorithm used during Run-1 which was based on boosted decision tree (BDT) methods [258].

[8] The Z' is a heavy hypothetical neutral gauge boson predicted by certain SM extensions [259].

arise from variation in the simulated $t\bar{t}$ and background simulated-samples. Specifically, these uncertainties are estimated as variations in the tagging efficiencies, which leads to large number of variations [260]. Similarly to the JES calibration uncertainty prescription, a covariance matrix is constructed and an eigen-decomposition performed to provide a streamlined uncertainty prescription for physics analyses.

5.6 Missing Transverse Momentum

There are some particles which ATLAS cannot detect. Foremost on that list is the neutrino, but BSM particles with particular properties may also feature. There is, however, a way to infer the presence of such particles. The conservation of momentum states that the total momentum of all collision products should vanish in the transverse plane, assuming that the incoming protons collide completely head-on. This fact can be exploited to derive a *missing transverse momentum* (MET) object $E_{\mathrm{T}}^{\mathrm{miss}}$: the vector of transverse energy required for p_{T} momentum conservation. This can be used as a proxy for undetected final-states, though $E_{\mathrm{T}}^{\mathrm{miss}}$ can also arise due to mis-measurement of detectable particles.

The reconstruction of $E_{\mathrm{T}}^{\mathrm{miss}}$ is made up of two parts [261]. The first consists of 'hard objects': fully calibrated and reconstructed physics objects, derived from mutually-exclusive signals to avoid ambiguity in the signal. In order of descending priority, electrons, photons, τ-leptons and jets are employed. Muons, whose reconstruction does not depend strongly on calorimeter signals, are also used and suffer from little overlap with the other objects. The second contribution is built up from 'soft-event' signals, which are reconstructed charged-particle tracks not associated with the above hard objects, but associated with the hard-scatter vertex. Explicitly,

$$E_a^{\mathrm{miss}} = -\sum_{i \in \{\text{ hard objects }\}} p_{a,i} - \sum_{j \in \{\text{ soft signals }\}} p_{a,j}, \tag{5.6.1}$$

for $a \in \{x, y\}$, giving $\mathbf{E}_{\mathrm{T}}^{\mathrm{miss}} = \left(E_x^{\mathrm{miss}}, E_y^{\mathrm{miss}}\right)$. The performance of $E_{\mathrm{T}}^{\mathrm{miss}}$ is assessed by comparing $W \to \nu l$ samples, with a high expected component of $E_{\mathrm{T}}^{\mathrm{miss}}$, to $Z \to \mu\mu$, which has no expected $E_{\mathrm{T}}^{\mathrm{miss}}$. This performance is illustrated in Figure 5.7

5.7 Bringing It All Together

Figure 5.8 is the "event display" for a candidate Run-2 $t\bar{t}$ production event at $\sqrt{s} =$ 13 TeV [262]. It is a wonderful illustration of the concepts introduced in this chapter. The primary image is a rendering of the entire ATLAS detector, whilst the secondary image in the bottom-left shows a close-up view of activity in the Pixel Detector. In

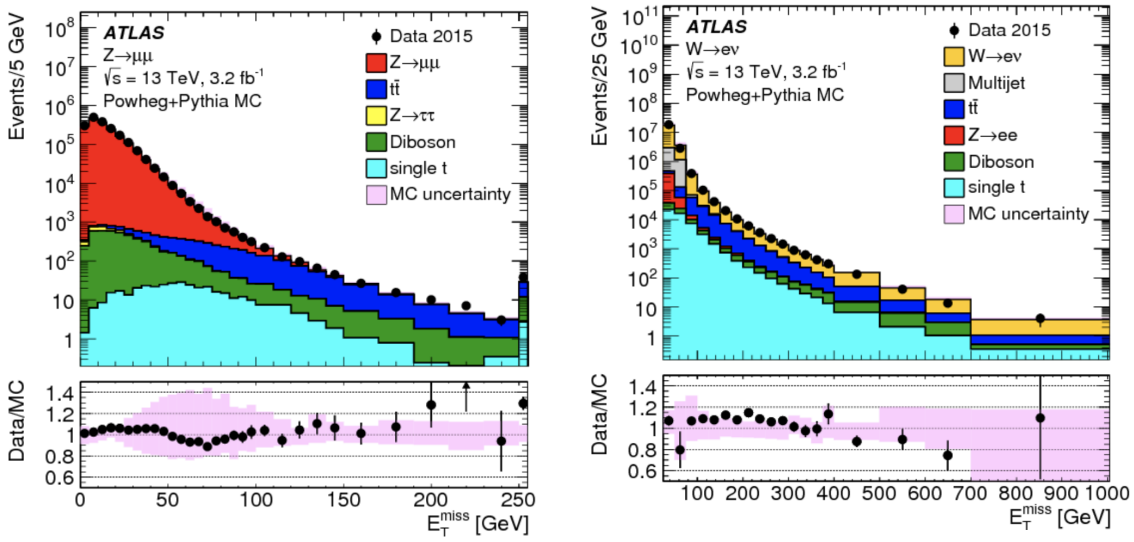

(**a**) $Z \to \mu\mu$ (**b**) $W \to \nu l$

Figure 5.7: The data-simulation comparison for $E_{\mathrm{T}}^{\mathrm{miss}}$. The $E_{\mathrm{T}}^{\mathrm{miss}}$ reconstruction performs well for processes with both a large (5.7a), and small (5.7b), number of expected $E_{\mathrm{T}}^{\mathrm{miss}}$ events. This is shown by the strong data-simulation agreement, with the MC uncertainty given by the pink band. Taken from [261].

the latter, each golden dot represents a pixel hit, with the layered structure of the PD apparent. Barely-visible white discs are the intersection of tracks which constitute primary vertices, whilst the other blue disks are secondary vertices from likely B-hadron decays.

The characteristic features of a $t\bar{t}$ decay are also visible. The red and blue lines represent a muon and an electron, respectively. In the larger view, the electron is seen to deposit energy in a narrow band in the ECAL (green polyhedra), whilst the muon propagates out and registers hits in the MS. Additional activity in the ECAL and HCAL (yellow polyhedra) is strongest in the regions corresponding to two b-tagged jets, with the jet cone is shown in yellow. These jets have a p_{T} of 228 and 154 GeV.

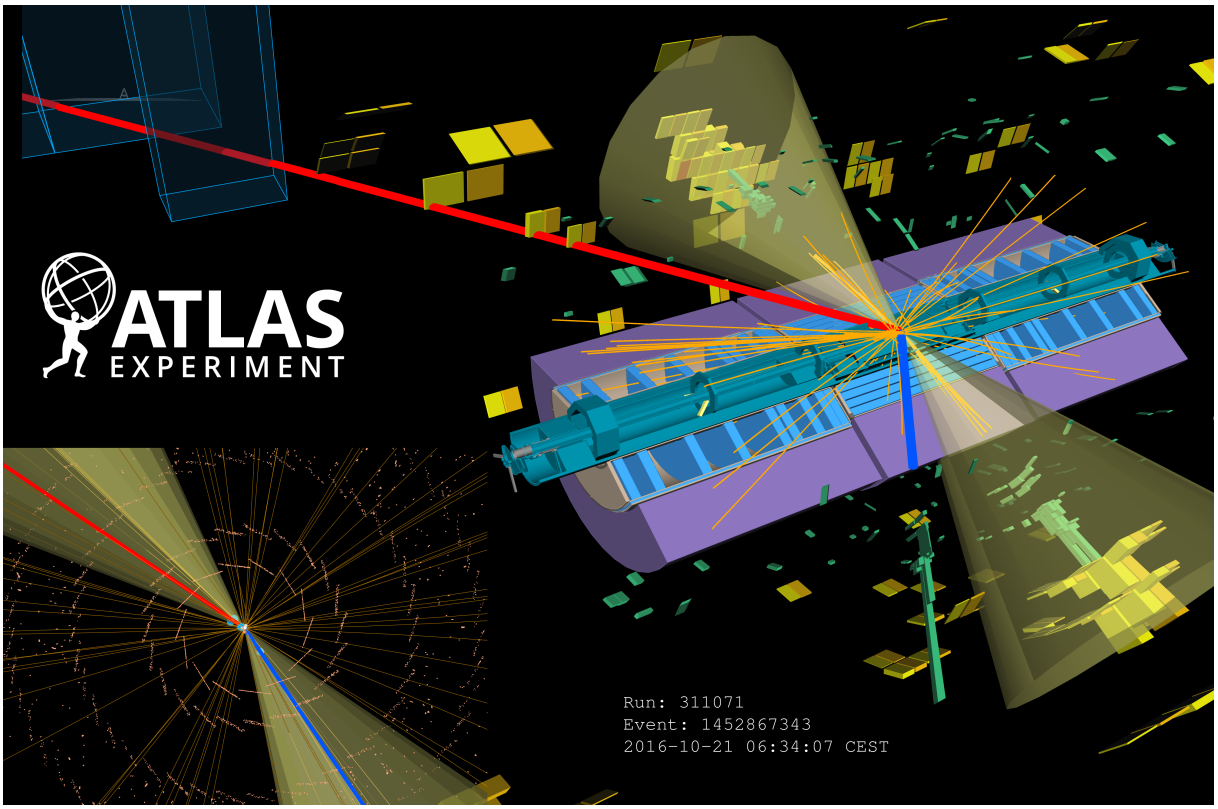

Figure 5.8: A beautiful event display representing the reconstruction of the decay products of a $t\bar{t}$ collision by the ATLAS detector [262].

Chapter 6

Modelling of LHC Collisions

"General-purpose event generation,
Relies on stochastic integration,
Producing MC events,
and parton showers circumvent,
Doing a full perturbative calculation."
—

In high-energy physics, a great deal of research is invested in generating state-of-the-art Standard Model predictions which can be compared to experimental data. These predictions are of fundamental importance to particle physics. On one hand, they allow the Standard Model to be tested and ratified against experimental data; on the other, they provide estimates of signal and background contributions in data, and so form a key feature of the experimental measurement process. The precision of many experimental results in the LHC's top-quark physics programme are now limited by the precision of those predictions. This is particularly true for $t\bar{t}$ production, where the large total cross-section, and excellent control of experimental uncertainties, contrive to give fantastic experimental precision, with the accuracy of $t\bar{t}$ simulation lagging as a consequence. The development of ever more accurate predictions and simulation tools ultimately tests the SM to higher precision, and reduces uncertainties when comparing to experimental data.

This chapter presents a high-level view of the methods used to generate theoretical predictions and simulate hadronic collisions, and discusses the modelling tools utilised in the physics studies presented in this thesis . The chapter draws heavily from [263]–[265].

6.1 Anatomy of a Collider Event

Hadrons are complicated, composite beasts. The collision of two hadrons is a downright nightmare. The proton-proton collisions taking place at the LHC are really the interactions of the internal partons. The factorisation theorem presented in Section 2.6.1 introduced how, in proton collisions, the scattering of high-energy partons could be de-coupled from the dynamics of the proton's structure. This idea is central to the modelling of high-energy hadron collisions. Of interest in this thesis are inelastic, hard scattering processes where both protons dissociate, where the partons form new states through intermediate vector boson exchange, where the final states may decay or split into hadronic showers, and where the entire scene is complicated by a mess of other proton collisions happening in the background. That's enough to be getting on with. Thank goodness there is no discussion of heavy ion collisions in this thesis...

SM predictions of proton-proton scattering can be obtained in several ways. Dedicated *theoretical predictions* provide the most precise comparison to experimental data. These are calculations of the scattering amplitudes of the 'interesting partons', performed to some fixed-order in perturbation theory, as introduced in Section 2.5 and discussed further in Section 6.2. An example is the NNLO-QCD predictions of $t\bar{t}$ SDM elements described in Section 3.3.6, which constitute the most precise theoretical estimations of these observables. Although representing the state-of-the-art in precision, these dedicated calculations are predictions of specific SM properties, and adapting the methods employed to different processes or observables is highly non-trivial.

Complimentary to these dedicated calculations are the so-called *Monte Carlo event generators* which sacrifice precision for flexibility. Event generators take the results of fixed-order scattering calculations, and place them in a more realistic collider context. They are simulators of particle colliders, generating collision *events* which can be used for a wide variety of purposes, and studied on an equal footing with measured data collisions. Generating realistic events is achieved by considering the following:

- The scattering of hard partons through *matrix element calculations*.
- The effects of soft and collinear radiation on the hard partons, which give rise to particle showers which are modelled using *parton showers*.
- The hadronisation of colour-charged states below Λ_{QCD} through phenomenological *hadronisation models*.
- The effects of other interactions which underlie the primary hard scatter — *the underlying event* — or interactions between remnant partons — *multi-parton interactions*.
- The effects of different proton-proton interactions in the same, or adjacent, bunch crossings — a messy phenomenon known as *pile-up*

Each aspect is discussed in this chapter. Figure 6.1 illustrates the complexity of a single simulated proton-proton collision event.

After this arduous event generation process, the interaction of the final-state particles with the detector must be considered. This *detector simulation* constitutes a very large portion of the ATLAS computation budget, which Chapter 7 discusses in detail. From this point forward, simulated events are treated with the same dignity as 'real' data events: the detector response is converted into low-level objects which together form high-level physics objects through the processes of digitisation [266] and the reconstruction techniques described in Chapter 5. Several definitions are presented, each representing a different stage in the simulation process.

- **Parton-level:** The simulation state prior to hadronisation. In many cases, the decay of unstable particles is also not performed, thus objects like top-quarks (and their differential spectra) are still defined.
- **Particle-level:** The state post-hadronisation, including only stable final-states. This is what would be observed with a perfect detector.
- **Reconstruction-level:** The state after simulation of detector response.

The first two definitions may be termed "truth-level", in that they encode the true representation of the underlying physics, which the detector response then distorts. These definitions are important in Chapter 7, where mappings between particle-level and reconstruction-level events are developed, and in Chapter 10, where knowledge of the detector response is used to estimate the underlying truth-level value of the measurement.

There are several prominent event generator tools used in the various studies presented in this thesis. They are Pythia, Herwig, Sherpa, Powheg and MadGraph_aMC@NLO. Each tool has numerous, overlapping specialities, and the tools are frequently combined to provide the most realistic collision event simulation for a given use case. In particular, the combination of MadGraph_aMC@NLO and Pythia is used to generate simulated collision events for studying $t\bar{t}Z$ spin correlations in Chapter 8; Powheg is combined with either Pythia or Herwig in the ATLAS simulation of $t\bar{t}$ production, relevant in Chapters 7 and 10. As the physics of event generators is introduced through this chapter, reference is made to these specific tools and the methods they employ.

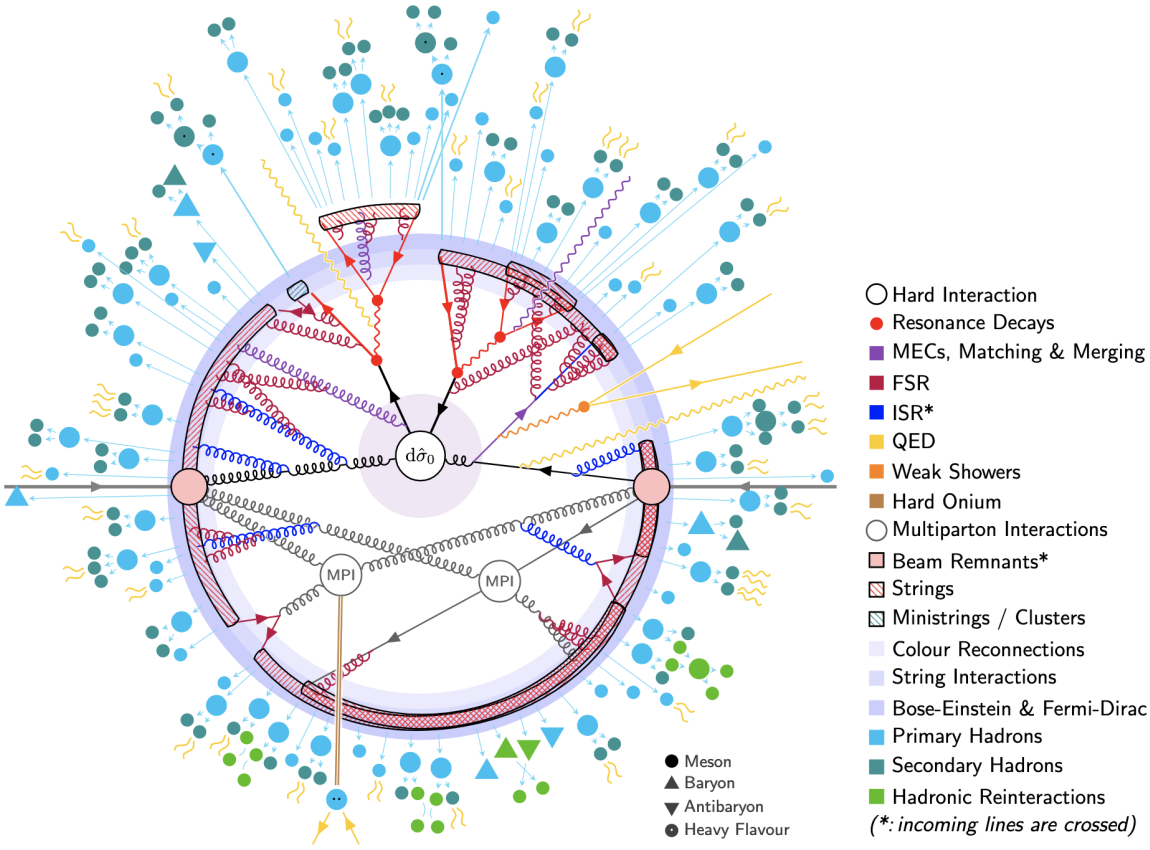

Figure 6.1: A proton-proton collision is an enormous mess and a nightmare to model. This image is taken from the PYTHIA 8.3 manual [267]. PYTHIA is one of a number of tools used to model these hadronic collisions. The hard interaction, labelled $d\hat{\sigma}_0$, decays through a series of partonic splittings. Multi-parton interactions (MPIs) constitute other parton interactions from the same hadron-hadron collision, and these interactions lead to their own slew of decay products. PYTHIA uses a string hadronisation model to gather up decay products into hadrons below Λ_{QCD}. These hadrons can then decay and interact. The methods used to model these features are described in this chapter.

6.2 Scattering Hard: Computing Matrix Elements

The *hard scatter* is the computation of high-energy partons scattering through the techniques of perturbative QFT. Recall again the general statement,

$$\hat{\sigma}_n = \int \frac{1}{2\hat{s}} d\Pi_{\text{LIPS}} \, |\mathcal{A}|^2 \tag{6.2.1}$$

where $\hat{\sigma}_n$ is now understood as the partonic cross-section of 2.6.1. The squared matrix element $|\mathcal{A}|^2$ must be computed for the process in question, up to a given order in

perturbation theory, and its integral over the phase-space $d\Pi_{\text{LIPS}}$ evaluated. At LO-QCD, scattering amplitudes can generally be evaluated analytically using 'textbook' Feynman diagram methods. Certain event generators may not even compute matrix elements, but simply have the results to common known processes hard-coded. Due to the high-dimensionality of the phase-space, the integration is generally performed numerically: Monte Carlo event generators are so named because of the Monte Carlo techniques employed to perform the phase-space integration. Furthermore, the complicated structure of the integrand generally requires specialised sampling algorithms [268]–[271].

Comparisons to experimental data frequently illustrate the importance of including higher-order corrections [272]: this is shown in Figure 6.2, which presents the $m_{t\bar{t}}$ spectrum for the process $pp \to t\bar{t}$, computed to NLO- and NNLO-QCD precision and compared to CMS data. The NNLO prediction yields lower theoretical uncertainties, whilst matching the experimental data more closely then the NLO prediction. Several critical issues arise when attempting to compute these higher-order corrections. Computing the on-shell scattering amplitudes becomes intractable using the standard Feynman diagrammatic methods, as both the number of possible diagrams, and the complexity of evaluating each, increase enormously at each higher order[1]. Modern methods utilise alternative techniques to evaluate scattering amplitudes in more a computationally-efficient manner [273]. In addition, ultra-violet (UV) divergences arise at NLO and above from loop-corrections, but are controllable through appropriate regularisation and renormalisation techniques [274].

The soft and collinear regimes refer to cases where additional radiation has negligible momentum, or splits at very small angle from a parent parton (as mentioned in the discussion on IR-safe jet algorithms in Section 5.5.1). Divergences in these regimes are collectively termed infra-red (IR) divergences and present a computational problem. They are tackled through phase-space slicing [275], [276], subtraction techniques [277]–[280], or higher-order generalisations [281]–[283]. In addition, at any given order in the coupling expansion, the amplitude can depend on certain *threshold logarithmic* terms, which can grow problematically-large in soft and collinear regimes. The technique of *resummation* is used to sum up particular troublesome logarithms to all orders in perturbation theory. One frequently sees fixed-order cross-section calculations supplemented by additional resummed logarithmic corrections, which has the twin effects of altering the central value of the cross-section, and lowering the associated theoretical uncertainties.

The computation of SM NLO-QCD processes is generally completely automated for $2 \to 2$ scatterings, and represents the state-of-the-art in event generation. Accuracy to higher orders in QCD, or the inclusion of NLO-EW corrections, is in general not yet realised in standard event generators. This is primarily down to the issues in matching hard matrix element corrections to parton shower algorithms discussed below. The Sherpa, Powheg and MadGraph_aMC@NLO event generators are able

[1] These issues are known as algebraic and analytic complexity respectively.

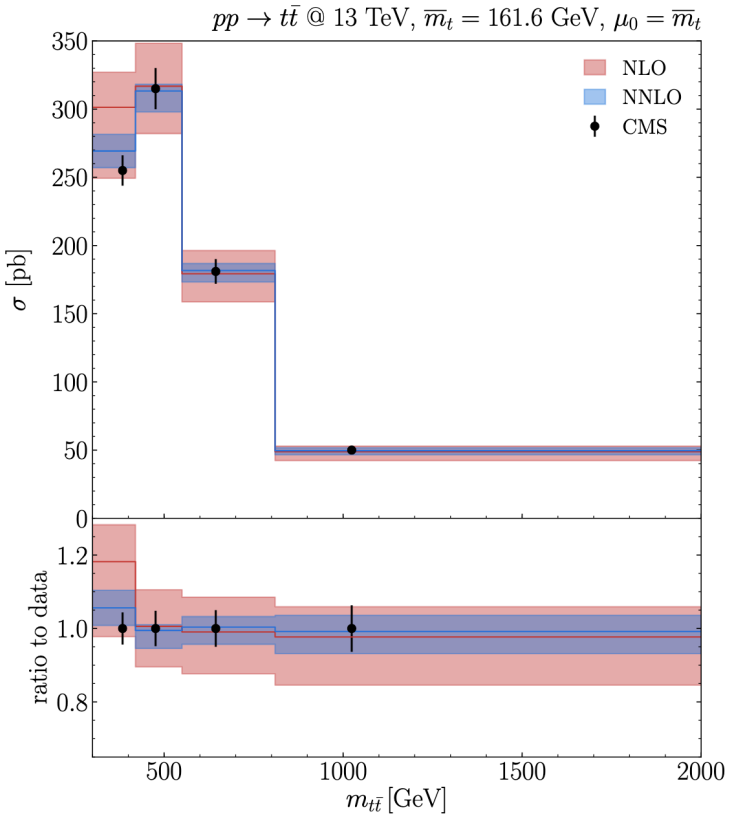

Figure 6.2: A comparison of NLO and NNLO predictions of the differential cross-section $\mathrm{d}\sigma(t\bar{t})/\mathrm{d}m_{t\bar{t}}$ to CMS data [272]. Higher-order corrections (NNLO) more closely match the experimental data whilst having lower theoretical uncertainties. he renormalisation and factorisation scales are set to the top mass in the $\overline{\text{MS}}$ subtraction scheme.

to generate NLO-QCD events for many SM and BSM processes, whilst Herwig has limited NLO-QCD capabilities and Pythia can only generate events to LO-QCD.

6.3 Showering the Partons

A cross-section evaluated perturbatively must be curtailed at some fixed-order, and thus only represents an approximation of the true cross-section. The *parton shower* is a tool applied to augment the fixed-order hard scatter, covering the effect of the splitting and branching of colour-charged objects from hard partons, and thus approximating the effects of all higher-order corrections in the soft and collinear regimes. Parton showers are in effect a probabilistic approach to logarithmic resummation, but more flexible in that they give an exclusive description of the final state, plus the results can

be applied in hadronisation models [284]. Applying parton showering to events gives a closer resemblance to data.

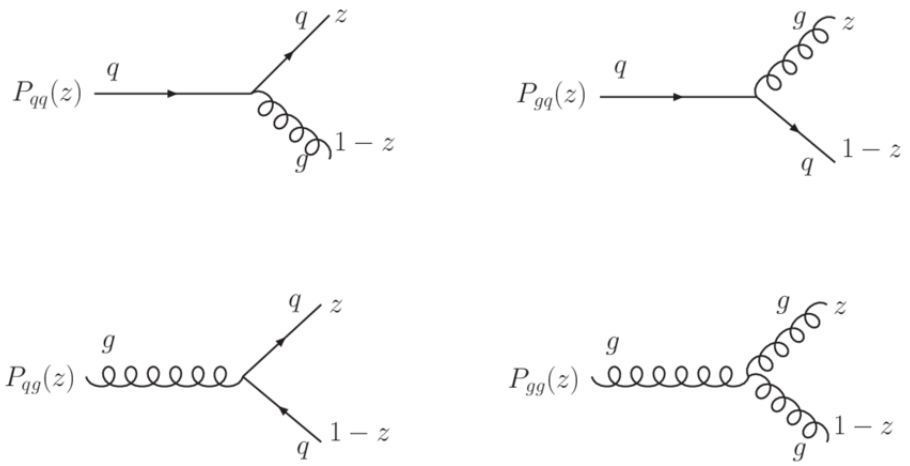

Figure 6.3: The splitting of a single coloured parton into two coloured partons is controlled through so-called parton splitting functions. Taken from [285].

The differential cross-section for some hard processes, accompanied by some parton splitting of the types shown in Figure 6.3, is given by a parton evolution equation of universal form,

$$\mathrm{d}\sigma_{n+1} \approx \mathrm{d}\sigma_n \frac{\alpha_\mathrm{s}}{2\pi} \frac{\mathrm{d}\theta^2}{\theta^2} \, \mathrm{d}z P_{ji}(z,\phi)\mathrm{d}\phi, \tag{6.3.1}$$

where θ is the opening angle between the hard system and the splitting, z the momentum fraction of the new parton, and the sum is taken over all initial state partons i which could lead to parton j. The term P_{ji} denotes the DGLAP splitting functions, which encode the probability of a particular $i \to j$ splitting occurring, as a function of the $\mathrm{SU}(3)_\mathrm{C}$ invariants and momentum z. The power of this expression, 6.3.1, is that it is universal: it can be applied to any process, since the parton splitting is entirely separate from the hard process. The basic notion of the parton shower algorithm is readily seen. By considering each branching as part of the next hard process, successive branchings are described iteratively. To consider the branching of individual partons, some ordering parameter τ is introduced. This ordering parameter is usually taken to be either the virtual mass-squared (virtuality q^2), as employed by the Pythia event generator, or the angular separation θ as utilised in the Herwig parton shower. This key difference in these two shower algorithms is found to have a large impact on the measurement of entanglement in $t\bar{t}$ production presented in Chapter 10.

The parton shower evolves by stepping through increments of τ, and considering the probability of a branching occurring, or not occurring, between each increment. The shower terminates when the ordering parameter passes some lower-bound, in place to avoid IR divergences. The probability that no branching will occur between

increments of the ordering parameter τ_0 and τ is given by the *Sudakov form factor*,

$$\Delta\left(\tau_0, \tau\right) = \exp\left[-\int_{\tau_0}^{\tau} \frac{\mathrm{d}\tau'}{\tau'} \int_{z_{\min}}^{z_{\max}} \mathrm{d}z P(z)\right]. \tag{6.3.2}$$

The Monte Carlo implementation of this idea assigns a random number solution $\Delta\left(\tau_0, \tau\right) = \rho, \rho \in [0, 1]$, and solves for τ, determining whether a resolvable branching is generated. For final-state parton evolution, if a resolvable branching was generated, the process is re-applied to the produced partons, and so on down to the cut-off. The values of z and ϕ are sampled from the distribution $P_{ji}(z, \phi)$ using the Monte Carlo method. For the evolution of the two initial-state partons, the process is reversed — so-called *backwards evolution* — starting from the scale of the hard scatter, and stepping backwards up the energy scale.

Parton showers are complimentary to fixed-order matrix element calculations. Whilst the latter describes well-separated, hard parton emissions, the former specialises in the soft and collinear regimes. The aim is to combine the two techniques to generate realistic collider events with high-jet multiplicities. The challenge is to employ each technology in the phase-space region in which it is applicable, whilst avoiding double counting of emissions, and managing the transition from the hard to soft regimes [286], [287]. The process of *matching* combines one matrix element calculation with a parton shower, and at NLO-accuracy there are two widely utilised matching methods. The MC@NLO scheme works by computing the parton shower to fixed order, then subtracting this from the matrix element calculation, and showering the final result [288], [289]. The POWHEG method stipulates that the hardest radiation from the parton shower is restricted to a phase-space softer than matrix element [290]. In contrast, *multijet-merging* performs a separate tree-level calculation for all parton multiplicities of interest, with cuts used to avoid soft and collinear divergences, and showers the merged combination. Merging tools are available at LO **catani_2001**, [291], [292] and NLO [291], [293]–[295] with Pythia , Herwig and Sherpa employing various methods. Combinations of modern event generators can facilitate the generation of events at NLO QCD-accuracy, implementation of the parton shower, and matching and merging of the matrix element with the shower. The entanglement measurement presented in Chapter 10 uses Powheg in conjunction with Pythia and with Herwig to achieve two complimentary, state-of-the-art descriptions of $t\bar{t}$ production. The combination of NLO+PS yields completely NLO-accurate inclusive or exclusive observable calculations, thus reduced theory uncertainties over the LO case.

6.4 Hadronisation Schemes

Hadronisation schemes are a means of mapping from the partonic final state to the hadronic final state which would be measured by the detector: a way of wrapping all the coloured detritus up as colour-neutral hadrons. Given the lack of rigorous and usable techniques for operating in this strongly-coupled, non-perturbative regime[2], phenomenological models are used. All such *hadronisation models* possess several important features [233]: parton-hadron duality, a specification where the kinematics of produced hadrons are similar to those of the partons [296]; appropriate consideration of the flow of colour into colour-neutral hadrons; and sets of free parameters which require careful tuning against experimental data. Early models [297], [298] were quickly succeeded by the two major techniques around which event generators are built. These are the string and cluster models.

The *Lund string model* is the most well-known and well used string model [299], [300]. It is predicated on linear confinement in the large-distance limit, and models the movement of two partons $q\bar{q}$ receding from one another as the linear stretching of a relativistic, one-dimensional string of constant tension. When it becomes energetically favourable, the string breaks in two: this constitutes the production of a new pair of quarks. The probability of such a splitting is controlled by a fragmentation function which is parameterised by factors like quark flavour. The splitting process continues until some stopping criterion is met. Groupings of adjacent quarks and anti-quarks are finally identified as mesons; similarly, grouping a composite state of two quarks or anti-quarks with a single quark or anti-quark defines a baryon. Gluons are introduced as kinks in the strings. The Lund string model is characterised by a large number of free parameters which are tuned from experimental data, but has the benefit of being IRC-safe. Figure 6.4 illustrates the stretching and splitting of the string, and the effect of a gluon's presence in the model. The Lund string model is the hadronisation model employed by Pythia.

Cluster models [302], [303] rely on the property of pre-confinement, an observation that partons in the shower at scales far below the hard process are clustered into colourless groups [304]. This clustering is independent of the underlying scatter process. In cluster models, gluons are forced to split into $q\bar{q}$ pairs and form clusters near the hadronisation scale. These clusters are identified as proto-hadrons and classified by their mass. Clusters can then be matched to known hadron masses, subject to some reshuffling of the kinematics; alternatively, clusters are decayed, with the decay model determined by the mass. Either approach yields the final-state hadrons identified by detectors. The accuracy of the cluster model approaches that of the string model, but requires fewer tuned parameters. Herwig employs the cluster hadronisation model.

[2] Only lattice QCD provides a means of computing in the strong-coupled regime. Dynamic problems, like the evolution of partons into hadrons discussed here, cannot be formulated on the lattice.

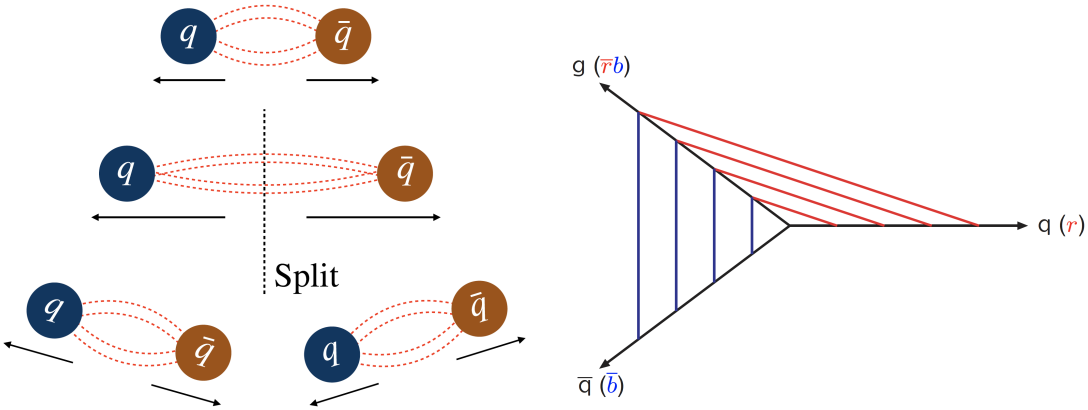

Figure 6.4: Illustrations of Lund string hadronisation model concepts. (**a**) A quark-anti-quark pair are modelled as being connected by a string. Under recession from one another, the energy in the string grows until it becomes energetically-favourable for the string to snap, and the system to become two pairs of quark-anti-quarks. Image borrowed from [301] with permission. (**b**) Gluons are introduced into the model through kinks in the string.

6.5 Sweating the Soft Stuff

The hard scatter, and its subsequent showering and hadronisation, takes centre stage in the analysis of a collider event. But one cannot ignore the action in the background. The term *underlying event* (UE) is used to label all interactions which are not associated with the primary hard scatter. A key phenomenon in the UE are interactions between remnant partons, so-called *multi-parton interactions* (MPI). In general these cannot be handled by appropriate factorisation theorems, and must be modelled or measured such that their impact on hard-scattering measurements can be estimated. Numerous models for MPI have been developed, predicting how often MPIs occur as a function of the individual protons' p_{T} [305], [306]. The complexity of these models ranges from treating parton interactions independently with some degree of correlated kinematics, to more complex interacting scattering models. Other UE factors include intrinsic parton p_{T} within the proton, the dynamics of remnant partons from the beam protons, the showering of MPIs, and issues related to colour reconnection. ATLAS has performed dedicated measurements of the UE [307]–[309], to better inform and tune relevant MC MPI models [310].

Pileup is label given to the background activity which does not arise from the primary, 'interesting' proton-proton interaction in the event. Pile-up can transpire in the ATLAS detector from additional proton-proton collisions from the same or adjacent bunch crossings, from interactions with particles emitted by other sources in the cavern, and from the interaction of the beam with its environment [311]. The pileup conditions as a function of the 2015 - 2018 data-taking periods of Run-2 are shown in

Figure 6.5. The study of pileup conditions is conducted on so-called minimum-bias events, which are defined using selections which minimise the probability of interesting hard scatters in such events. ATLAS employs both MC simulation and data-driven techniques, derived from minimum-bias studies, to "overlay" the effects of pileup conditions on signal events prior to digitisation [312], [313]. The increase in pileup as the LHC transitions to higher centre-of-mass energies constitutes a major hurdle for the experimental collaborations to overcome [313].

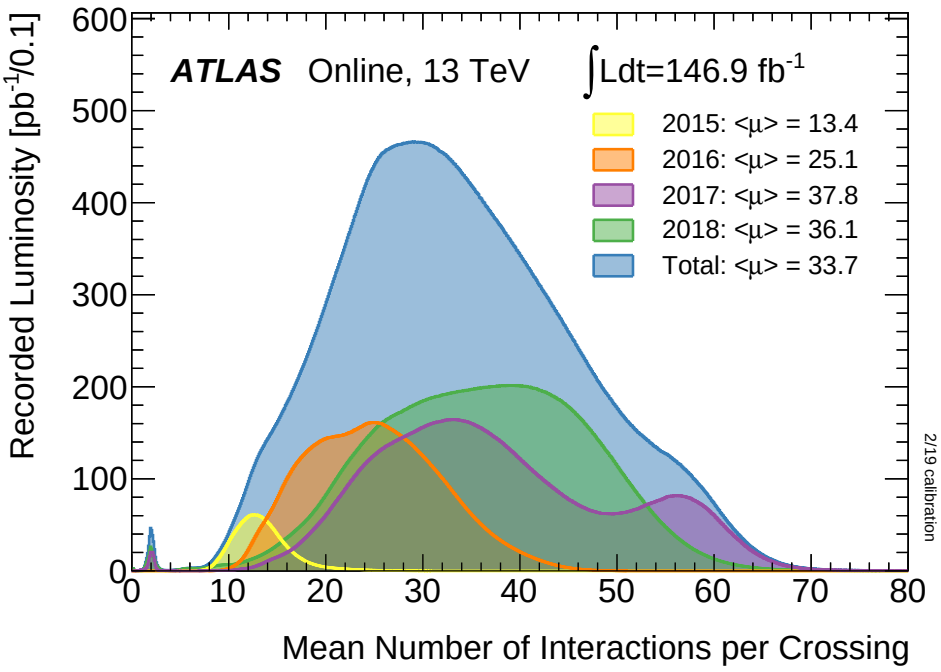

Figure 6.5: The recorded luminosity as a function of the mean number of interactions per crossing is a direct illustration of the pile-up conditions in the ATLAS detector [183]. The four years of the Run-2 campaign are shown.

6.6 Applications in ATLAS

The ATLAS top-quark physics programme employs a combination of the above software frameworks to achieve robust, NLO-accurate modelling of top-quark physics processes at the LHC. The complexity of event generators is reflected in the large sets of free parameters they possess. ATLAS seeks to find a configuration of parameters which generates simulated events that most closely match ATLAS data. To this end, *tuning* is periodically employed, where comparison to data helps inform internal generator settings to better model aspects like ISR, FSR, MPI and hadronisation [314]. The famous A14 Pythia tune to $\sqrt{s} = 7$ TeV data [315] dictates the nominal Pythia settings for $t\bar{t}$ production simulation in Chapters 7 and 10. In cases where a creative choice of

parameterisation remains, modelling uncertainties can be defined to cover the lack of knowledge in the optimal generator setting. In the context of the presented entanglement measurement, Section 10.10.2 discusses many such modelling uncertainties related to Pythia settings.

A short final word on the modelling of top-quark decays and spin correlations. In general, there are different means of handling the decay of heavy resonances like $t\bar{t}$ pairs in event generators. Decaying the top-quarks using the parton shower is highly efficient but undesirable in the case of this thesis because the spin correlation information is lost. The other extreme is performing the full off-shell calculation, $pp \rightarrow b\bar{b}l^{+}\bar{\nu}_{l}l'^{-}\nu_{l'}$, which contains all desired double-resonance and spin correlation effects, amongst additional off-shell effects, but is computationally-expensive. The MadSpin tool, interfaced to some matrix element generator (Powheg or MadGraph_aMC@NLO) provides an efficient means of generating events where spin correlations are preserved to tree-level accuracy in the top-quark decays [316], [317]. The MadSpin tool is used in Chapter 8 in the context of modelling spin correlations in $t\bar{t}Z$ production. MadSpin can also be used to "turn off" spin correlations, providing a 'no spin correlation' hypothesis which is also used in Chapter 8. A systematic uncertainty related to the decay of the top-quark is defined in Chapter 10 by interfacing MadSpin to the nominal simulation set-up to provide a comparison between Powheg and MadSpin.

Chapter 7

High-Level Detector Simulation Studies

"Detector response simulations,
Are CPU-intense operations,
So can crude smearing maps,
A neural network perhaps,
Hasten truth-to-reco transformations?"
—

Despite the contributions of thousands of scientists and engineers, millions of person-hours of work, and billions of pounds-worth of investment, the ATLAS detector, like any piece of experimental equipment, is not perfect. The resolutions of the various detector components, their location within the detector, and the efficiencies of the reconstruction algorithms are all sources of measurement imperfections. Any measurement made is likely to have been distorted away from the underling true value by these detector effects. The collective effect of these distortions is sometimes called the "detector response". This chapter discusses how this response simulated, and why existing processes constitute the dominant sink of ATLAS computing resources. It then presents several novel methods of emulating this detector response.

7.1 Existing Simulation Methods

7.1.1 Full Simulation using GEANT4

The physics of detector behaviour and response is fundamentally the physics of high-energy particles passing through matter. This constitutes a transport problem, governed by a set of transport equations which describe the probability and dynamics of interactions between detector materials and high-energy traversing particles [318]. At high energies, the characteristic feature of particle interaction is the creation of electromagnetic showers and hadronic cascades, which form and then die away as the total energy is distributed over a high multiplicity of constituents. Such complex transport

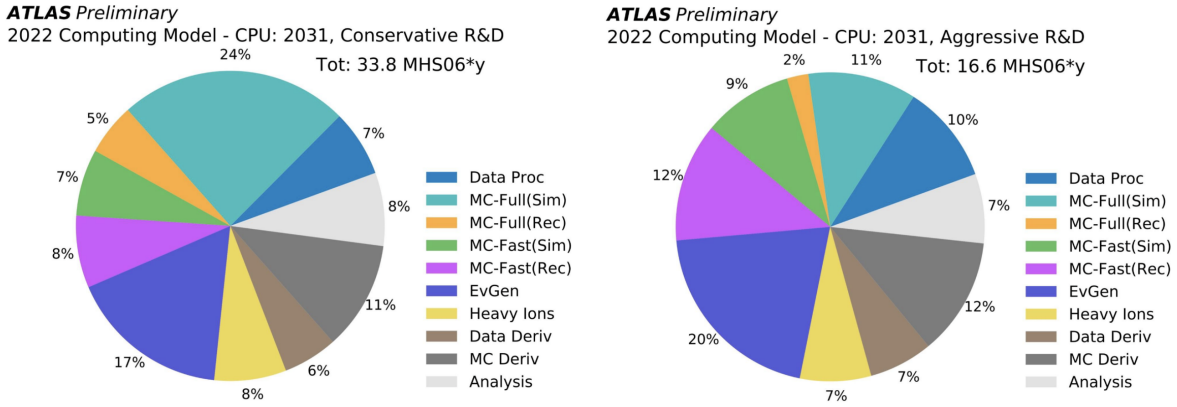

Figure 7.1: The projected ATLAS CPU-budget for 2031, taken from [253]. The left plot shows how the CPU-budget is expected to be dominated by detector simulation (Sim).

problems can really only be modelled numerically using Monte Carlo methods [319]. The key player in the world of MC particle transport solvers — in the high-energy particle physics world at least — is the GEANT4 simulation toolkit [320]. ATLAS uses GEANT4 to model the detector response on final-state particles [321], passing each through a GEANT4 model of ATLAS detector. GEANT4 considers the electromagnetic and nuclear interactions of the traversing particles through each layer of the detector, as well as the possibility of unstable particle decays.

Simulating the full behaviour of every single particle propagating through the ATLAS detector places an immense strain on ATLAS computing resources, constituting the largest single sink of computing power This trend is expected to continue unless significant development of new, more efficient simulation techniques takes place [253]. Figure 7.1 illustrates this point: detector simulation is expected to dominate the CPU-budget in the year 2031, but aggressive research and development should lower the simulation CPU demand significantly. ATLAS has developed a number of complimentary tools to GEANT4, designed to ease the computational load for detector-simulation tasks with minimal physics penalty.

7.1.2 ATLAS Fast-Simulation

In contrast to the "full-simulation" (Full-Sim) approach that is GEANT4, "fast-simulation" (Fast-Sim) approaches approximate some part of the full-simulation chain in the name of speed. This can be achieved through a combination of simplified detector geometries and simplified models of particle interaction; or by defining certain functions which parameterise detector response for particular physics objects. An example of the latter case is ATLFAST1, a fast-simulation effort from the 1990s which was used for ATLAS feasibility studies before the detector was even constructed [322], [323]. ATLFAST1

used simple parameterisations of detector response and reconstruction to "smear" the kinematics of physics objects, rather than simulating the actual passage of each object through the detector. For example, the p_{T} of each muon was smeared based on a Gaussian distribution which was a function of kinematics $(p_{\mathrm{T}}, \eta, \phi)$, with that distribution derived from full simulation. AtlFast1 led to a time-saving of around five orders of magnitude, but its accuracy in comparison to newer simulation methods leaves a lot to be desired.

It was found that around 80% of the Geant4 simulation time was taken up by the modelling of particles in the calorimeter systems, with electromagnetic shower modelling being by far the most computationally-expensive aspect [321]. Some fast-simulation algorithms replace full modelling of the showering with reduced-order models, or pre-simulated responses. The successor to AtlFast1, AtlFast2, is such an example. In capability, AtlFast2 sat somewhere between AtlFast1 and full Geant4 simulation. In its default form, AtlFast2 employed full Geant4 simulation for the ID and MS, and used an algorithm called FastCaloSim for modelling the calorimeter response. FastCaloSim replaced particle showers with parameterisations of the associated energy profiles in the calorimeters, derived from full simulation: a photon parameterisation was used for both photons and electrons, and a charged pion parameterisation for all hadronic showers [324]. AtlFast2 then introduced simplified modelling of the ID and MS in the form as Fatras [325]. Fatras brought a simplified model of both system geometry and particle interactions, offering a factor of 100 reduction in CPU-time. In Run 2, over 60 % of simulated events, a figure exceeding 30 billion, were generated with AtlFast2.

The state-of-the-art in fast simulation within ATLAS is AtlFast3 [326]. It introduces several developments: FastCaloSimV2 and FastCaloGAN, which again seek to expedite simulation of showers in the calorimeter through parameterised models. FastCaloSimV2, a development of the original FastCaloSim, factorises the shower parameterisation into lateral and longitudinal components. FastCaloGAN uses a general adversarial network (GAN) to model the electromagnetic calorimeter response [327], building on the attention that deep generative models have garnered in the context of calorimeter shower modelling over recent years [328]–[330]. FastCaloSimV2 is used to simulate electromagnetic showers of all energies, and hadronic showers at low and high energies. FastCaloGAN simulates hadronic showers of intermediate energy scale. Geant4 is retained for all modelling in the ID, and for muon interaction with calorimeters and the MS. The consequences of these developments are major improvements in the modelling of response in the forward calorimeters, and shower substructure within jets. AtlFast3 agrees with Geant4 to within several percentage points in almost all cases, whilst using only one-fifth of the computational processing power.

7.1.3 Non-ATLAS Simulation Tools

Several simulation tools beyond GEANT4 also exist in the wider particle physics community. The most popular is the DELPHES framework, an experiment- and collaboration-independent simulation tool designed to serve the needs of the phenomenological community [331]. DELPHES uses its own model of a generic detector which includes electronic and hadronic calorimeters and a muon detection system. The simulated detector response and subsequent object reconstruction algorithms are designed to be flexible; their simplicity aims to reduce computation time over the analogous GEANT4 simulation. Detector conditions can be specified, and so a lightweight proxy of ATLAS detector response can be achieved, though at the expense of considerable accuracy.

Recent developments in the RIVET framework [332], a tool for validating MC event generators and preserving experimental analysis work-flows, include functionality for emulating detector response [333]. Individual transfer functions are designed which smear truth-level physics objects, similarly to ATLFAST1. A set of standard ATLAS and CMS transfer functions are provided, with the transfer functions built from parameterisations used in DELPHES, in conjunction with public Run-2 detector performance results from both experiments. Buckley et al. provide a comparison of the RIVET transfer functions to DELPHES [333], highlighting differences in response for various kinematic spectra and showing that in general, emulating the response of particular detectors is extremely challenging without access to full detector performance results.

7.2 High-Level Smearing Maps

The following sections present studies of new fast-simulation techniques in the style of ATLFAST1 and the RIVET transfer functions. The methods could more accurately be described as detector response *emulation*, rather than *simulation*: the physics of particles interacting with detector materials is abstracted away, and the techniques instead attempt to capture the detector distortions to some representation of the event.

The main advantages of response-emulation techniques are their speed and accessibility. The primary motivation for fast simulation is to reduce the computational load of detector response simulation; parameteric emulation methods are highly efficient because there is no expensive simulation involved. In addition, emulation techniques should be easy to implement, such that the particle physics community at large can take advantage of them, without requiring expert knowledge of particular detector geometries. There is usually a compromise in accuracy made when using high-level emulation methods: they are not envisioned to be used when high precision is required. Instead, such methods come into their own in scenarios where any traditional simulation methods are prohibitively expensive. A possible use case is BSM model parameter space scans, where some form of detector response may augment simulated-samples generated for thousands or millions of different parameter combinations. Simulating

reconstruction-level events for many variations of Wilson coefficients in an EFT study is one such example.

This research aims to extend existing work on detector response emulation in several ways. Firstly, this research makes use of actual ATLAS simulated samples, which include the full GEANT4 response. It is thought that building emulation methods using this simulation should give a more accurate description of the specific ATLAS detector response. Existing emulation methods in the literature do not have this advantage. Additionally, this research investigates whether novel techniques can be applied to the detector-emulation problem, and whether these techniques can generate a more accurate response than existing emulation methods. Implementation of ultra-fast detector emulation techniques, specifically tailored for the ATLAS detector response, would be of great value to the phenomenological community given the mediocre performance of DELPHES[1]. These techniques would also ease the strain on the internal ATLAS computation budget.

Detector emulation considers the problem of finding an efficient transformation from a truth-level space $\mathcal{T}$ to a reconstruction-level space $\mathcal{R}$. In the most general sense, one could find a representation of truth-level event $T, T \in \mathcal{T}$, and corresponding reconstruction-level event $R, R \in \mathcal{R}$, and seek the mapping $T \mapsto R$. Most methods decompose this problem into finding a transformation for specific physics objects, or even a specific object's individual kinematics, and re-building the reconstructed event afterwards. There are several effects that need to be accounted for:

- **Smearing** effects alter the value of some variable by a finite amount due to mis-measurement. For example, the p_{T} of an electron at truth-level may be 40 GeV, but the measured value may be smeared to 50 GeV. In binned distributions, this can have the effect of migrating events from one bin to another, an effect which is captured in two-dimensional migration matrices.

- **Efficiency** describes the situation where objects or events exist at truth-level but not at reconstruction-level. In an event with a high-multiplicity of jets for example, some of these jets may not end up reconstructed. In a binned distribution, the efficiency in the j^{th} bin is given by,

$$f_j^{\mathrm{eff}} = \frac{N_j^{\mathrm{R}} \bigcap N_j^{\mathrm{T}}}{N_j^{\mathrm{T}}}, \tag{7.2.1}$$

  where N indicates number of events, and the superscripts T and R denote truth-level and reconstruction-level, respectively.

- **Acceptance** describes the situation where objects or events exist at reconstruction-level, but have no truth-level counterpart. This is usually the result of mis-identifying another type of physics object: for example, a jet may be incorrectly reconstructed as an electron, with the electron then appearing at reconstruction-

[1] Assuming that the tool was made available to those outside the collaboration...

level but not at truth-level. In a binned distribution, the acceptance in the i^{th} bin is given by,

$$f_i^{\text{acc}} = \frac{N_i^{\text{R}} \bigcap N_i^{\text{T}}}{N_i^{\text{R}}}. \tag{7.2.2}$$

This chapter presents two different methods for emulating detector response, focusing on smearing and efficiency effects.

7.3 Probabilistic Maps

Smearing effects are formalised through the integral transform of a truth-level distribution $x(t)$ to a reconstruction-level distribution $y(r)$[2]:

$$\int_{\Omega} K(r,t)x(t)\mathrm{d}t = y(r), \tag{7.3.1}$$

with Ω some truth-level phase-space and $K(r,t)$ a kernel generally derived by comparing truth-level and reconstruction-level simulation [335]. In the discretised case where the functional form of the distributions is not known, the probability density functions (PDFs) of x and y are represented by histograms with bin contents X_j and Y_i, respectively. The corresponding convolution is a matrix equation in terms of each bin entry:

$$Y_i = \sum_{j=1}^{M} R_{ij} X_j, \tag{7.3.2}$$

for a reconstruction-level histogram of M bins [336].

A simple attempt at building high-level transfer functions is inspired by the "response matrix" R_{ij} in 7.3.2. This matrix is re-imagined as a set of binned PDFs $y(r)_j$ in random variable r, indexed by the truth-level binning. The truth-level value t_0 selects a particular PDF $y(r)_j$, which is then sampled to produce the corresponding reconstruction-level value r_0. Figure 7.2 illustrates the concept. This idea can be extended to higher dimensions by considering that a reconstruction-level parameter may depend on several truth-level kinematic parameters, $t_1, t_2, t_3, ...$ There exists now an N-dimensional array of univariate PDFs indexed by each truth-level parameter $y(r)_{j_1 \ldots j_N}$. A truth-level state vector $t = (t_1, ..., t_N)$ selects the corresponding PDF, which is then sampled to yield r. For any physics object, a set of probabilistic *smearing functions* can

[2]This equation is Fredholm equation of the first kind [334]. This is sometimes referred to as a convolution, which takes slight liberties with the true definition of the convolution operation.

be built which are functions of the truth-level kinematics. Consideration must then be given to which kinematics are important to smear for each type of physics object.

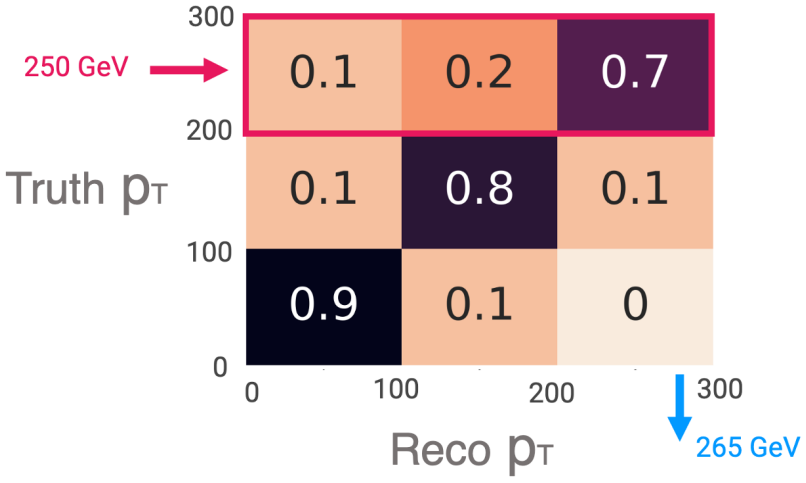

Figure 7.2: A illustrative example of a probabilistic smearing function. The two-dimensional array is indexed by truth-level and reconstruction-level p_{T} for some arbitrary physics object. The rows of the array correspond to binned probability density functions. A truth-level value of 250 GeV selects the top row of the array, as outlined in pink. The corresponding PDF is sampled, yielding an output of 265 GeV. In this way, a distribution of reconstruction-level p_{T} values can be obtained through repeated sampling, where the chosen PDF to sample depends on truth-level information. This idea can be extended to higher dimensions by considering dependence on other truth-level information.

Efficiency effects are applied to whole physics objects through simple efficiency functions, which are constructed from ATLAS public Run-2 detector performance studies. Published binned histograms give the fraction of objects which are reconstructed as a function of object kinematics, exactly as shown in Figure 5.3. This information can be used to veto a certain fraction of objects as a function of their truth-level phase-space position: if the efficiency of the detector at identifying electrons with $p_{\mathrm{T}} > 20\,\mathrm{GeV}$ is 80 %, the efficiency functions will randomly discard one event in every five [235]. Acceptance effects are not considered.

The combination of smearing functions and efficiency functions define a transfer function for each physics object. The input is the truth-level state vector $t = (t_1, ..., t_N)$, for which the efficiency functions return a boolean corresponding to whether the event will be constructed, then the smearing functions return a vector $r = (r_1, ..., r_N)$, the corresponding reconstruction-level kinematics. This approach is a "factorised" approach, as it considers the detector effects on each object to be independent of all other objects in the event. This is a fair assumption under the condition that objects are well isolated.

An implementation of the above transfer function method is constructed as a Python framework, built on top of ROOT data analysis framework [337]. The framework is designed for users to achieve two things: to build their own smearing functions from their own full simulation datasets, and to apply pre-constructed transfer functions to truth-level MC-simulated samples [338]. The smearing functions are realised as sets of two-dimensional ROOT histograms, indexed by truth-level parameters, which can be sampled using in-built ROOT methods. Information for efficiency functions are stored as arrays of one-dimensional ROOT histograms.

7.3.1 Study in $t\bar{t}$

To investigate the potential value of the probabilistic transfer function approach, a set of smearing functions were built using ATLAS full-simulation $t\bar{t}$ samples. A total of two million $pp \rightarrow t\bar{t}$ events, decaying through the lepton + jets channel, were generated at NLO-QCD using the Powheg + Pythia8 generator set-up. This is the primary event generation set-up for top-quark physics studies in ATLAS, and so the nominal set of Pythia settings was implemented. The details of the ATLAS Powheg + Pythia $t\bar{t}$ simulation approach are described at length in Section 10.2. Electrons were specified using a `Tight` identification working-point, muons using a `Medium` identification working-point, and PFlow jets defined with $\Delta R = 0.4$. A minimum cut of $p_{\mathrm{T}} > 25$ GeV was applied to all objects. Events are defined at particle-level and reconstruction-level, with the latter obtained through full detector simulation with Geant4.

The implementation of the transfer function method is completely generic, thus one could build a transfer function for any object present in the final-state. In the $t\bar{t}$ case, transfer functions are built for electrons, muons, and jets, with no distinction made regarding jet flavour. Each object is characterised by the kinematic variables $(p_{\mathrm{T}}, \eta, \phi, E)$. Detector smearing effects have negligible impact on angular parameters η and ϕ for all physics objects in question, therefore no smearing maps were constructed for these observables, and their truth-level values were propagated straight to reconstruction-level. The smearing function for p_{T} is set to depend only on truth-level p_{T}, and the E smearing function to depend only on truth-level E. Higher-dimensional smearing functions are studied for jets below. The reconstruction efficiency of jets across the phase-space is taken to be unity, so no efficiency functions are required. Efficiency effects are far more important for the charged leptons. Leptonic efficiency functions were built using published ATLAS trigger and reconstruction efficiencies for muons [229], in bins of p_{T} and η. Trigger and identification efficiencies functions, parameterised solely in terms of p_{T}, were built for electrons [235].

Several key results are shown below. Figure 7.3 shows the simulated p_{T} and E spectra for electrons. The reconstruction-level (Reco-level) and particle-level (Truth-level) distributions are shown in red and blue, respectively. The result of detector-emulation transfer function approach are shown in purple (No efficiency) and green (With effi-

ciency), where the former considers only the application of smearing functions, and the latter includes smearing functions and efficiency functions. It is clear that inclusion of the efficiency functions has a sizeable effect as expected. The efficiency functions are able to emulate the detector response simulation closely for electron energy, whilst failing to do so for electron p_{T}. Figure 7.4 shows how the transfer functions implemented were unable to capture the detector distortions at all for muons.

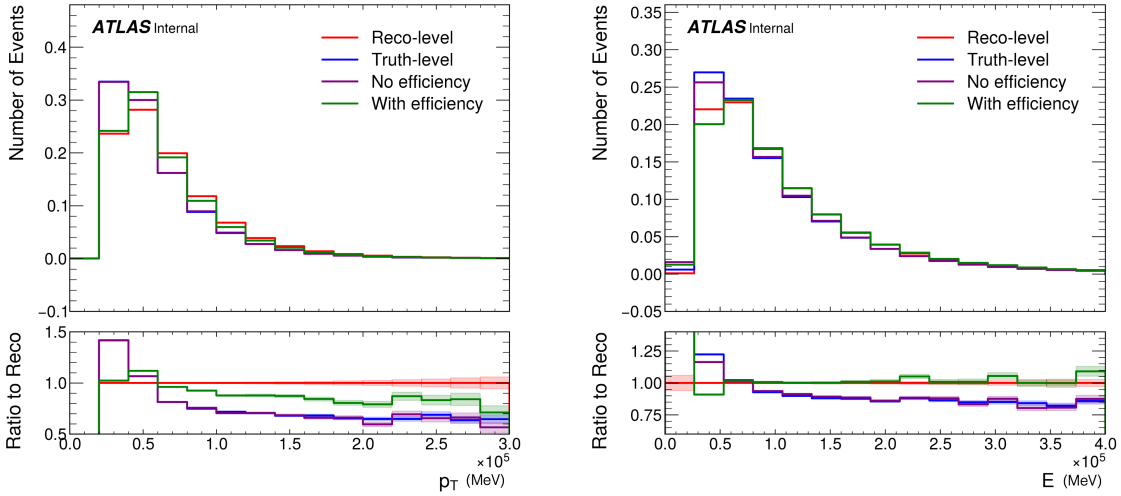

(**a**) Electron p_{T}.

(**b**) Electron E.

Figure 7.3: The electron p_{T} transfer function fails to emulate the full-simulation, whilst the electron E function performs well when efficiency effects are included.

The results of the two-dimensional jet smearing functions are shown in Figure 7.5, where it is seen that the jet energy spectrum is reproduced, but not the jet p_{T} spectrum. The effect of employing higher-dimensional jet smearing functions is investigated, to test the proposal that binning smearing functions in additional kinematic variables may better capture the detector response. The jet p_{T} smearing function is adapted to be differential also in η, and the jet energy function differential also in p_{T} and η. The result is presented in Figure 7.6, where it is seen that no improvement in response emulation is achieved from using higher-dimensional smearing functions for jets.

It is seen that the proposed transfer function method can in some cases emulate the detector response (as it is modelled in GEANT4 full simulation) for a subset of kinematic variables and physics objects. The method did not model distortions to p_{T} spectra well. Efficiency effects were shown to be completely dominant over smearing effects for leptons, and the use of higher-dimensional jet smearing maps shown to be ineffective. The deficiencies of the proposed method motivate investigation into more novel techniques for building transfer functions. Attempts to implement a multivariate technique for directly learning smearing and efficiency distortions is outlined below.

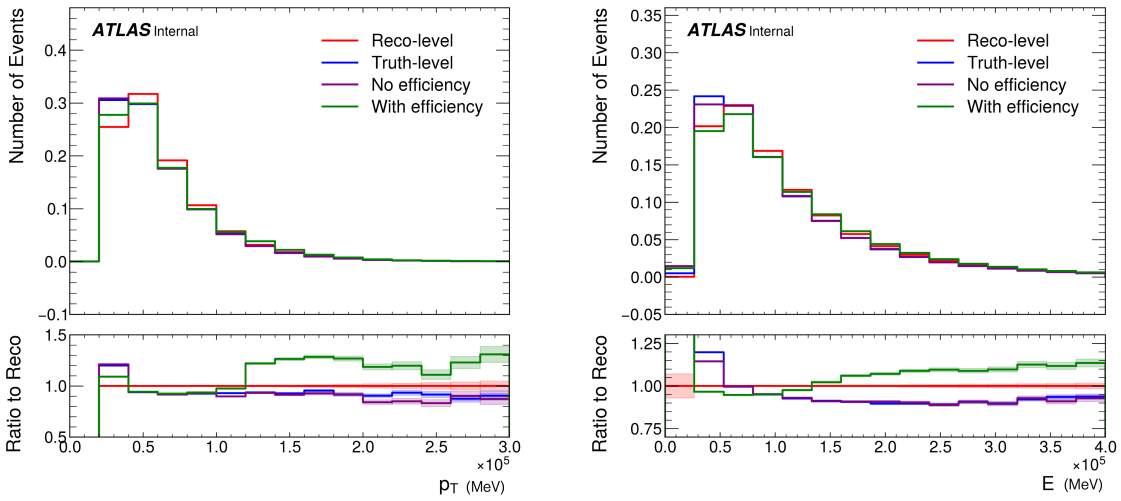

(**a**) Muon p_{T} (**b**) Muon E.

Figure 7.4: Transfer functions built for muon p_{T} and muon energy are unable to capture the effects of detector distortions.

7.4 A Dense Neural Network Approach

Machine learning (ML) techniques are transforming the landscape of particle physics[3]. ML methods in all guises have been applied to such diverse problems as signal-background separation [339], jet flavour-tagging [340], and the improvement of track reconstruction [341]. Several reviews of this dynamic field exist [342]–[344].

The application of ML techniques to detector simulation problems is also blooming. The bulk of studies in the literature have focused on applying generative ML techniques to modelling calorimeter showering[4] — see [345] for a review. Relatively few studies focus on detector response emulation: using ML to learn mappings between high-level physics objects defined in truth- and reconstruction-level spaces. Chen et al. present a deep neural network (DNN) architecture for high-level simulation, trained on W+ jets production with the effects of the CMS detector approximated using Delphes [346]. Benjamin et al. attempt to regress binned probability density functions of jet kinematics using jet four-momenta inputs [347]. Darulis et al. present a two-stage process, where an initial ML alogirthm determines whether a particle should be reconstructed, and

[3]This is a consequence of increased sophistication of computational hardware, the explosion of accessible machine learning software, the recognised potential of applying novel techniques to enormous LHC datasets, and the ability to accurately generate synthetic training data.

[4]There are now examples of VAEs, GANs, normalising flows, diffusion models and even transformers architectures being applied to detector simulation using low-level information. Frequently such techniques are part of larger simulation-based inference work.

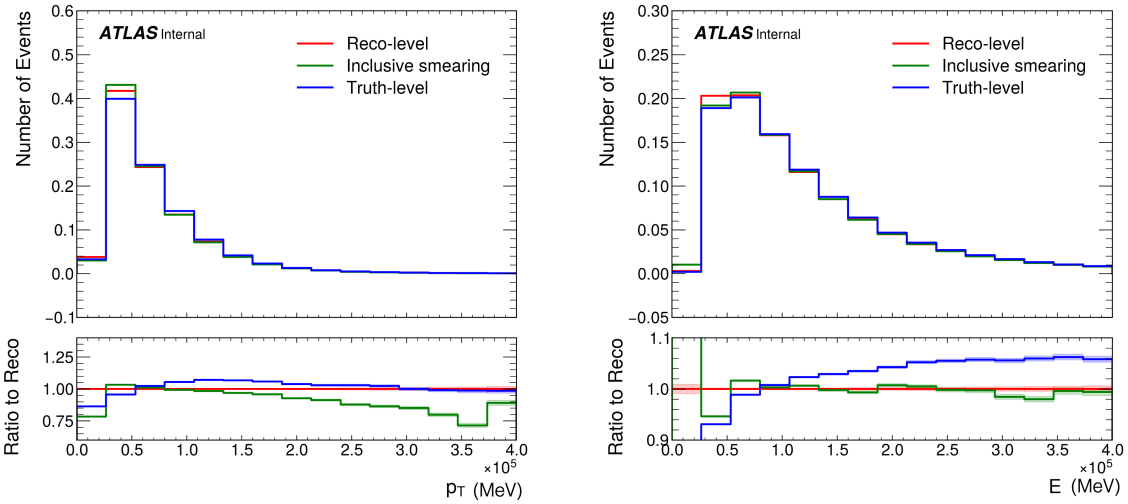

(**a**) Jet p_{T} (**b**) Jet E.

Figure 7.5: One-dimensional smearing functions constructed for jet kinematics. The jet p_{T} smearing function does not capture the detector distortions to jet p_{T} distribution, whilst the jet E smearing function does capture detector distortion to jet energy.

a second algorithm reconstructs the particle [348]. Xu et al. apply generative ML techniques to high-level particle features to generate reconstruction-level quantities [345].

The claim is made that ML techniques offer several advantages over existing high-level transfer function methods. Chief amongst these is that they do not rely on sampling from binned distributions, but can instead benefit from learning from continuous kinematic spectra. ML techniques may be able to capture complex correlations between kinematic parameters; novel data structures may be able to capture correlations between distinct physics objects. Once trained, the application of ML-derived transfer functions to truth-level samples should be extremely fast.

The above studies all either utilise Delphes to generate reconstruction-level simulated data, or use toy detector models with simple transfer functions. The work presented here introduces a DNN method which shares some common features with the studies described above, but is trained on ATLAS full-simulation samples, as processed with Geant4. As such, this study may be considered an application of ML techniques to a more realistic and useful detector environment. In the following, the mechanics of DNNs are introduced, before a specific implementation, trained on simulated $t\bar{t}$ events, is introduced.

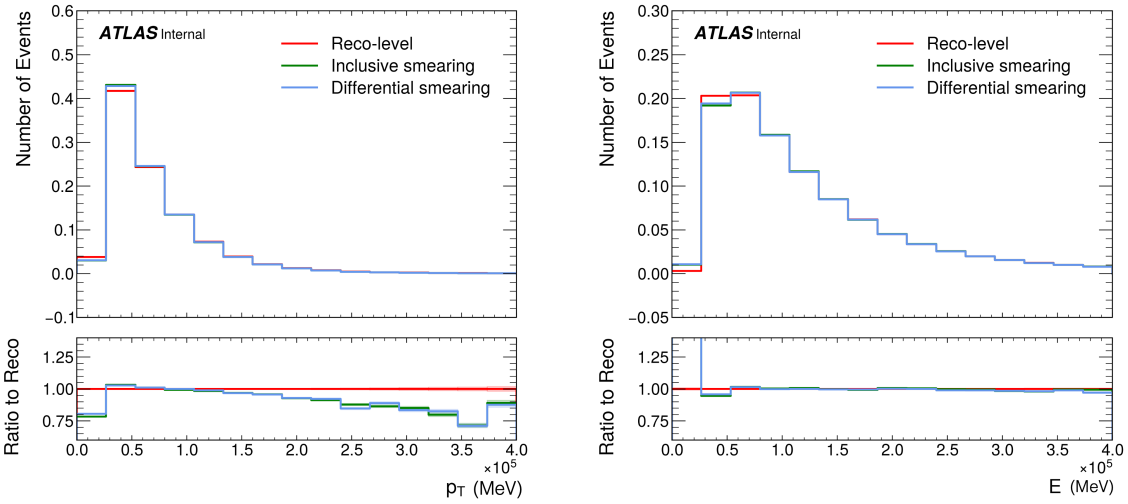

(**a**) Jet p_{T} (**b**) Jet E.

Figure 7.6: The effect of binning jet smearing maps in additional kinematic variables is investigated, but found to have no effect on the ability of the smearing function to emulate detector distortions.

7.4.1 The Mechanics of DNNs

Artificial neural networks [349], henceforth referred to as NNs, are perhaps the most popular machine learning technique in the world currently. They are tools which provide some mapping $f : \mathbb{R}^m \to \mathbb{R}^n$ from input space $\mathbb{R}^m$ to output space $\mathbb{R}^n$. Their goal is to learn a parametric form of the mapping f which will approximate some data transformation[5]. This is achieved by mapping input data through a series of intermediate (frequently higher-dimensional) spaces. In the supervised learning case, the result in the output space is then compared to a reference case, and the parameters of the mappings between each space are updated accordingly. This iterative updating of the internal neural network parameters (the parameters of f) constitutes the 'learning'.

In practical terms, a NN is a directed graph characterised by discrete sets of nodes called *layers*, connected by weighted edges. An illustration of such an architecture is shown in Figure 7.7. Each layer can be thought of as representing a vector in the corresponding space. The input data X^0, living in $\mathbb{R}^m$, is the set of m node values in the *input layer*. Node values are passed to successive layers of the NN via the weighted edges, such that a particular layer's node values are some function of the previous layer's, $X^{t+1} = f^t(X^t)$ for layer t. The *output layer* is the composition of the

[5]The "Universal Approximation Theorem" states that any continuous function can be approximated with arbitrary precision by a sufficiently-large NN.

transformation performed in each previous layer:

$$X^N = (f^{N-1} \circ \ldots f^1 \circ f^0)(X^0), \tag{7.4.1}$$

for a NN with input layer $t = 0$, output layer $t = N$, and t spanning the range between them. The output of a NN is seen to be a function both of the input data X^0, and the specifics of the NN: the form of each f^t and the topology of the network.

Each layer's mapping f^t can be decomposed into two parts: a linear transformation

$$x_i \mapsto \sum_j \omega_{ij} x_j + b_i, \tag{7.4.2}$$

followed by evaluation of a non-linear *activation function* $x_i \mapsto \sigma(x_i)$. The terms ω_{ij} and b_i in equation 7.4.2 are called the *weights* and *biases*, respectively, and constitute the trainable parameters of the NN. The inclusion of activation functions introduces non-linearity, generalising the NN beyond a simple regressional model.

The output of the NN must now be compared quantitatively to the corresponding true result. This is achieved using an appropriate *loss function*, which provides a metric for the accuracy of the NN in its current state. *Backpropagation* then computes the gradient of the loss function with respect to the NN parameters, such that the NN weights can be optimised to yield a more accurate output. Backpropagation procedures rely on a form of — usually stochastic — gradient descent algorithm to find minima of the chosen loss function in the NN parameter space.

Implementing NNs has a large creative element, with a choice of loss function, activation functions, and gradient descent algorithm to be made. Equally important is the choice of *hyperparameters*, including the number of nodes and layers in the network, and the learning rate which determines the step-size in the gradient descent algorithm.

7.4.2 Application to Detector Response Emulation

Detector smearing can be recast as a regression ML problem. A NN is designed whose input and output layers are feature vectors representing truth-level and reconstruction-level kinematics of particular physics objects. The NN learns the mapping between the two states.

Matching truth-level objects to the correct reconstruction-level counterpart is a vital stage of data preparation[6]. As angular information is essentially uninfluenced by smearing effects, it can be used to match truth-level objects to their reconstruction-level partners. *Truth-matching* is therefore implemented by computing the quantity $\Delta R(\text{truth}, \text{reco})$ for every combination of truth-level jet and reconstruction-level jet,

[6]For the probabilistic smearing functions discussed in Section 7.3, this step is automated in construction of two-dimensional ROOT histograms.

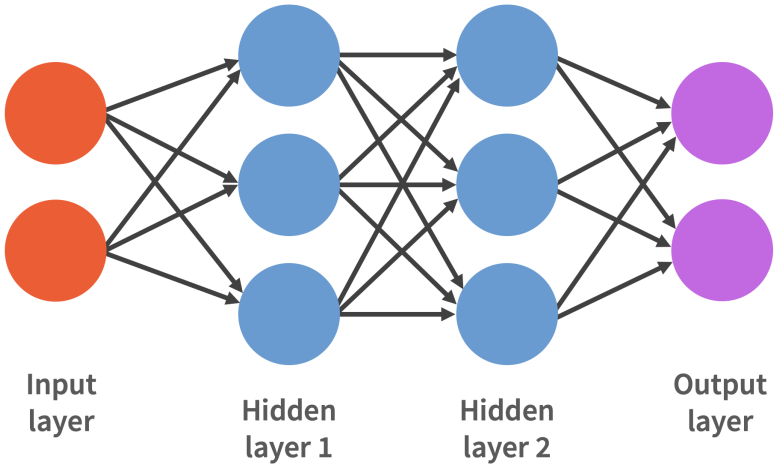

Figure 7.7: A sketch of a neural network. Two nodes define an input layer (orange). Information is passed through the directed edges to two subsequent hidden layers (blue nodes), before being passed to the output layer (purple). Each layer has a characteristc activation function and bias, and each edge is characterised by a weight. These parameters alter over the training epochs, hopefully converging to a state which provides the optimal output i.e. one which minimises an appropriate loss function.

with ΔR defined as in 4.2.3. The distinct pairs with smallest $\Delta R(\text{truth}, \text{reco})$ are taken to be equivalent objects. This process is applied independently to electrons and to muons. Additionally, angular kinematic parameters η, ϕ, are scaled linearly to fall in the range [-1 , +1]; other kinematic parameters are scaled into the range [0 , 1]. This is known to improve the performance and stability of the model training [350]. Data processing is carried out using the Scikit-HEP Python package [351].

A total of 1.7 million jets are extracted from the $t\bar{t}$ events generated for Section 7.3.1, and split in training, validation and testing sets in proportions of 10 : 2 : 5. Each simulated event can contain multiple jets: all truth-matched jets are used to define a dataset which is diverse in flavour-tagging information[7] and jet p_{T}. Fully-connected feed-forward NNs (Figure 7.7) are defined using the Keras API [352], built on top of the TensorFlow ML framework [353], and the Adam optimiser is used for stochastic gradient descent [354]. Various input and output feature vectors were considered from the set of kinematics $\{p_{\mathrm{T}}, p_x, p_y, p_z, E, m, \eta, \phi\}$[8]. A five-dimensional input vector $(p_{\mathrm{T}}, E, m, \eta, \phi)$ was eventually chosen to map to a two-dimensional output

[7] The flavour-tagging information in the simulated samples define each jet to be either b-tagged or not, using the 85% working point definition. In principle the methods discussed in this chapter could be applied separately to b-tagged and non-b-tagged jets by defining separate smearing functions.

[8] Naturally four kinematic parameters are required to uniquely define a jet's four-momentum. Not all combinations are permissible, for example the set $\{p_{\mathrm{T}}, p_x, p_y\}$ is redundant as any of two of these quantities span the transverse momentum space. However, the NN may benefit from additional information in the input vector, as it has know *a priori* knowledge of the physical relationship between these parameters.

vector (p_{T}, m) for the smearing of jets. The network architecture comprises three hidden layers with 100, 50 and 25 nodes, respectively. The activation function selected for the final layer is the Linear function; all other layers employ the Scaled Exponential Linear Unit (SELU) activation function [355]. The mean squared error (MSE) loss function is selected, and the learning rate set at 0.003. The maximum number of epochs was set to 100, with early-stopping employed when the loss function plateaus[9]

The jet p_{T} and mass spectra are shown in Figure 7.8. Similarly to the results of the Section 7.3.1, the normalised number of events is presented in bins of the kinematic in the upper plot, and the ratio with respect to the full simulation in the lower plot. Unlike the probabilistic smearing functions described above, the full-simulation behaviour of the p_{T} variable is captured to some extent by the DNN. Though the ML-emulation distribution does not exactly match the full-simulation distribution, the similarity can be considered close enough for the use-cases detector response emulation is intended for.

A DNN binary classifier was conjectured to be able to derive efficiency functions for leptons, by assigning each truth-level physics object a boolean value depending on whether or not the particle was also present at reconstruction-level. NNs of varying size were tested, along with a number of activation functions suitable for classification-type problems. No set of hyperparameters was found which defined a NN capable of classifying leptons in the manner described. For example, the NNs tested were not able to uncover the p_{T}-dependence of electron identification efficiencies. Since efficiency effects were seen to cause the dominant distortions to lepton kinematics, with smearing utterly subdominant, no NN smearing functions were built for electrons and muons.

7.5 Conclusions and Further Work

This chapter began by summarising and motivating the need for expedient techniques to emulate full-simulation detector response. A binned probabilistic approach and a DNN approach were presented as means of capturing the smearing effects of detector simulation. The DNN approach was shown to better capture jet smearing effects. Efficiency effects were implemented as transfer functions built out of published binned data on lepton efficiencies; these functions had limited success in capturing the efficiency effects in full-simulation lepton kinematic spectra. Efforts to train a NN classifier to emulate these efficiency effects failed.

This study focused on detector smearing emulation in $t\bar{t}$ events, and it appears as if the DNN method was better able to capture the jet response than was the probabilistic method. This suggests that research into multivariate methods may prove fruitful in developing new detector emulation techniques, a conclusion supported by growing

[9] Early-stopping terminates the training before all epochs are run over if the rate of decrease of the loss function drops too low. This is to avoid over-fitting, where the model learns specific idiosyncrasies of the training dataset, but then is unable to generalise when presented with new data.

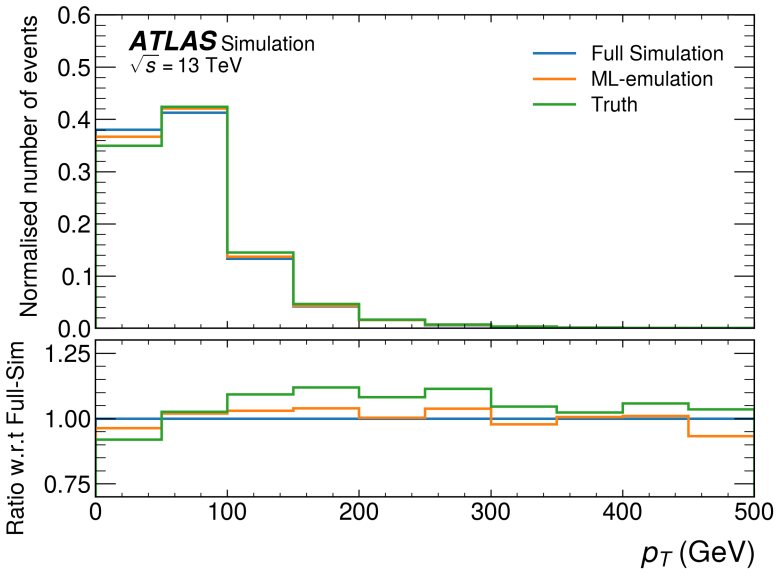

(**a**) Jet p_{T}

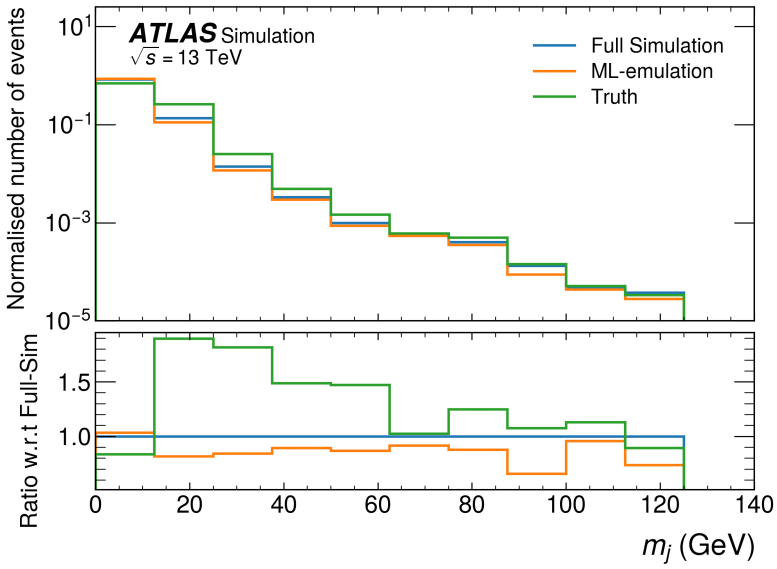

(**b**) Jet mass, m_j

Figure 7.8: ML-based smearing functions which map the set of kinematics $(p_{\mathrm{T}}, E, m, \eta, \phi)$ to (p_{T}, m) are trained on 1 million jets and compared to the full-simulation response. They are able to capture emulate the full-simulation response to reasonable accuracy. Note that the lower figure has uses a logarithmic y-axis on the upper plot.

work in the literature. The DNN approach had success in defining smearing functions for whole physics objects; use of novel NN architectures may allow for building mappings for whole events. In particular, graph neural networks (GNNs) have seen to be successful in a number of particle physics contexts [356]–[359]. Graphs are useful for learning high-level collider physics phenomena because they can embed entire events into their non-Euclidean structures, defining individual particles as graph nodes with relevant feature vectors, and using graph edges to specify relational information between the particles. Future research could investigation posing detector response emulation as a graph regression problem, where some learnable mapping translates truth-level event graphs into reconstruction-level event graphs, with the smearing, efficiency and even acceptance effects both accounted for.

Any promising techniques should also be tested on different simulated events, with a view to constructing a deep learning model which is trained on a wide variety of different physics processes, and which is therefore robust against factors like jet multiplicity and particular leptonic final-states. With the advent of ever more advanced deep learning techniques, and accessible software for designing architectures around these techniques, it is likely that fast simulation and detector response emulation efforts will continue to improve in accuracy.

Chapter 8

Spin Properties in $t\bar{t}Z$ Production

"It is hard to measure properties,
In the rare process of $t\bar{t}Z$,
But spin correlations,
And polarisations,
May be observed by the end of Run-3!"
—

The physics of top-quark production in association with additional bosons is a fascinating sub-field. It provides a unique playground for measuring and interpreting top-boson couplings. Understanding and measuring these processes is important as they constitute large backgrounds for each other and for a variety of other SM and BSM processes. The LHC Run-2 delivered sufficient statistics to make observations of many such processes, and subsequent measurements begin to study each topology in greater detail: making measurements of cross-sections in different final-state channels, unfolding kinematic spectra, and interpreting the results in SMEFT and other NP contexts. Of particular interest are so-called $t\bar{t}$ + X processes. Here X can signify an electroweak gauge boson, with several measurements of the $t\bar{t}W$ [360], [361], $t\bar{t}Z$ [360], [362], [363] and $t\bar{t}\gamma$ [307], [364] processes already complete. The $t\bar{t}$ + X process may also consider $t\bar{t}$ production in association with a Higgs boson [365], [366], which is interesting because it is a direct probe of the top-quark Yukawa coupling.

The measurement of top-quark properties from angular distributions in the $t\bar{t}X$ sector remains in its infancy. Charge asymmetries are asymmetries in rapidity or pseudorapidity distributions between top-quarks and anti-top-quarks. These have recently been measured by ATLAS in dedicated analyses in $t\bar{t}W$ [367] and $t\bar{t}\gamma$ [368] production. Measurements of spin properties — spin correlations between $t\bar{t}$ pairs, individual top-quark polarisations, related observables for inferring quantum information-properties — had not been attempted nor studied theoretically. Such measurements offer an entirely new domain for studying top-quarks' spin, and provide a complimentary set of observables for top-quark SMEFT interpretations.

This chapter presents a phenomenological study on the physics and prospective measurements of the spin density matrix in the context of $t\bar{t}Z$ production at the LHC. The study draws from historic ATLAS and CMS $t\bar{t}Z$ results [362], [363], particularly with regards to estimations of event yields in various $t\bar{t}Z$ channels. The work in this chapter was published in the article [129], and the latest ATLAS $t\bar{t}Z$ measurement builds on this work [369].

8.1 $t\bar{t}Z$ Production

The $t\bar{t}Z$ process differs from $t\bar{t}$ at LO-QCD through the emission of a Z-boson from an initial state quark, or from one of the top-quarks in the $t\bar{t}$ final state. The former and latter set of topologies are referred to initial-state radiation (ISR) and final-state radiation (FSR) respectively. The corresponding production diagrams are shown in Figure 8.1. The $t\bar{t}Z$ process is well understood and modelled: current predictions of the $t\bar{t}Z$ inclusive cross-section, both at NLO QCD with EW corrections [370] and NLO QCD with NNLL resummation [371], [372], exhibit no tensions with the latest experimental results from ATLAS and CMS [362], [369]. The ISR case is expected to leave the spin properties of the $t\bar{t}$ system unaltered, whilst the FSR case will flip the spin state of the top-quark from which it radiates, inducing some level of polarisation and altering the spin correlations between the top-quarks.

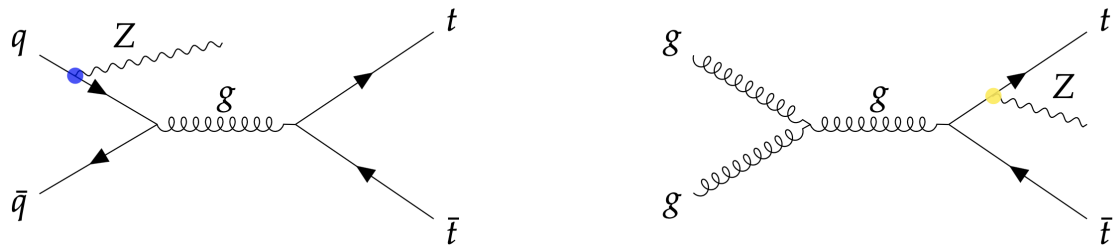

Figure 8.1: Leading-order $t\bar{t}Z$ production diagrams. Note that the FSR diagram can also be initiated by $q\bar{q}$-annihilation to the intermediate gluon. Coloured dots indicate SM quark–Z-boson couplings, not EFT interactions. Taken from [373].

8.2 Computation of the Spin Density Matrix in $t\bar{t}Z$

The SDM formalism, presented in Section 3.3, is applied to the $t\bar{t}Z$ production process [111]. The $t\bar{t}Z$ spin density matrix elements are extracted from MC-simulated samples through expectation values of leptonic angular observables, as discussed in Section 3.3.3. Ten million $t\bar{t}Z$ events are generated at LO-precision for 13 TeV using the MadGraph_aMC@NLO 2.8.1 event generator, and at NLO-precision in the NLO+PS mode

at both 13 TeV and 14 TeV. In both cases, the event generation is interfaced to Pythia 8.244 to provide appropriate showering, which has the effect of reshuffling partonic momenta. The five-flavour scheme (5FS) is employed, in which all flavours of quark other than the top-quark as assumed to be massless[1]. The following numerical values are specified for the relevant input parameters:

$$\begin{aligned} m_t &= 172.5\,\text{GeV}, & \Gamma_t &= 1.3197\,\text{GeV}, \\ m_W &= 80.399\,\text{GeV}, & \Gamma_W &= 2.085\,\text{GeV} \\ m_Z &= 91.1876\,\text{GeV}, & \Gamma_Z &= 2.4952\,\text{GeV}, \\ G_F &= 1.16637 \times 10^{-5}\text{GeV}^{-2}, & \alpha_s\left(m_Z\right) &= 0.118 \end{aligned} \tag{8.2.1}$$

and $\mu_R = \mu_F = m_t + m_Z$. The top-quarks are decayed using the the MadSpin tool [317].

The LO and NLO SM predictions for the $t\bar{t}Z$ spin parameters, evaluated at $\sqrt{s}$ = 13 TeV, are presented in columns one and two of Table 8.1. The third column includes the corresponding 13 TeV $t\bar{t}$ spin parameter predictions, as presented in [374], for comparison. Table 8.2 lists the $t\bar{t}Z$ and $t\bar{t}$ spin parameters for $\sqrt{s}$ = 14 TeV. The central values in each case correspond to the prediction at renormalisation and factorisation scale choices. The standard deviations quantify the statistical uncertainty, plus an uncertainty associated to the choice of factorisation and renormalisation scales. These correspond to three uncertainties:

- $\mu_R = \{0.5, 2\} \times \mu_0$, $\mu_F = \mu_0$,
- $\mu_R = \mu_0$, $\mu_F = \{0.5, 2\} \times \mu_0$,
- $\mu_R = \mu_F = \{0.5, 2\} \times \mu_0$.

where the factors 0.5 and 2 are the 'down'- and 'up'-variations. These are summed in quadrature along with the statistical uncertainty to give the total standard deviation. Other typical theoretical uncertainties, such as those arising from the PDFs, have had a negligible impact in experimental measurements of the $t\bar{t}Z$ process so are neglected here. Theoretical uncertainties associated to modelling of phenomena like parton showers are seen to have a big impact on angular observables in Chapter 10, but their consideration is beyond the scope of this preliminary study.

At both 13 TeV and 14 TeV, the $t\bar{t}Z$ diagonal spin correlation matrix elements,

$$(C_{rr}, C_{kk}, C_{nn}), \tag{8.2.2}$$

are markedly different from their $t\bar{t}$ counterparts. All three elements are negative, in comparison to the $t\bar{t}$ case where C_{kk} and C_{nn} are positive and C_{rr} essentially zero. This implies that $t\bar{t}Z$ production produces increased proportion of opposite-helicity $t\bar{t}$ pairs compared to the $t\bar{t}$ case, in accordance with 3.3.18. This is a direct consequence of

[1] The other commonly used scheme is the four-flavour scheme (4FS) in which the b-quark is massive. Both the 4FS and 5FS schemes are important in the modelling of single-top backgrounds in the entanglement measurement, specifically in Section 10.5.1.

the emission of the spin-1 Z-boson. The opening of the mixed qg initial state at NLO manifests a small positive correction to the three coefficients, as seen in the comparison of the 13 TeV LO and NLO $t\bar{t}Z$ predictions. The spin cross-correlations (the off-diagonal elements of the spin correlation matrix) are more similar to the $t\bar{t}$ case. Most strikingly, the Z-boson emission induces non-zero longitudinal polarisations ($B_r^{\pm}, B_k^{\pm}$) which are not present in the $t\bar{t}$ case. The transverse polarisations $B_n^{\pm}$ remain negligible.

Table 8.1: Spin correlation, cross-correlation and polarisation coefficients in the SM, extracted at NLO QCD precision for $t\bar{t}Z$ events at $\sqrt{s}$ = 13 TeV. The central values correspond to a choice of scales $\mu = \mu_R = \mu_F = m_t + m_Z$, while the standard deviations reflect both the Monte Carlo statistical uncertainties and variations of the scales (2μ and $\mu/2$). The third column displays the results of a similar calculation in $t\bar{t}$ events at mixed NLO QCD and electroweak precision ("NLOW"); these numbers are quoted from Ref. [374].

Coefficient	$t\bar{t}Z$ LO	$t\bar{t}Z$ NLO	$t\bar{t}$ NLOW
C_{rr}	-0.207 ± 0.007	-0.198 ± 0.004	0.071 ± 0.008
C_{kk}	-0.197 ± 0.013	-0.193 ± 0.004	0.331 ± 0.002
C_{nn}	-0.125 ± 0.003	-0.117 ± 0.004	0.326 ± 0.002
C_{rk}^{+}	-0.163 ± 0.003	-0.173 ± 0.006	-0.206 ± 0.002
C_{kn}^{+}	0.000 ± 0.003	0.012 ± 0.006	$\lesssim 2 \cdot 10^{-3}$
C_{rn}^{+}	0.003 ± 0.003	-0.004 ± 0.006	$\lesssim 1 \cdot 10^{-3}$
C_{rk}^{-}	0.008 ± 0.003	0.007 ± 0.006	$\lesssim 1 \cdot 10^{-3}$
C_{kn}^{-}	-0.003 ± 0.003	0.003 ± 0.006	$\lesssim 1 \cdot 10^{-3}$
C_{rn}^{-}	0.001 ± 0.003	0.005 ± 0.006	$\lesssim 1 \cdot 10^{-3}$
B_r^{+}	0.058 ± 0.003	0.055 ± 0.001	$\lesssim 2 \cdot 10^{-3}$
B_r^{-}	0.060 ± 0.003	0.055 ± 0.001	$\lesssim 2 \cdot 10^{-3}$
B_k^{+}	-0.069 ± 0.002	-0.077 ± 0.001	$\lesssim 4 \cdot 10^{-3}$
B_k^{-}	-0.071 ± 0.002	-0.076 ± 0.001	$\lesssim 4 \cdot 10^{-3}$
B_n^{+}	-0.001 ± 0.001	0.001 ± 0.001	$\lesssim 3 \cdot 10^{-3}$
B_n^{-}	0.001 ± 0.001	0.001 ± 0.001	$\lesssim 3 \cdot 10^{-3}$

Table 8.2: Spin correlation, cross-correlation and polarisation coefficients in the SM, extracted at NLO QCD precision for $t\bar{t}Z$ events at $\sqrt{s} = 14\,\text{TeV}$. Central values and standard deviations are as described for Table 8.1 and the NLOW $t\bar{t}$ values are again quoted from [374].

Coefficient	$t\bar{t}Z$ NLO	$t\bar{t}$ NLOW
C_{rr}	-0.190 ± 0.004	0.072 ± 0.008
C_{kk}	-0.182 ± 0.004	0.331 ± 0.002
C_{nn}	-0.118 ± 0.004	0.325 ± 0.002
C_{rk}	-0.180 ± 0.006	-0.204 ± 0.004
C_{kn}	-0.001 ± 0.006	$\lesssim 2 \cdot 10^{-3}$
C_{rn}	0.006 ± 0.006	$\lesssim 1 \cdot 10^{-3}$
C^{-}_{rk}	-0.004 ± 0.006	$\lesssim 1 \cdot 10^{-3}$
C^{-}_{kn}	0.001 ± 0.006	$\lesssim 1 \cdot 10^{-3}$
C^{-}_{rn}	-0.008 ± 0.006	$\lesssim 1 \cdot 10^{-3}$
B^{+}_{r}	0.055 ± 0.001	$\lesssim 2 \cdot 10^{-3}$
B^{-}_{r}	0.057 ± 0.001	$\lesssim 2 \cdot 10^{-3}$
B^{+}_{k}	-0.077 ± 0.001	$\lesssim 4 \cdot 10^{-3}$
B^{-}_{k}	-0.074 ± 0.001	$\lesssim 4 \cdot 10^{-3}$
B^{+}_{n}	0.001 ± 0.001	$\lesssim 3 \cdot 10^{-3}$
B^{-}_{n}	-0.001 ± 0.001	$\lesssim 3 \cdot 10^{-3}$

8.3 Proposed Measurements at the LHC

ATLAS and CMS measurements categorise the $t\bar{t}Z$ process into several channels depending on how the top-quarks decay, with the Z-boson considered to always decay leptonically. Hadronic $t\bar{t}$ decays define a two-lepton (2L) channel [2]. Semi-leptonic $t\bar{t}$ decays define the three-lepton (3L) channel whilst di-leptonic $t\bar{t}$ decays define the four-lepton (4L) channel. Either can be used to extract top-quark polarisations in the $t\bar{t}Z$ process, but only the 4L channel permits a measurement of the spin correlations when using leptons as spin-analysers.

A recent measurement of $t\bar{t}Z$ production by the ATLAS experiment, corresponding to an integrated luminosity of $139.1\,\text{fb}^{-1}$, reported around 430 $t\bar{t}Z$ events in the 3L channel and 90 events in the 4L channel, based on the selection criteria defined in that analysis [363]. The analogous CMS measurement was based on a lower integrated

[2] Perhaps in the not-to-distant future, hadronic top reconstruction techniques will open up measurements of properties in $t\bar{t}X$ channels.

luminosity of 77.5 fb^{-1}, with higher signal acceptance providing 400 3L $t\bar{t}Z$ events and 60 4L events [362]. Based on these figures, an estimate of 100 4L $t\bar{t}Z$ events is conjectured to be measurable by a legacy Run-2 analysis. An additional estimate of 500 3L $t\bar{t}Z$ events gives 600 total events which can be used to extract polarisations.

Following the method utilised by ATLAS and CMS in the first measurements of spin correlations in $t\bar{t}$ production, a template fit is proposed. Two alternate MC samples are generated: a "spin-on" sample with spin correlations present in the simulation (MadSpin `spinmode` parameter set to `madspin`), and a "spin-off" sample where the spin correlations are forced to vanish (`spinmode = nospin`) respectively. These samples constitute two alternate hypotheses. The observable O is measured from experimental data and then assumed to be a linear composition of the observable as computed by the two hypotheses, $O_{\text{spin-on}}$ and $O_{\text{spin-off}}$:

$$O = f_{\text{SM}} \cdot O_{\text{spin-on}} + (1 - f_{\text{SM}}) \cdot O_{\text{spin-off}} . \tag{8.3.1}$$

The parameter f_{SM} gives the fraction of events which are compatible with the spin-on hypothesis. It is extracted through a fit to data.

A prudent choice of observable O will maximise the difference between the two hypotheses, and hence give the strongest bounds on f_{SM}. In the $t\bar{t}$ case, ATLAS and CMS used the observable $|\Delta\phi(l^+, l^-)|$, the opening angle between the charged leptons in the laboratory frame, as defined in Section 3.3.3. Figure 8.2 shows $|\Delta\phi(l^+, l^-)|$ for the $t\bar{t}Z$ process for the spin-on and spin-off hypotheses. The distributions are similar, with the ratio panel exhibiting no obvious monotonic slope as seen in the $t\bar{t}$ case. The observable $|\Delta\phi(l^+, l^-)|$ is therefore a poor choice for the $t\bar{t}Z$ template fit. Figure 8.3 presents the distribution of the observable $\cos\varphi(l^+, l^-)$, as defined in 3.3.19 and where (l^+, l^-) explicitly indicates this observable is defined between the charged lepton decay products, for $t\bar{t}Z$. Far clearer separation between the spin-on and spin-off hypotheses is observed, indicating that this observable shows promise for obtaining a precise extraction of f_{SM}. The template fit need not only consider a single observable however. Three sets of observables are tested in the template fit. The first is $\cos(l^+, l^-)$ in four bins of equal width over the range $[-1, 1]$. The second set combines all elements of spin parameters (spin correlations and polarisations), totalling 15 variables. The last set combines both the spin parameters and the four bins of $\cos\varphi(l^+, l^-)$. In each case, a correlation matrix is defined between the variables used in the fit.

The template fit is performed in the context of Bayesian statistics, using the EFTFitter package based on the `BAT.jl` Bayesian Analysis Toolkit. In this Bayesian framework, a set of measurements $\mathbf{x} = \{x_i\}$ are compared to a set of predictions $\mathbf{y} = \{y_i\}$. In general, the measurements x_i may be correlated with one another: a covariance matrix is defined, $\mathcal{M}_{ij} = \text{cov}\left[x_i, x_j\right]$, which can be decomposed linearly into respective contributions

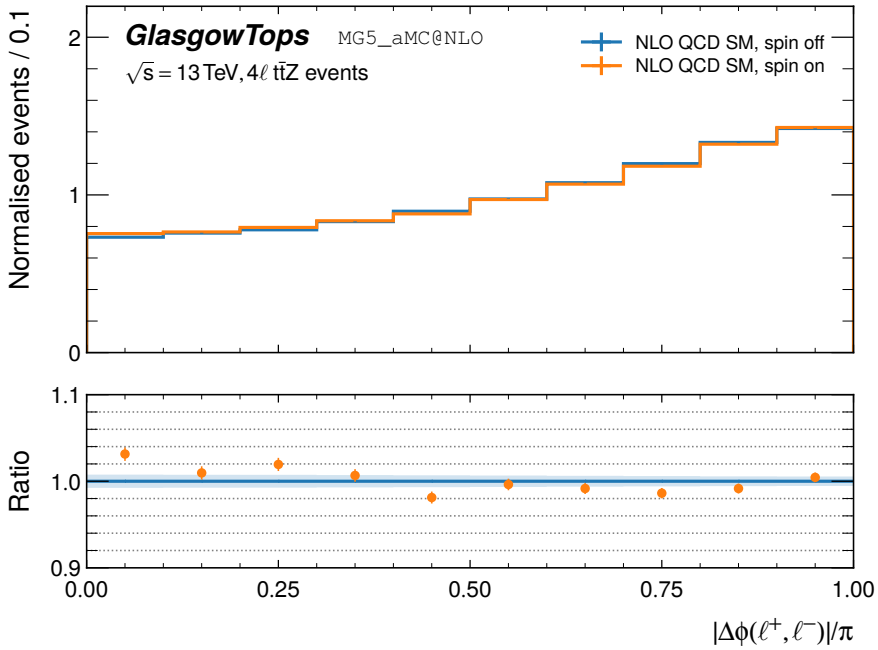

Figure 8.2: $|\Delta\phi(l^+, l^-)|$ in the $t\bar{t}Z$ 4L channel. In $t\bar{t}$ production, a large difference is found in the observable $|\Delta\phi(l^+, l^-)|$ between the spin-on and spin-off hypotheses. In the $t\bar{t}Z$ channel, little difference is observed.

from each source:

$$\mathcal{M}_{ij} = \text{cov}\left[x_i, x_j\right] = \sum_{k=1}^{M} \text{cov}^{(k)}\left[x_i, x_j\right]. \tag{8.3.2}$$

EFTFitter implements a Gaussian likelihood function $\mathcal{L}(\mathbf{x} \mid \mathbf{y})$, the log-likelihood of which is written as,

$$-2\ln p(\mathbf{x} \mid \mathbf{y}) = \sum_{i=1}^{n}\sum_{j=1}^{n}[\mathbf{x} - U\mathbf{y}]_i^{\intercal}\mathcal{M}_{ij}^{-1}[\mathbf{x} - U\mathbf{y}]_j, \tag{8.3.3}$$

with $\mathcal{M}_{ij}$ the total covariance matrix. Bayes theorem states that the inference of free parameters $\boldsymbol{\lambda}$ in the model under scrutiny can be made from the posterior probability $p(\boldsymbol{\lambda} \mid \mathbf{x})$ through

$$p(\boldsymbol{\lambda} \mid \mathbf{x}) = \frac{p(\mathbf{x} \mid \boldsymbol{\lambda}) \cdot p(\boldsymbol{\lambda})}{p(\mathbf{x})}, \tag{8.3.4}$$

with $p(\mathbf{x} \mid \boldsymbol{\lambda})$ the likelihood, $p(\boldsymbol{\lambda})$ some prior, and $p(\mathbf{x})$ the evidence, usually given as,

$$p(\mathbf{x}) = \int \mathrm{d}\boldsymbol{\lambda} p(\mathbf{x} \mid \boldsymbol{y}) \cdot p(\boldsymbol{\lambda}). \tag{8.3.5}$$

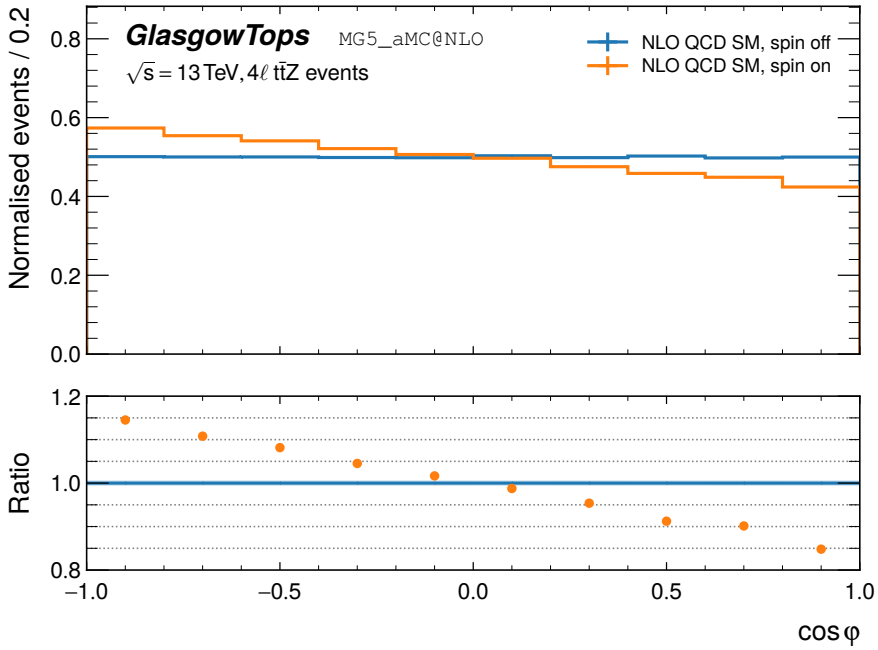

Figure 8.3: There is noticeable shape in the observable $\cos\varphi(l^+, l^-)$ between the spin-on and spin-off hypotheses in $t\bar{t}Z$ production.

Hence, the combination of 8.3.3 and 8.3.4 allows for sampling of the posterior through Markov chain MC techniques, subject to some known relationship between $\boldsymbol{\lambda}$ and $\boldsymbol{y}$, and yields a particular set of free parameters $\hat{\boldsymbol{\lambda}}$ at some credibility level: a range within which the "true values" of $\boldsymbol{\lambda}$ are likely to fall, to a certain degree of credibility.

In the context of the template fit to $t\bar{t}Z$ spin observables, there is only one free parameter in the model, f_{SM} . The various spin parameters discussed above constitute the (expected) measurements $\mathbf{x}$. In this feasibility study, these parameters are extracted from a pseudo-dataset, which is the MC-simulated sample defined according to the spin-on hypothesis. Each is defined as a central value with some associated uncertainty, which is a combination of the statistical uncertainty corresponding the limited number of events in the sample, and a theoretical uncertainty as defined in Section 8.2. In a "real" measurement, the measured values in data, and associated uncertainties, would be used here. The predictions $\mathbf{y}$ are the values as given by the MC, for the various hypotheses. The statistical correlations between the various parameters are taken into account, and so form the covariance matrix defined in 8.3.2. An illustration of such a correlation matrix is presented in Figure 8.4, showing the statistical correlations between C_{ij}, the spin correlation matrix elements. It is observed that the matrix is reasonably diagonal.

A flat prior $p(\boldsymbol{\lambda})$, is assumed in each fit. Each fit returns bounds on the parameter f_{SM} corresponding to some specified credibility level: this is set to 90%. The "Bayes factor" K constitutes a metric which quantifies how strongly one hypothesis is favoured

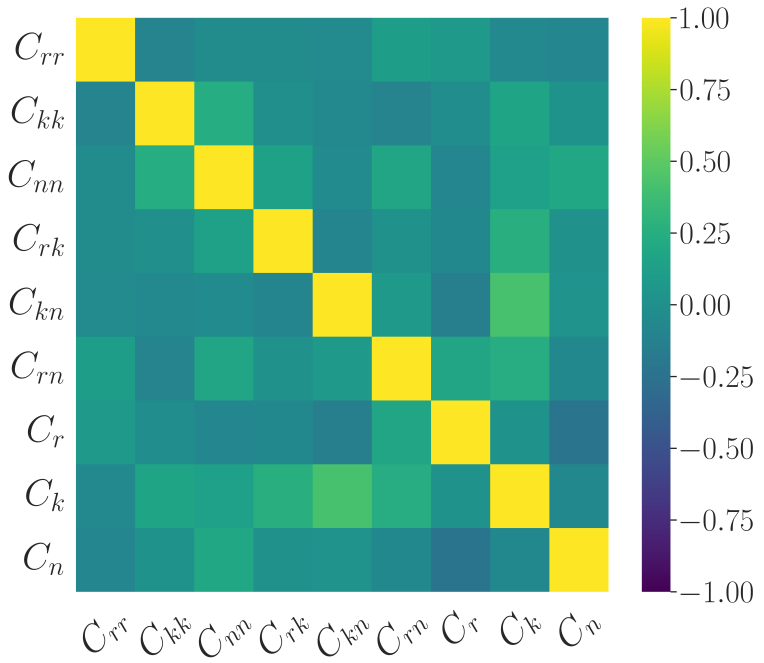

Figure 8.4: The portion of the correlation matrix pertaining to the spin-correlation matrix elements. It is reasonably diagonal.

over the other. It is defined as the ratio of the posterior of the spin-on hypothesis to the posterior of spin-off hypothesis, such that $K > 1$ favours the spin-on variant; the larger the Bayes factor, the more strongly the spin-off hypothesis is excluded. The 90% credibility bounds are found to be [0.12,1.88] when the four bins of $\cos\varphi(l^+, l^-)$ are the measurements used, with corresponding $K = 1.44$. Applying the template fit to spin parameters $\{C_{ij}, \mathbf{B}_i^{\pm}\}$ elements yields a tighter credibility interval of [0.24,1.76], with $K = 3.83$; including both sets of observables yields [0.46,1.54] and $K = 13.5$. Stronger rejection of the spin-off hypothesis is seen when more observables are included.

Future LHC running conditions are therefore also considered in this study, to assess whether an observation — corresponding to a 5σ preference for the spin-on hypothesis — is attainable at the LHC. Scenarios considered are: Run-3 conditions with an integrated luminosity of 300 fb^{-1}; a combination of Run-2 and Run-3 datasets; HL-LHC conditions with an integrated luminosity of 3000 fb^{-1}; and a further HL-LHC scenario, where the proposed systematic uncertainties are reduced by a factor of two. Both Run-3 and HL-LHC scenarios are assumed to have a $\sqrt{s} = 14$ TeV which is expected to increase the inclusive $t\bar{t}Z$ cross-section by around 20 % [375]. The proposed signal event yields are therefore scaled by the increase in cross-section and by the increase in integrated luminosity: for example, 100 4L events in Run-2 corresponds to around 260 events in Run-3. The credibility bounds for these scenarios are presented in Table

8.3 and in Figure 8.5. The results clearly show that the limits on f_{SM} grow tighter as the number of 3L- and 4L-channel $t\bar{t}Z$ increase in future running conditions. The spin parameters constrain f_{SM} more tightly than the $\cos\varphi(l^+, l^-)$ distribution in each scenario, with their combination providing the strongest bounds in every case. These results underline the power of including multiple observables in the template fit, and the increased statistical power which comes from future LHC conditions. This point is further illustrated in Figure 8.6 which shows Bayes factors corresponding to each set of observables used, in each LHC scenario. Decisive evidence is likely to be achievable using a combination of the Run-2 and Run-3 datasets.

Table 8.3: 90% credibility intervals on the parameter-of-interest f_{SM}, according to the various scenarios described in the text. Here, "HL-LHC ⊕" refers to the HL-LHC setup with improved systematic uncertainties.

Scenario	$\cos\varphi$ only	$C_{ij} + B_i^{\pm}$ only	full information
Run 2	[0.12, 1.88]	[0.24, 1.76]	[0.46, 1.54]
Run 3	[0.17, 1.84]	[0.37, 1.62]	[0.58, 1.43]
Run 2 + Run 3	[0.20, 1.82]	[0.49, 1.52]	[0.66, 1.33]
HL-LHC	[0.42, 1.58]	[0.58, 1.43]	[0.68, 1.31]
HL-LHC ⊕	[0.58, 1.43]	[0.74, 1.26]	[0.82, 1.18]

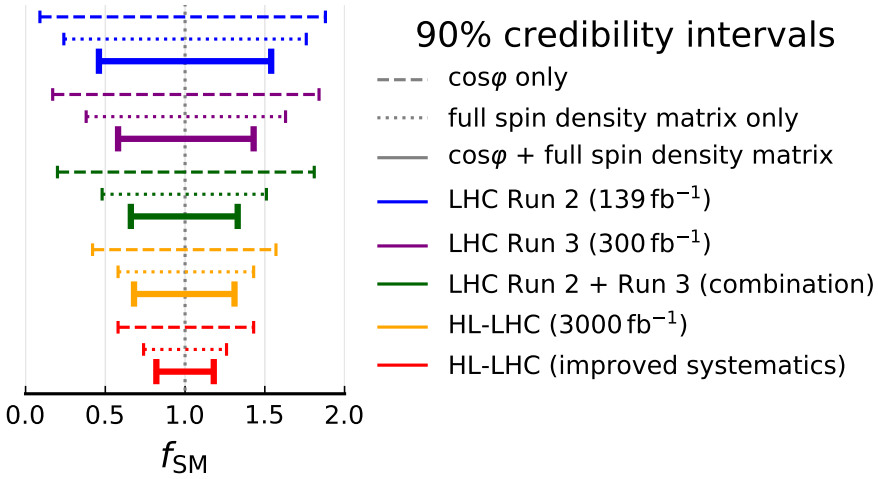

Figure 8.5: 90 % credibility intervals for the five LHC running scenarios considered in this study. In each scenario, including more measurements in the fit results in stronger constraint of the free parameter f_{SM}, with the combination of spin parameter measurements and the binned distribution of $\cos\varphi(l^+, l^-)$ providing the tightest constraint in each case.

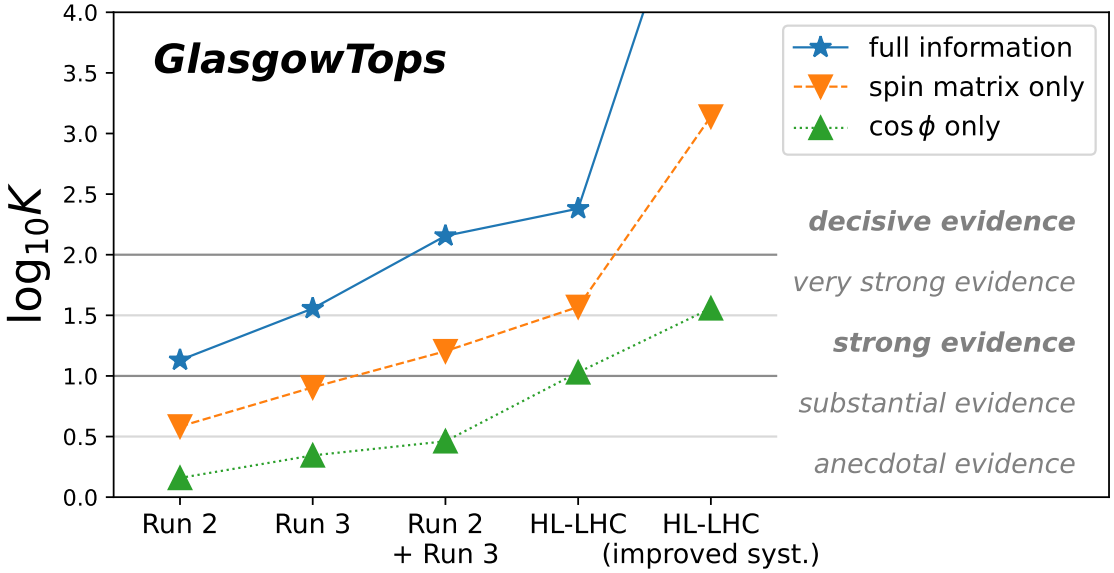

Figure 8.6: The Bayes Factor, which quantifies the extent to which the spin-on hypothesis is favoured over the spin-off hypothesis, for each set of measurements, in each LHC running scenario. Decisive evidence should be achievable using a combination of Run-2 and Run-3 data.

8.4 SMEFT interpretation of $t\bar{t}Z$ spin observables

The $t\bar{t}Z$ process is sensitive to a number of SMEFT operators, particularly those linking fermions to heavy bosons [71]. The latest ATLAS results use a range of unfolded kinematic spectra to set constraints on a number of such operators [363], [369], [376]. The EFT-operators initially considered in this study are the following six-dimensional operators:

$$\begin{aligned}
Q_{uG}^{(ij)} &= \left(\bar{q}_i \sigma^{\mu\nu} T^A u_j\right) \tilde{\varphi} G^A_{\mu\nu}, \\
Q_{uB}^{(ij)} &= \left(\bar{q}_i \sigma^{\mu\nu} u_j\right) \tilde{\varphi} B_{\mu\nu}, \\
Q_{uW}^{(ij)} &= \left(\bar{q}_i \sigma^{\mu\nu} \tau^I u_j\right) \tilde{\varphi} W^I_{\mu\nu}, \\
Q_{\varphi u}^{(ij)} &= \left(\varphi^\dagger i\overleftrightarrow{D}_\mu \varphi\right) \left(\bar{u}_i \gamma^\mu u_j\right) \\
Q_{\varphi q}^{1(ij)} &= \left(\varphi^\dagger i\overleftrightarrow{D}_\mu \varphi\right) \left(\bar{q}_i \gamma^\mu q_j\right) \\
Q_{\varphi q}^{3(ij)} &= \left(\varphi^\dagger i\overleftrightarrow{D}^I_\mu \varphi\right) \left(\bar{q}_i \gamma^\mu \tau^I q_j\right)
\end{aligned} \tag{8.4.1}$$

with notation identical to that introduced in Section 2.7.1. Operators of higher-dimension are expected to generate sub-leading corrections to scattering amplitudes and, as is common practice, neglected in this study. The relevant Wilson coefficients are:

$$\begin{aligned}
c_{tG} &\equiv \mathrm{Re}\left\{C_{uG}^{(33)}\right\}, \\
c_{tZ} &\equiv \mathrm{Re}\left\{-\sin\theta_W C_{uB}^{(33)} + \cos\theta_W C_{uW}^{(33)}\right\}, \\
c_{\varphi Q}^{3} &\equiv C_{\varphi q}^{3(33)}, \\
c_{\varphi Q}^{-} &\equiv C_{\varphi q}^{1(33)} - C_{\varphi q}^{3(33)}, \\
c_{\varphi t} &\equiv C_{\varphi u}^{(33)},
\end{aligned} \tag{8.4.2}$$

with θ_W the weak-mixing angle, and with the imaginary parts of c_{tG} and c_{tZ} omitted as the study restricts itself to CP-conserving effects.

A study on the impact of $t\bar{t}Z$ spin observable measurements in $t\bar{t}Z$ EFT fits is presented, seeking to show whether the supplementary information provided by the spin observables can provide additional power to constrain particular Wilson coefficients. The EFT fit procedure proceeds by first specifying the parameterisation of each spin observable in terms of the Wilson coefficients in question, then using this parameterisation in a global fit, in which the measured values of the observables constitute the fit inputs, and the outputs are a set of credibility intervals on the Wilson coefficients. Only one EFT vertex is inserted into each production Feynman diagram, a

state known as *single-insertion* [3]. The parameterisation of each spin observable is given by

$$O = O_{\text{SM}} + \sum_i \frac{c_i^{(6)}}{\Lambda^2} O_i^{(6)} + \sum_i \frac{c_i^{(6)2}}{\Lambda^4} O_{ii}^{(6)} + \sum_{i,j,i\neq j} \frac{c_i^{(6)} c_j^{(6)}}{\Lambda^4} O_{ij}^{(6)}, \tag{8.4.3}$$

which is simply equation 2.7.2 under the restriction to six-dimensional operators, and where the Λ^4 terms are separated into two cases, the interference of an EFT-operator with itself ($i = j$), and its interference with another operator ($i \neq j$). The numerical values of the terms $O_i^{(6)}, O_{ii}^{(6)}, O_{ij}^{(6)}$ are required for the observable parameterisations to be known explicitly, and are derived from simulation. The MadGraph_aMC@NLO and Pythia event generators are again employed, generating 10 million $t\bar{t}Z$ events using the same SM input parameters listed in Section 8.2, this time at LO-precision in QCD. The UFO model `dim6top_LO` [377] is used to generate MC-simulated samples at particular non-zero values of the Wilson coefficients listed in 8.4.2. Simulated samples are generated for many different points in the Wilson coefficient parameter space. The spin parameters are then extracted through the usual expectation values of angular observables. A fit can be performed to these observables with the parameterisation 8.4.3 to yield the coefficients. Normalisation effects in each observable are cancelled by extracting the observables from normalised differential cross-sections. Additionally, best practice from the LHC Top Working Group recommends a re-scaling of observables to the best SM prediction: $O \to O \times O_{\text{SM}}^{\text{best}}/O_{\text{SM}}$, where $O_{\text{SM}}^{\text{best}}$ is simply the NLO computation for the relevant spin observable given in Table 8.1. For the $\cos\varphi(l^+, l^-)$ differential observable this re-scaling is applied bin-by-bin.

This SMEFT interpretation is based on the same EFTFitter framework used in Section 8.3. Once again, pseudo-data in the form of the NLO MC-simulated samples are used in lieu of experimental data. The elements of the spin correlation matrix $\mathbf{C}$, the polarisations $\mathbf{B}^{\pm}$, and the four bins of $\cos\varphi(l^+, l^-)$ constitute the set of measurements, with the same projected statistical correlations and total uncertainties. Two LHC scenarios are considered: the nominal Run-2 scenario, and the combination Run-2 + Run-3. The prior for each Wilson coefficient is chosen to be Gaussian, and to reflect limits on that Wilson coefficient found in the literature: the priors take a mean of zero and width equal to half the marginalised bounds reported by the Smefit collaboration at 95 % confidence level [378].

The Wilson coefficient $c_{\varphi Q}^3$ was dropped from the interpretation as all observables were found to be insensitive to it. Table 8.4 presents the expected limits on the four remaining Wilson coefficient, for both Run-2 and combined Run-2 + Run-3 scenarios. Limits derived from various fits in the literature are also shown.

[3] This is a deliberate and widely-adopted position. By definition this precludes EFT operating-mixing at amplitude-level, though operators still mixed at squared-matrix-element level.

Table 8.4: Projected 95 % confidence bounds on Wilson coefficients, derived from pseudo-data using the EFTFitter framework are shown in the top panel. Priors informed by current bounds in the literature are used. The bottom panel shows corresponding bounds presented in the literature, either from a global fit by the theory community (SMEFiT), or dedicated fits by the ATLAS and CMS collaborations using $t\bar{t}Z$ measurements.

95% bounds		c_{tZ}	$c^{-}_{\phi Q}$	c_{tG}	$c_{\phi t}$
Run 2		[-2.7, 3.4]	[-2.6, 2.6]	[-0.4, 0.4]	[-6.0, 5.6]
Run 2 + Run 3		[-2.2, 2.8]	[-2.6, 2.6]	[-0.4, 0.4]	[-5.0, 4.6]
SMEFiT	[378]	[-4.6, 5.9]	[-2.6, 3.3]	[-0.4, 0.4]	[-23, 7.3]
ATLAS $36\,\text{fb}^{-1}$	[360]	[-4.9, 4.9]	[-3.3, 4.2]	—	[-25, 5.5]
CMS 45	[379]	[-3.3, 3.2]	[-7.6, 22]	[-1.4, 1.2]	[-19, 12]
CMS 77.5	[362]	[-1.1, 1.1]	[-4.0, 0.0]	—	[0.3, 5.4]

8.4.1 Information Geometry Analysis

In the SMEFT interpretation presented above, each Wilson coefficient had its own prior with bounds derived from the literature. Such an approach would be used to give the most 'competitive' bounds, but it is instructive to also understand the constraining power of the spin measurements when all Wilson coefficients share the same prior. The bounds derived on each Wilson coefficient would then directly illustrate the power of the spin information to constrain that Wilson coefficient; phrased differently, it would show which Wilson coefficients are dominant in controlling the behaviour of the spin observables. An alternative EFT fit is performed, with priors set to uniform distributions spanning the range [-10,10] and the covariance matrix recomputed. Table 8.5 shows the results of the fit, where it is seen that the quark-vector boson Wilson coefficients c_{tZ} and c_{tG} show the greatest constraint.

A complimentary interpretation is to use the Fisher information matrix, I_{ij}, a tool from information geometry which has found some usage in particle physics contexts [380]. It defines a metric in the space of model parameters and can shed light on the power of particular measurements. Large entries in the Fisher information matrix indicate directions which can be measured well, whilst small entries correspond to blind directions. Use of the Fisher information matrix in a SMEFT context was initiated in the Higgs sector [380], and has been applied to global fits to identify combinations of Wilson coefficients which are insensitive to current measurements (so-called flat directions) [381]. This is achieved by noting that the eigenvectors of the Fisher information matrix correspond to the combinations of SMEFT operators being probed, with the corresponding eigenvalues quantifying the strength of the sensitivity.

An alternative EFT fit is performed to test the utility of the Fisher information-inspired analysis in the case of $t\bar{t}Z$ spin measurements.

Table 8.5: Exclusion bounds on the four operators of interest, given as 95% Bayesian credibility intervals. The two scenarios quoted are described in the accompanying text, and uniform priors are chosen for all the Wilson coefficients.

95% bounds	c_{tZ}	$c^{-}_{\phi Q}$	c_{tG}	$c_{\phi t}$
Run 2	[-3.1, 4.4]	[-10, 8.1]	[-2.0, 3.4]	[-9.8, 7.0]
Run 2 + Run 3	[-2.5, 3.5]	[-10, 7.0]	[-1.4, 2.8]	[-8.1, 6.4]

The Cramer-Rao bound links the covariance matrix V_{ij} in the EFT parameter space to the inverse of the Fisher information matrix [381]:

$$V_{ij} \geq \left(I^{-1}\right)_{ij}. \tag{8.4.4}$$

An approximation of the Fisher information matrix is therefore found by constructing the inverse of the covariance matrix. The eigen-decomposition of the resulting matrix is performed, and the eigenvectors $\mathcal{F}_i$ are listed below along with their respective eigenvalues λ_i:

$$\begin{aligned}
\lambda_1 &= 0.03,\ \mathcal{F}_1 : 0.84 \cdot c^{-}_{\varphi Q} - 0.54 \cdot c_{\varphi t},\\
\lambda_2 &= 0.12,\ \mathcal{F}_2 : 0.48 \cdot c^{-}_{\varphi Q} + 0.79 \cdot c_{\varphi t} + 0.37 \cdot c_{tZ},\\
\lambda_3 &= 0.69,\ \mathcal{F}_3 : 0.21 \cdot c^{-}_{\varphi Q} + 0.26 \cdot c_{\varphi t} - 0.86 \cdot c_{tZ} - 0.39 \cdot c_{tG},\\
\lambda_4 &= 0.83,\ \mathcal{F}_4 : 0.11 \cdot c^{-}_{\varphi Q} + 0.14 \cdot c_{\varphi t} - 0.34 \cdot c_{tZ} + 0.92 \cdot c_{tG}.
\end{aligned} \tag{8.4.5}$$

These four eigenvectors represent the directions being probed by the set of spin observables in the EFT parameter space, and the eigenvalues quantify the sensitivity of the measurements: $\mathcal{F}_4$ has the largest eigenvalue $\lambda_4 = 0.83$ corresponding to the most sensitive direction and thus to the highest expected constraint. The Wilson coefficients c_{tG} and c_{tZ} appear with large coefficients in the eigenvectors with largest eigenvalues. This suggests that these Wilson coefficients have the largest impact and will be most constrained by the spin observable dataset. The $c^{-}_{\varphi Q}$ Wilson coefficient features most strongly in $\mathcal{F}_1$ which is characterised by its small eigenvalue: this should translate to weak constraint on this degree of freedom.

8.5 Conclusions

This chapter introduced a phenomenological study of spin correlations and polarisations in $t\bar{t}Z$ production. Several novel results and conclusions were presented. This

study constitutes the first computation of the SDM in $t\bar{t}Z$ production, and indeed the first such computation which extends the SDM application into associated top-quark production. In particular, a set of predictions for SDM-derived spin parameters was presented at NLO-accuracy. The spin properties of the $t\bar{t}$ system in $t\bar{t}Z$ production were shown to be manifestly different to those in the standard $t\bar{t}$ production case. A proposed measurement strategy was also outlined, and credibility levels in the presence of spin correlations, for five different LHC running scenarios, given. It was suggested that combining a number of different spin measurements could lead to observation of spin correlation effects in $t\bar{t}Z$ production by the end of Run-3. Suggested limits for relevant Wilson coefficients were also presented. The structure of the EFT parameter space was probed using techniques from information geometry, where it was shown that effective operators which couple the top-quark to gauge bosons are the dominant contributors to SMEFT corrections to the spin observables studied.

This study resulted in the publication "Observing $t\bar{t}Z$ spin correlation at the LHC" [129]. The most recent ATLAS $t\bar{t}Z$ publication presents the first effort to extract spin information in $t\bar{t}Z$ production in data [369], and was based on methodology introduced in this study. In particular, [369] reports an observed f_{SM} of $1.20 \pm 0.63(\mathrm{stat.}) \pm 0.25(\mathrm{syst.})$, a rejection of the no-spin hypothesis with a significance of 1.8σ. It is hoped that the spin density matrix formalism will be applied to other $t\bar{t}X$ processes. Future phenomenological work could consider studies of spin-correlations in other associated production channels. Future experimental measurements will benefit from the increased statistics brought with larger integrated luminosities provided by the LHC Run-3 campaign and beyond.

Chapter 9

Phenomenology of Entanglement in Hadronic $t\bar{t}$ Pair Production

"An entirely new application,
Of techniques from quantum information.
We need no longer wait,
The $t\bar{t}$ quantum state,
Will become our newest fixation."
—

Quantum entanglement is perhaps the most counter-intuitive and thought-provoking concept arising from quantum physics, one which has escaped into the wider public's collective imagination. It has been the subject of famous scientific debate in the context of the Einstein-Podolski-Rosen paradox [382], it forms the basis for violations of infamous Bell inequalities [9], and the 2022 Nobel Prize in Physics was awarded to experimentalists for pioneering work in the measurement of quantum entanglement in photon systems [10]. The next two chapters present work towards an observation of quantum entanglement in $t\bar{t}$ pair production at the LHC, the first ever measurements of entanglement between quarks. In this chapter, relevant concepts from the field of quantum information are introduced, and specific criteria for establishing the presence of entanglement in $t\bar{t}$ production are given. The gory technical details of the ATLAS measurement of quantum entanglement in $t\bar{t}$ production are presented in Chapter 10.

9.1 Spooky Action at a Distance

Quantum information [383] is the glorious union of quantum mechanics (QM) with the classical information theory of Claude Shannon [384]. In some sense, quantum information is applied QM: quantum information science and communication deal with the extraction of information from, and transmission of information between, quantum systems [385]; quantum information processing concerns the manipulation of

such systems for the purposes of computation [386]. Quantum computing in particular has become a field which holds much fascination for both the scientific community and the public, with the potential to revolutionise everything from the simulation of physical systems [387], to the cryptography techniques employed to keep information secure [388].

A phenomenon ubiquitous in quantum information is quantum entanglement, once dubbed "the characteristic trait of quantum mechanics" [389]. It is that most quantum of quantum phenomena: a statement regarding statistical correlations between quantum states; correlations which are inherently non-classical. The most famous results in quantum information theory, the celebrated Bell inequalities [9], introduced an underlying "local hidden variable" (LHV) description of QM. The resultant formalism imposes strict constraints on the statistical correlations in bipartite (two-part) quantum systems: the Bell inequalities [390]. Bell showed that measurements on entangled quantum states violate these inequalities, disproving the validity of any LHV model. These arguments have since been generalised[391]–[393]. The "spooky-action-at-a-distance" of entanglement lies at the heart of quantum information science, and underlies everything from quantum teleportation [394], Shor's algorithm for prime factorisation on a quantum computer [395], and quantum cryptography [396].

9.2 Quantum Entanglement Formalism

A *pure* quantum mechanical state is represented by a d-dimensional vector $|\psi\rangle$ in a Hilbert space $\mathcal{H}$ of corresponding dimensionality. A more general, *mixed* quantum system — a statistical ensemble of quantum states — is described by a density operator, or density matrix, $\hat{\rho}$:

$$\hat{\rho} = \sum_{i}^{N} W_i \left|\psi_i\right\rangle \left\langle\psi_i\right|, \tag{9.2.1}$$

with W_i statistical weights [118]. This provides the most complete description of a general quantum system. Defining a basis for state-vectors $|\psi\rangle$ allows an explicit matrix form of $\hat{\rho}$ to be written down. The density matrix has a number of properties. It is Hermitian and has unit trace. Its time-evolution is given by the von Neumann equation [397] (with the time-evolution of a pure state $|\psi\rangle$ given by the Schrödinger equation). The measurement of some observable O is given by $\langle O\rangle = \mathrm{Tr}(O\hat{\rho})$. Study of additional properties of $\hat{\rho}$ can provide further insight into the quantum system; the property of entanglement is one such example.

The idea of entanglement is quantified with the notion of separability of the density matrix. Consider now a two-level ensemble quantum system, described completely by a density operator $\hat{\rho}$ defined in the bipartite Hilbert space $\mathcal{H} = \mathcal{H}_a \otimes \mathcal{H}_b$[1]. If the density

[1]Note that the Hilbert spaces need not be on the same dimension.

matrix can be written as a convex combination of product states i.e. in the form:

$$\hat{\rho} = \sum_k p_k \hat{\rho}_k^a \otimes \hat{\rho}_k^b = \sum_k p_k \left|\psi_k^a\right\rangle \left\langle\psi_k^a\right| \otimes \left|\psi_k^b\right\rangle \left\langle\psi_k^b\right|, \tag{9.2.2}$$

with $\sum_k p_k = 1, p_k \geq 0$, the system is said to be *separable* [398]. A non-separable state, one for which 9.2.2 does not hold, is then by definition entangled, and cannot be written as the product state of individual subsystems. Calculating whether an arbitrary quantum system is entangled — the so-called *Quantum Separability Problem* (QUSEP) — was shown to be NP-hard[2] [399]. A number of proposed criteria exist in the literature for detecting entanglement in particular cases, a review of which is beyond the scope of this chapter. Two criteria are outlined for the relevant two-qubit system in Section 9.3; for general reviews, refer to [400], [401].

Armed with a formal definition of entanglement, and criteria for detecting it in a particular physical system, experimentalists have found evidence of entanglement in a wide variety of physical phenomena. Pioneering work in the late 1960s and early 1970s with polarised photons constituted the first experimental evidence of "stronger-than-classical" correlations [402] and progress towards experimental violation of a Bell inequality [403]. Aspect et al. famously produced further measurements using entangled photons to close several loopholes[3] in Bell inequality interpretations [405], [406]. Loophole-free violations of Bell inequalities were measured far more recently, using entangled photons [407] and electrons [408]. Further extensions beyond the photonic case include entanglement measurements in atoms [409], neutral mesons [410], Bell-type inequality violations using neutrinos [411], and entanglement evidence in quantum Hawking radiation [412].

Theoretical work on entanglement in high-energy systems has received limited attention — see [413]–[415] for a scant selection of examples. In recent years, however, the work of Afik and de Nova [130] has brought attention to the possibility of measurements of entanglement, and other quantum information phenomena, in particle collider experiments. Experimental verification in such conditions would represent evidence of entanglement at far higher energy scales than in existing measurements. Afik and de Nova suggested that entanglement can be measured in $t\bar{t}$ pair-production at the LHC, in certain regions of phase-space. This work forms the basis for the measurement of entanglement in $t\bar{t}$ production presented in Chapter 10, and is presented below.

[2] This is a statement about the algorithmic complexity in *computational complexity theory*. The point here is that it is highly non-trivial to determine whether an arbitrary quantum state is entangled.

[3] Loopholes in Bell test experiments are proposed mechanisms through which a Bell-type inequality may be violated yet some hidden underlying theory of local realism is not invalidated. See [404] for a review.

9.3 Entanglement in Two-Qubit System

Famously, information in classical systems is expressed in *bits*, and carried by a physical system which can exist in one of two states. In contrast, quantum information can expressed as the superposition of quantum states. The quantum equivalent of the bit is the *qubit*, and the concept can be extended by considering higher-level quantum systems. A canonical example of a qubit is a spin-1/2 particle, which can exist in some superposition of spin-up and spin-down states. The top-quark is such a particle. A bipartite system of dimension 2×2 can be built by considering the Hilbert space formed by two qubits. The corresponding density matrix takes the form:

$$\rho = \frac{1}{4}\left(\mathbb{1}_4 + \sum_i \left(\hat{B}_i^+ \sigma^i \otimes \mathbb{1}_2 + \hat{B}_i^- \mathbb{1}_2 \otimes \sigma^i\right) + \sum_{i,j} \hat{C}_{ij} \sigma^i \otimes \sigma^j\right), \tag{9.3.1}$$

for $i, j = 1, 2, 3$. This is a general expression for the density matrix of a two-qubit system.

Compare 9.3.1 to 3.3.7. It should be obvious from the functional form of these expression that they describe the same object, subject to different normalisation: the spin-density matrix R (3.3.7) which governs the dynamics of $t\bar{t}$ production is an un-normalised version of the density matrix $\hat{\rho}$ which describes the underlying two-qubit quantum system. The appropriate normalisation factor is $\mathrm{Tr}(R)$:

$$\rho = \frac{R}{\mathrm{Tr}(R)} = \frac{R}{4A}, \quad \hat{B}_i^{\pm} = \frac{B_i^{\pm}}{A}, \quad \hat{C}_{ij} = \frac{C_{ij}}{A}, \tag{9.3.2}$$

with the relationship between the normalised and un-normalised polarisation vectors and spin-correlation matrix shown explicitly[4]. This association allows one to perform full quantum tomography of the $t\bar{t}$ quantum system through measurement of the spin correlations and polarisations of the top-quarks [130]; or to make some reduced statement about particular quantum information properties through some simpler study of the spin-density matrix.

The *positive partial transpose* (PPT), or *Peres-Horodecki*, criterion provides a necessary and sufficient condition for signalling entanglement in bipartite systems of dimension 2×2 [416], [417]. The partial transpose of ρ with respect to the B system is defined as the tensor product of the identity I and transposition T maps acting on the density matrix: $\rho^{T_B} = (I \otimes T)\rho$. In the separable case, the criterion states that the matrix ρ^{T_B} should also be a density matrix i.e. correspond to a quantum state [401]. This is equivalent to the statement that ρ^{T_B} is non-negative: elements ${\rho^{T_B}}_{ij} \geq 0 \quad \forall\, i, j$, which is readily assessed through measurement of the individual spin density matrix elements.

[4] In this thesis, the caret symbol on top of spin density matrix elements is used to indicate that these are normalised in the sense of equation 9.3.2. This is contrasted with spin density matrix elements discussed in previous chapters, which are unnormalised.

An additional parameter which can quantify the strength of entanglement is the *concurrence*, derived from an alternative set of entanglement criteria [418]. The matrix $C(\rho) \coloneqq (\sqrt{\rho}\tilde{\rho}\sqrt{\rho})^{\frac{1}{2}}$ is defined, with $\tilde{\rho} = (\sigma_2 \otimes \sigma_2)\,\rho^*\,(\sigma_2 \otimes \sigma_2)$ and ρ^* the complex conjugate of the density matrix. The concurrence is then defined as

$$C[\rho] \equiv \max\left(0, \lambda_1 - \lambda_2 - \lambda_3 - \lambda_4\right), \tag{9.3.3}$$

where λ_i are the four eigenvalues of $C(\rho)$, indexed in order of decreasing magnitude i.e. $\lambda_{i-1} > \lambda_i$.

9.4 Entanglement in $t\bar{t}$ Pair Production

Explicit expressions for the Peres-Horodecki criterion and concurrence can be derived for the $t\bar{t}$ system by considering the explicit form of the spin-density matrix. Afik and de Nova restrict their attention to the LO-QCD production case, where the polarisations $B_i^+ = B_i^- \approx 0$ and the spin-correlation matrix C_{ij} is symmetric [130]. Under these conditions, the density matrix is written in the simple form,

$$\rho = \frac{1}{4}\begin{bmatrix} 1+\hat{C}_{nn} & 0 & 0 & \hat{C}_{kk}-\hat{C}_{rr} \\ 0 & 1-\hat{C}_{nn} & \hat{C}_{kk}+\hat{C}_{rr} & 0 \\ 0 & \hat{C}_{kk}+\hat{C}_{rr} & 1-\hat{C}_{nn} & 0 \\ \hat{C}_{kk}-\hat{C}_{rr} & 0 & 0 & 1+\hat{C}_{nn} \end{bmatrix}. \tag{9.4.1}$$

Computing the partial transpose and assessing the result for non-negativity yields the condition[5]

$$\Delta \coloneqq -\hat{C}_{nn} + \left|\hat{C}_{kk} + \hat{C}_{rr}\right| - 1 > 0. \tag{9.4.2}$$

If condition 9.4.2 is met, the $t\bar{t}$ system is entangled. Crucially, the Peres-Horodecki criterion can be expressed as a stricter statement[6]:

$$\mathrm{Tr}[C_{ij}] < -1, \tag{9.4.3}$$

where Tr denotes the trace operation. The concurrence of the $t\bar{t}$ system can be computed by realising that ρ is a real matrix, thus $C(\rho) = \rho$, and the eigenvalues λ_i required are simply the eigenvalues of ρ. The result is also a function of Δ:

$$C[\rho] = \frac{1}{2}\max(\Delta, 0). \tag{9.4.4}$$

[5]The full derivation is given in [130].

[6]This result relies on the fact that $|C_{kk} + C_{rr}| \geq -(C_{kk} + C_{rr}) = -C_{kk} - C_{rr}$. This means $-C_{nn} + \left|C_{kk} + C_{rr}\right| - 1 > -C_{nn} - C_{kk} - C_{rr} - 1 > 0$, which is rewritten as $C_{nn} + C_{kk} + C_{rr} < -1$, which is immediately recognisable as the trace of C.

At LO-QCD, Δ can be expressed analytically for both gg-fusion and $q\bar{q}$-annihilations production modes as functions of the mass ratio β and the angle Θ, defined as the production angle with respect to the beam-line, $\cos\Theta = \hat{\mathbf{k}} \cdot \hat{\mathbf{p}}$. Explicitly, the gg-channel is given by:

$$\Delta^{gg} = \frac{2 - 4\beta^2\left(1 + \sin^2\Theta\right) + 2\beta^4\left(1 + \sin^4\Theta\right)}{1 + 2\beta^2\sin^2\Theta - \beta^4\left(1 + \sin^4\Theta\right)}, \ \beta^2\left(1 + \sin^2\Theta\right) < 1; \tag{9.4.5}$$

$$\Delta^{gg} = \frac{2\beta^4\left(1 + \sin^4\Theta\right) - 2}{1 + 2\beta^2\sin^2\Theta - \beta^4\left(1 + \sin^4\Theta\right)}, \ \beta^2\left(1 + \sin^2\Theta\right) \geq 1. \tag{9.4.6}$$

and the $q\bar{q}$-channel by,

$$\Delta^{q\bar{q}} = \frac{\beta^2\sin^2\Theta}{2 - \beta^2\sin^2\Theta} \geq 0. \tag{9.4.7}$$

The $t\bar{t}$ state is entangled at any point where the concurrence is non-zero. These expressions allow one study how the entanglement of the $t\bar{t}$-pair varies across the (β, Θ) phase-space. A visualisation of that variation is given in Figure 9.1. Specifically, Figures 9.1(a) and 9.1(b) show the variation in Δ^{gg} and $\Delta^{q\bar{q}}$ across the $t\bar{t}$ phase-space, as parameterised by $M_{t\bar{t}}$ and Θ. The combined $\Delta^{gg+q\bar{q}}$ concurrence is shown in 9.1(c); 9.1(d) is the double-differential cross-section:

$$\frac{\mathrm{d}^2\sigma}{\mathrm{d}M_{t\bar{t}}\mathrm{d}\Theta} = 2\pi\sin\Theta\frac{\mathrm{d}\sigma}{\mathrm{d}M_{t\bar{t}}\mathrm{d}\Omega}. \tag{9.4.8}$$

It is immediately apparent that entanglement is present in certain regions. Initial-state gluon pairs can have their spin polarisations aligned in arbitrary directions, which leads to two specific regions of quantum entanglement in the gg-channel. At low values of $m_{t\bar{t}}$, the produced $t\bar{t}$ pairs form a spin-singlet state which is maximally entangled. In addition, such a spin-singlet state is rotationally-invariant. This region is labelled the *threshold region* in reference to its proximity the $m_{t\bar{t}}$ threshold of around 340 GeV, below which on-shell $t\bar{t}$ pairs are not produced. In the highly-boosted regime, for large production angles, $t\bar{t}$ pairs are produced in a spin-triplet state which is also maximally entangled. Separating these two regimes exists a region in which the $t\bar{t}$ pairs are completely un-entangled. In stark contrast, the $q\bar{q}$ channel produces $t\bar{t}$ pairs which are entangled across the phase-space, save on the boundaries $M_{t\bar{t}} = 0$ or $\Theta = 0$.

The work of Afik and de Nova therefore shows that $t\bar{t}$ pairs are maximally entangled in two particular regions, initiating the tantalising prospect of a measurement of this phenomenon at the LHC. A measurement in either region presents challenges. The production of entangled $t\bar{t}$ pairs in the highly-boosted regime is driven primarily by $q\bar{q}$-annihilation which is a sub-dominant mechanism for $t\bar{t}$ production at the LHC, leading to limited statistical power. This issue is compounded by studying the $t\bar{t}$ normalised

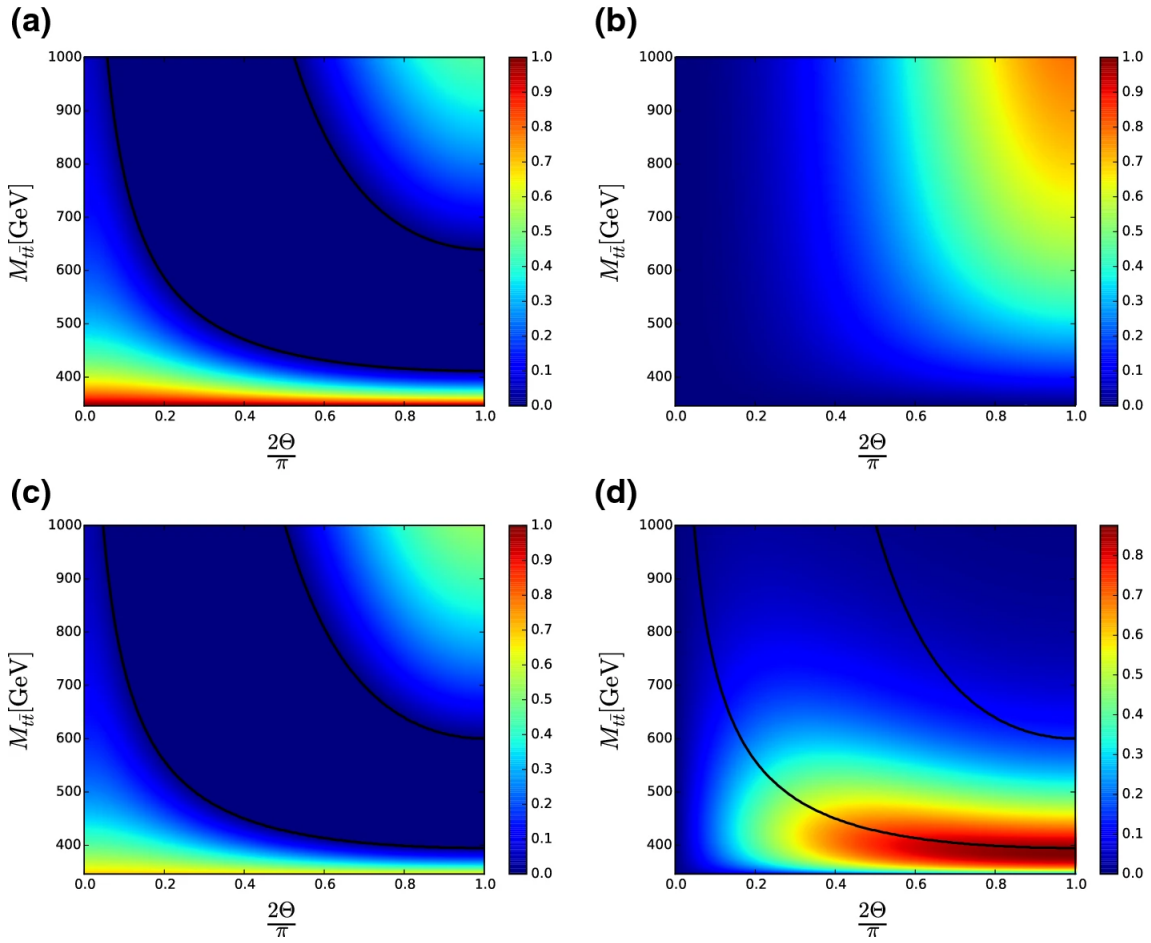

Figure 9.1: The concurrence is a measure of entanglement strength [130]. Sub-figures (**a**) - (**c**) visualise the concurrence across the $t\bar{t}$ production phase-space as parameterised by the kinematic variables (β, Θ). Sub-figure (**a**) gives the concurrence for gg-fusion, which is strongest near the $m_{t\bar{t}}$ threshold; (**b**) gives the concurrence for $q\bar{q}$-annihilation, which is strongest in the boosted regime; (**c**) is the combined concurrence of the two production channels. Sub-figure (**d**) shows the double differential cross-section $\frac{\mathrm{d}^2\sigma}{\mathrm{d}M_{t\bar{t}}\mathrm{d}\Theta}$, for $pp \to t\bar{t}$, indicating that the majority of $t\bar{t}$ pairs produced at $\sqrt{s} = 13\,\mathrm{TeV}$ exist in the low $m_{t\bar{t}}$ regime.

double-differential cross-section shown in 9.1(d), which illustrates the well-known fact that $t\bar{t}$ pairs are produced preferentially at lower values of $m_{t\bar{t}}$. These compounding issues indicate that a measurement of entanglement in the boosted regime would be statistically-limited.

By way of contrast, the threshold regime benefits from plentiful statistics. Measurement of the trace of the spin-correlation matrix should be made easier by the rotational symmetry of the spin-singlet state: one could make a measurement of the diagonal elements in any orthonormal basis. Yet a simpler method is at hand. The differential

cross-section

$$\frac{1}{\sigma}\frac{\mathrm{d}\sigma}{\mathrm{d}\cos\varphi} = \frac{1}{2}(1 - D\cos\varphi) \tag{9.4.9}$$

was first introduced in Chapter 3, with φ the angle between the two top-quark decay products, as defined in their respective parent-top's reference frame. Realising that $D = \mathrm{Tr}[C]/3$, the trace of the spin-correlation matrix can be extracted through measurement of this single angular observable. The trace condition 9.4.3 is then expressed in terms of the *entanglement marker* D:

$$D < -\frac{1}{3} \tag{9.4.10}$$

implies the presence of entanglement between the $t\bar{t}$ spins. Afik and de Nova conclude their study by implying that evidence of quantum entanglement in $t\bar{t}$ pairs should be possible in existing Run-2 ATLAS data, provided the systematic uncertainties are sufficiently small.

9.5 Quantum Information in High-Energy Physics

This chapter concludes with a review of other quantum information work, both phenomenological and experimental, in the field of high-energy physics. The literature goes beyond simply considering how entanglement would manifest in particle physics contexts, and considers the unique high-energy perspective collider physics can play in testing various quantum phenomena.

Considering only $t\bar{t}$ production initially, Aguilar-Saavedra and Casas suggested that additional kinematic cuts can improve sensitivity to entanglement in the $t\bar{t}$ system [419]. Afik and de Nova also showed that additional quantum information phenomena, namely "quantum discord" and "steering", should also be present in the $t\bar{t}$ system [420]. Reconstruction of the full quantum state of the $t\bar{t}$ system, a process known as quantum tomography, is also shown to be possible at the LHC [130], [420], but presents a more involved measurement than that which is presented in Chapter 10. Some studies have also considered the implications of BSM physics on entanglement, and the utility of quantum information-derived observables in setting limits on NP models [421], [422]. Research has also investigated the possibility of testing Bell-type inequalities [419], [420], [423]–[425], which constitute a stronger statement about the underlying quantum system. The literature identifies the boosted $t\bar{t}$ regime as the most promising area for performing Bell-type tests, but disagrees about whether such tests are feasible even with the entire proposed dataset of the LHC.

Looking beyond the top-quark sector, studies have also considered opportunities for measuring quantum information phenomena in the production of weak bosons [426]–[430] and of tau-lepton pairs [431], [432]. The decay of the Higgs boson to a pair

of W bosons is thought to provide a promising avenue for performing Bell-type tests in a two-qutrit[7] system. New experimental techniques are being proposed to reconstruct the W bosons [433] to facilitate such a measurement.

On-going research is also investigating how collider experiments can study the experimental implications of so-called "beyond–quantum mechanics" theories. Such models constitute a more radical definition of New Physics (NP). The NP normally mentioned in particle physics contexts refers essentially to extensions of the SM constructed using the same field-theoretic building blocks, or more general extensions in which QM still holds. Beyond-QM theories do away with QM as a prerequisite; examples include generalised probabilistic theories [434]. Specific Bell tests can directly probe stronger-than-quantum correlations. Proposals are also being made for experimental procedures in colliders which can test for deviations from quantum mechanics [435].

Chapter 10 presents the first dedicated measurement of quantum entanglement at the LHC. However, entanglement was actually measured in the decays of $\Upsilon(4S)$ mesons at the Belle experiment [436]. The $\Upsilon(4S)$ is a bound bottom–antibottom quark state which can decay to two B-mesons. These mesons form a maximally-entangled spin-singlet state, with the flavour of the B-mesons constituting the entangled quantum number: the flavour-specific decay of one meson fixes the flavour of the other meson. By studying the semi-leptonic decays of around 150 million B-mesons pairs, the Belle collaboration made the first measurement of entanglement in a collider physics context.

A recent study by Fabbrichesi et al. can lay claim to being the first measurement of quantum entanglement at the LHC [437]. The study reconstructs the polarisation density matrix of the decay $B^0 \to J/\psi K^*(892)^0$, using helicity amplitude pp collision data gathered by the LHCb collaboration during Run-1 [438]. An alternative definition of entanglement, the von Neumann entropy

$$\mathscr{E} = -\,\mathrm{Tr}\left[\rho_A \log \rho_A\right] \tag{9.5.1}$$

is employed [401], with ρ_A a reduced density matrix of the polarisation density matrix. The study presents a result of $\mathscr{E} = 0.756 \pm 0.009$, with any value of $\mathscr{E}$ above zero indicating entanglement between the qutrit final states. In addition, the study defines an appropriate observable $\mathcal{I}_3$ with which to measure the CGLMP inequality, the optimal generalisation of the Bell inequality to the two-qutrit state[8]. This observable is measured to be $\mathcal{I}_3 = 2.548 \pm 0.015$, with $\mathcal{I}_3 > 2$ corresponding to a violation of the CGLMP inequality. This corresponds to a reported significance of 36σ.

In light of these experimental results, the significance of the ATLAS observation of entanglement in $t\bar{t}$ production, presented in the next chapter, must be carefully stated. The Belle measurement is made on $\sqrt{s} = 11.5\,\mathrm{GeV}$ e^+e^- data; the Fabbrichesi et al is

[7] The qutrit state is the quantum analogue of the classical 'trit', or ternary digit, unit of information

[8] The practice is to define this observable based on the relationship $\mathcal{I}_3 = \mathrm{Tr}[\rho\mathcal{B}]$ with ρ the density matrix and $\mathcal{B}$ an appropriately-defined Bell operator, whose explicit form is given in the paper.

conducted on $\sqrt{s} = 7\,\text{TeV}$ e^+e^- data. The presented ATLAS measurement therefore constitutes the highest lab-based measurement of a quantum information phenomenon, and the first such dedicated measurement at a hadron collider. In addition, the ATLAS measurement is unique in that it studies free quarks. In each of the results presented above, the fundamental objects in question are quarks, but they are bound in mesons and therefore cannot be thought of as free, as the term is understood within the framework of perturbative QCD. The ATLAS measurement therefore constitutes the first measurement of quantum entanglement between free quarks.

Chapter 10

A Measurement of Entanglement Between $t\bar{t}$ Pairs at the LHC

"With techniques that are hardly new-fangled,
We study how top-quark pairs are angled:
For events near threshold
(though we couldn't unfold)
We can state that these tops are entangled!"
—

Evidence of quantum entanglement in $t\bar{t}$ pair production in $\sqrt{s}$ = 13 TeV ATLAS data is presented. The work undertaken is introduced chronologically, and details several experimental challenges which necessitated adjustments to the preconceived measurement strategy. The measured data, corresponding simulations, physics object definitions and phase-space selections are all described in detail. A set of particle-level results, accompanied by relevant experimental and theoretical uncertainties is presented.

10.1 Strategy Summary

This measurement addresses whether measured data support the hypothesis that quantum entanglement is present in $t\bar{t}$ pair production close to the $m_{t\bar{t}}$ threshold. This is achieved through an extraction of entanglement marker D from the mean of the angular $\cos\varphi$ distribution, 9.4.9. The basic strategy is outlined as follows. Measured proton-proton collision events in data, and analogous simulated events, are selected based on particular features likely to correspond to di-leptonic $t\bar{t}$ decays, Section 10.3. Events are sub-divided into three regions delineated by cuts on $m_{t\bar{t}}$ (Section 10.4) with the region closest to the $m_{t\bar{t}}$ threshold constituting the signal region (SR), where a measured value of D should signal strong presence of entanglement. Background processes are estimated using both simulation and data-driven methods (Section 10.5) ,

and subtracted from the measured data. The kinematics of the top- and anti-top-quarks are reconstructed from their decay products through dedicated techniques (Section 10.6), such that the charged lepton decay products can be boosted into their parent top-quark's reference frame. The observable $\cos\varphi$ is measured in each event and the distribution 9.4.9 constructed. The data are compared to simulation in Section 10.7. The original strategy focused on correcting this differential cross-section for detector effects through unfolding, Section 10.8. Complications in the unfolding procedure necessitated a change of strategy, such that now only the entanglement marker D is corrected to fiducial particle-level using a calibration curve, Section 10.9. A selection of modelling, experimental and background uncertainties are considered in Section 10.10. The particle-level observed value of D is compared to the simulation prediction in Section 10.11, and detailed discussion of the findings given in Section 10.12.

As is common practice in particle physics measurements, the analysis was performed "blind" until the strategy was set. This means that the data were not studied prior a final *unblinding*, with the various analysis components tested exclusively on simulation prior to this. This general practice is employed to prevent any bias towards the observed data in the construction of the measurement strategy. Data were unblinded in the Control and Validation Regions (defined in 10.4) first. The last stage of the measurement was the unblinding of the data in the Signal Region.

A cut on $m_{t\bar{t}}$ is the most important phase-space selection required to isolate the threshold region. Figure 10.1 illustrates the variation in D with an upper threshold cut on $m_{t\bar{t}}$. Any point $(m_{t\bar{t}}, D)$ lying on either curve should be interpreted as the value of D obtained from 9.4.9 when considering all $t\bar{t}$ events in the invariant mass window $[2m_t, m_{t\bar{t}}]$. The solid blue curve denotes the variation computed analytically using the LO-QCD assumption, and the black dashed curve is the variation found from LO MC simulation. As a cut is applied closer to the threshold value $m_{t\bar{t}} = 2m_t$, the value of D decreases, indicating a stronger presence of entanglement. The cost of applying a cut too close to threshold is a weakening of statistical power: the more events which are excluded from the measurement, the higher the statistical uncertainty on the result. The $m_{t\bar{t}}$ selection must thus strike a balance between "entanglement strength" and statistical precision.

10.2 Data and Signal Modelling

This measurement uses the full Run-2 ATLAS dataset corresponding exclusively to pp collisions at $\sqrt{s} = 13\,\text{TeV}$. This data was collected between 2015 and 2018 and has been subject to scrutiny with regards to the quality of each event; as shown in Figure 4.2, a subset of collected data is removed, leaving a dataset corresponding to a total luminosity of $140.1\,\text{fb}^{-1}$ [439]. A further requirement is made that each event must pass at least one of the standard single electron or muon triggers mentioned in Section 4.6 and described in detail in [219], [220].

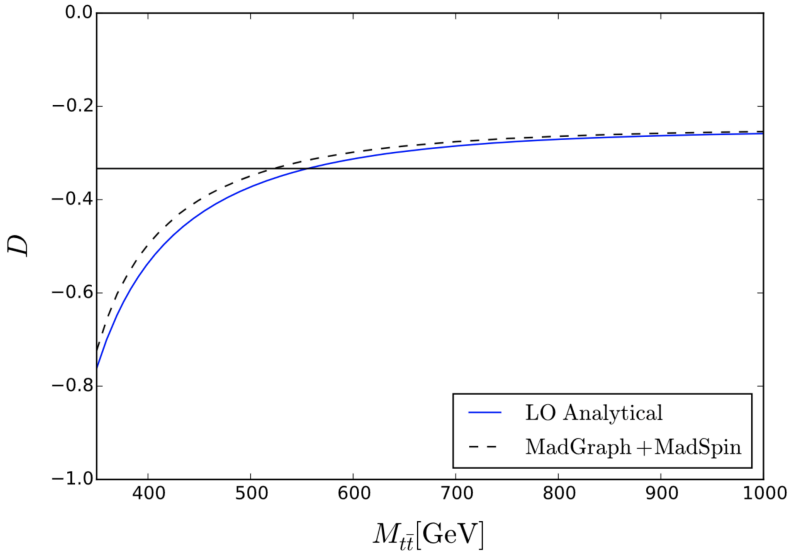

Figure 10.1: The entanglement marker D as computed in the window $[2m_t, m_{t\bar{t}}]$: the x-axis indicates the upper-bound on that invariant mass window. Taken from [130].

Recorded data are compared to a number of simulations of the $t\bar{t}$ production process, with simulated events produced through the general prescription outlined in Chapter 6. The nominal $t\bar{t}$ signal process is modelled using the Powheg Box V2 generator at NLO with the NNPDF3.0nlo set of PDFs [440], using the Powheg "heavy quark" (hvq) model [441]. Generated events are interfaced to Pythia 8.230 to provide modelling of the parton showering, hadronisation and underlying event. The Pythia parameters are set in accordance with the A14 tune [442], and the showering is employed in conjunction with the NNPDF2.3lo PDF set [443]. A top mass value of $m_{\text{top}} = 172.5\,\text{GeV}$ is used. The h_{damp} parameter controls the matching between the matrix element and the parton shower, effectively regulating high p_{T} radiation in the simulation [444]: its value is set to m_{top}. The renormalisation and factorisation scales take on dynamical values, with a functional form given by $\sqrt{m_{\text{top}}^2 + p_{\text{T}}^2}$. The decays of heavy quarks (bottom and charm) are simulated separately using the EvtGen programme [445].

Two alternative modellings set-ups are employed to serve as robust comparisons to the nominal Powheg + Pythia simulation. The Powheg Box Res framework was developed to treat decaying resonances within the Powheg infrastructure [446]. Commonly referred to in the ATLAS top-quark community as "*bb4l*", this set-up is considered to have improved modelling of top-quark decays; it also handles off-shell, non-resonant and interference effects in matrix element calculation [447]. The *bb4l* generator performs the full off-shell calculation $pp \to b\bar{b}l^+\bar{\nu}_l l'^- \nu_{l'}$, and therefore includes events corresponding to Wt-production. The measurement requires two on-shell top-quarks to decay and pass their spin information to the charged leptons, therefore the Wt and off-shell contributions in the *bb4l* simulated sample must somehow be removed if comparison to data and other generator set-ups is to be made. At reconstruction-level

this can be achieved by subtracting the Wt contribution at histogram-level. Generated events are showered using Pythia 8.230, with showering parameters equal to those of the nominal simulation set-up, but interfaced to the NNPDF2.3lo PDF set. A third set of simulated $t\bar{t}$ events is generated using the Powheg Box hvq model — thus identical to the nominal simulation in terms of the matrix element calculation — but interfaced Herwig 7.2. Pythia and Herwig provide different descriptions of parton showering and hadronisation, with the specifics of the shower-ordering differences explained in Section 6.3. The differences in the two generator prescription turns out of to be of high importance for this measurement.

Numerous additional simulated-samples are employed to model backgrounds processes, and to define systematic uncertainties. These are detailed specifically in the Sections 10.5 and 10.10.2, respectively.

10.3 Object Definitions and Event Selections

All physics objects utilised in this measurement are based on the definitions presented in Chapter 5. A selection is then applied to both data and simulated samples to isolate events with final-states physics objects compatible with $t\bar{t}$ di-leptonic production. Analogous requirements are specified for both reconstruction-level and particle-level object definitions.

10.3.1 Reconstruction-Level Event Selections

A di-leptonic $t\bar{t}$ pre-selection is applied, stipulating that each event must contain the following:

- Exactly one electron and exactly one muon. This lepton pair must have opposite-sign electric charge. Both leptons should meet the requirement, $p_{\mathrm{T}} > 15\,\mathrm{GeV}$.
- At least one trigger-matched lepton with: $p_{\mathrm{T}} > 25\,\mathrm{GeV}$ for data taken in years 2015 and 2016; $p_{\mathrm{T}} > 27\,\mathrm{GeV}$ for data taken in 2017; and $p_{\mathrm{T}} > 28\,\mathrm{GeV}$ for data taken in 2018. The year-on-year differences are a result of changes to trigger thresholds.
- At least two jets with $p_{\mathrm{T}} \geq 25\,\mathrm{GeV}$.
- At least one b-tagged jet, defined using the DL1r algorithm with the 85 % efficiency working point.

A set of additional criteria are introduced to minimise signal interference when reconstructing separate physics objects The following procedure, called *overlap removal*, is followed sequentially:

1. Electrons that share an ID track with a muon are removed.

2. If a jet is within $\Delta R < 0.2$ of an electron, the jet is removed. If multiple jets exist inside that proximity criterion, only the closet jet is removed.
3. Electrons reconstructed within $\Delta R < 0.4$ of any remaining jets are then removed.
4. Jets reconstructed from fewer than three tracks, which exist within $\Delta R < 0.2$ of a muon, are removed.
5. Muons reconstructed within $\Delta R < 0.4$ of any remaining jets are then removed.

10.3.2 Particle-Level Event Selections

Particle-level objects are reconstructed using stable particles defined in the simulation, where stable particles are those which have a mean lifetime in excess of 30 ps. All leptons considered — electrons, muons and neutrinos — are required to have originated from the decay of a W- or Z-boson, including decays through intermediate tau leptons. Leptons arising from hadronic decays can be identified in the MC truth-record, and are excluded. Final-state photons in close proximity to charged leptons, $\Delta R(l, \gamma) < 0.1$, have their momenta summed into the lepton's four-momentum, in a process known as *dressing*. Electrons and muons are required to meet criteria $p_{\mathrm{T}} > 10\,\mathrm{GeV}$ and $|\eta| < 2.5$. The photon dressing procedure is not applied to neutrinos, which are not subject to any additional phase-space selection requirements.

Electrons, muons, neutrinos and photons satisfying the above conditions are all omitted from contributing to final-state jets. All other stable particles are included. Jets are reconstructed using the anti-K_t algorithm defined with a distance parameter of $R = 0.4$. Particle-level jets are required to have $p_{\mathrm{T}} > 25\,\mathrm{GeV}$ and $|\eta| < 2.5$. The ghost-matching procedure is used to identify particle-level b-jets [448]. Jets may therefore be defined as b-tagged if they contain at least one B-hadron with a $p_{\mathrm{T}} > 5\,\mathrm{GeV}$.

The particle-level selection reflects the selection presented in Section 10.3.1. An additional requirement on the presence of neutrinos is made, stating that exactly one electron neutrino and one muon neutrino must be present, and that each should be the matter–anti-matter counterpart to the electron and muon charged leptons present. For example, an event containing a final-state electron and an anti-muon must also possess an electron anti-neutrino and a muon neutrino. The correct flavour combination of charged lepton and neutrino is used to reconstruct two W-bosons for each event. Top-quarks are reconstructing through a combinatorial pairing of the W-bosons and the b-tagged jets. The correct combination of is assumed to be that pairing which minimises

$$\left|m_{\mathrm{top}} - m(W_1 + b_{1/2})\right| + \left|m_{\mathrm{top}} - (W_2 + b_{2/1})\right|, \tag{10.3.1}$$

with $m(W_X + b_{X/Y})$ the combined invariant mass of a particular W-boson–b-jet combination. In events with only one b-tagged jet, the highest p_{T} non–b-tagged jet is chosen to be the second b-jet.

10.4 Region Definition

Events are categorised into separate regions through selections on particular event parameters. Figure 10.2 illustrates the regions defined in the measurement. The *signal region* (SR) is defined through a selection on $m_{t\bar{t}}$, designed to maximise the number of entangled events whilst accommodating detector resolution effects. Afik and de Nova conjecture that a cut on $m_{t\bar{t}}$ below 500 GeV should yield a value of D below the entanglement limit, provided the systematic uncertainties are sufficiently small. In reality, this measurement is subject to resolution effects, where the $m_{t\bar{t}}$ spectrum is smeared as a consequence of top-quark reconstruction technique (see Section 10.6). For any random event, the reconstructed $t\bar{t}$ pair can obtain an $m_{t\bar{t}}$ value which differs by a non-negligible amount from the truth-level value. This $m_{t\bar{t}}$ smearing necessitates a far tighter selection: $m_{t\bar{t}} < 380$ GeV. Top-anti-top-quark pair production is also subject to additional Coulomb effects which can lead to bound $t\bar{t}$ states being produced close to threshold [449]. A lower cut of $m_{t\bar{t}} > 340$ GeV is included to reduce instances of Coulomb effects, and because the re-weighting procedure, introduced in Section 10.9, requires top-quarks close to on-shell at parton-level.

Two additional *validation regions* are defined with the intention of validating the measurement strategy in different areas of $|Mtt$ phase-space. These are defined using invariant mass windows, 380 GeV $< m_{t\bar{t}} <$ 500 GeV (VR1), and $m_{t\bar{t}} >$ 500 GeV (VR2). In the former, some level of entanglement is expected in the ensemble of $t\bar{t}$ pairs, but significantly diluted over the signal region due to the aforementioned reconstruction inefficiencies. In the latter, high-mass validation region, negligible entanglement should be present. The entanglement marker D is measured in the signal region and both validation regions.

The term *Inclusive Region* is used to refer to the combination of the signal and validation regions. Any event which passes the $e\mu$ selection is contained in this region. The entanglement marker D is not measured inclusively in $m_{t\bar{t}}$ but this region is used for comparison between data and simulation for a variety of other kinematic spectra.

A *control region* (CR) is also defined to estimate the contamination from occurrences in which a jet is mis-reconstructed as a lepton. Such events are known as "fakes", with the mis-identified jet "faking" the desired di-leptonic final-state. The control region is inclusive in $m_{t\bar{t}}$ and requires a same-sign charge electron-muon pair, $e^{\pm}\mu^{\pm}$. This requirement defines a phase-space with a high population of fake events. In this control region, the contamination from $t\bar{t}$ di-leptonic events possessing a lepton with mis-identified charge is small. Estimation of the rate of fake-lepton events is discussed in Section 10.5.2.

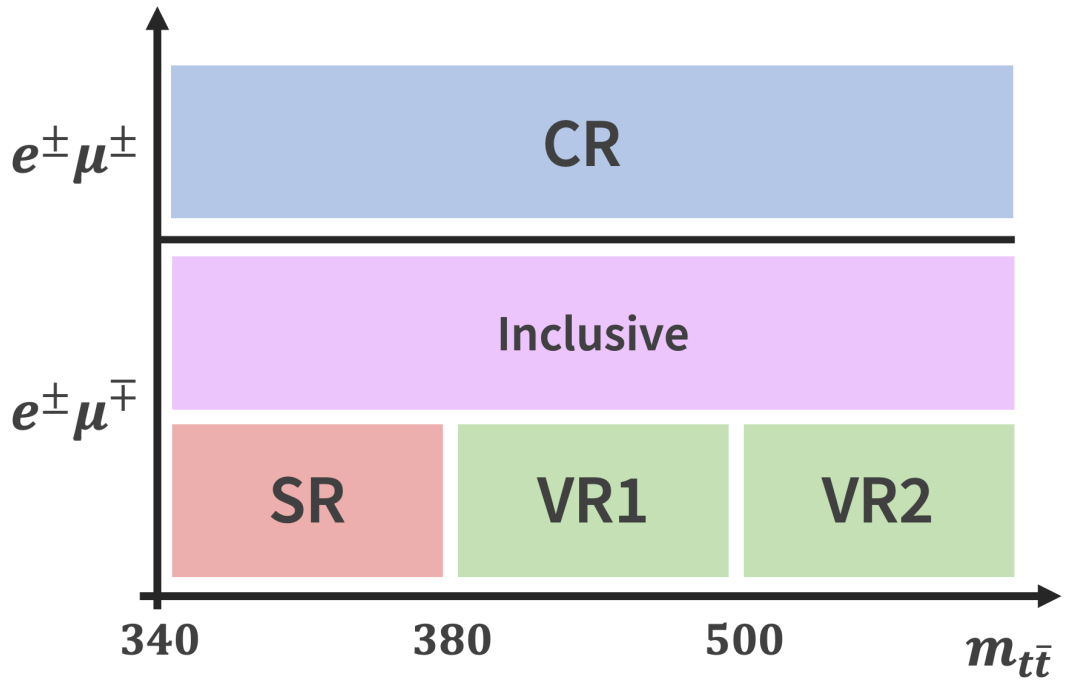

Figure 10.2: The final-state of this measurement is required to have exactly one electron and one muon. Events with opposite-sign electron and muon pair ($e^{\pm}\mu^{\mp}$), with 340 GeV < $m_{t\bar{t}}$ < 380 GeV, fall into the signal region (SR). Two validation regions are defined, also in the $e^{\pm}\mu^{\mp}$ channel, with bounds 380 GeV < $m_{t\bar{t}}$ < 500 GeV (VR1) and $m_{t\bar{t}}$ > 500 GeV (VR2). An inclusive region is defined which is the combination of the signal region and two validation regions. A control region (CR), inclusive in $m_{t\bar{t}}$ but requiring two same-sign leptons ($e^{\pm}\mu^{\pm}$), is also defined. The control region is included to source a data-driven estimation of fake lepton events.

10.5 Estimation of Standard Model Backgrounds

The desired reconstructed final-state can arise from a number of additional processes besides that of $t\bar{t}$ production. Such processes constitute *backgrounds*, with the $t\bar{t}$ production process defining the *signal*. The background processes considered include:

- the production of a single-top quark in association with a W-boson, "single-top production";
- the production of an electroweak boson with additional jets, V + jets;
- the production of pairs of electroweak bosons, $WW/WZ/ZZ$, "diboson production";
- the production of $t\bar{t}$ pairs with an additional heavy final-state, "$t\bar{t}X$".
- 'fake' leptons arising from mis-identification of jets, "fakes".

The number of events pertaining to each of these background modes is estimated through simulation, except the "fakes" background which is estimated through a data-driven method.

10.5.1 Background Modelling

Production of a single top-quark in association with a W-boson, and both s- and t-channel single top-quark production, are all modelled using the Powheg Box V2 event generator at NLO-QCD, with the NNPDF3.0nlo set of PDFs. In the Wt production channel, the five-flavour quark mass scheme is employed, whilst in the s- and t-channel modelling, the four-flavour scheme is used. In all cases, generated events are interfaced to Pythia 8.230 using the A14 tune, and employing the NNPDF2.3lo PDF set, identically to the nominal $t\bar{t}$ production modelling. Interference and overlap of higher-order diagrams with $t\bar{t}$ production diagrams must be accounted for in the case of Wt production. The *diagram removal* scheme, in which specific diagrams are removed at amplitude-level, is used to remove such cases [450]. The *diagram subtraction* scheme, in which the overlapping diagrams are removed at cross-section level, is used to define a systematic uncertainty on this process [444], [450]. This uncertainty is defined in Section 10.10.4.

The production of a vector boson with additional jets is modelled using Sherpa 2.2.11 at NLO in QCD for up two final-state partons. The production of up to four additional partons is modelled using the Comix [451] and OpenLoops libraries [452], [453]. Showering is provided by Sherpa, with the shower-matching achieved through the MEPS@NLO prescription [451]. The NNPDF3.0nnlo PDF set is again employed, and all samples are normalised to a NNLO-QCD prediction of V + jets production [454].

Diboson production is modelled using the Sherpa 2.2.2 generator, which has the benefit of generating amplitudes for a number of final-state partons at NLO in QCD, and several additional partons at LO in QCD. In this manner, fully leptonic and semi-leptonic final-states are modelled by considering up to one additional parton at NLO, and three at LO. Loop-induced processes, $gg \to VV$, are modelled at LO for up to one additional parton in the final-state, for both semi-leptonic and di-leptonic decay channels. The Sherpa matrix element calculations are matched to the Sherpa parton shower, and additional virtual QCD corrections to the matrix-element calculation are provided by the OpenLoops library [452], [453]. The NNPDF3.0nnlo PDF set is used in all cases, along with a custom set of tuned parameters recommended by the Sherpa authors.

The production of $t\bar{t}W$ and $t\bar{t}Z$ events is modelled using MadGraph_aMC@NLO 2.3.3 at NLO-accuracy, with the NNPDF3.0nlo PDF set. Generated events are interfaced to Pythia 8.210 using the A14 tune and the NNPDF2.3lo PDF set. Additionally, the decay of bottom and charm hadrons is simulated using EvtGen 1.2.0. The four-top-quark final state, $t\bar{t}t\bar{t}$, is also modelled with MadGraph_aMC@NLO 2.3.3, this time

employing the NNPDF3.1NLO PDF set. The tuned showering and associated PDF set is identical to the $t\bar{t}W/t\bar{t}Z$ set-up, but in this instance the bottom and charm hadron decays are performed using EvtGen 1.6.0. Finally, the production of $t\bar{t}H$ events is modelled using an identical set-up to that of the nominal $t\bar{t}$ production.

10.5.2 Consideration of Fakes

In simulation, fake leptons can be identified from the event truth-level information. Any simulated events from which pass the reconstruction-level di-leptonic selection and contain at least one fake lepton are considered "fakes". Contributing processes are $t\bar{t}$, single-top-quark and di-boson production. It is known that fake lepton events are poorly described by simulation, therefore an additional data-driven approach is employed to estimate corrections which are applied to the simulation. This correction is derived in the control region, which is designed specifically to be rich in fake-lepton events. The leakage of true signal events into the control region — occurring due to electron charge mis-identification in a $t\bar{t}$ decay — is small. The correction takes the form of a "fake factor", which is a scale factor derived from a comparison between simulation and data. Explicitly, this scale factor is defined as the ratio between what are presumed to be fake-lepton events in data, and what are known to be fake-lepton events in simulation:

$$\mathrm{SF} = \frac{N^{\mathrm{data}} - N^{\mathrm{MC}}_{\text{non-fakes}}}{N^{\mathrm{MC}}_{\text{fakes}}}, \tag{10.5.1}$$

where N denotes number of events. The main assumption is that the scale factors computed in the control region are also valid in the signal region.

In experimental data, the *yield* refers to the total number of events present in some selection. In simulation, yield refers to the predicted number of events, and can be defined for particular processes e.g. separately for the signal process and various backgrounds processes. Yields in the control region are used to compute the fake factor correction. The majority of fake leptons are conjectured to arise due to the mis-identification of jets as electrons at low values of p_{T}. Three separate scale factors are derived, based on three different definitions of N:

- N is the total number of events (inclusive yield).
- N is the number of events meeting the low-p_{T} requirement, $15\,\mathrm{GeV} < p_{\mathrm{T}}(e) < 25\,\mathrm{GeV}$.
- N is the number of events meeting requirement $0 < E_{\mathrm{T}}^{\mathrm{miss}} < 50\,\mathrm{GeV}$.

The yields for the three variables are shown in Table 10.1. The 'fakes' row corresponds to $N^{\mathrm{MC}}_{\text{fakes}}$, the 'data' row to N^{data}, and the remaining rows sum to give $N^{\mathrm{MC}}_{\text{non-fakes}}$. To assign a single fake factor from the three scale factors derived, a value of 1.5 with an

uncertainty of 50 % is chosen. This reflects the spread of the three scale factors, with the uncertainty the difference between the $p_{\mathrm{T}}(e)$ and MET scale factors.

Table 10.1: The observed yields (total number of events) in the control region for three selection requirements: inclusive, 15 GeV $< p_{\mathrm{T}}(e) <$ 25 GeV, $0 < E_{\mathrm{T}}^{\mathrm{miss}} <$ 50 GeV. The chosen fake factor is 1.5 with an uncertainty of 50 %.

Process	Total Yield	$p_{\mathrm{T}}(e)$	MET
fakes	7907.9 ± 88.9	834.6 ± 28.9	3070.7 ± 55.4
$t\bar{t}X$	949.9 ± 30.8	65.2 ± 8.1	228.0 ± 15.1
$WW/WZ/ZZ$	2063.8 ± 45.4	148.7 ± 12.2	1037.4 ± 32.2
$Z+$ jets	105.9 ± 10.3	8.6 ± 2.9	56.8 ± 7.5
tW	370.8 ± 19.3	16.4 ± 4.0	124.5 ± 11.2
$t\bar{t}$	6228.4 ± 78.9	336.9 ± 18.4	1930.3 ± 43.9
Data	20678	1862	9429
Fake SF	1.4	1.5	2.0

10.6 Kinematic Reconstruction of Top-Quarks

The kinematics of the individual top- and anti-top-quarks in $t\bar{t}$ production can be inferred from the kinematics of their respective decay products. This presents several challenges, depending on the decay-channel considered. In the all-hadronic case, the task is correctly identifying which jets in the event correspond to the top-quark and anti-top-quark decay products. This becomes extremely challenging in events with high jet-multiplicities, where additional jets arise due to QCD radiation. In contrast, top-quarks which decay leptonically produce a neutrino whose presence is only inferred in the detector through MET. This presents a problem in the lepton + jets channel, where several methods exist for reconstructing the $t\bar{t}$ kinematics [455], but is most problematic in the di-leptonic channel used in the current measurement.

The top-quark and anti-top-quark kinematics are given in terms of the four-momenta of their decay products:

$$p_t = p_b + p_{l^+} + p_\nu, \tag{10.6.1a}$$
$$p_{\bar{t}} = p_{\bar{b}} + p_{l^-} + p_{\bar{\nu}}, \tag{10.6.1b}$$

where the components of neutrino four-momenta, p_ν and $p_{\bar{\nu}}$, total eight unknowns. The system can be rendered tractable through considering kinematic equations of

constraint, with the particle masses assumed to be known. Explicitly:

$$m_t^2 = (p_b + p_{l^+} + p_\nu)^2 = (p_{\bar{b}} + p_{l^-} + p_{\bar{\nu}})^2 \tag{10.6.2}$$

$$m_W^2 = (p_{l^+} + p_\nu)^2 = (p_{l^-} + p_{\bar{\nu}})^2, \tag{10.6.3}$$

with known m_t and m_W. Additionally, assuming the neutrino masses to be zero, $p_\nu \cdot p_\nu = p_{\bar{\nu}} \cdot p_{\bar{\nu}} = 0$, and using the MET definition, $E_{\mathrm{T}}^{\mathrm{miss}}{}_x = p_{\nu_x} + p_{\bar{\nu}_x}$, $E_{\mathrm{T}}^{\mathrm{miss}}{}_y = p_{\nu_y} + p_{\bar{\nu}_y}$, eight constraint equations exist for the eight unknowns.

The literature provides several exact methods of solution for evaluating the neutrino four-momenta. The "Sonnenschein method" [456] reduces the system to two quadratic equations in $p_{\nu x}, p_{\nu y}$, which are solved analytically[1]. The additional neutrino four-momenta components follow from the above kinematic relationships. The "Ellipse method" [457] solves the same system of equations geometrically, by realising that the W^+ and W^- kinematics are constrained to individual ellipsoids in momentum-space, and that their intersection define two ellipses which constrain the neutrino momenta.

Both the Ellipse and Sonnenschein methods can yield multiple solutions. Only one of these solutions is physical. In such instances, the $t\bar{t}$ pair with lowest $m_{t\bar{t}}$ is always taken to be the physical solution. Additionally, the effects of detector smearing should be incorporated into the Ellipse and Sonnenschein methods such that they can better reconstruct realistic $t\bar{t}$ collider data. To achieve this, artificial smearing is applied to the p_{T} and angular kinematics of electrons, muons and jets, using smearing functions derived from a comparison of truth- and reconstruction-level simulation generated by MadGraph_aMC@NLO[2]. Smearing functions are applied 100 times to each kinematic quantity.

By way of contrast, the NeutrinoWeighter method [458] is an approximate numerical method which does not strictly solve for the unknown neutrino four-momenta. Instead, the method estimates the neutrino pseudorapidity, η_ν, by sampling from corresponding η_ν distributions generated from Powheg + Pythia NLO-QCD $t\bar{t}$ production. Crucially, these distributions are independent of the underlying spin structure [459] of the $t\bar{t}$ production. The remaining neutrino four-momenta components are solved using the constraint equations as before. Each sampled solution is ascribed a weight w, defined as:

$$w = \exp\left(\frac{-\Delta E_x^2}{2\sigma_x^2}\right) \cdot \left(\frac{-\Delta E_y^2}{2\sigma_y^2}\right), \tag{10.6.4}$$

where $-\Delta E$ is the difference between observed MET and the MET of the calculated solution, and $\sigma_{x/y}^2$ is the resolution on the MET, as measured in $\sqrt{s} = 7$ TeV data and compared to simulation [460]. The final neutrino momentum is the solution with the

[1] The method of resultants is used to re-write these as a univariate equation of degree four in $p_{\nu x}$.

[2] The ratio of the truth-level to the reconstruction-level kinematic distribution is constructed, and sampled stochastically to yield a scale factor, which is then applied to the kinematic in question.

highest weight. The NeutrinoWeighter method has been used extensively in several measurements of top-quark properties since its discovery [39], [458]. No kinematic smearing is applied to the NeutrinoWeighter procedure, as detector smearing effects are considered to be included in the sampled η_ν distributions.

The Ellipse method is found to have superior accuracy over the Sonnenschein method. The NeutrinoWeighter algorithm can achieve superior accuracy when the number of sampled solutions is high, but at considerable computational expense. The NeutrinoWeighter implementation chosen samples the η_ν distributions 10 times to avoid excessive computation time; in this guise its reconstruction accuracy is less than that of the Ellipse method. The Ellipse method is therefore chosen as the nominal reconstruction technique; however, it is hampered by the fact that it only derives real solutions in around 85 % of the $t\bar{t}$ events considered, a symptom of particular final-state kinematic configurations which conspire to yield occasional complex solutions. The Sonnenschein method is found to fail in each instance where the Ellipse method does. The NeutrinoWeighter method is therefore implemented in cases where the Ellipse method fails. This takes the total number of reconstructable events to 90 %, but all described techniques are found to fail for around 10 % of $t\bar{t}$ events. In such instances, a crude approximation of the top- and anti-top-quarks' kinematics is derived through the following procedure: both charged leptons are paired to the b-tagged jet closest to them, and the MET is split evenly between the constructed two lepton-jet pairs. In this manner, all simulated $t\bar{t}$ events can be reconstructed, such that the $\cos\varphi$ observable can be defined for every event.

10.6.1 Transforming into the Parent Tops' Reference Frames

The leptonic decay products of the $t\bar{t}$ pair have 4-momenta $p_l^\pm$ defined in the laboratory frame, in which the spatial components are defined with respect to the standard ATLAS coordinate system, Section 4.2.1. The 3-momenta $\hat{\mathbf{l}}^+, \hat{\mathbf{l}}^-$, which define $\cos\varphi = \hat{\mathbf{l}}^+ \cdot \hat{\mathbf{l}}^-$, are defined in the individual rest frames of the parent top-quark and anti-top-quark. These reference frames are defined from Lorentz transformations from the $t\bar{t}$ centre-of-mass reference frame, in which the spin density matrix formalism is defined. It is therefore necessary to boost the lepton 4-momenta $p_l^\pm$ first to the $t\bar{t}$ centre-of-mass frame, and then individually to their respective parent rest frames; boosting directly to the individual top-quark rest frames results in an incorrect Wigner rotation [461].

10.7 Agreement Between Simulation and Data

Various kinematic spectra are constructed for final-state objects in data events which pass the reconstruction-level selection detailed in Section 10.3.1. The analogous observables are then extracted from MC-simulated events for both the $t\bar{t}$ signal process and all backgrounds. A comparison can then be made between the data and the simulation, and the quality of the modelling assessed[3]. The entire suite of systematic uncertainties, presented in Sections 10.10.2 and 10.10.3, is included for each of the observables presented below. The binning of each observable is arbitrary, with the exception of $m_{t\bar{t}}$ and $\cos\varphi$. In the former case, the first two bins correspond to the signal region and validation region 1, with validation region 2 further split into several bins. The $\cos\varphi$ distribution is defined in eight bins through this measurement. Unless otherwise stated, each observable is constructed from all events in the inclusive region.

Figure 10.3 presents the data-simulation agreement for reconstructed leptons, namely electron p_{T} in Figure 10.3a and muon η in Figure 10.3b, The latter shows good agreement. The observed slope in the electron p_{T} is a well-known feature of event generation, where missing higher-order corrections to the top-quark cross-section manifest as a harder p_{T} prediction than is observed in the data, for both the top-quark and its decay products. The same feature is visible in Figure 10.4a which shows the p_{T} of all b-tagged jets. The number of b-tagged jets, known as "b-tagged jet multiplicity", is shown in Figure 10.4b.

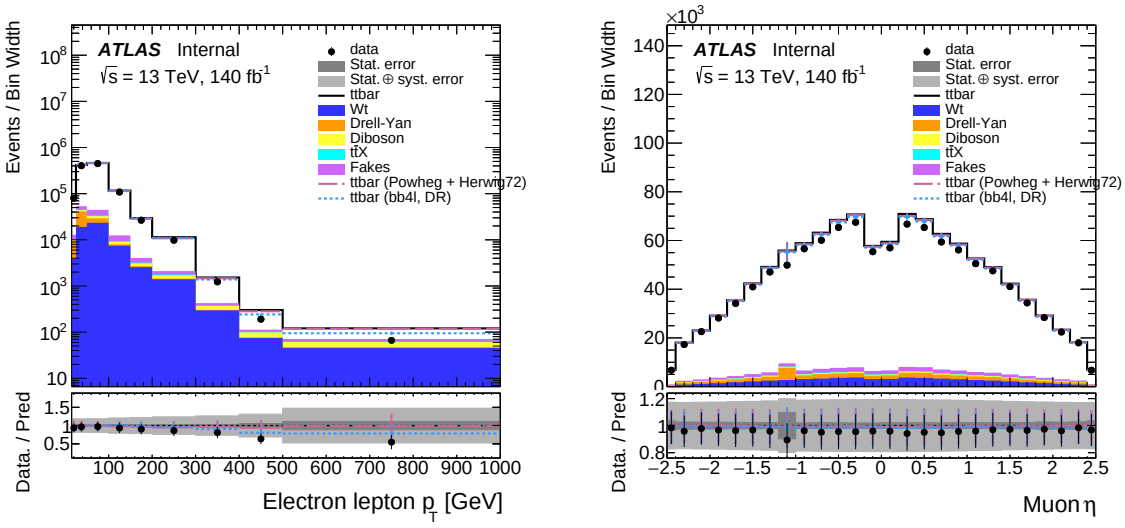

(**a**) Electron p_{T} (**b**) Muon η.

Figure 10.3: Data-simulation agreement for leptonic kinematics

[3]Additionally, simulated differential cross-sections predictions which differ drastically from the observed data may indicate the absence of some background process

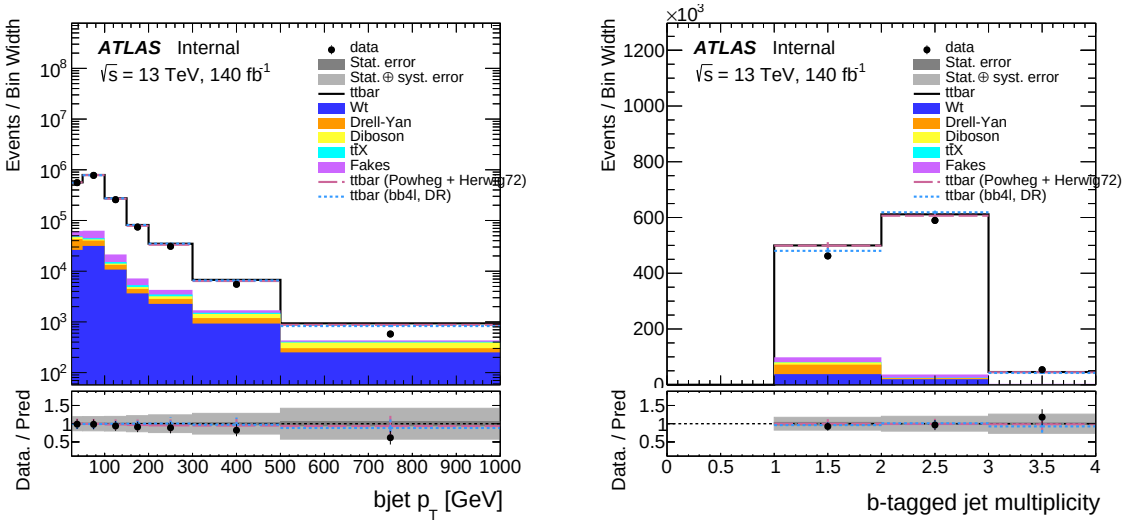

(**a**) b-jet p_{T}. (**b**) Number of b-jets.

Figure 10.4: Two b-jet observables, showing reasonable data-simulation agreement.

Comparison of simulated top-quark and $t\bar{t}$ kinematics to data not only assesses the quality of the modelling, but also the performance of the $t\bar{t}$ kinematic reconstruction methods. Figure 10.5 presents the following distributions in data and simulation: the top-quark p_{T} in Figure 10.5a, the p_{T} of the $t\bar{t}$ pair in Figure 10.5b, and the $m_{t\bar{t}}$ of the $t\bar{t}$ in Figure 10.5c, which is an important observable in this particular measurement. Additionally, the effect of bin-to-bin migrations in $m_{t\bar{t}}$ is estimated by constructing a migration matrix for the signal simulation. This is shown in Figure 10.6.

Figure 10.7 shows the important distribution, $\cos\varphi$, in the inclusive region. The various background contributions are shown, and the agreement between data and simulation is reasonable. Superior agreement would be reached through better modelling of $t\bar{t}$ production, and better top-quark reconstruction techniques. A detailed discussion on this matter is presented in Section 10.12.

The expected event yields in simulation for the signal and background processes are tabulated in Table 10.2, for the inclusive, signal, and validation regions. The individual process yields are totalled to give the simulation expectation yield. The data yield, and the ratio of data-to-simulation, are also presented. It is seen that the agreement between data and simulation is strongest at lower values of $m_{t\bar{t}}$ but agrees well across the phase-space.

10.7.1 Comparison of Data to Alternative Simulations

A comparison is also made between different event generators. In Figure 10.8, on the left of each figure, the $\cos\varphi$ distribution in data is presented along with the predictions

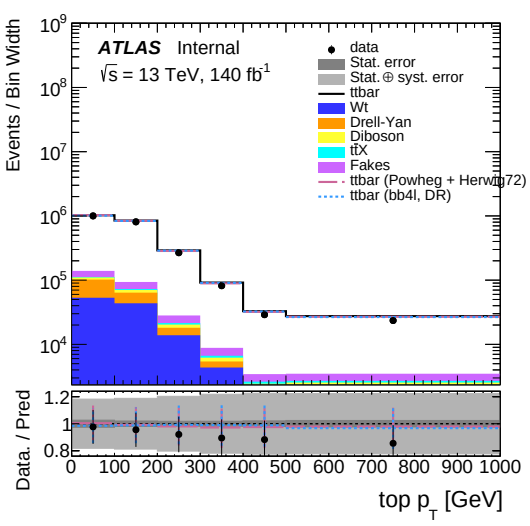

(**a**) Top-quark p_{T}.

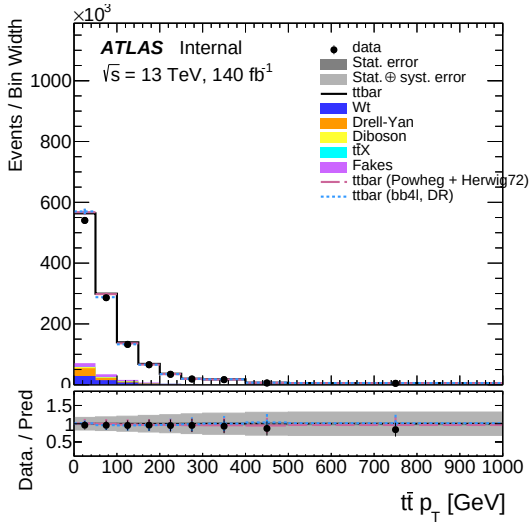

(**b**) Top-anti-top-quark pair p_{T}.

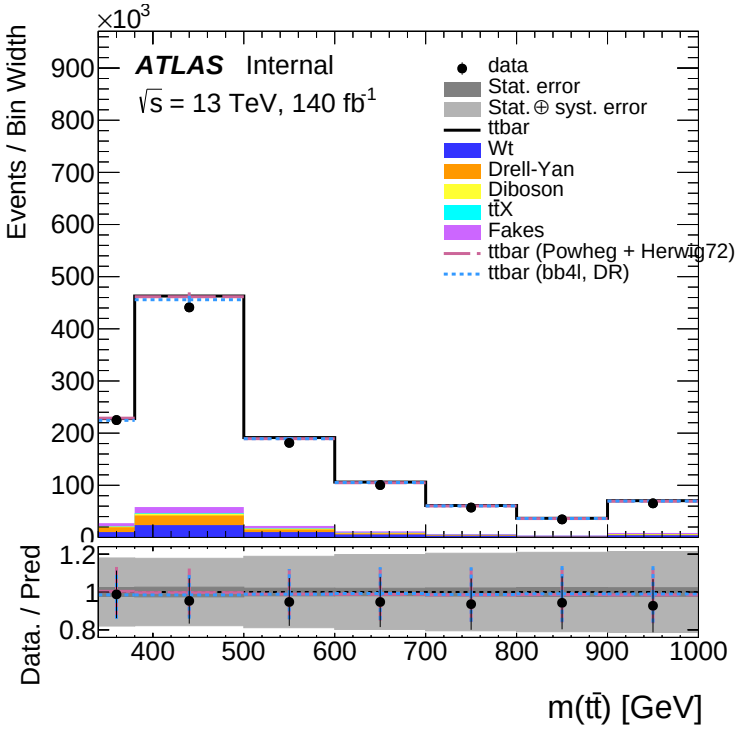

(**c**) $m_{t\bar{t}}$.

Figure 10.5: The data-simulation agreement for several top-quark or *ttbar*-related observables.

from the nominal simulation and two alternative event generators. One observes that in all cases, the agreement between data and all three simulated predictions is strong for $\cos\varphi$ distribution: all predictions match the data well in all bins, with the exception of $[0.75, 1.0]$ bin (the right-most bin as displayed in the plots) in both validation regions, where all predictions over-estimate this bin yield with respect to the data. The right portion of each figure presents the entanglement marker D as extracted from the mean

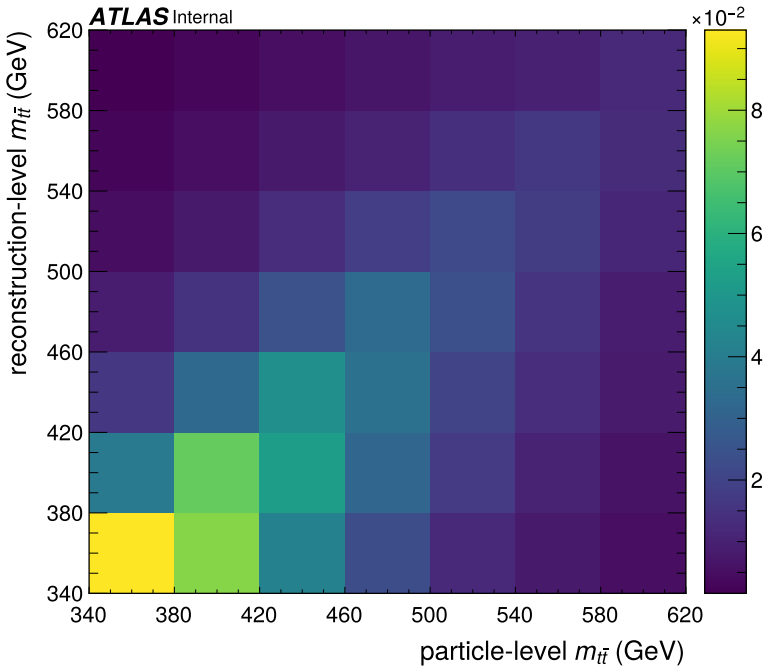

Figure 10.6: Migrations in simulated $m_{t\bar{t}}$ between particle-level and reconstruction-level. The migration matrix is normalised by the total number of events passing the selection, with an upper bound of $m_{t\bar{t}} \leq 620\,\text{GeV}$, chosen so as to focus primarily on migrations in the SR and VR1.

of each distribution. A greater variation is visible than when comparing the $\cos\varphi$ distributions, as shown in the ratio-to-data portion of the figure. (Note that the $\cos\varphi$ ratio-to-data plot and the entanglement marker D ratio-to-data plot have different y-axis scales.) In particular, the entanglement markers in the signal region show significant variation between the three theoretical predictions, and each prediction is an overestimation when compared to the data. Note that the entanglement marker shown here is defined at reconstruction-level, and not yet subject to detector corrections which form the next sections of this chapter. Nevertheless, a general impression is formed that a greater variation between measured and predicted entanglement marker D is found in the signal region than either validation regions, with the data at reconstruction-level supporting a stronger entanglement hypothesis than any simulation model predicts.

10.8 Unfolding Efforts

The $\cos\varphi$ distribution, and the entanglement marker D, are both distorted away from their true shape or value by detector effects. Emulating these detector distortions was the main focus of research in Chapter 7. In this instance, the detector distortions must

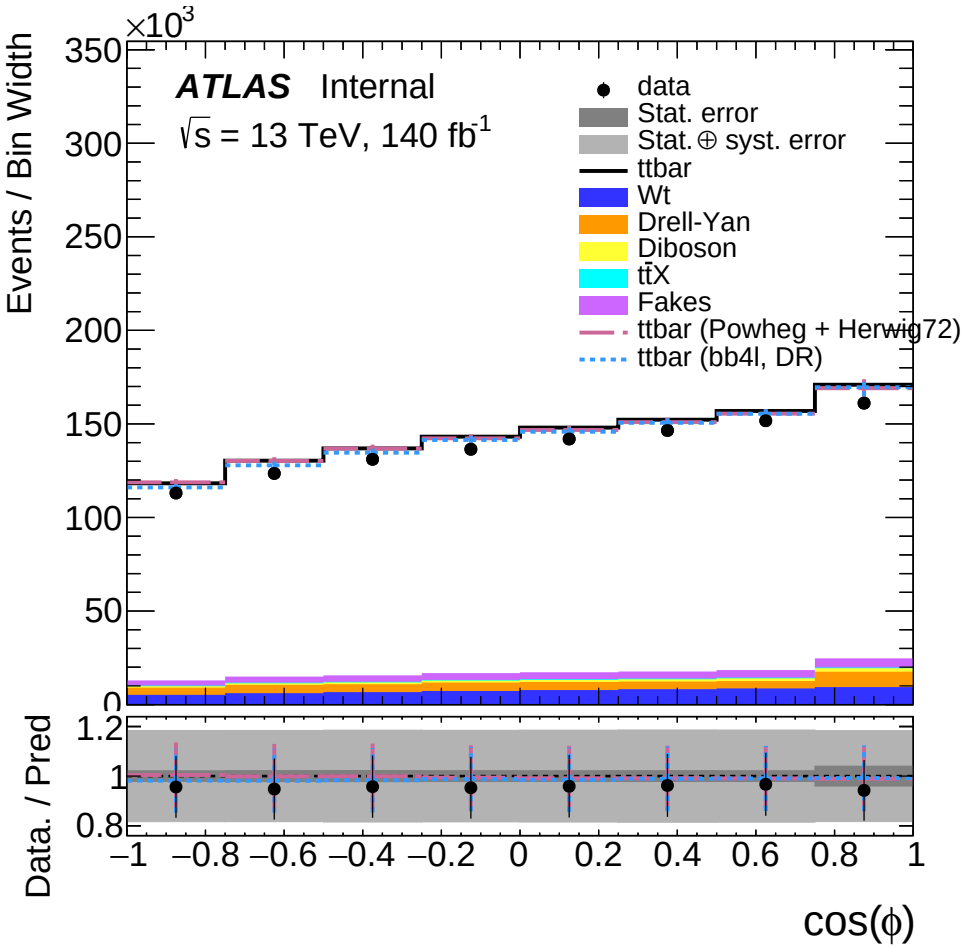

Figure 10.7: The data-simulation comparison for the $\cos\varphi$ distribution in the inclusive region, with a full breakdown of the background contributions.

be removed in order to compare any entanglement measurements with theoretical predictions or equivalent measurements from other experiments. This is the task of *unfolding*: estimating the underlying truth parameters X_i from the measurement Y_i in the language of equation 7.3.2. This is really a question of inverting the migration matrix R_{ij} in 7.3.2, and numerous methods of varying complexity exist in the literature to achieve this.

Initial attempts to mitigate the detector distortions focused on unfolding the measured distribution $\cos\varphi$ to the truth-level distribution $\cos\varphi^{(U)}$, with superscript (U) standing for "unfolded". The *Iterative Bayesian* unfolding (IBU) technique was attempted [462], as implemented in the RooUnfold package [463]. The total number of events in each bin X_i of the distribution in question is given by:

$$X_i = \frac{1}{f_i^{\text{eff}}} \sum_j M_{ji}^{-1} f_j^{\text{acc}} Y_j. \tag{10.8.1}$$

Table 10.2: The yields of the various simulated signal and backgrounds processes are presented. The total expectation yield from the sum of all simulated processes, the measured data yield, and the ratio of the former to the latter, are also given. For simulation yields, the MC statistical uncertainty is also shown.

Process	Inclusive	340 – 380 GeV	380 – 500 GeV	> 500 GeV
$t\bar{t}$	1030000 ± 40000	202000 ± 8000	408000 ± 16000	417000 ± 17000
tW	59800 ± 1100	10330 ± 200	23800 ± 500	25700 ± 500
Z+jets	38000 ± 4000	9300 ± 400	19000 ± 4000	9730 ± 270
$WW/WZ/ZZ$	9140 ± 340	1320 ± 50	3280 ± 120	4540 ± 170
$t\bar{t}X$	2959 ± 6	437.7 ± 2.1	1080.1 ± 3.4	1441 ± 4
fakes	17700 ± 8900	3600 ± 1900	7100 ± 3800	7000 ± 3700
Expectation	1150000 ± 40000	227000 ± 8000	462000 ± 17000	466000 ± 17000
Data	1105403	225056	441196	439151
data/MC	0.96 ± 0.03	0.99 ± 0.04	0.95 ± 0.04	0.94 ± 0.04

Each reconstruction-level bin value Y_j is the difference in the the number of events in bin j between the data and the total background: $Y_j = \left(N_j^{\text{data}} - N_j^{\text{bkg}}\right)$. The migration matrix M_{ji} accounts for detector smearing effects, where events migrate to different bins at reconstruction-level from their truth-level position. The correction factors f_i^{eff} and f_j^{acc} are the efficiency and acceptance factors, respectively, defined in Section 7.2.

The method applies Bayes theorem, introduced in Chapter 8 in the context of Bayesian inference, to the distribution $\cos\varphi$, to compute the inverse migration matrix M_{ji}^{-1}. In the context of binned unfolding, Bayes' theorem may be written:

$$P\left(X_i \mid Y_j\right) = \frac{P\left(Y_j \mid X_i\right) P\left(X_i\right)}{\sum_k P\left(Y_j \mid X_k\right) P\left(X_k\right)}, \tag{10.8.2}$$

with $P\left(X_i \mid Y_j\right)$ the probability of some event reconstructed in bin j originating from bin i. The prior, $P\left(X_i\right)$, is some initial distribution which corresponds to a "guess" of the underlying distribution, $\cos\varphi^{(0)}$. The result of the first iteration, $\cos\varphi^{(1)}$, becomes the prior for a second application of the procedure, and the process is repeated for some m iterations, at which point $\cos\varphi^{(m)} \equiv \cos\varphi^{(U)}$. The number of iterations chosen,

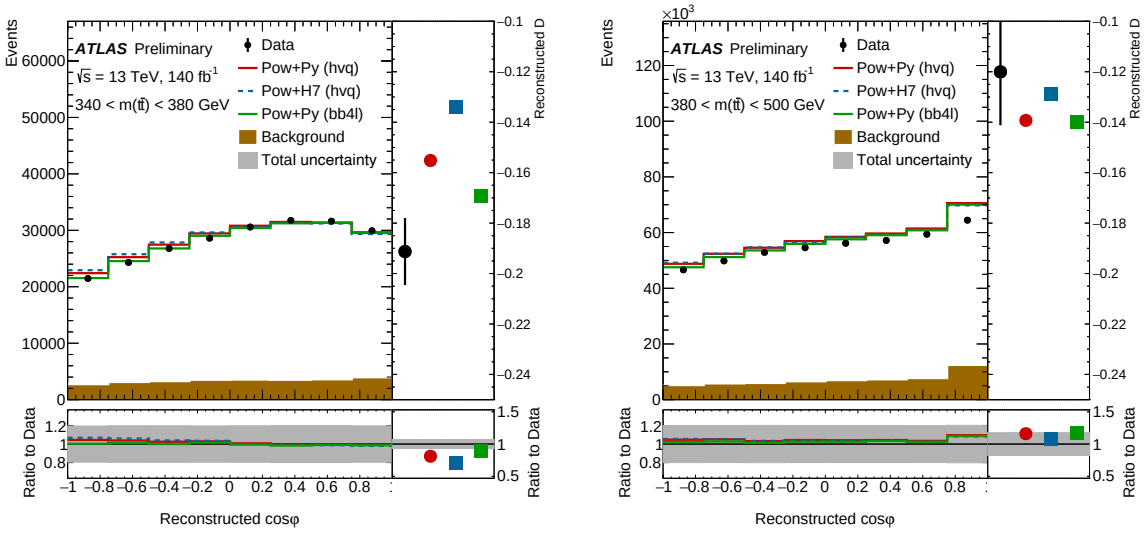

(**a**) signal region (**b**) validation region 1

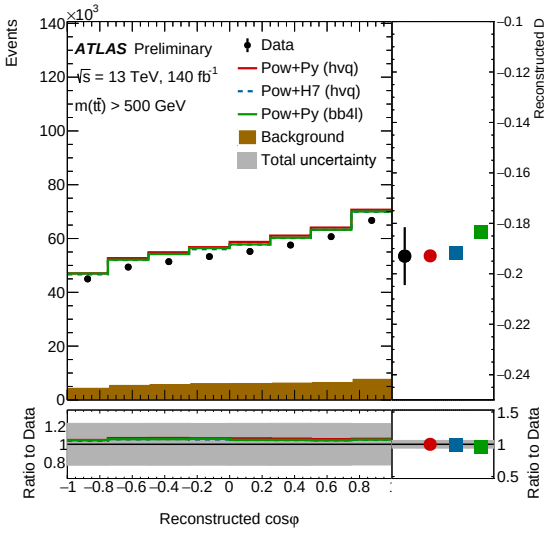

(**c**) validation region 2

Figure 10.8: Comparisons between data and three different event generators: Powheg + Pythia8 , Powheg + Herwig 7.2, Powheg + Pythia(bb4l), for distribution $\cos\varphi$ and entanglement marker D. Agreement between data and simulation is generally strong for the $\cos\varphi$ distribution in all Signal and validation regions, with the exception of the right-most bin in the two validation regions. Agreement is less strong for entanglement marker D, with the greatest variation occurring in the signal region, where there is considerable spread between the three theoretical predictions, all of which over-estimate the value of D compared to the data.

m, also controls the degree of regularisation[4]. The truth-level MC distribution, $\cos\varphi^{(T)}$, was chosen as the initial prior.

[4]Regularisation is a form of simplification often employed in ill-posed or inverse-type problems, of which unfolding is a typical example.

10.8.1 Testing for Bias in the Unfolding

Prior to unfolding the measured data distribution $\cos\varphi$, the unfolded methodology must be tested on simulation. This is done by using the reconstruction-level simulated distribution $\cos\varphi^{(R)}$ as an input, and attempting to recover the underlying truth-distribution $\cos\varphi^{(T)}$. The unfolding procedure must be checked for bias, such that if the distribution in data turns out to differ drastically from the $\cos\varphi^{(R)}$ simulation prediction, one can be confident that the unfolding still deliver the true underlying distribution. Bias can enter the procedure through the migration matrix, which is central to all binned unfolding methodologies including IBU. The migration matrix is derived from a comparison between truth-level and reconstruction-level simulation i.e. it is constructed from considering the bin-to-bin migrations between distributions $\cos\varphi^{(T)}$ and $\cos\varphi^{(R)}$. These MC-simulated distributions are derived from event generators which assume the Standard Model as the underlying physical model; if some alternative (new) physics model alters the measured $\cos\varphi$ distribution, the implicit SM assumption in the unfolding procedure may present a problem.

The *stress test* method constitutes a check for such biases. The distribution of $\cos\varphi$ is always a straight line characterised by slope $D/2$, and so any physical NP effects would manifest only as a change in this slope. Changes in the shape of the $\cos\varphi$ distribution from NP effects are not possible. A set of stress tests were therefore implemented which consisted of altering the slope of the $\cos\varphi^{(R)}$ and $\cos\varphi^{(T)}$ distributions, then unfolding the altered $\cos\varphi^{(R)}$ distribution through the IBU method, and comparing the result to the altered $\cos\varphi^{(T)}$ distribution. Significant difference between the two is an indicator of possible bias. Alterations of the $\cos\varphi$ distribution slopes were implemented by re-weighting each simulated event, which amounts to multiplying the MC event weight by some numerical factor. In the case of these stress tests, this factor was given by a simple linear re-weighting in $\cos\varphi$:

$$w = 1 + K\,(\cos\varphi - 1)\,, \tag{10.8.3}$$

with K a chosen scale factor. Slope changes corresponding to K-values of 5, 10, 15 and -10 were applied. The results of the stress tests are shown in Figure 10.9, which presents the ratio $\cos\varphi^{(U)}/\cos\varphi^{(T)}$ in the inclusive regions (left) and signal region (right). The ratio $\cos\varphi^{(U)}/\cos\varphi^{(T)}$ should be very close to unity for unfolding procedures which are unbiased. Such is the case in the inclusive unfolding tests 10.9a, where deviations from unity are of the order of one percent. Contrastingly, significant deviations from unity are present when the stress test is applied to the signal region $\cos\varphi$ distribution, 10.9b, with the deviations increasing as the value of K increases. This corresponds to an increased level of bias as one distorts the $\cos\varphi$ distributions further from their expected SM forms.

The implemented unfolding procedure is therefore unable to return the true distribution when the slope of the $\cos\varphi$ distribution differs significantly from the predicted

SM value. This represents a serious problem. One cannot now be confident that the true distribution can be resolved, should the measured $\cos\varphi$ distribution look markedly different from the SM. This unfolding bias can in principle be ameliorated through adding in bias corrections, though such corrections are often felt to be undesirable. The decision was made that unfolding the $\cos\varphi$ distribution is untenable.

It is interesting to consider why a bias is present in this unfolding, when many other measurements of $t\bar{t}$ differential cross-sections are untroubled by such problems. It is important to point out that the problems are not connected with the IBU procedure. Instead, the biases are a result of poor resolution of the $m_{t\bar{t}}$ spectrum, and are exaggerated in this measurement because very tight selections are imposed on this parameter. Each event's value of $m_{t\bar{t}}$ is ultimately derived from the top-quark kinematic reconstruction procedure. It is now seen that the methods presented in Section 10.6 are not able to reconstruct this distribution closely enough to the true distribution. In other words, smearing of the reconstructed $m_{t\bar{t}}$ spectrum leads to a non-diagonal migration matrix which is fed directly into the unfolding. This has implications when the event selections are applied at truth-level and reconstruction-level, but such effects are essentially negligible in measurements of $t\bar{t}$ kinematics which do not apply such a strict $m_{t\bar{t}}$ selection. Unfolding kinematic spectra in this narrow threshold-region of the $m_{t\bar{t}}$ phase-space is now seen to present a difficult challenge; one which may ultimately be tackled through a combination of improved top-quark reconstruction techniques, and development of unfolding methods. See Section 10.12 for an further discussion.

10.9 The Calibration Curve

Obtaining an unfolded $\cos\varphi$ spectrum appears to be unattainable. Salvation lies in realising that a truth-level $\cos\varphi$ distribution is not strictly required to observe entanglement in the $t\bar{t}$ system: only the value of entanglement marker D is required, corrected for detector effects. The *calibration curve* method is proposed as an alternative technique which parameterises the relationship between two different definitions of D. For example, $D^{(R)}$ and $D^{(T)}$ could represent D as defined at reconstruction-level and truth-level, with the calibration curve a parameterisation of how one varies with the other. This technique essentially amounts to the unfolding procedure reduced to the zero-dimensional case: the estimation of a single parameter based on a derived relationship — the calibration curve — between two definitions of D. The calibration curve is constructed by considering the nominal pair $\left(D^{(T)}, D^{(R)}\right)$ as computed through simulation, plus a set of alternative hypotheses $\{D_i^{(T)}, D_i^{(R)}\}$, also derived from simulation. The curve is found through interpolation, and using it, one can map a value of D from reconstruction-level to truth-level. Figure 10.10 provides a cartoon illustration of an example calibration curve, showing how a set of different hypotheses generate a set of points $\{D_i^{(T)}, D_i^{(R)}\}$ which form the curve. A measurement D (as indicated by

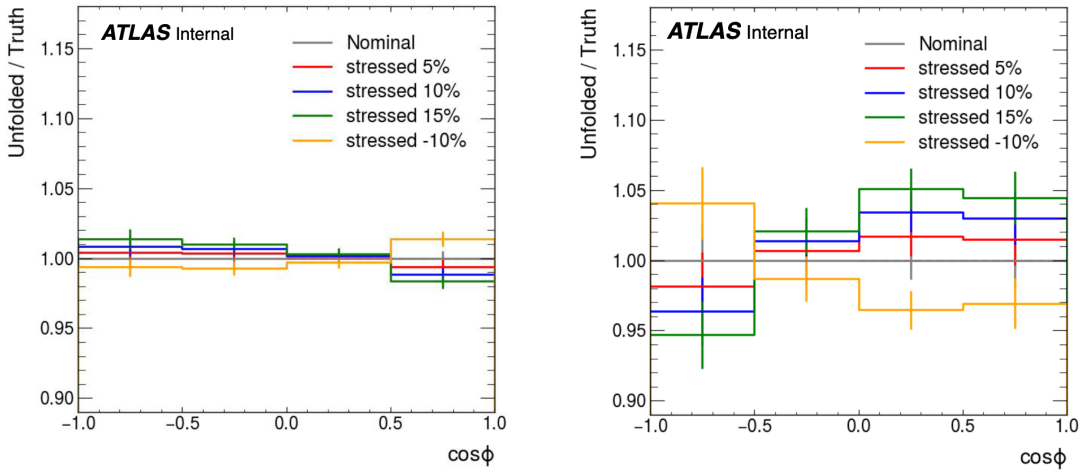

(**a**) (**b**)

Figure 10.9: Stress tests are performed to validate the unfolding procedure against a bias towards the SM. Both plots show the ratio of the unfolded distribution over the truth-level distribution, $\cos\varphi^{(U)}/\cos\varphi^{(T)}$, which should be close to unity in the case of unbiased unfolding. (**a**) In the inclusive $m_{t\bar{t}}$ phase-space, the unfolding procedure is shown to be essentially unbiased. (**b**) In the signal region, the unfolding induces significant biases towards the SM result. These biases increase as the $\cos\varphi$ distribution is stressed further away from the SM expectation.

the orange arrow) can then be mapped to a truth-level value $D^{(T)}$ with an associated uncertainty.

The calibration curve is used to obtain a fiducial particle-level value of D, using the following procedure. The calibration curve is constructed using reconstruction-level and particle-level simulation for a number of hypotheses, using a re-weighting of the $\cos\varphi$ distribution discussed in Section 10.9.1. The measured $\cos\varphi$ distribution is found from data, and the expected background contribution subtracted. Entanglement marker D is found from $-3\langle\cos\varphi\rangle$, and corrected using the calibration curve to yield a particle-level nominal result. Alternative calibration curves are defined for each source of systematic uncertainty, as discussed in Section 10.10. The results of the measurement are presented in Section 10.11. This full calibration curve procedure is implemented independently for the signal region, validation region 1 and validation region 2.

The "entanglement limit" of $D < -1/3$ is defined at parton-level, and since the presented measurement corrects the observed D to particle-level, the entanglement limit must also be converted into the particle-level phase-space. An additional calibration curve is used for this conversion, built analogously to the particle-level–reconstruction-level curve, but using parton-level and particle-level event definitions. At particle-level, objects in the event have been showered and hadronised using the Pythia or Herwig generators. It is therefore prudent to include a set of modelling uncertainties on the

parton-level–particle-level entanglement limit correction. This is done by building a different calibration curve for each individual modelling uncertainty. The parton shower uncertainty is omitted, for reasons which are discussed in Section 10.12.2. Pythia is the nominal tool used to model the parton shower and hadronisation of $t\bar{t}$ events in the ATLAS top-quark community, and has a larger prescription of uncertainties than does Herwig. Therefore, modelling uncertainties are included for the Powheg + Pythia entanglement limit but not the Powheg + Herwig limit.

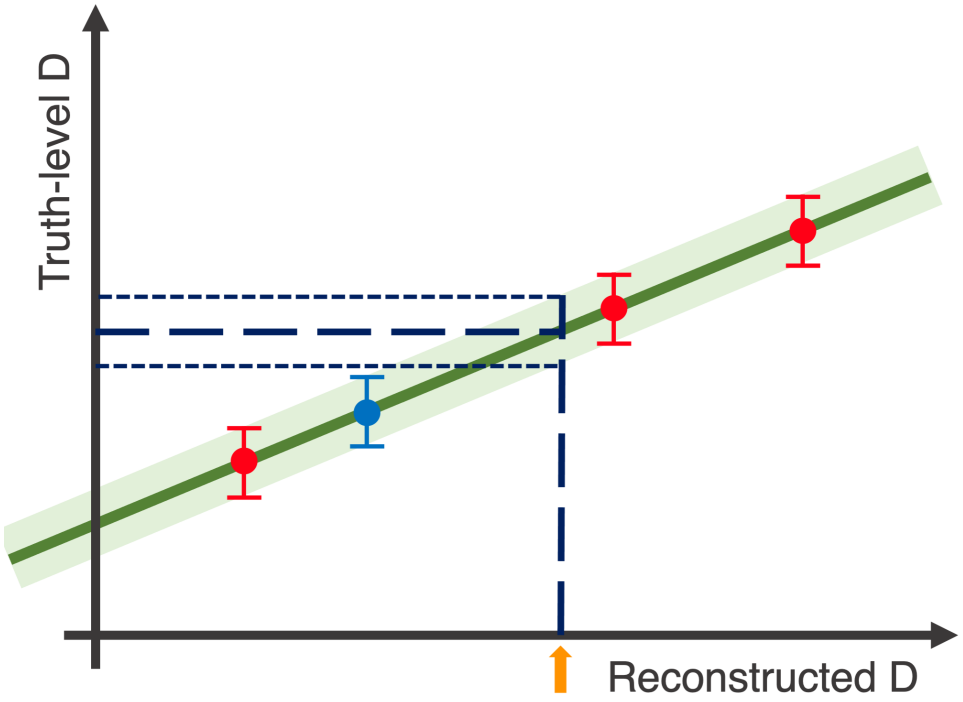

Figure 10.10: A cartoon example of a calibration curve. The blue dot indicates the nominal SM prediction as found in simulation, evaluated at reconstructed-level (x-axis) and some truth-level y-axis. The red dots then indicate alternative values of $\left(D^{(T)}, D^{(R)}\right)$, derived from simulation under some alternative hypothesis. The relationship between the points is parameterised through linear interpolation to give a linear calibration curve, the dark green line. Similarly, each individual systematic considered at each re-weighting point, giving N additional calibration curves for N systematics. This defines an uncertainty band around the central value calibration curve (the light green band around the dark green line), and the total uncertainty at each point is indicated by the vertical "uncertainty bands". A possible measured value of D is given by the orange arrow. The long dashed navy lines show how the calibration curve maps this value into the truth-level space, and the short-dashed lines indicate the total uncertainty associated with the central value $D^{(T)}$.

10.9.1 Deriving the Calibration Curve: Re-weighting cos ϕ

The calibration curve is constructed from different values of D at truth- and reconstruction-level. Each pair of alternative hypothesis values, $\left(D_i^{(T)}, D_i^{(R)}\right)$, could in principle be derived from MC-simulated samples generated with the new hypothesis as an input. Unfortunately, the entanglement marker D is not an input to general-purpose event generators; indeed all event generators implicitly assume a particular value of D in their expressions for the $t\bar{t}$ scattering amplitude, because the phenomenon of entanglement is built in to the underlying field theory. Thus D is not something which can be altered at a generator level. Instead, the value of D can be changed through a re-weighting of each generated event. Events are re-weighted at parton-, particle- and reconstruction-level. The parton-level is used only to check the behaviour of the cos φ distribution under re-weighting, whilst the particle- and reconstruction-level values are used in the calibration curve construction.

The question is then how to formulate a meaningful re-weighting procedure. The entanglement marker D is proportional to the slope of the cos φ distribution. A desirable re-weighting procedure would alter each event's kinematics in such a way that the cos φ distribution remains linear, and that the slope of the distribution changes linearly as a function of some re-weighting variable. It should be understood that this re-weighting is an artificial process, similar to that applied in the stress tests described in Section 10.8.1.

A re-weighting procedure is selected which scales each event's generator weight such that the linearity of the cos φ distribution is maintained at all times. The re-weighting is a linear function of $m_{t\bar{t}}$, cos φ, and a scaling parameter K, meeting the requirements set out above. Each event's re-weighting factor is given by:

$$w = \frac{1 - K \cdot D\left(m_{t\bar{t}}\right) \cos\varphi}{1 - D\left(m_{t\bar{t}}\right) \cos\varphi}. \tag{10.9.1}$$

The terms $D\left(m_{t\bar{t}}\right)$ are the entanglement marker D parameterised as a function of $m_{t\bar{t}}$, and evaluated per-event. The functional form of $D\left(m_{t\bar{t}}\right)$ is found through a fit to MC-simulated events as:

$$D\left(m_{t\bar{t}}\right) = \sum_{i=0}^{3} \frac{a_i}{m_{t\bar{t}}^i}, \tag{10.9.2}$$

with coefficients a_i the free parameters in the fit. In evaluating particular modelling uncertainties, different event generators are employed, as is discussed in Section 10.10.2. When considering modelling systematic uncertainties, the distribution $D\left(m_{t\bar{t}}\right)$ is generated and fitted separately for each generator configuration used, leading to different numerical value for a_i. This means the computed weight w will differ between generators for events with identical kinematics.

The $\cos\varphi$ distribution is re-weighted event-by-event using 10.9.1 with four separate values of K: $K = 0.4, 0.6, 0.8, 1.2$, corresponding to altering the $\cos\varphi$ distribution slope (and thus the value of D) by -60 %, -40 %, -20 % and +20 %, respectively. This defines five separate hypotheses for $\left(D_i^{(T)}, D_i^{(R)}\right)$: the SM expectation and the four re-weighted points, giving five points to which the calibration curve can be fitted. The parton-level $\cos\varphi$ distribution in the signal region is shown in Figure 10.11 (black), along with the four re-weighted distributions. The $\cos\varphi$ distributions remain linear under the re-weighting by construction. The parton-particle entanglement limit calibration curve is generated using the same values of K.

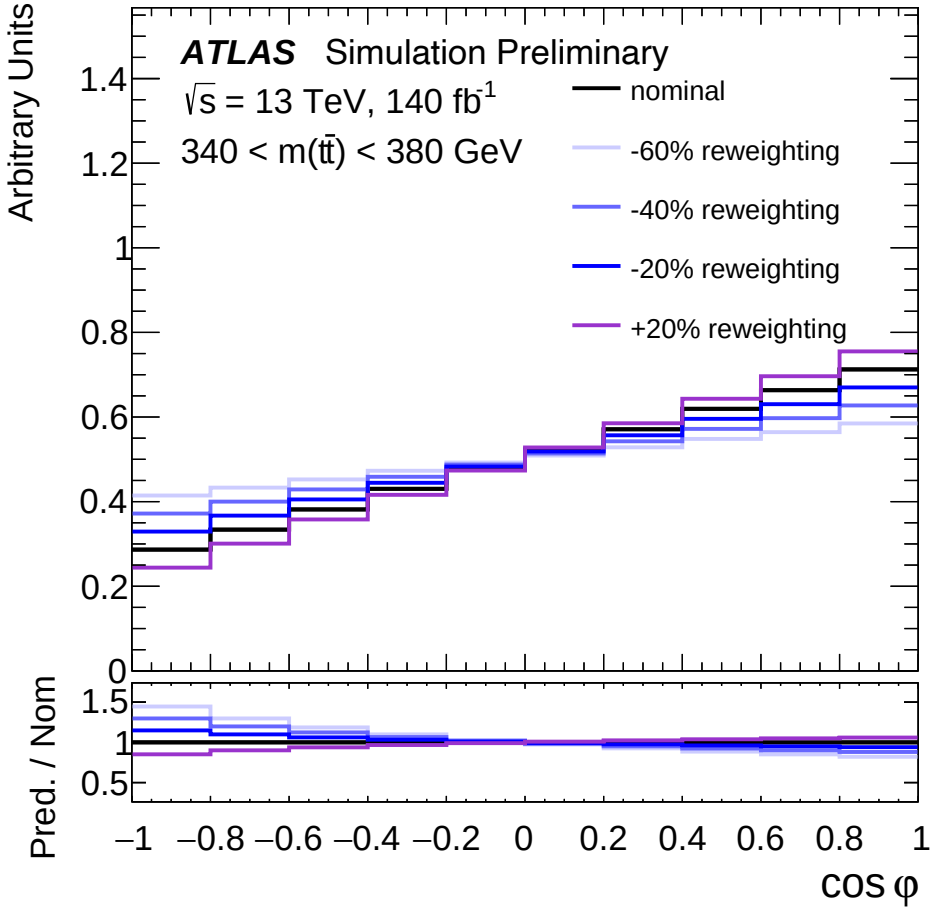

Figure 10.11: The re-weighted $\cos\varphi$ in simulation, for a number of different K factors, defined at parton-level. The distribution retains its linearity under the specified re-weighting prescription.

10.10 Uncertainties

A large set of systematic uncertainties are included in the measurement to cover lack of precise knowledge about factors including the ATLAS detector, the reconstruction techniques used and the modelling of signal and background processes. Each source of systematic uncertainty will alter the $\cos\varphi$ distribution, leading to a shift in the unweighted, SM prediction point $(D^{(T)}, D^{(R)})$. Therefore, for each source of systematic uncertainty, a new calibration curve is created. This involves applying the re-weighting procedure (used to generate the calibration curve) for every single systematic uncertainty. The background-subtracted value of D, $D^{\text{D-B}}$, is then corrected using that particular systematic calibration curve, giving a systematic-shifted value D'. Most uncertainties are then defined as the difference between the nominal D result and the systematic-shifted value D'. Many uncertainties are paired, with an up-variation and down-variation: in these instances, a calibration curve is constructed individually for the up-variation and down-variation, with the final uncertainty given by $D + \Delta D^{\text{up}} - \Delta D^{\text{down}}$.

10.10.1 Statistical Uncertainties

This measurement is conducted on a finite number of measured data events, and so a statistical uncertainty is included to account for the consequences of finite statistical power. This is achieved through so-called Poisson 'pseudo-experiments', where the $\cos\varphi$ distribution is fluctuated according to a Poisson distribution. This is repeated 1000 times. The value of D extracted through the expectation value of the distribution and the standard deviation of the results of these pseudo-experiments is taken as the statistical uncertainty on D.

10.10.2 Modelling Uncertainties

Modelling or "theoretical" uncertainties are included to account for possible shortcomings of any one event generator model, or to cover ambiguity in the setting of particular degrees of freedom within any one simulation set-up. They will alter the $\cos\varphi$ distribution at both particle-level and parton-level. Many modelling uncertainties are one-sided, meaning that a single variation is compared to the nominal D[5]. In these instances, the uncertainty is symmetrised, giving a value of $D \pm \Delta D$ with ΔD the symmetric uncertainty.

The effect of missing higher-order corrections to simulated cross-section predictions can be estimated using the standard method of variation of renormalisation and factorisation scales μ_R and μ_F. Such uncertainties are sometimes labelled "theoretical scale

[5]Uncertainties of this type are sometimes referred to as "two-point systematics".

uncertainties". In this measurement, these uncertainties are defined by considering variation of both scales by a factor of two, identically to the scale variations employed in Section 8.2. The envelope of results from all of these variations defines a total **Scales** uncertainty. An additional uncertainty is included to cover the absence of higher-order corrections on the $t\bar{t}$ prediction. An event-by-event re-weighting is applied to the nominal simulation such that $p_{\mathrm{T}}(t)$, $p_{\mathrm{T}}(t\bar{t})$ and $m_{t\bar{t}}$ spectra more closely match the NNLO predictions from recent literature [97]. The variation between the value of D obtained from the nominal MC-simulated sample and the NNLO-re-weighted sample defines the **NNLO** uncertainty.

The matching of matrix element calculations to parton showers was introduced in Section 6.3. In practice, both pieces of software must be parameterised such that they have a consistent definition of which areas of phase-space each tool is designed to cover. Pythia provides the capacity to "veto" showering in certain phase-space regions which Powheg defines to be sufficiently "hard". Ambiguity in this definition of hardness motivates including several dedicated uncertainties which are defined by changing particular Powheg or Pythia parameters. In particular, the **pThard** uncertainty covers ambiguity in choice of definition of the shower veto scale [464]. An **Hdamp** uncertainty is also defined for the `hdamp` parameter (which as a reminder, effectively regulates high-p_{T} radiation) by symmetrising the difference between its nominal value, m_{top} and a higher value of $1.5m_{\mathrm{top}}$. Additionally, the Pythia `recoil` parameter defines which final-state constituent additional hard radiation will recoil off. The difference between the two settings `recoiltoTop` and `recoiltoColor` define this the **Recoil** uncertainty.

The manner in which different event generators handle spin correlations in the decay of heavy resonances can lead to tangible differences in $t\bar{t}$ kinematics in different simulations. A **TopDecay** uncertainty is introduced to cover such differences. The uncertainty is defined as the difference between the nominal simulation, in which Pythia handles the top-quark decays, and a Powheg + Pythia set-up in which MadSpin is employed to decay the top-quarks. In the latter case, Pythia still handles the parton shower.

Uncertainties are also assigned to the amount of initial- and final-state radiation present in the parton shower. The **ISR** uncertainty is defined through variation of the `var3c` parameter in the A14 tune, which is equivalent to a variation in the strong coupling α_S which controls the shower evolution 6.3.1. The **FSR** uncertainty is defined through variation of the renormalisation and factorisation scales.

The effects of different parton shower prescriptions are quantified in a **PartonShower** uncertainty by comparing the nominal Powheg + Pythia simulation to the Powheg + Herwig simulation introduced in Section 10.2. As described in Section 6.3, Herwig implements an angular-ordered shower and the cluster hadronisation model, whilst Pythia implements a p_{T}-ordered shower and the Lund string hadronisation model. Differences between the two prescriptions are observed to be large when examining the $\cos\varphi$ distribution at particle-level, but not at parton-level, as shown in 10.12.2. This

motivates correcting the measured result to particle-level, with a discussion on possible sources of the observed discrepancy given in Section 10.12.2.

An uncertainty on the choice of PDF set used in simulation covers the fundamental uncertainty in knowledge of proton structure. The PDF4LHC working group provides a prescription for defining such uncertainties [465], wherein several distinct PDF sets are combined, and the dimensionality of the output reduced to a set of 30 **PDF uncertainties** through Principal Component Analysis. A total of 15 pairs of eigenvector variations are applied to this measurement.

Uncertainty on precise knowledge of the top-quark mass motivates including a **Top mass** uncertainty, defined by taking the central difference in D as evaluated using the nominal simulation, and MC-simulated samples in which m_{top} is varied upwards and downwards by 1 GeV from its nominal value.

The magnitude of each uncertainty is listed in Table 10.3 in terms of decreasing magnitude. The **TopDecay** uncertainty is the largest, reflecting the importance of a correct treatment of spin correlations in $t\bar{t}$ decays for measurements which rely on angular observables.

Table 10.3: A comparison of the relative size of the uncertainties related to signal modelling, defined at the SM expectation point with respect to $D^{particle}$.

Systematic	Relative Size
TopDecay	1.65 %
PDF (Sum)	1.20 %
Recoil	1.13 %
FSR (α_s)	1.11 %
Scales	1.11 %
NNLO	1.10 %
pThard	0.76 %
Top mass	0.73 %
ISR	0.16 %
PartonShower	0.15 %
Hdamp	0.14 %

10.10.3 Experimental Uncertainties

Experimental uncertainties reflect a lack of complete knowledge of the ATLAS detector, and associated reconstruction algorithms', precision. They alter the $\cos\varphi$ distribution only at reconstruction-level. The vast majority of experimental uncertainties considered in this measurement have negligible effect on the precision of the final result.

Uncertainties in the total **luminosity** have the effect of changing the total normalisation of the signal and the background. The entanglement marker D is extracted from a normalised differential cross-section, thus D is affected by the uncertainty in the total luminosity only through the background subtraction. The total statistical uncertainty is however affected by the luminosity uncertainty. The final Run-2 luminosity is quoted as 140.07 pb ± 0.83% [439], and the effect of this uncertainty is less than 0.1 %.

With regard to **lepton uncertainties**, Sections 5.4.1 and 5.4.2 discussed how scale factors were used to correct simulation to better match data for electrons and muons[6], respectively, and how variations in these scale factors led to an uncertainty prescripton which is applied to this measurement. A total of seven uncertainties are defined for electrons, each with an effect of around or less than one part in one thousand. The electron energy scale and resolution uncertainties were found to be larger than the uncertainties on reconstruction, isolation, identifcation and trigger efficiencies. For muons, separate uncertainties are defined from both momentum scale and resolution in the MS and the ID. Muon uncertainties total 14, and are all of the order of 0.1 % in the signal region, with the muon energy scale uncertainty being the largest.

Sources of **jet uncertainty** are described in Section 5.5.2. A total of 13 uncertainties are defined for the jet energy resolution, 14 which concern jet pile-up and jet flavour, 6 which concern the calibration of the jet η, and 15 uncertainties defined from eigenvector variations pertaining to the JES correction. The largest single uncertainty is related to the flavour composition of jets. The total effect of all jet uncertainties on D^{observed} in the signal region is 0.5 %.

Secttion 5.5.3 introduced how **flavour-tagging uncertainties** were estimated through variation of tagging efficiencies, and reduced to manageable size through the eigen-decomposition of a constructed covariance matrix. The result of that eigen-decomposition is a set of 17 eigen-variations: nine pertaining to b-tagging, four to c-tagging and four light-jet-tagging. Two further uncertainties are considered on the extrapolation of calibrated scale factors to higher p_{T}, necessary due to the lack of high-p_{T} b-jets ($p_{\text{T}}(b) > 400\,\text{GeV}$) present in data [260]. The total uncertainty in the signal region arising from flavour-tagging uncertainties is 0.4 %.

Recall from Section 5.6 that the $E_{\text{T}}^{\text{miss}}$ of an event is constructed from both calibrated reconstructed physics objects, and soft event behaviour which corresponds to charged tracks not associated with the hard event objects [261]. The hard $E_{\text{T}}^{\text{miss}}$ constituents

[6] These scale factors were derived from the ratio of data and simulation efficiencies for considerations in the construction of physics-ready leptons.

are leptons and jets; uncertainties on these reconstructed objects are propagated into uncertainties on the resolution and energy scale of the $E_{\mathrm{T}}^{\mathrm{miss}}$ object itself. Three additional uncertainties are considered to cover scale and resolution uncertainties on the soft event signals. The resolution case is defined for parallel and perpendicular projection of $E_{\mathrm{T}}^{\mathrm{miss}}$ onto $p_{\mathrm{T}}^{\mathrm{hard}}$, giving two uncertainties. All three uncertainties have vanishing contribution to the precision of this measurement.

Pile-up is modelled by overlaying simulated hard-scatter events with inelastic pp collision events. A pile-up re-weighting procedure defines the **pile-up uncertainty** by re-weighting the simulation to account for a different mean number of collisions per bunch crossing [312]. The pile-up uncertainty has an effect of less than 0.1 %, in large part due to object reconstruction techniques like the particle-flow algorithm which is designed to be robust against pile-up variation.

10.10.4 Background Uncertainties

All background samples are normalised to the state-of-the-art prediction for the inclusive cross-section for the background process in question. This cross-section value has an associated uncertainty, which must be translated into a normalisation uncertainty on each background sample. Other background uncertainties are occasionally considered for particular processes. In each case, the uncertainty variations lead to different MC-simulated samples which provide a alternative estimate of the particular background contribution. This alternative estimate is subtracted from the data, and then the measured value of D in the background-subtracted data is propagated through the nominal calibration curve. The difference between the nominal D and alternative background-derived value define the uncertainty.

Two uncertainties are defined for the **single-top-quark** background. The first is an uncertainty in the overall NNLO cross-section [466]. The second is based on the choice of scheme used to avoid the double-counting of higher-order diagrams between Wt and $t\bar{t}$ production, as discussed in Section 10.5.1. The DR scheme is implemented in the nominal background estimation, and the DS scheme constitutes the alternative background estimation, with the difference between the two defining the uncertainty. The cross-section uncertainty has a 0.4 % effect on the measurement, and the effect of the DR/DS uncertainty is less than one part in a thousand.

Normalisation uncertainties are also considered for the **ttX**: $t\bar{t}W$ and $t\bar{t}Z$ backgrounds. Both are derived from the NLO cross-section uncertainty. The effects of these uncertainties on the final result is entirely negligible. A normalisation uncertainty of 10 % is included for **diboson** backgrounds. This accounts for the difference between the Sherpa NLO-accurate cross-section predictions and the state-of-the-art NNLO QCD + NLO EW theoretical predictions. The effect of this uncertainty is less than one part in a thousand: shape effects due to EW corrections are typically observed in high-p_{T} tails for these electroweak processes.

The production of **vector bosons with additional heavy-flavour** (HF) jets can be difficult to model. In particular, the process $Z \to \tau\tau$ + HF presents a challenge, with previous di-leptonic $t\bar{t}$ measurements noting a mis-modelling rate on the order of 5 %. A conservative cross-section uncertainty of 20 % is applied to cover heavy-flavour mis-modelling effects and the uncertainty in the predicted cross-section. The effect of this estimate is an uncertainty of 1.3 % on the final result, constituting the largest background-related uncertainty. This is understood as arising from shape differences between the $\cos\varphi$ distributions in the $Z \to \tau\tau$ and $t\bar{t}$ channels.

A normalisation uncertainty of ±50 % is adopted for the **fake lepton** background, to account for the differences in scale factors derived, as discussed in Section 10.5.2. This is considered conservative given the observed data-simulation agreement in the control region, and has a 0.1 % effect on the final result.

10.11 Results

Entanglement marker D is extracted in the signal region and both validation regions, and corrected to to fiducial particle-level using the calibration curve. The results for the entanglement marker D at particle-level are:

$$D^{\text{observed}} = -0.547 \pm 0.002\ (\text{stat.}) \pm 0.020\ (\text{syst.}),$$
$$D^{\text{expected}} = -0.470 \pm 0.002\ (\text{stat.}) \pm 0.017\ (\text{syst.})$$

in the signal region,

$$D^{\text{observed}} = -0.202 \pm 0.001\ (\text{stat.}) \pm 0.028\ (\text{syst.}),$$
$$D^{\text{expected}} = -0.258 \pm 0.001\ (\text{stat.}) \pm 0.026\ (\text{syst.})$$

in validation region 1, and

$$D^{\text{observed}} = -0.098 \pm 0.001\ (\text{stat.}) \pm 0.021\ (\text{syst.}),$$
$$D^{\text{expected}} = -0.103 \pm 0.001\ (\text{stat.}) \pm 0.021\ (\text{syst.})$$

in validation region 2. The *observed* values are those measured in data and the *expected* values are the corresponding SM predictions. The total statistical and systematic uncertainties are stated, where the total systematic uncertainty is the sum in quadrature of all individual systematic uncertainty contributions.

The calibration curve used to correct the measured value of D in the signal region for detector effects is shown in Figure 10.12. The dashed line gives the entanglement limit in the fiducial particle-level phase space. The black dot represents the value of D extracted from data, and the squares the predicted simulation value for the different re-weighting points which were used to construct the curve. In particular, the red square represents the SM prediction for entanglement marker D as extracted from the nominal simulation. The calibration curve is the linear interpolation between the square prediction points, with the yellow and grey bands denoting the statistical and total (statistical plus systematic) uncertainty as a function of the measured value of D.

The analogous calibration curves for the validation regions are shown in Figure 10.13. Although the set of re-weighting factors $\{K\}$ is the same for the signal and both validation regions, the SM prediction (shown in these figures in blue) and re-weighted predictions show considerable variance between regions, with the predictions showing greatest spread in the signal region. As a result, the axes limits are not identical between calibration curve figures, but chosen based on the predicted D values.

The uncertainties discussed in Section 10.10 are categorised and summed in quadrature, such that the total contribution from each source of systematic uncertainty, as well as the statistical uncertainty, is presented for the signal region in Table 10.4, for validation region 1 in 10.5, and for validation region 2 in 10.6. The middle column

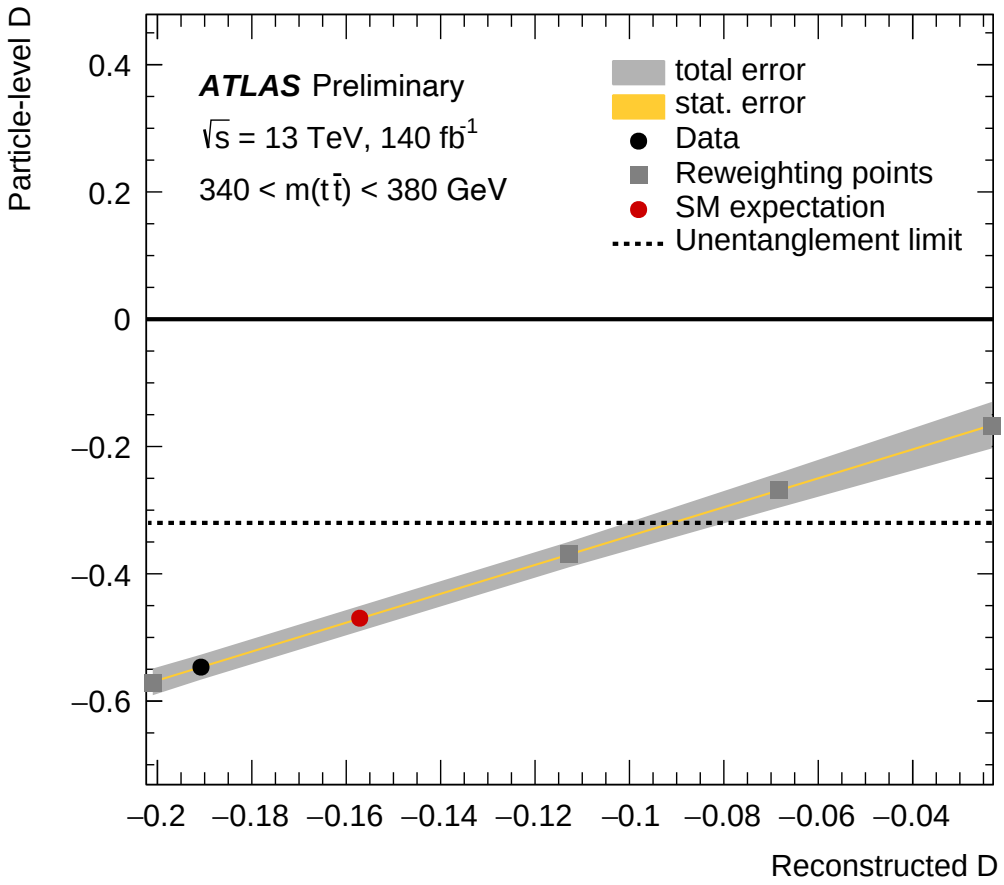

Figure 10.12: Calibration curve for the signal region, with "SM expectation" and "re-weighting points" giving the D values from which the curve is built. Statistical and total uncertainty variation with reconstructed D is given by the yellow and grey bands. The data point is shown in black, and the entanglement limit as defined at parton-level is given by the dotted black line.

presents the uncertainties evaluated at the expected D^{expected} value derived from the nominal simulation. The right-most column presents the uncertainties on D^{observed} derived from corrected data. The modelling systematics are seen to dominate, with the backgrounds the second largest uncertainty contribution. No drastic variation is seen in any uncertainty magnitude between the expected and observed sets. The absolute values of the modelling uncertainties show little variation across the three regions, however the jet uncertainties are seen to grow at high $m_{t\bar{t}}$ and become the second largest contribution in validation region 2.

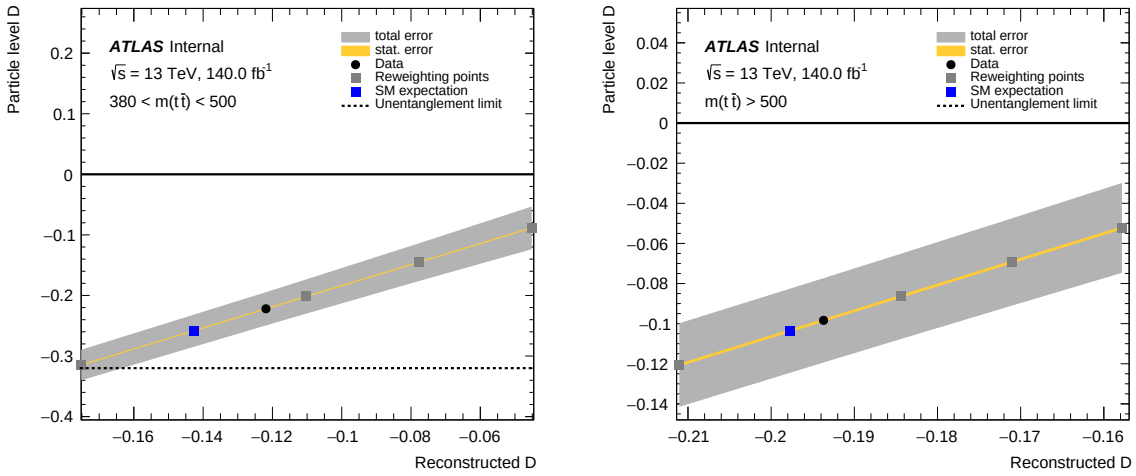

(**a**) Validation region 1 (**b**) Validation region 2

Figure 10.13: Calibration curves for validation regions, with features similar to Figure 10.12, except that the SM prediction is given in blue. Note that the axes scale differ between the figures.

The values of D^{particle} are presented in Figure 10.14 for both the signal region and validation regions. SM predictions for entanglement marker D, as computed by various event generators, are also shown. The agreement between the various predictions of D and the value extracted from data is strongest in validation region 2.

The entanglement limit at particle-level is shown for the signal region for both Powheg + Pythia and Powheg + Herwig. The Powheg + Pythia entanglement limit is -0.322 ± 0.009, whilst the Powheg + Herwig limit is -0.27. The validation regions are included in the measurement to assess the agreement between data and simulation in different regions of the $m_{t\bar{t}}$ phase-space, and to corroborate the prediction that the measured value of D increases in higher $m_{t\bar{t}}$ regions. A statement regarding the presence of quantum entanglement in the validation regions is not required, and therefore no correction of the entanglement limit to particle-level is performed in these regions.

The *bb4l* simulation performs the full off-shell calculation from two intial-state partons to the final four–lepton, two–b-jet state. The measurement requires two on-shell top-quarks to decay and pass their spin information to the charged leptons. The off-shell component of the *bb4l* cross-section prediction would have to be removed for a particle-level comparison with the other simulation predictions and with the data. This removal is not well-defined, so the *bb4l* prediction is only included a reconstruction-level, and therefore absent from Figure 10.14.

Table 10.4: A summary of the effect of the groups of systematic uncertainty at the expected SM value for $D_{\text{expected}} = -0.470$, corresponding to the POWHEG + PYTHIA simulation, and the observed value $D_{\text{observed}} = -0.547$ in the signal region. The absolute effects are quoted to three decimal places and the relative size of the effect is quoted to one decimal place.

Systematic source	$\Delta D_{\text{expected}}(D = -0.470)$	ΔD (%)	$\Delta D_{\text{observed}}(D = -0.547)$	ΔD (%)
Signal Modelling	0.017	3.2	0.017	3.1
Electron	0.002	0.4	0.001	0.2
Muon	0.001	0.1	0.001	0.2
Jets	0.004	0.7	0.003	0.5
b-tagging	0.002	0.4	0.002	0.4
Pileup	< 0.001	< 0.1	< 0.001	< 0.1
$E_{\text{T}}^{\text{miss}}$	0.002	0.3	0.001	0.4
Backgrounds	0.010	1.8	0.008	1.8
Stat.	0.002	0.3	0.002	0.4
Syst.	0.021	3.8	0.017	3.1
Total	0.021	3.8	0.017	3.1

10.12 Discussion

In the signal region, both the observed and expected values of D are seen to sit well below the corrected entanglement limit, as shown in Figure 10.14. The significance of both D^{observed} and D^{expected} with respect to either corrected entanglement limit is well in excess of five standard deviations. This is demonstrable proof that a significant portion of the $t\bar{t}$ pairs exist in entangled spin-singlets within the range, $340\,\text{GeV} < m_{t\bar{t}} < 380\,\text{GeV}$. The data and predictions agree to within the uncertainties in both validation regions, serving as a consistency check to validate the measurement method.

Di-leptonic $t\bar{t}$ measurements at the LHC benefit from plentiful statistics. This measurement places stringent requirements on the $t\bar{t}$ final-state, focusing only on the $e\mu$ channel, and selecting only events which meet the requirement, $340\,\text{GeV} < m_{t\bar{t}} < 380\,\text{GeV}$. Despite this, the statistical uncertainty is found to be an order of magnitude smaller than the total systematic uncertainty, and so any refined measurements of entanglement in $t\bar{t}$ production would benefit most from improvement to specific systematic uncertainties.

Table 10.5: A summary of the effect of the groups of systematic uncertainty at the expected SM value for $D_{\text{expected}} = -0.258$, corresponding to the Powheg + Pythia simulation, and the observed value $D_{\text{observed}} = -0.202$ in validation region 1. The absolute effects are quoted to three decimal places and the relative size of the effect is quoted to one decimal place.

Systematic source	$\Delta D_{\text{expected}}(D = -0.258)$	ΔD (%)	$\Delta D_{\text{observed}}(D = -0.202)$	ΔD (%)
Signal Modelling	0.0158	6.13	0.0175	7.89
Electron	0.00123	0.476	0.0012	0.55
Muon	0.000431	0.167	0.0004	0.20
Jets	0.0105	4.06	0.0105	4.74
b-tagging	0.00102	0.396	0.0011	0.49
Pileup	5.59×10^{-5}	0.0216	< 0.0001	0.02
$E_{\text{T}}^{\text{miss}}$	0.000949	0.367	0.0010	0.45
Backgrounds	0.0176	6.83	0.0185	8.32
Stat.	0.000958	0.371	0.0010	0.44
Syst.	0.0258	10.0	0.0274	12.40
Total	0.0258	10.0	0.0275	12.40

Background uncertainties are a sub-leading factor in limiting the precision of both D^{observed} and D^{expected}. This is largely driven by a conservative estimate for the uncertainty on the $Z \to \tau\tau$ + HF cross-section. Possible refinements of this measurement could consider further study of the effects of the $Z \to \tau\tau$ + HF process, and the measurement would benefit from improved modelling of this process.

Top-quark reconstruction techniques were also seen to be a limiting factor, leading to a smearing of the $m_{t\bar{t}}$ spectrum which ultimately drove biased unfolding efforts. Novel top-quark reconstruction techniques, such as proposals to use generative artificial intelligence to derive the distribution of neutrino momenta in di-leptonic $t\bar{t}$ decays [467], may prove useful here. Additionally, it may be beneficial to consider higher-dimensional differential cross-sections — for example, the double differential cross-section $\frac{\mathrm{d}^2\sigma}{\mathrm{d}\cos\varphi \mathrm{d}m_{t\bar{t}}}$ — and utilise profile likelihood unfolding techniques to investigate whether the additional information in the differential cross-section can lead to unbiased unfolding results.

This measurement presents entanglement marker D at fiducial particle-level, with the correction for detector effects accounted for through the calibration curve. It should be made clear that the re-weighting procedure used to generate the calibration

Table 10.6: A summary of the effect of the groups of systematic uncertainty at the expected SM value for $D_{\text{expected}} = -0.103$, corresponding to the POWHEG + PYTHIA simulation, and the observed value $D_{\text{observed}} = -0.098$ in validation region 2. The absolute effects are quoted to three decimal places and the relative size of the effect is quoted to one decimal place.

Systematic source	$\Delta D_{\text{expected}}(D = -0.103)$	ΔD (%)	$\Delta D_{\text{observed}}(D = -0.098)$	ΔD (%)
Signal Modelling	0.0166	16.0	0.0167	17.00
Electron	0.0011	1.06	0.0011	1.12
Muon	0.000528	0.51	0.0005	0.54
Jets	0.0118	11.4	0.0118	12.00
b-tagging	0.0019	1.83	0.0019	1.91
Pileup	0.000726	0.701	0.0007	0.74
$E_{\text{T}}^{\text{miss}}$	0.000288	0.279	0.0003	0.27
Backgrounds	0.00488	4.71	0.0049	4.93
Stat.	0.000698	0.675	0.0007	0.71
Syst.	0.0209	20.2	0.0210	21.40
Total	0.0209	20.2	0.0210	21.40

curves represents a creative choice in the measurement strategy. The particular form of the re-weighting was chosen to maintain the linearity of the $\cos\varphi$ distribution, and vary linearly with the scaling factor K. Other choices of re-weighting could be used. However, it is argued that the chosen method is physically-motivated because it maintains that linearity of the $\cos\varphi$ distribution. Unfolding the $\cos\varphi$ distribution in any future measurement of D would circumvent having to implement a re-weighting procedure — provided of course that a means of unfolding in an unbiased way is found.

10.12.1 Modelling $t\bar{t}$ Production in the Threshold Regime

The dominant modelling uncertainty in the signal region for D^{expected} is the **Top Decay** uncertainty, illustrating how challenges remain in the modelling of $t\bar{t}$ decays when spin information is of high priority. It is expected that improvements in the modelling of spin correlations in heavy resonance decays will ultimately improve the precision of ATLAS and CMS measurements of angular $t\bar{t}$ di-leptonic observables. Most modelling uncertainties included in this measurement are larger than experimental or background

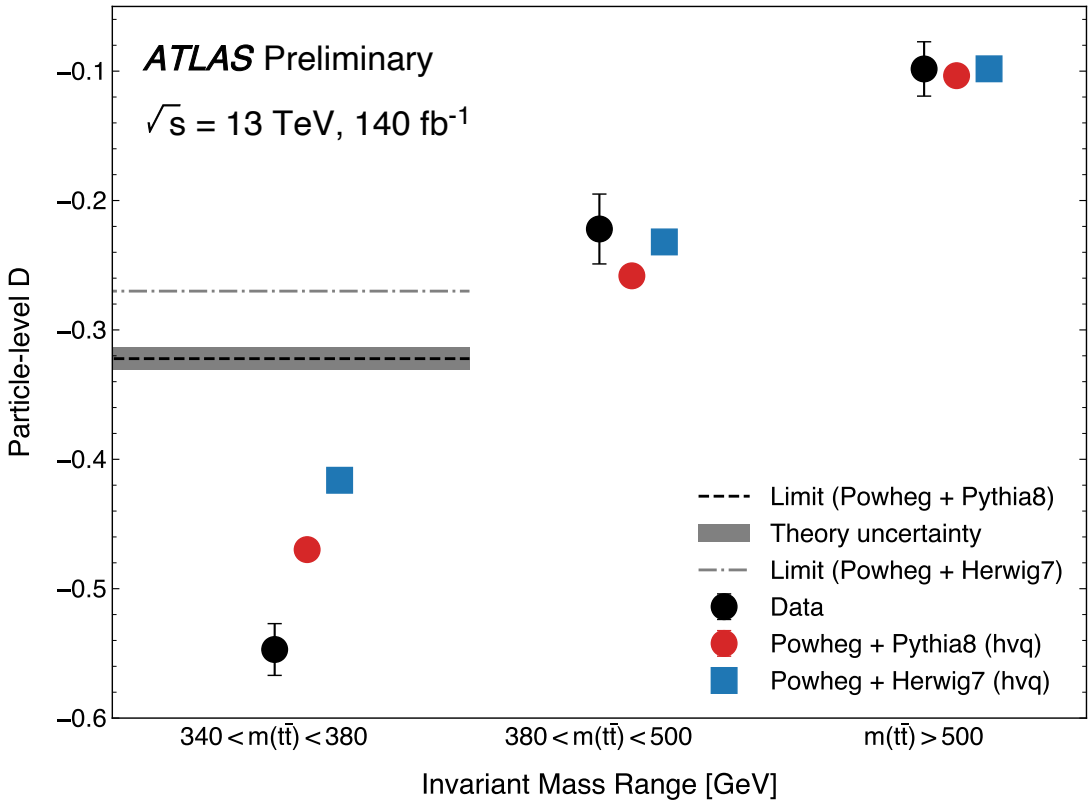

Figure 10.14: Particle-level values of entanglement marker D from data (black dot) and two simulation predictions: Powheg+Pythia8 and Powheg+Herwig7. In each case, these particle-level values have been obtained by mapping the values given in Figure 10.8 through the appropriate region calibration curve, as given in Figures 10.12 and 10.13. Discrepany between data and between individual predictions is largest in the SR, and lowest in VR2. The entanglement/unentanglement limit of $-1/3$ is folded in to the particle-level phase-space using two different calibration curves corresponding to Pythia showering and Herwig showering, in the signal region only. These limits are given by the dashed and dotted-dashed horizontal lines, respectively. A theory uncertainty is associated with the Pythia-derived limit. Visual inspection clearly shows that the entanglement hypothesis is strongly favoured by the data.

uncertaitnies, highlighting the necessity of improved simulation for precision top-quark measurements like this one.

This point is further illustrated by considering that the particle-level predictions for D in the signal region are in some tension with the corrected data value. This is most readily seen in Figure 10.14, but also visible at reconstruction-level as seen in Figure 10.8. The predictions also exhibit some level of disagreement with one another. In contrast, all predictions and the data agree with each other, to within the bounds of the total uncertainty D, for both validation regions. This indicates that the simulation

methods employed do not provide an accurate description of $t\bar{t}$ pair production close to threshold, but that the modelling is adequate at higher values of $m_{t\bar{t}}$. There are several factors which could explain the observed discrepancies in the signal region.

Firstly, the particle-level $\cos\varphi$ predictons from Powheg + Pythia and Powheg + Herwig are seen to differ, as shown in Section 10.12.2. This is indication of possible mis-modelling of parton shower or hadronisation in events near threshold. Section 10.12.2 discusses these discrepancies in detail, concluding that differences in the parton shower algorithms is responsible for the tension between the two predictions.

The difference between the measured and predicted values of D may be resolved by considering additional effects in the matrix element calculation, prior to any showering. Such effects would be required to enhance the production of $t\bar{t}$ pairs at high values of $\cos\varphi$, such that the slope of the distribution is increased, in turn leading to a smaller prediction for D. The simulation employed in this measurement is NLO-QCD accurate in the production of the $t\bar{t}$ state, and LO-QCD accurate in the top-quark decays. NLO-EW corrections are known to enhance the $t\bar{t}$ cross-section at low values of $m_{t\bar{t}}$ [97], but are not included in the default Powheg modelling of the $t\bar{t}$ cross-section. Whether these NLO-EW corrections have a strong impact on the $\cos\varphi$ distribution has not been studied. It will be interesting to observe whether predictions for D match more closely to the observed value as event generators with higher-order QCD and EW corrections are made available for experimental top-quark analyses.

Another possible contribution which is known to enhance the $t\bar{t}$ cross-section around threshold is that of bound effects [468]. At low $m_{t\bar{t}}$, the top-quarks are essentially non-relativistic, $\beta << 1$, and look to form a bound state through so-called "Coulomb effects". These effects are not generally modelled by general-purpose event generators, and so the impact on predictions for D will be hard to assess without dedicated study. However, Ju et al. report that "toponium"-type bound-state effects may lead to an enhanced production cross-section of colour-singlet, spin-singlet $t\bar{t}$ pairs of the order of 20 % [468]. This is encouraging as the entangled $t\bar{t}$ state at threshold is precisely this spin-singlet state. In other words, the simulation tools used in the ATLAS entanglement measurement may underestimate the number of spin-singlet states produced very close to threshold. The inclusion of this effect may lead to a SM prediction of entanglement which more closely matches the ATLAS data.

10.12.2 Comments on Pythia and Herwig Comparison

Differences in the predicted values of D between Pythia and Herwig motivate additional study of these simulation tools. Ultimately, a full phase-space parton-level value of D would be most easily compared to other experimental measurements[7], and would require no conversion of the entanglement limit to particle-level, and therefore no uncertainty on that limit. This section discusses how differences in the parton showering

[7] Although so far, this measurement is the first of its kind

between Pythia and Herwig lead to discrepancies in their predicted particle-level $\cos\varphi$ distributions, which would ultimately drive an unmanageable modelling uncertainty should the correction back to parton-level be attempted. It is for this reason that the parton shower uncertainty is not included in the uncertainty prescription applied to the entanglement limit at particle-level.

Figure 10.15 presents the $\cos\varphi$ distribution as derived from Powheg + Pythia and Powheg + Herwig simulations. Figure 10.15a shows that at parton-level, the two set-ups yield almost identical results for the inclusive $\cos\varphi$ distribution. It is a different story at particle-level as Figure 10.15b shows: here there is a large discrepancy and marked slope between the two predictions. Figure 10.15c illustrates how this discrepancy is larger for the particle-level $\cos\varphi$ prediction in the signal region. Since the parton-level predictions of D are essentially identical, as can be inferred from 10.15a, the particle-level to parton-level corrections for Pythia and Herwig would need to be substantially different i.e. the Pythia calibration curve would look very different to the Herwig one. It is this difference that would drive a large modelling uncertainty on a correction to parton-level.

The differences between the Pythia and Herwig event generators are highlighted in Chapter 6. The largest physics differences are the type of parton shower used — in particular the ordering parameter which controls the evolution of the shower — and the hadronisation models. Both effects are tested.

The Sherpa event generator (Chapter 6) allows the user to employ the cluster hadronisation or Lund string hadronisation model. A comparison between the two hadronisation models is presented in Figure 10.16, in which the default cluster model is labelled 'def'. It is observed that altering hadronisation model has a negligible effect on the observable.

Herwig allows the user to select between an angular-ordered shower and dipole (p_{T}-ordered) shower, and can therefore be used to test the effects of different parton shower algorithms on $\cos\varphi$. In this particular study, Herwig is also used to generate the $t\bar{t}$ events at LO-QCD, as well as for modelling of the hadronisation and underlying event. Figure 10.17 shows the $\cos\varphi$ distribution for the inclusive region, Figure 10.17a, and signal region, Figure 10.17b. Clear differences are seen between the angular- and dipole-showers in the inclusive region, and these differences are exacerbated in the signal region. This confirms that the choice of ordering parameter in the parton shower algorithm is directly responsible for the discrepancies observed in particle-level $\cos\varphi$ distributions.

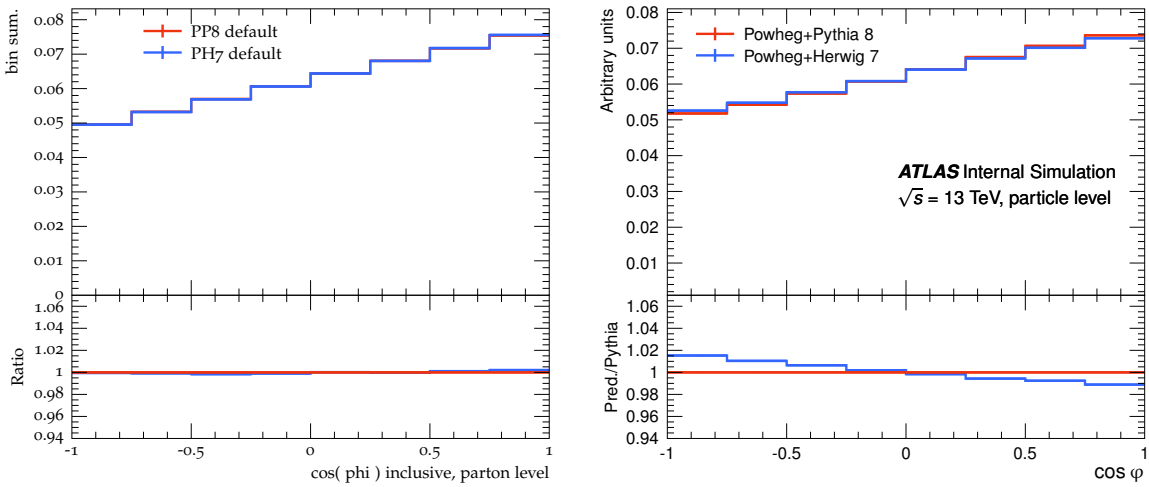

(a) (b)

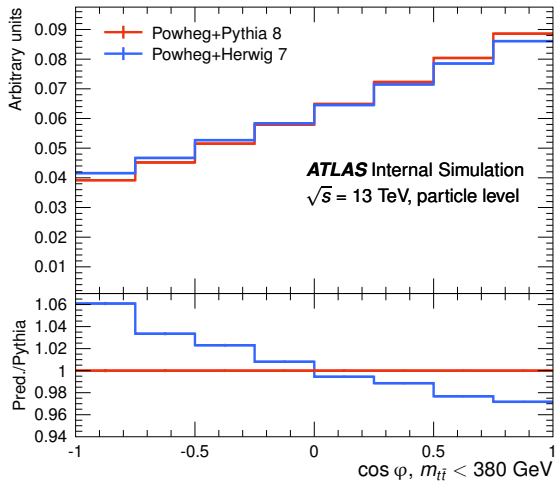

(c)

Figure 10.15: A comparison between PYTHIA and HERWIG generators for the $\cos\varphi$ observables. **(a):** $\cos\varphi$ at parton-level in the inclusive region. The parton shower has not yet been applied. The differences between the generators are vanishingly small. **(b):** $\cos\varphi$ at particle-level in the inclusive region. A clear difference is observed. **(c):** $\cos\varphi$ at partcile-level in the signal region. The differences between the two generators are even more pronounced.

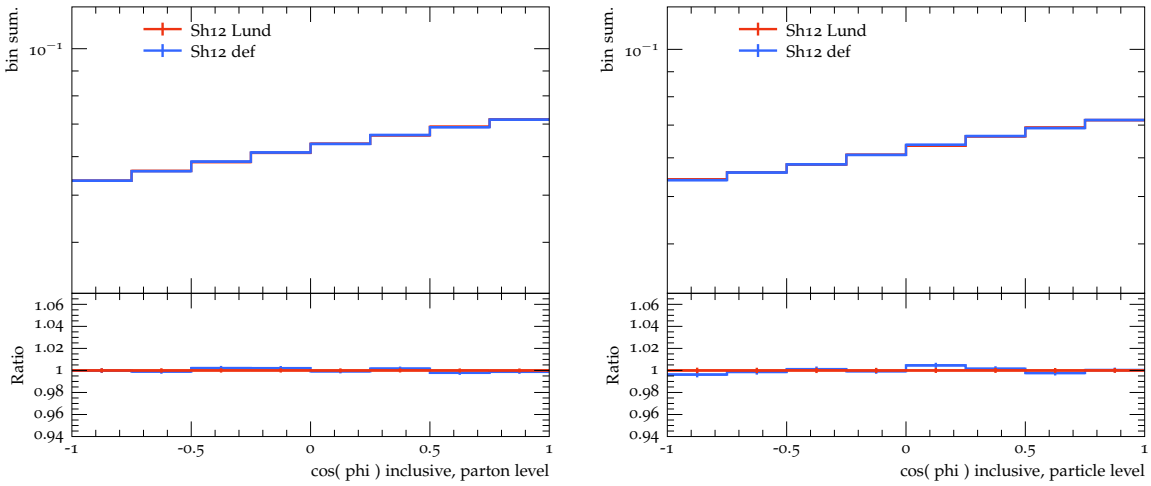

(**a**) Parton-level (**b**) Particle-level

Figure 10.16

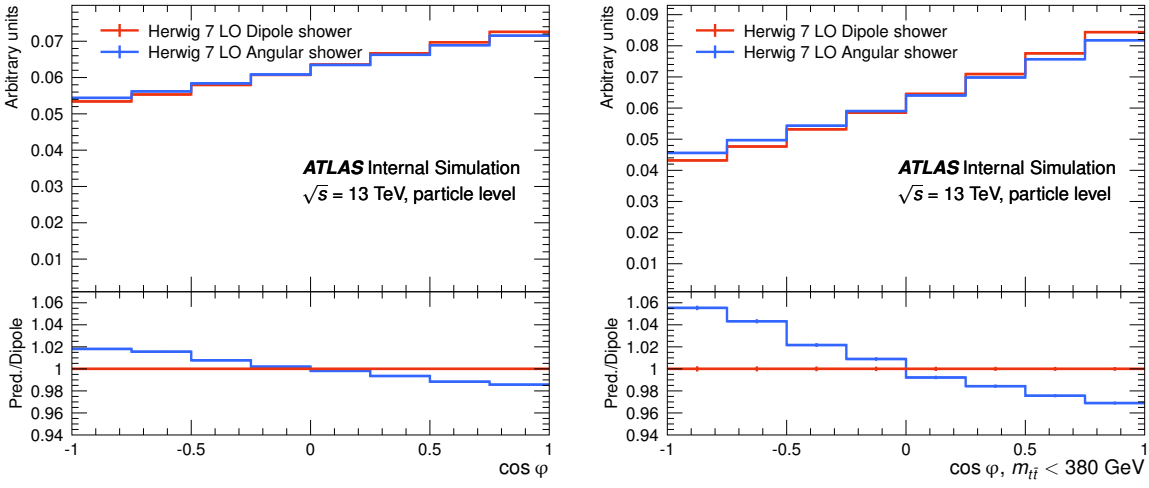

(**a**) (**b**)

Figure 10.17: Herwig has the capability to alter between an angular- and a dipole-shower. The $\cos\varphi$ distribution is shown for both types of shower procedure, in the (**a**) inclusive region, (**b**) signal region. Large differences between the shower algorithm results are observed, in agreement with Figure 10.15.

Chapter 11

Conclusions

Often have I marvelled to myself over the course of this PhD how amazingly diverse particle physics is as a field of study. The first few chapters of this thesis are testament to that. Chapter 2 introduced the Standard Model and the SMEFT; Chapter 3 the top-quark; Chapter 4 the LHC and ATLAS detector. The next chapters were given over to important methods, with Chapter 5 discussing the reconstruction techniques employed to build physics objects from signals in the ATLAS detector, and Chapter 6 summarising the methods used to simulate proton-proton collisions.

Chapter 7 reviewed various fast simulation methods, and motivated the requirement for efficient tools which could emulate the response of a particle detector with no actual simulation. Several such tools exist in the literature, and are useful in instances when any form of simulation is prohibitively expensive. Two methods for building transfer functions, designed to map representations of truth-level events to reconstruction-level events, were put forward. Probabilistic smearing functions were derived from $t\bar{t}$ simulation and their ability to capture the effects of full simulation tested. Efficiency functions were built from public ATLAS electron and muon performance data. It was found that, in general, the combination of these two functions was insufficient to capture detector response effects for the kinematics of electrons, muons and jets. Deep neural networks were used to build alternative smearing functions, and seen to better capture the smearing effects on jet kinematics. Further developments in detector response emulation are likely to be driven by novel machine learning techniques.

The spin properties of top-quarks played an important role in this thesis, as have the angular observables which are used to measure those properties. Spin correlations and polarisations are well understood and measured in $t\bar{t}$ production, but unexplored in associated top-quark production. Chapter 7 presented a study on the measurement of spin properties in $t\bar{t}Z$ production. The spin density matrix was derived for $t\bar{t}Z$ production using NLO-QCD simulation for the first time, showing that the spin correlations of the $t\bar{t}$ pair are markedly different to the $t\bar{t}$-production case, and that the emission of the Z-boson induces longitudinal polarisation in the parent top-quark. A measurement strategy was proposed, wherein a set of spin observables could be combined in a template fit to provide observation of spin correlations at the LHC. Estimates of yields in various LHC operating conditions led to the prediction that observation of spin correlations should be possible by the end of Run-3. The utility

of using spin observables to constrain particular Wilson coefficients in an EFT fit was also assessed, and an information geometry interpretation showed the most sensitive combination of Wilson coefficients.

There is great excitement in the community about the application of quantum information ideas to high-energy physics. Chapter 9 reviewed the literature on possible quantum information-type measurements at the LHC, and give a concrete definition of quantum entanglement, which can be measured in $t\bar{t}$ pair production. Chapter 10 presented just that measurement, the first ever experimental verification of quantum entanglement between quarks.

The measurement of quantum entanglement focused on extracting an entanglement marker D from an angular distribution, $\frac{1}{\sigma}\frac{\mathrm{d}\sigma}{\mathrm{d}\cos\varphi}$, measured in $\sqrt{s} = 13$ TeV $t\bar{t}$ data recorded by the ATLAS detector. The measurement focused on a region of phase-space close to the $m_{t\bar{t}}$ threshold, by implementing the selection $340\,\mathrm{GeV} < m_{t\bar{t}} < 380\,\mathrm{GeV}$ on $t\bar{t}$ events to define a signal region. Consideration was given to a variety of background sources, which were estimated using simulation or data-driven methods and subtracted from the recorded data. Unfolding of the $\cos\varphi$ distribution to parton-level proved impossible without inducing significant biases, arising because of the poor resolution on the $m_{t\bar{t}}$ spectrum, a consequence of top-quark kinematic reconstruction techniques. A calibration curve method was instead used to parameterise differences between truth-level and reconstruction-level definitions of D; this required a novel re-weighting technique which altered the slope of the $\cos\varphi$ distribution in a consistent way. The measured value of D was corrected to a particle-level definition using the calibration curve, and a set of experimental, modelling and background systematics included.

An observed value of entanglement marker D at particle-level was reported as $D^{\text{observed}} = -0.547 \pm 0.002\ (\text{stat.}) \pm 0.020\ (\text{syst.})$, in the signal region. This is well in excess of five standard deviations from the "no-entanglement limit". Systematic uncertainties dominate the measurement, with modelling uncertainties being the primary contributors. Further developments in $t\bar{t}$ modelling near the $m_{t\bar{t}}$ threshold, particularly with regard to the parton showering, higher-order corrections and bound-state effects, should drive closer agreement between data and simulation. A correction back to the full parton-level phase-space was not implemented because of a large discrepancy in the particle-level predictions of D. The source of this discrepancy was found to be the difference in parton shower algorithms between the Pythia and Herwig event generators.

This last result is exciting. It constitutes the first direct measurement of quantum information phenomena in a collider environment, the highest energy measurement of quantum entanglement ever made, and the first measurement of entanglement between quarks. It paves the way for future measurements of quantum information phenomena at the LHC, with a view to even searching for New Physics using quantum information-derived observables. This measurement is a glorious combination of Old and New Physics: spooky action at a distance is alive and well at the Large Hadron Collider.

Bibliography

[1] L. Evans and P. Bryant, "LHC machine," *Journal of instrumentation*, vol. 3, no. 08, S08001, 2008. DOI: 10.1088/1748-0221/3/08/S08001 (cit. on pp. 1, 41).

[2] S. Weinberg, "Implications of dynamical symmetry breaking," *Phys. Rev. D*, vol. 13, pp. 974–996, 4 Feb. 1976. DOI: 10.1103/PhysRevD.13.974 (cit. on p. 1).

[3] G. Jungman, M. Kamionkowski, and K. Griest, "Supersymmetric dark matter," *Physics Reports*, vol. 267, no. 5, pp. 195–373, 1996, ISSN: 0370-1573. DOI: 10.1016/0370-1573(95)00058-5 (cit. on p. 1).

[4] C. Kiefer, "Why quantum gravity?" In *Approaches to Fundamental Physics: An Assessment of Current Theoretical Ideas*, Springer, 2007, pp. 123–130 (cit. on p. 1).

[5] G. Isidori, *B anomalies: Hopes, disillusions, and future prospects*, Mar. 2023. [Online]. Available: https://ep-news.web.cern.ch/node/3398 (cit. on p. 1).

[6] D. P. Aguillard, T. Albahri, D. Allspach, *et al.*, "Measurement of the positive muon anomalous magnetic moment to 0.20 ppm," *Phys. Rev. Lett.*, vol. 131, p. 161 802, 16 Oct. 2023. DOI: 10.1103/PhysRevLett.131.161802 (cit. on p. 1).

[7] T. Aaltonen, B. Álvarez González, S. Amerio, D. Amidei, *et al.*, "Precise measurement of the W-boson mass with the CDF II detector," *Phys. Rev. Lett.*, vol. 108, p. 151 803, 15 Apr. 2012. DOI: 10.1103/PhysRevLett.108.151803 (cit. on p. 1).

[8] B. Capdevila, A. Crivellin, and J. Matias, "Review of semileptonic B anomalies," *arXiv preprint arXiv:2309.01311*, 2023. DOI: 10.48550/arXiv.2309.01311 (cit. on p. 1).

[9] J. S. Bell, "On the Einstein Podolsky Rosen paradox," *Physics Physique Fizika*, vol. 1, no. 3, p. 195, 1964. DOI: 10.1103/PhysicsPhysiqueFizika.1.195 (cit. on pp. 3, 125, 126).

[10] *2022 Nobel Prize in Physics Summary*, https://www.nobelprize.org/prizes/physics/2022/summary/, Accessed: 2023-05-24 (cit. on pp. 3, 125).

[11] ATLAS Collaboration, " Observation of quantum entanglement in top-quark pair production using pp collisions of $\sqrt{s} = 13$ TeV with the ATLAS detector," Sep. 2023. DOI: 10.48550/arXiv.2311.07288 (cit. on p. 3).

[12] R. Feynman. "Richard feynman on the scientific method," Youtube. (1964), [Online]. Available: https://www.youtube.com/watch?v=EYPapE-3FRw (cit. on p. 5).

[13] M. D. Schwartz, *Quantum field theory and the standard model*. Cambridge University Press, 2014 (cit. on pp. 5, 10).

[14] W. Buchmüller and C. Lüdeling, *Field theory and standard model*, 2006. DOI: 10.48550/ARXIV.HEP-PH/0609174 (cit. on p. 5).

[15] M. Srednicki, *Quantum field theory*. Cambridge University Press, 2007 (cit. on pp. 5, 7).

[16] S. Weinberg, *The quantum theory of fields*. Cambridge university press, 1995, vol. 2 (cit. on p. 5).

[17] W. A. Bardeen, H. Fritzsch, and M. Gell-Mann, "Light-Cone current Algebra, π^0 Decay and e^+e^- Annihilation," CERN, Geneva, Tech. Rep., 1972. [Online]. Available: https://cds.cern.ch/record/593283 (cit. on p. 6).

[18] S. Weinberg, "Non-abelian gauge theories of the strong interactions," *Phys. Rev. Lett.*, vol. 31, pp. 494–497, 7 Aug. 1973. DOI: 10.1103/PhysRevLett.31.494 (cit. on p. 6).

[19] H. Fritzsch, M. Gell-Mann, and H. Leutwyler, "Advantages of the color octet gluon picture," *Physics Letters B*, vol. 47, no. 4, pp. 365–368, 1973. DOI: 10.1016/0370-2693(73)90625-4 (cit. on p. 6).

[20] S. L. Glashow, "Partial-symmetries of weak interactions," *Nuclear Physics*, vol. 22, no. 4, pp. 579–588, 1961. DOI: 10.1016/0029-5582(61)90469-2 (cit. on p. 6).

[21] S. Weinberg, "A model of leptons," *Physical review letters*, vol. 19, no. 21, p. 1264, 1967. DOI: 10.1103/PhysRevLett.19.1264 (cit. on p. 6).

[22] A. Salam and J. C. Ward, "Weak and electromagnetic interactions," *Il Nuovo Cimento (1955-1965)*, vol. 11, pp. 568–577, 1959. DOI: 10.1142/9789812795915_0034 (cit. on p. 6).

[23] S. Coleman and J. Mandula, "All possible symmetries of the s matrix," *Physical Review*, vol. 159, no. 5, p. 1251, 1967. DOI: 10.1103/PhysRev.159.1251 (cit. on p. 6).

[24] E. Witten, "Introduction to supersymmetry," in *The Unity of the Fundamental Interactions*, A. Zichichi, Ed. Boston, MA: Springer US, 1983, pp. 305–371, ISBN: 978-1-4613-3655-6. DOI: 10.1007/978-1-4613-3655-6_7 (cit. on p. 6).

[25] T. Friedrich, *Dirac operators in Riemannian geometry*. American Mathematical Soc., 2000, vol. 25 (cit. on p. 6).

[26] E. C. G. Sudarshan and R. E. Marshak, "Chirality invariance and the universal fermi interaction," *Phys. Rev.*, vol. 109, pp. 1860–1862, 5 Mar. 1958. DOI: 10.1103/PhysRev.109.1860.2 (cit. on p. 6).

[27] R. P. Feynman and M. Gell-Mann, "Theory of the fermi interaction," *Phys. Rev.*, vol. 109, pp. 193–198, 1 Jan. 1958. DOI: 10.1103/PhysRev.109.193 (cit. on p. 6).

[28] J. I. Friedman and V. L. Telegdi, "Nuclear emulsion evidence for parity nonconservation in the decay chain $\pi^+ \to \mu^+ \to e^+$," *Phys. Rev.*, vol. 106, pp. 1290–1293, 6 Jun. 1957. DOI: 10.1103/PhysRev.106.1290 (cit. on p. 7).

[29] C. S. Wu, E. Ambler, R. W. Hayward, D. D. Hoppes, and R. P. Hudson, "Experimental test of parity conservation in beta decay," *Phys. Rev.*, vol. 105, pp. 1413–1415, 4 Feb. 1957. DOI: 10.1103/PhysRev.105.1413 (cit. on p. 7).

[30] J. P. Lees, V. Poireau, V. Tisserand, *et al.*, "Observation of time-reversal violation in the B^0 meson system," *Phys. Rev. Lett.*, vol. 109, p. 211 801, 21 Nov. 2012. DOI: 10.1103/PhysRevLett.109.211801 (cit. on p. 7).

[31] R. F. Streater and A. S. Wightman, *PCT, Spin and Statistics, and All That*. Princeton University Press, 1989. [Online]. Available: http://www.jstor.org/stable/j.ctt1cx3vcq (cit. on p. 7).

[32] C. Cheung, "TASI Lectures on Scattering Amplitudes," in *Proceedings, Theoretical Advanced Study Institute in Elementary Particle Physics: Anticipating the Next Discoveries in Particle Physics (TASI 2016): Boulder, CO, USA, June 6-July 1, 2016*. 2018, pp. 571–623. DOI: 10.48550/arXiv.1708.03872 (cit. on p. 7).

[33] D. Tong, "Gauge theory," *Lecture notes, DAMTP Cambridge*, vol. 10, 2018. [Online]. Available: https://www.damtp.cam.ac.uk/user/tong/gaugetheory.html (cit. on p. 8).

[34] C. Froggatt and H. Nielsen, "Hierarchy of quark masses, cabibbo angles and cp violation," *Nuclear Physics B*, vol. 147, no. 3, pp. 277–298, 1979. DOI: 10.1016/0550-3213(79)90316-X (cit. on p. 8).

[35] M. R. Francis, *The mystery of particle generations*, May 2015. [Online]. Available: https://www.symmetrymagazine.org/article/august-2015/the-mystery-of-particle-generations (cit. on p. 9).

[36] F. Englert and R. Brout, "Broken symmetry and the mass of gauge vector mesons," *Phys. Rev. Lett.*, vol. 13, pp. 321–323, 9 Aug. 1964. DOI: 10.1103/PhysRevLett.13.321 (cit. on p. 10).

[37] P. W. Higgs, "Broken symmetries and the masses of gauge bosons," *Phys. Rev. Lett.*, vol. 13, pp. 508–509, 16 Oct. 1964. DOI: 10.1103/PhysRevLett.13.508 (cit. on p. 10).

[38] G. S. Guralnik, C. R. Hagen, and T. W. B. Kibble, "Global conservation laws and massless particles," *Phys. Rev. Lett.*, vol. 13, pp. 585–587, 20 Nov. 1964. DOI: 10.1103/PhysRevLett.13.585 (cit. on p. 10).

[39] G. Aad, B. Abbott, B. Abeloos, *et al.*, "Observation of a new particle in the search for the standard model higgs boson with the ATLAS detector at the LHC," *Physics Letters B*, vol. 716, no. 1, pp. 1–29, 2012. DOI: 10.1016/j.physletb.2012.08.020 (cit. on pp. 10, 41, 146).

[40] S. Chatrchyan, V. Khachatryan, A. M. Sirunyan, *et al.*, "Observation of a new boson at a mass of 125 gev with the CMS experiment at the LHC," *Physics Letters B*, vol. 716, no. 1, pp. 30–61, 2012. DOI: 10.1016/j.physletb.2012.08.021 (cit. on pp. 10, 41).

[41] K. Nguyen, "The higgs mechanism," *uni-muenchen. de*, 2009. [Online]. Available: https://www.theorie.physik.uni-muenchen.de/lsfrey/teaching/archiv/sose_09/rng/higgs_mechanism.pdf (cit. on p. 11).

[42] W. Wang, "Recent developments on the CKM matrix," *International Journal of Modern Physics A*, vol. 29, no. 20, p. 1 430 040, 2014. DOI: 10.1142/S0217751X14300403 (cit. on p. 12).

[43] F. Archilli, M. Bettler, P. Owen, and K. A. Petridis, "Flavour-changing neutral currents making and breaking the Standard Model," *Nature*, vol. 546, no. 7657, pp. 221–226, 2017. DOI: 10.1038/nature21721 (cit. on p. 12).

[44] S. L. Glashow, J. Iliopoulos, and L. Maiani, "Weak interactions with lepton-hadron symmetry," *Physical review D*, vol. 2, no. 7, p. 1285, 1970. DOI: 10.1103/PhysRevD.2.1285 (cit. on p. 12).

[45] Wikipedia Commons, *Standard model of elementary particle physics*, 2023. [Online]. Available: https://upload.wikimedia.org/wikipedia/commons/0/00/Standard_Model_of_Elementary_Particles.svg (cit. on p. 14).

[46] H. Lehmann, K. Symanzik, and W. Zimmermann, "Zur formulierung quantisierter feldtheorien," *Il Nuovo Cimento (1955-1965)*, vol. 1, pp. 205–225, 1955. [Online]. Available: https://link.springer.com/article/10.1007/bf02731765 (cit. on p. 15).

[47] B. A. Kniehl, A. F. Pikelner, and O. L. Veretin, "mr: a C++ library for the matching and running of the Standard Model parameters," *Comput. Phys. Commun.*, vol. 206, pp. 84–96, 2016. DOI: 10.1016/j.cpc.2016.04.017 (cit. on p. 17).

[48] M. Veltman *et al.*, "Regularization and renormalization of gauge fields," *Nuclear Physics B*, vol. 44, no. 1, pp. 189–213, 1972. DOI: 10.1016/0550-3213(72)90279-9 (cit. on p. 15).

[49] D. J. Gross and F. Wilczek, "Ultraviolet behavior of non-abelian gauge theories," *Phys. Rev. Lett.*, vol. 30, pp. 1343–1346, 26 Jun. 1973. DOI: 10.1103/PhysRevLett.30.1343 (cit. on p. 17).

[50] H. D. Politzer, "Reliable perturbative results for strong interactions?" *Phys. Rev. Lett.*, vol. 30, pp. 1346–1349, 26 Jun. 1973. DOI: 10.1103/PhysRevLett.30.1346 (cit. on p. 17).

[51] J. Greensite, *An introduction to the confinement problem*. Springer, 2011, vol. 821 (cit. on p. 18).

[52] S. Marzani, G. Soyez, and M. Spannowsky, *Looking Inside Jets*. Springer International Publishing, 2019. DOI: 10.1007/978-3-030-15709-8 (cit. on p. 18).

[53] J. C. Collins, D. E. Soper, and G. Sterman, "Factorization of hard processes in QCD," 2004. DOI: 10.48550/arXiv.hep-ph/0409313 (cit. on p. 18).

[54] Y.-Q. Ma and J.-W. Qiu, "Extracting parton distribution functions from lattice QCD calculations," *Physical Review D*, vol. 98, no. 7, p. 074 021, 2018. DOI: 10.1103/PhysRevD.98.074021 (cit. on p. 19).

[55] S. Bhattacharya, K. Cichy, M. Constantinou, A. Metz, A. Scapellato, and F. Steffens, "Parton distribution functions beyond leading twist from lattice QCD: The $h_L(x)$ case," *Physical Review D*, vol. 104, no. 11, Dec. 2021. DOI: 10.1103/physrevd.104.114510 (cit. on p. 19).

[56] H. W. Kendall, "Deep inelastic scattering: Experiments on the proton and the observation of scaling," *Reviews of Modern Physics*, vol. 63, no. 3, p. 597, 1991. DOI: 10.1007/978-1-4419-8507-1_9 (cit. on p. 19).

[57] V. Chekelian, "Proton structure and parton distribution functions from HERA," in *EPJ Web of Conferences*, EDP Sciences, vol. 126, 2016, p. 02 005. DOI: 10.1051/epjconf/201612602005 (cit. on p. 19).

[58] T.-J. Hou, J. Gao, T. J. Hobbs, *et al.*, "New CTEQ global analysis of quantum chromodynamics with high-precision data from the LHC," *Phys. Rev. D*, vol. 103, p. 014 013, 1 Jan. 2021. DOI: 10.1103/PhysRevD.103.014013 (cit. on p. 19).

[59] R. D. Ball, S. Carrazza, J. Cruz-Martinez, *et al.*, "The path to proton structure at 1% accuracy," *The European Physical Journal C*, vol. 82, no. 5, p. 428, 2022. DOI: 10.1140/epjc/s10052-022-10328-7 (cit. on pp. 19, 20).

[60] S. Bailey, T. Cridge, L. A. Harland-Lang, A. D. Martin, and R. S. Thorne, "Parton distributions from LHC, HERA, Tevatron and fixed target data: MSHT20 PDFs," *The European Physical Journal C*, vol. 81, no. 4, p. 341, 2021. DOI: 10.1140/epjc/s10052-021-09057-0 (cit. on p. 19).

[61] V. N. Gribov and L. N. Lipatov, "Deep inelastic ep scattering in perturbation theory," *Sov. J. Nucl. Phys.*, vol. 15, pp. 438–450, 1972. [Online]. Available: https://inspirehep.net/literature/73449 (cit. on p. 19).

[62] Y. L. Dokshitser, "Calculation of structure functions of deep-inelastic scattering and e+ e-annihilation by perturbation theory in quantum chromodynamics," *Soviet Journal of Experimental and Theoretical Physics*, vol. 46, p. 641, 1977. [Online]. Available: https://inspirehep.net/literature/126153 (cit. on p. 19).

[63] G. Altarelli and G. Parisi, "Asymptotic freedom in parton language," *Nuclear Physics B*, vol. 126, no. 2, pp. 298–318, 1977. DOI: 10.1016/0550-3213(77)90384-4 (cit. on p. 19).

[64] M. Diehl, "Generalized parton distributions," *Physics Reports*, vol. 388, no. 2-4, pp. 41–277, 2003. DOI: 10.1016/j.physrep.2003.08.002 (cit. on p. 19).

[65] A. V. Manohar, "Introduction to effective field theories," 2018. DOI: 10.48550/arXiv.1804.05863 (cit. on p. 20).

[66] S. Davidson, P. Gambino, M. Laine, M. Neubert, and C. Salomon, *Effective Field Theory in Particle Physics and Cosmology: Lecture Notes of the Les Houches Summer School: Volume 108, July 2017*. Oxford University Press, 2020, vol. 108. DOI: 10.1093/oso/9780198855743.001.0001 (cit. on p. 20).

[67] R. Shankar, "Effective field theory in condensed matter physics," *Conceptual foundations of quantum field theory*, pp. 47–55, 1999. DOI: 10.48550/arXiv.cond-mat/9703210 (cit. on p. 20).

[68] B. Kol and M. Smolkin, "Non-relativistic gravitation: From newton to einstein and back," *Classical and Quantum Gravity*, vol. 25, no. 14, p. 145 011, 2008. DOI: 10.1088/0264-9381/25/14/145011 (cit. on p. 20).

[69] S. Endlich, A. Nicolis, R. A. Porto, and J. Wang, "Dissipation in the effective field theory for hydrodynamics: First-order effects," *Physical Review D*, vol. 88, no. 10, p. 105 001, 2013. DOI: 10.1103/PhysRevD.88.105001 (cit. on p. 20).

[70] C. N. Yang, "Fermi's beta-decay theory," *Int. J. Mod. Phys. A*, vol. 27, p. 1 230 005, 2012. DOI: 10.1142/S0217751X12300050 (cit. on p. 20).

[71] I. Brivio and M. Trott, "The standard model as an effective field theory," *Physics Reports*, vol. 793, pp. 1–98, 2019. DOI: 10.1016/j.physrep.2018.11.002 (cit. on pp. 21, 25, 120).

[72] S. Weinberg, "Phenomenological lagrangians," *Physica, A;(Netherlands)*, vol. 96, 1979. DOI: 10.1016/0378-4371(79)90223-1 (cit. on p. 21).

[73] B. Grzadkowski, M. Iskrzyński, M. Misiak, and J. Rosiek, "Dimension-six terms in the Standard Model Lagrangian," *Journal of High Energy Physics*, vol. 2010, no. 10, pp. 1–18, 2010. DOI: 10.1007/JHEP10%282010%29085 (cit. on p. 22).

[74] L. Lehman, "Extending the standard model effective field theory with the complete set of dimension-7 operators," *Physical Review D*, vol. 90, no. 12, p. 125 023, 2014. DOI: 10.1103/PhysRevD.90.125023 (cit. on p. 22).

[75] L. Lehman and A. Martin, "Low-derivative operators of the standard model effective field theory via hilbert series methods," *Journal of High Energy Physics*, vol. 2016, no. 2, pp. 1–31, 2016. DOI: 10.1007/JHEP02%282016%29081 (cit. on p. 22).

[76] B. Henning, X. Lu, T. Melia, and H. Murayama, "Hilbert series and operator bases with derivatives in effective field theories," *Communications in Mathematical Physics*, vol. 347, pp. 363–388, 2016. DOI: 10.1007/s00220-015-2518-2 (cit. on p. 22).

[77] E. E. Jenkins, A. V. Manohar, and P. Stoffer, "Low-energy effective field theory below the electroweak scale: Operators and matching," *Journal of High Energy Physics*, vol. 2018, no. 3, pp. 1–45, 2018. DOI: 10.1007/JHEP03%282018%29016 (cit. on p. 22).

[78] A. Greljo, A. Palavrić, and A. E. Thomsen, "Adding flavor to the smeft," *Journal of High Energy Physics*, vol. 2022, no. 10, pp. 1–58, 2022. DOI: 10.1007/JHEP10%282022%29005 (cit. on p. 22).

[79] C. Zhang and S. Willenbrock, "Effective-field-theory approach to top-quark production and decay," *Physical Review D*, vol. 83, no. 3, p. 034 006, 2011. DOI: 10.1103/PhysRevD.83.034006 (cit. on p. 22).

[80] M. Kobayashi and T. Maskawa, "CP-violation in the renormalizable theory of weak interaction," *Progress of theoretical physics*, vol. 49, no. 2, pp. 652–657, 1973. DOI: 10.1143/PTP.49.652 (cit. on p. 23).

[81] M. L. Perl, G. S. Abrams, A. M. Boyarski, *et al.*, "Evidence for Anomalous Lepton Production in $e^+ - e^-$ Annihilation," *Phys. Rev. Lett.*, vol. 35, pp. 1489–1492, 22 Dec. 1975. DOI: 10.1103/PhysRevLett.35.1489 (cit. on p. 23).

[82] S. Herb, D. Hom, L. Lederman, *et al.*, "Observation of a dimuon resonance at 9.5 GeV in 400-GeV proton-nucleus collisions," *Physical Review Letters*, vol. 39, no. 5, p. 252, 1977. DOI: 10.1103/PhysRevLett.39.252 (cit. on p. 23).

[83] W. Bartel, L. Becker, C. Bowdery, *et al.*, "A measurement of the electroweak induced charge asymmetry in $e^+e^- \to b\bar{b}$," *Physics Letters B*, vol. 146, no. 6, pp. 437–442, 1984. DOI: 10.1016/0370-2693(84)90156-4 (cit. on p. 23).

[84] T. M. Liss and P. L. Tipton, "The discovery of the top quark," *Scientific American*, vol. 277, no. 3, pp. 54–59, 1997. [Online]. Available: https://www.jstor.org/stable/24096562 (cit. on p. 24).

[85] F. Abe, H. Akimoto, A. Akopian, *et al.*, "Observation of Top Quark Production in $\bar{p}p$ Collisions with the Collider Detector at Fermilab," *Phys. Rev. Lett.*, vol. 74, pp. 2626–2631, 14 Apr. 1995. DOI: 10.1103/PhysRevLett.74.2626 (cit. on p. 24).

[86] S. Abachi, B. Abbott, M. Abolins, *et al.*, "Observation of the Top Quark," *Phys. Rev. Lett.*, vol. 74, pp. 2632–2637, 14 Apr. 1995. DOI: 10.1103/PhysRevLett.74.2632 (cit. on p. 24).

[87] G. L. Kane, G. A. Ladinsky, and C. .-. Yuan, "Using the top quark for testing standard-model polarization and CP predictions," *Phys. Rev. D*, vol. 45, pp. 124–141, 1 Jan. 1992. DOI: 10.1103/PhysRevD.45.124 (cit. on p. 24).

[88] A. H. Hoang, "What is the top quark mass?" *Annual Review of Nuclear and Particle Science*, vol. 70, pp. 225–255, 2020. DOI: 10.1146/annurev-nucl-101918-023530 (cit. on p. 24).

[89] G. Degrassi, S. Di Vita, J. Elias-Miro, *et al.*, "Higgs mass and vacuum stability in the Standard Model at NNLO," *Journal of High Energy Physics*, vol. 2012, no. 8, pp. 1–33, 2012. DOI: 10.1007/JHEP08(2012)098 (cit. on p. 24).

[90] G. Panico and A. Wulzer, *The composite nambu-goldstone higgs*. Springer, 2016, vol. 1506 (cit. on p. 25).

[91] E. Malkawi, T. Tait, and C.-P. Yuan, "A model of strong flavor dynamics for the top quark," *Physics Letters B*, vol. 385, no. 1-4, pp. 304–310, 1996. DOI: 10.1016/0370-2693%2896%2900859-3 (cit. on p. 25).

[92] R. Franceschini, "Beyond-Standard-Model physics associated with the top quark," 2023. DOI: 10.48550/arXiv.2301.04407 (cit. on p. 25).

[93] S. Tosi, "Top quark physics by CMS," World Scientific, 2021, pp. 363–365. DOI: 10.1142/9789811233913_0066 (cit. on p. 25).

[94] R. L. Workman *et al.*, "Review of Particle Physics," *PTEP*, vol. 2022, p. 083C01, 2022. DOI: 10.1093/ptep/ptac097 (cit. on pp. 25, 26).

[95] M. Czakon, P. Fiedler, and A. Mitov, "Total top-quark pair-production cross section at hadron colliders through $O(\alpha_S^4)$," *Phys. Rev. Lett.*, vol. 110, p. 252 004, 25 Jun. 2013. DOI: 10.1103/PhysRevLett.110.252004 (cit. on p. 25).

[96] S. Catani, S. Devoto, M. Grazzini, S. Kallweit, and J. Mazzitelli, "Top-quark pair production at the LHC: Fully differential QCD predictions at NNLO," *Journal of High Energy Physics*, vol. 2019, no. 7, pp. 1–27, 2019. DOI: 10.1007/JHEP07%282019%29100 (cit. on p. 25).

[97] M. Czakon, D. Heymes, A. Mitov, D. Pagani, I. Tsinikos, and M. Zaro, "Top-pair production at the LHC through NNLO QCD and NLO EW," *Journal of High Energy Physics*, vol. 2017, no. 10, pp. 1–23, 2017. DOI: 10.1007/JHEP10(2017)186 (cit. on pp. 25, 161, 173).

[98] G. Aad, B. Abbott, D. C. Abbott, *et al.*, "Inclusive and differential cross-sections for dilepton $t\bar{t}$ production measured in $\sqrt{s}$= 13 TeV pp collisions with the ATLAS detector," *Journal of High Energy Physics*, vol. 2023, no. 7, p. 141, 2023. DOI: 10.1007/JHEP07(2023)141 (cit. on p. 26).

[99] L. T. W. Group, *LHCTopWG Summary Plots*, Accessed: 2010-09-30. [Online]. Available: https://twiki.cern.ch/twiki/bin/view/LHCPhysics/LHCTopWGSummaryPlots (cit. on pp. 26, 27).

[100] G. Aad, B. Abbott, D. C. Abbott, *et al.*, "Differential $t\bar{t}$ cross-section measurements using boosted top quarks in the all-hadronic final state with 139 fb^1 of ATLAS data," *Journal of High Energy Physics*, vol. 2023, no. 4, p. 80, 2023. DOI: 10.1007/JHEP04(2023)080 (cit. on p. 26).

[101] G. Aad, B. Abbott, D. Abbott, *et al.*, "Measurements of differential cross-sections in top-quark pair events with a high transverse momentum top quark and limits on beyond the Standard Model contributions to top-quark pair production with the ATLAS detector at $\sqrt{s}$ = 13 TeV," *Journal of High Energy Physics*, vol. 2022, no. 6, pp. 1–73, 2022. DOI: 10.1007/JHEP06(2022)063 (cit. on p. 26).

[102] G. Aad, B. Abbott, D. C. Abbott, *et al.*, "Measurements of top-quark pair single- and double-differential cross-sections in the all-hadronic channel in pp collisions at $\sqrt{s}$ = 13 TeV using the ATLAS detector," *Journal of High Energy Physics*, vol. 2021, no. 1, pp. 1–76, 2021. DOI: 10.1007/JHEP01%282021%29033 (cit. on p. 26).

[103] G. Aad, B. Abbott, D. C. Abbott, *et al.*, "Measurement of the $t\bar{t}$ production cross-section in the lepton+ jets channel at $\sqrt{s}$ = 13 TeV with the ATLAS experiment," *Physics Letters B*, vol. 810, p. 135 797, 2020. DOI: 10.1016/j.physletb.2020.135797 (cit. on p. 26).

[104] P. D. Group, P. Zyla, R. Barnett, *et al.*, "Review of particle physics," *Progress of Theoretical and Experimental Physics*, vol. 2020, no. 8, 2020. [Online]. Available: https://pdg.lbl.gov/ (cit. on pp. 28, 29, 45).

[105] T. Dado, T. Peiffer, M. Racko, E. Shabalina, S. Tokar, and A. Quadt, "Measurement of the top-quark decay width in top-quark pair events in the dilepton channel at $\sqrt{s}$ = 13TeV with the ATLAS detector," ATLAS-COM-CONF-2019-052, Geneva, 2019. [Online]. Available: https://cds.cern.ch/record/2684952 (cit. on p. 28).

[106] W. Bernreuther, "Top quark physics at the LHC," *The Large Hadron Collider: Harvest of Run 1*, pp. 259–300, May 2008. DOI: 10.1007/978-3-319-15001-7_7 (cit. on pp. 28, 30).

[107] K. Melnikov, A. Scharf, and M. Schulze, "Top quark pair production in association with a jet: QCD corrections and jet radiation in top quark decays," *Physical Review D*, vol. 85, no. 5, p. 054 002, 2012. DOI: 10.1103/PhysRevD.85.054002 (cit. on p. 29).

[108] N. Kauer and D. Zeppenfeld, "Finite-width effects in top quark production at hadron colliders," *Physical Review D*, vol. 65, no. 1, p. 014 021, 2001. DOI: 10.1103/PhysRevD.65.014021 (cit. on p. 29).

[109] C. Uhlemann and N. Kauer, "Narrow-width approximation accuracy," *Nuclear physics B*, vol. 814, no. 1-2, pp. 195–211, 2009. DOI: 10.1016/j.nuclphysb.2009.01.022 (cit. on p. 29).

[110] D. Berdine, N. Kauer, and D. Rainwater, "Breakdown of the narrow width approximation for new physics," *Physical review letters*, vol. 99, no. 11, p. 111 601, 2007. DOI: 10.1103/PhysRevLett.99.111601 (cit. on p. 30).

[111] M. Beneke, I. Efthymiopoulos, M. L. Mangano, *et al.*, "Top quark physics," 2000. DOI: 10.48550/arXiv.hep-ph/0003033 (cit. on pp. 30, 32, 34, 110).

[112] G. Mahlon and S. Parke, "Single top quark production at the LHC: Understanding spin," *Physics Letters B*, vol. 476, no. 3-4, pp. 323–330, Mar. 2000. DOI: 10.1016/s0370-2693(00)00149-0 (cit. on pp. 30, 38).

[113] A. Brandenburg, Z. Si, and P. Uwer, "QCD-corrected spin analysing power of jets in decays of polarized top quarks," *Physics Letters B*, vol. 539, no. 3, pp. 235–241, 2002, ISSN: 0370-2693. DOI: https://doi.org/10.1016/S0370-2693(02)02098-1 (cit. on p. 31).

[114] J. A. Aguilar-Saavedra, J. Carvalho, N. Castro, A. Onofre, and F. Veloso, "Probing anomalous *Wtb* couplings in top pair decays," *The European Physical Journal C*, vol. 50, no. 3, pp. 519–533, 2007. DOI: 10.1140/epjc/s10052-007-0289-4 (cit. on p. 31).

[115] C. Severi and E. Vryonidou, "Quantum entanglement and top spin correlations in SMEFT at higher orders," *Journal of High Energy Physics*, vol. 2023, no. 1, p. 148, 2023. DOI: 10.1007/JHEP01(2023)148 (cit. on pp. 31, 32, 39).

[116] M. J. Fenton, A. Shmakov, T.-W. Ho, S.-C. Hsu, D. Whiteson, and P. Baldi, "Permutationless many-jet event reconstruction with symmetry preserving attention networks," *Physical Review D*, vol. 105, no. 11, p. 112 008, 2022. DOI: 10.1103/PhysRevD.105.112008 (cit. on p. 32).

[117] A. Shmakov, M. J. Fenton, T.-W. Ho, S.-C. Hsu, D. Whiteson, and P. Baldi, "SPANet: Generalized permutationless set assignment for particle physics using symmetry preserving attention," *SciPost Physics*, vol. 12, no. 5, p. 178, 2022. DOI: 10.21468/SciPostPhys.12.5.178 (cit. on p. 32).

[118] K. Blum, *Density matrix theory and applications*. Springer Science & Business Media, 2012, vol. 64 (cit. on pp. 32, 126).

[119] S. D. Kunikeev and D. A. Lidar, "Spin density matrix of a two-electron system. I. General theory and exact master equations," *Phys. Rev. B*, vol. 77, p. 045 319, 4 Jan. 2008. DOI: 10.1103/PhysRevB.77.045319 (cit. on p. 32).

[120] H. M. McConnell, "Spin density matrices for paramagnetic molecules," *The Journal of Chemical Physics*, vol. 28, no. 6, pp. 1188–1192, 1958. DOI: 10.1063/1.1744365 (cit. on p. 32).

[121] S. Adhikari, C. Akondi, M. Albrecht, *et al.*, "Measurement of spin density matrix elements in Λ (1520) photoproduction at 8.2–8.8 GeV," *Physical Review C*, vol. 105, no. 3, p. 035 201, 2022. DOI: 10.1103/PhysRevC.105.035201 (cit. on p. 32).

[122] S. I. Manaenkov and on behalf of the HERMES Collaboration, "Study of spin-density matrix in exclusive electroproduction of ω meson at HERMES," *Journal of Physics: Conference Series*, vol. 678, no. 1, p. 012 043, Jan. 2016. DOI: 10.1088/1742-6596/678/1/012043 (cit. on p. 32).

[123] G. Alexeev, M. Alexeev, A. Amoroso, *et al.*, "Spin density matrix elements in exclusive ω ω meson muoproduction," *The European Physical Journal C*, vol. 81, pp. 1–22, 2021. DOI: 10.1140/epjc/s10052-020-08740-y (cit. on p. 32).

[124] I. R. Bailey, "The W boson spin density matrix at OPAL," Cambridge University, 2004. [Online]. Available: https://cds.cern.ch/record/878813/files/Theisis-2007-Bailey.pdf (cit. on p. 32).

[125] F. Becattini and M. A. Lisa, "Polarization and vorticity in the quark–gluon plasma," *Annual Review of Nuclear and Particle Science*, vol. 70, pp. 395–423, 2020. DOI: 10.1146/annurev-nucl-021920-095245 (cit. on p. 32).

[126] S. Parke and Y. Shadmi, "Spin correlations in top-quark pair production at e^+e^- colliders," *Physics Letters B*, vol. 387, no. 1, pp. 199–206, 1996. DOI: 10.1016/0370-2693%2896%2900998-7 (cit. on p. 32).

[127] W. Bernreuther, D. Heisler, and Z. G. Si, "A set of top quark spin correlation and polarization observables for the LHC: Standard Model predictions and new physics contributions," *Journal of High Energy Physics*, vol. 2015, no. 12, pp. 1–36, 2015. DOI: 10.1007/JHEP12(2015)026 (cit. on pp. 32, 36–39).

[128] M. Baumgart and B. Tweedie, "A new twist on top quark spin correlations," *Journal of High Energy Physics*, vol. 2013, no. 3, pp. 1–41, 2013. DOI: 10.1007/JHEP03(2013)117 (cit. on pp. 32–34).

[129] B. Ravina, E. Simpson, and J. Howarth, "Observing $t\bar{t}Z$ spin correlations at the LHC," *The European Physical Journal C*, vol. 81, no. 9, pp. 1–11, 2021. DOI: 10.1140/epjc/s10052-021-09605-8 (cit. on pp. 32, 110, 124).

[130] Y. Afik and J. R. M. de Nova, "Entanglement and quantum tomography with top quarks at the LHC," *The European Physical Journal Plus*, vol. 136, no. 9, pp. 1–23, 2021. DOI: 10.1140/epjp/s13360-021-01902-1 (cit. on pp. 32, 33, 127–129, 131, 132, 137).

[131] W. Bernreuther, M. Flesch, and P. Haberl, "Signatures of Higgs bosons in the top quark decay channel at hadron colliders," *Physical Review D*, vol. 58, no. 11, p. 114 031, 1998. DOI: 10.1103/PhysRevD.58.114031 (cit. on pp. 34, 37).

[132] G. Mahlon and S. Parke, "Angular correlations in top quark pair production and decay at hadron colliders," *Phys. Rev. D*, vol. 53, pp. 4886–4896, 9 May 1996. DOI: 10.1103/PhysRevD.53.4886 (cit. on p. 38).

[133] W. Bernreuther, A. Brandenburg, and P. Uwer, "Transverse polarization of top quark pairs at the Tevatron and the large hadron collider," *Physics Letters B*, vol. 368, no. 1-2, pp. 153–162, 1996. DOI: 10.1016/0370-2693(95)01475-6 (cit. on p. 38).

[134] W. G. D. Dharmaratna and G. R. Goldstein, "Single quark polarization in quantum chromodynamics subprocesses," *Phys. Rev. D*, vol. 53, pp. 1073–1086, 3 Feb. 1996. DOI: 10.1103/PhysRevD.53.1073 (cit. on p. 38).

[135] G. Aad, B. Abbott, D. C. Abbott, *et al.*, "Measurement of the polarisation of single top quarks and antiquarks produced in the t-channel at $\sqrt{s} = 13 TeV and bounds on the twb dipo$ *Journal of High Energy Physics*, vol. 2022, no. 11, p. 40, 2022. DOI: 10.1007/JHEP11(2022)040 (cit. on p. 38).

[136] W. Bernreuther, A. Brandenburg, Z. G. Si, and P. Uwer, "Top quark pair production and decay at hadron colliders," *Nuclear Physics B*, vol. 690, no. 1-2, pp. 81–137, 2004, ISSN: 05503213. DOI: 10.1016/j.nuclphysb.2004.04.019. arXiv: 0403035 [hep-ph] (cit. on p. 38).

[137] V. Barger, J. Ohnemus, and R. Phillips, "Spin correlation effects in the hadroproduction and decay of very heavy top quark pairs," *International Journal of Modern Physics A*, vol. 4, no. 03, pp. 617–625, 1989. DOI: 10.1142/S0217751X89000297 (cit. on p. 38).

[138] B. Abbott, M. Abolins, V. Abramov, *et al.*, "Spin Correlation in production from $p\bar{p}$ Collisions at $\sqrt{s} = 1.8$TeV," *Physical Review Letters*, vol. 85, no. 2, pp. 256–261, Jul. 2000. DOI: 10.1103/physrevlett.85.256 (cit. on p. 38).

[139] V. Abazov, B. Abbott, B. Acharya, *et al.*, "Measurement of spin correlation in $t\bar{t}$ production using dilepton final states," *Physics Letters B*, vol. 702, no. 1, pp. 16–23, Aug. 2011. DOI: 10.1016/j.physletb.2011.05.077 (cit. on p. 38).

[140] V. M. Abazov, B. Abbott, B. S. Acharya, *et al.*, "Measurement of Spin Correlation in $t\bar{t}$ Production Using a Matrix Element Approach," *Physical Review Letters*, vol. 107, no. 3, Jul. 2011. DOI: 10.1103/physrevlett.107.032001 (cit. on p. 38).

[141] T. Aaltonen, B. Álvarez González, S. Amerio, *et al.*, "Measurement of $t\bar{t}$ spin correlation in $p\bar{p}$ collisions using the CDF II detector at the Tevatron," *Physical Review D*, vol. 83, no. 3, Feb. 2011. DOI: 10.1103/physrevd.83.031104 (cit. on p. 38).

[142] V. M. Abazov, B. Abbott, B. S. Acharya, *et al.*, "Evidence for spin correlation in $t\bar{t}$ production," *Physical Review Letters*, vol. 108, no. 3, Jan. 2012. DOI: 10.1103/physrevlett.108.032004 (cit. on p. 38).

[143] G. Aad, B. Abbott, J. Abdallah, *et al.*, "Observation of Spin Correlation in $t\bar{t}$ Events from pp Collisions at $\sqrt{s} = 7$ TeV Using the ATLAS Detector," *Phys. Rev. Lett.*, vol. 108, p. 212 001, 21 May 2012. DOI: 10.1103/PhysRevLett.108.212001 (cit. on p. 38).

[144] G. Aad, B. Abbott, J. Abdallah, *et al.*, "Measurements of spin correlation in top-antitop quark events from proton-proton collisions at $\sqrt{s}$= 7 TeV using the ATLAS detector," *Physical Review D*, vol. 90, no. 11, p. 112 016, 2014. DOI: 10.1103/PhysRevLett.114.142001 (cit. on p. 38).

[145] S. Chatrchyan, V. Khachatryan, A. M. Sirunyan, *et al.*, "Measurements of $t\bar{t}$ spin correlations and top-quark polarization using dilepton final states in pp collisions at $\sqrt{s}$= 7 TeV," *Physical review letters*, vol. 112, no. 18, p. 182 001, 2014. DOI: 10.1103/PhysRevLett.112.182001 (cit. on p. 38).

[146] M. Aaboud, G. Aad, B. Abbott, *et al.*, "Measurements of top quark spin observables in $t\bar{t}$ events using dilepton final states in $\sqrt{s}$ = 8TeV pp collisions with the ATLAS detector," *Journal of high energy physics*, vol. 2017, no. 3, pp. 1–50, 2017. DOI: 10.1007/JHEP03%282017%29113 (cit. on p. 38).

[147] V. Khachatryan, A. M. Sirunyan, A. Tumasyan, *et al.*, "Measurements of $t\bar{t}$ spin correlations and top quark polarization using dilepton final states in pp collisions at $\sqrt{s}$ = 8 TeV," *Physical Review D*, vol. 93, no. 5, p. 052 007, 2016. DOI: 10.1103/PhysRevD.93.052007 (cit. on p. 38).

[148] M. Aaboud, G. Aad, B. Abbott, *et al.*, "Measurements of top-quark pair spin correlations in the $e\mu$ channel at $\sqrt{s}$ = 13 TeV using pp collisions in the ATLAS detector," *The European Physical Journal C*, vol. 80, no. 8, p. 754, 2020. DOI: 10.1140/epjc/s10052-020-8181-6 (cit. on p. 38).

[149] A. M. Sirunyan, A. Tumasyan, W. Adam, *et al.*, "Measurement of the top quark polarization and $t\bar{t}$ spin correlations using dilepton final states in proton-proton collisions at $\sqrt{s}$ = 13 TeV," *Physical Review D*, vol. 100, no. 7, Oct. 2019. DOI: 10.1103/physrevd.100.072002 (cit. on pp. 39, 40).

[150] W. Bernreuther, A. Brandenburg, Z. Si, and P. Uwer, "Spin properties of top quark pairs produced at hadron colliders," 2003. eprint: hep-ph/0304244 (cit. on p. 39).

[151] W. Bernreuther, A. Brandenburg, Z. G. Si, and P. Uwer, "Top-Quark spin correlations at hadron colliders: predictions at next-to-leading order QCD," *Phys. Rev. Lett.*, vol. 87, p. 242 002, 24 Nov. 2001. DOI: 10.1103/PhysRevLett.87.242002 (cit. on p. 39).

[152] W. Bernreuther, A. Brandenburg, and Z. Si, "Next-to-leading order QCD corrections to top quark spin correlations at hadron colliders: the reactions $q\bar{q} \to t\bar{t}(g)$," *Physics Letters B*, vol. 483, no. 1, pp. 99–104, 2000. DOI: 10.1016/S0370-2693(00)00583-9 (cit. on p. 39).

[153] R. Frederix, I. Tsinikos, and T. Vitos, "Probing the spin correlations of $t\bar{t}$ production at NLO QCD+EW," *Eur. Phys. J. C*, vol. 81, no. 9, p. 817, 2021. DOI: 10.1140/epjc/s10052-021-09612-9 (cit. on p. 39).

[154] A. Behring, M. Czakon, A. Mitov, R. Poncelet, and A. S. Papanastasiou, "Higher order corrections to spin correlations in top quark pair production at the LHC," *Physical Review Letters*, vol. 123, no. 8, Aug. 2019. DOI: 10.1103/physrevlett.123.082001 (cit. on p. 39).

[155] M. Czakon, A. Mitov, and R. Poncelet, "NNLO QCD corrections to leptonic observables in top-quark pair production and decay," *Journal of High Energy Physics*, vol. 2021, no. 5, May 2021. DOI: 10.1007/jhep05(2021)212 (cit. on p. 39).

[156] F. Hasert, S. Kabe, W. Krenz, *et al.*, "Observation of neutrino-like interactions without muon or electron in the gargamelle neutrino experiment," *Nuclear Physics B*, vol. 73, no. 1, pp. 1–22, 1974. DOI: 10.1016/0370-2693(73)90499-1 (cit. on p. 41).

[157] G. Arnison, A. Astbury, B. Aubert, *et al.*, "Experimental observation of isolated large transverse energy electrons with associated missing energy at $\sqrt{s} = 540$ GeV," *Physics Letters B*, vol. 122, no. 1, pp. 103–116, 1983. DOI: 10.1016/0370-2693(83)91177-2 (cit. on p. 41).

[158] M. Banner, R. Battiston, P. Bloch, *et al.*, "Observation of single isolated electrons of high transverse momentum in events with missing transverse energy at the CERN pp collider," *Physics Letters B*, vol. 122, no. 5-6, pp. 476–485, 1983. DOI: 10.1016/0370-2693(83)91605-2 (cit. on p. 41).

[159] G. Arnison, A. Astbury, B. Aubert, *et al.*, "Experimental observation of lepton pairs of invariant mass around 95 GeV/c^2 at the CERN SPS collider," *Physics Letters B*, vol. 126, no. 5, pp. 398–410, 1983. DOI: 10.1016/0370-2693(83)90188-0 (cit. on p. 41).

[160] P. Bagnaia, M. Banner, R. Battiston, *et al.*, "Evidence for $Z^0 \to e^+e^-$ at the CERN $\bar{p}p$ collider," *Physics Letters B*, vol. 129, no. 1-2, pp. 130–140, 1983. DOI: 10.1016/0370-2693(83)90744-X (cit. on p. 41).

[161] V. Fanti, A. Lai, D. Marras, *et al.*, "A new measurement of direct CP violation in two pion decays of the neutral kaon," *Physics Letters B*, vol. 465, no. 1-4, pp. 335–348, 1999. DOI: 10.1016/S0370-2693%2899%2901030-8 (cit. on p. 41).

[162] U. Heinz and M. Jacob, "Evidence for a new state of matter: An assessment of the results from the cern lead beam programme," 2000. DOI: 10.48550/arXiv.nucl-th/0002042 (cit. on p. 41).

[163] G. Aad, J. Butterworth, J. Thion, *et al.*, "The ATLAS experiment at the CERN Large Hadron Collider," *Jinst*, vol. 3, S08003, 2008. DOI: 10.1088/1748-0221/3/08/S08003 (cit. on pp. 41, 47, 50).

[164] C. Collaboration, S. Chatrchyan, G. Hmayakyan, *et al.*, "The CMS experiment at the CERN LHC," *Jinst*, vol. 3, S08004, 2008. DOI: 10.1088/1748-0221/3/08/S08004 (cit. on p. 41).

[165] S. Myers and E. Picasso, "The design, construction and commissioning of the CERN Large Electron–Positron collider," *Contemporary Physics*, vol. 31, no. 6, pp. 387–403, 1990. DOI: 10.1080/00107519008213789 (cit. on p. 42).

[166] H. Wiedemann and H. Wiedemann, *Particle Beam Parameters*. Springer, 2015, pp. 353–399 (cit. on p. 42).

[167] D. Boussard, E. Chiaveri, E. Haebel, *et al.*, "The LHC superconducting cavities," in *Proceedings of the 1999 Particle Accelerator Conference (Cat. No.99CH36366)*, vol. 2, 1999, 946–948 vol.2. DOI: 10.1109/PAC.1999.795409 (cit. on p. 42).

[168] "Radiofrequency cavities," 2012. [Online]. Available: https://cds.cern.ch/record/1997424 (cit. on p. 42).

[169] E. Todesco, G. Willering, B. Auchmann, *et al.*, "Training of the main dipoles magnets in the large hadron collider toward 7 TeV operation," *IEEE Transactions on Applied Superconductivity*, vol. 28, no. 3, pp. 1–5, 2018. DOI: 10.1109/TASC.2018.2799570 (cit. on p. 43).

[170] M. Benedikt, P. Collier, V. Mertens, J. Poole, and K. Schindl, "LHC Design Report," CERN Yellow Reports: Monographs, 2004. DOI: 10.5170/CERN-2004-003-V-3 (cit. on p. 43).

[171] K. Schindl, "The Injector Chain for the LHC; rev. version," Tech. Rep., 1999. [Online]. Available: https://cds.cern.ch/record/384396 (cit. on p. 43).

[172] R. Scrivens, M. Kronberger, D. Küchler, *et al.*, "Overview of the status and developments on primary ion sources at CERN," 2011. [Online]. Available: https://cds.cern.ch/record/1382102 (cit. on p. 43).

[173] J. Maestre, C. Torregrosa, K. Kershaw, *et al.*, "Design and behaviour of the large hadron collider external beam dumps capable of receiving 539 MJ/dump," *Journal of Instrumentation*, vol. 16, no. 11, P11019, 2021. DOI: 10.1088/1748-0221/16/11/P11019 (cit. on p. 43).

[174] by Rende Steerenberg, "LHC report: full house for the LHC," 2017. [Online]. Available: http://cds.cern.ch/record/2272573 (cit. on p. 43).

[175] E. Lopienska, "The CERN accelerator complex, layout in 2022. Complexe des accélérateurs du CERN en janvier 2022," 2022, General Photo. [Online]. Available: https://cds.cern.ch/record/2800984 (cit. on p. 44).

[176] L. Rossi, "The LHC superconducting magnets," in *Proceedings of the 2003 Particle Accelerator Conference*, IEEE, vol. 1, 2003, pp. 141–145. DOI: 10.1109/PAC.2003.1288863 (cit. on p. 44).

[177] H. Wollnik, *Optics of charged particles*. Academic Press, 2021 (cit. on p. 44).

[178] W. Herr and B. Muratori, "Concept of luminosity," 2006. DOI: 10.5170/CERN-2006-002.361 (cit. on p. 45).

[179] S. Myers, *Particle Physics Reference Library: Volume 3: Accelerators and Colliders*. Springer Nature, 2020, vol. 3, ch. 2 (cit. on p. 45).

[180] M. G. Minty and F. Zimmermann, *Measurement and control of charged particle beams*. Springer Nature, 2003 (cit. on p. 45).

[181] B. Ravina, "Measurement of the top quark coupling to the Z boson, and applications to searches for physics Beyond the Standard Model," Ph.D. dissertation, University of Sheffield, 2020. [Online]. Available: https://etheses.whiterose.ac.uk/27850/ (cit. on p. 46).

[182] R. Bruce, G. Arduini, H. Bartosik, *et al.*, "LHC Run 2: Results and challenges," MOAM5P50, 2016. DOI: 10.18429/JACoW-HB2016-MOAM5P50 (cit. on p. 46).

[183] G. Aad, B. Abbott, D. C. Abbott, *et al.*, "ATLAS data quality operations and performance for 2015–2018 data-taking," *Journal of instrumentation*, vol. 15, no. 04, 2020 (cit. on pp. 46, 90).

[184] J. Pequenao, "Event Cross Section in a computer generated image of the ATLAS detector.," 2008. [Online]. Available: https://cds.cern.ch/record/1096081 (cit. on p. 48).

[185] H. Ten Kate, "The ATLAS superconducting magnet system at the Large Hadron Collider," *Physica C: Superconductivity*, vol. 468, no. 15-20, pp. 2137–2142, 2008. DOI: 10.1016/j.physc.2008.05.146 (cit. on p. 49).

[186] A. Yamamoto, Y. Makida, R. Ruber, *et al.*, "The ATLAS central solenoid," *Nuclear Instruments and Methods in Physics Research Section A: Accelerators, Spectrometers, Detectors and Associated Equipment*, vol. 584, no. 1, pp. 53–74, 2008. DOI: 10.1016/j.nima.2007.09.047 (cit. on p. 49).

[187] G. Aad, B. Abbott, J. Abdallah, *et al.*, "The ATLAS Inner Detector commissioning and calibration," *The European Physical Journal C*, vol. 70, no. 3, pp. 787–821, 2010. DOI: 10.1140/epjc/s10052-010-1366-7 (cit. on p. 50).

[188] J. Pequenao, "Computer generated image of the ATLAS inner detector," 2008. [Online]. Available: https://cds.cern.ch/record/1095926 (cit. on p. 51).

[189] G. Hall, "Semiconductor particle tracking detectors," *Reports on Progress in Physics*, vol. 57, no. 5, p. 481, 1994. DOI: 10.1088/0034-4885/57/5/002 (cit. on p. 50).

[190] M. S. Alam *et al.*, "ATLAS pixel detector: Technical design report," Tech. Rep., May 1998. DOI: 10.17181/CERN.FOZZ.ZP3Q (cit. on p. 51).

[191] A. La Rosa and o. b. o. ATLAS collaboration, "The ATLAS Insertable B-Layer: from construction to operation," *Journal of Instrumentation*, vol. 11, no. 12, p. C12036, 2016. DOI: 10.1088/1748-0221/11/12/C12036 (cit. on p. 51).

[192] G. Aad, M. Ackers, F. Alberti, *et al.*, "ATLAS pixel detector electronics and sensors," *Journal of instrumentation*, vol. 3, no. 07, P07007, 2008. DOI: 10.1088/1748-0221/3/07/P07007 (cit. on p. 52).

[193] S. D'Auria, "The atlas semiconductor tracker: Operations and performance," in *2012 IEEE Nuclear Science Symposium and Medical Imaging Conference Record (NSS/MIC)*, 2012, pp. 1509–1511. DOI: 10.1109/NSSMIC.2012.6551362 (cit. on p. 52).

[194] E. Abat, T. Addy, T. Åkesson, *et al.*, "The ATLAS Transition Radiation Tracker (TRT) proportional drift tube: design and performance," *Journal of Instrumentation*, vol. 3, no. 02, P02013, 2008. DOI: 10.1088/1748-0221/3/02/P02013 (cit. on p. 52).

[195] A. Bingül, "The ATLAS TRT and its Performance at LHC," in *Journal of Physics: Conference Series*, IOP Publishing, vol. 347, 2012, p. 012 025. DOI: 10.1088/1742-6596/347/1/012025 (cit. on p. 52).

[196] J. M. Stahlman and A. T. collaboration, "Commissioning and erformance of the ATLAS Transition Radiation Tracker with first high energy pp and Pb-Pb collisions at LHC," *Physics Procedia*, vol. 37, pp. 506–514, 2012. DOI: 10.1016/j.phpro.2012.02.396 (cit. on p. 52).

[197] C. W. Fabjan and F. Gianotti, "Calorimetry for particle physics," *Rev. Mod. Phys.*, vol. 75, pp. 1243–1286, 4 Oct. 2003. DOI: 10.1103/RevModPhys.75.1243 (cit. on p. 53).

[198] A. Airapetian *et al.*, "ATLAS calorimeter performance Technical Design Report," Dec. 1996. [Online]. Available: https://cds.cern.ch/record/331059 (cit. on p. 53).

[199] V. Grassi, "The ATLAS liquid argon calorimeter at the CERN Large Hadron Collider: General performance and latest developments of the high voltage system," CERN, Geneva, Tech. Rep., 2013. [Online]. Available: https://cds.cern.ch/record/1628748 (cit. on p. 53).

[200] B. Aubert, B. Beaugiraud, J. Colas, *et al.*, "Construction, assembly and tests of the ATLAS electromagnetic barrel calorimeter," *Nuclear Instruments and Methods in Physics Research Section A: Accelerators, Spectrometers, Detectors and Associated Equipment*, vol. 558, no. 2, pp. 388–418, 2006. DOI: 10.1016/j.nima.2005.11.212 (cit. on p. 53).

[201] A. Artamonov, D. Bailey, G. Belanger, *et al.*, "The ATLAS forward calorimeter," *Journal of Instrumentation*, vol. 3, no. 02, P02010, 2008. DOI: 10.1088/1748-0221/3/02/P02010 (cit. on p. 54).

[202] J. Pequenao, "Computer Generated image of the ATLAS calorimeter," 2008. [Online]. Available: https://cds.cern.ch/record/1095927 (cit. on p. 54).

[203] A. M. Henriques Correia, "The ATLAS Tile Calorimeter," CERN, Geneva, Tech. Rep., 2015. DOI: 10.1109/ANIMMA.2015.7465554 (cit. on p. 55).

[204] A. Ahmad, "The ATLAS Tile Calorimeter performance and its upgrade towards the High-Luminosity LHC," *Moscow Univ. Phys. Bull.*, vol. 77, no. 2, pp. 156–158, 2022. DOI: 10.3103/S0027134922020047 (cit. on p. 55).

[205] S. Palestini, "The muon spectrometer of the ATLAS experiment," *Nuclear Physics B-Proceedings Supplements*, vol. 125, pp. 337–345, 2003. DOI: 10.1016/S0920-5632(03)91013-9 (cit. on p. 55).

[206] A. M. Group and M. Livan, "Monitored drift tubes in ATLAS," *Nuclear Instruments and Methods in Physics Research Section A: Accelerators, Spectrometers, Detectors and Associated Equipment*, vol. 384, no. 1, pp. 214–218, 1996. DOI: 10.1016/S0168-9002(96)00851-0 (cit. on p. 55).

[207] T. Argyropoulos, K. A. Assamagan, B. H. Benedict, *et al.*, "Cathode strip chambers in ATLAS: Installation, commissioning and in situ performance," *IEEE Transactions on Nuclear Science*, vol. 56, no. 3, pp. 1568–1574, 2009. DOI: 10.1109/TNS.2009.2020861 (cit. on p. 55).

[208] A. M. Group and A. Di Ciaccio, "Resistive plate chambers in ATLAS," *Nuclear Instruments and Methods in Physics Research Section A: Accelerators, Spectrometers, Detectors and Associated Equipment*, vol. 384, no. 1, pp. 222–224, 1996. DOI: 10.1088/1742-6596/280/1/012001 (cit. on p. 56).

[209] G. Cattani *et al.*, "The Resistive Plate Chambers of the ATLAS experiment: performance studies," in *Journal of Physics: Conference Series*, IOP Publishing, vol. 280, 2011, p. 012 001. DOI: 10.1088/1742-6596/280/1/012001 (cit. on p. 56).

[210] K. Nagai, "Thin gap chambers in ATLAS," *Nuclear Instruments and Methods in Physics Research Section A: Accelerators, Spectrometers, Detectors and Associated Equipment*, vol. 384, no. 1, pp. 219–221, 1996. DOI: 10.1016/S0168-9002(96)01065-0 (cit. on p. 56).

[211] J. Pequenao, "Computer generated image of the ATLAS Muons subsystem," 2008. [Online]. Available: https://cds.cern.ch/record/1095929 (cit. on p. 56).

[212] A. collaboration *et al.*, "Operation of the ATLAS trigger system in Run 2," *Journal of Instrumentation*, vol. 15, no. 10, P10004, 2020. DOI: 10.1088/1748-0221/15/10/P10004 (cit. on pp. 57, 58).

[213] W. Buttinger, "The ATLAS Level-1 trigger system," in *Journal of Physics: Conference Series*, IOP Publishing, vol. 396, 2012, p. 012 010. DOI: 10.1088/1742-6596/396/1/012010 (cit. on p. 58).

[214] R. Achenbach, P. Adragna, V. Andrei, *et al.*, "The ATLAS Level-1 calorimeter trigger," *Journal of Instrumentation*, vol. 3, no. 03, P03001, 2008. DOI: 10.1088/1748-0221/3/03/P03001 (cit. on p. 58).

[215] ATLAS, "Performance of the ATLAS muon triggers in run 2," *Journal of Instrumentation*, vol. 15, no. 09, P09015–P09015, Sep. 2020. DOI: 10.1088/1748-0221/15/09/p09015 (cit. on p. 58).

[216] R. Simoniello, "The ATLAS Level-1 Topological Processor: from design to routine usage in Run-2," in *2018 IEEE Nuclear Science Symposium and Medical Imaging Conference Proceedings (NSS/MIC)*, 2018, pp. 1–4. DOI: 10.1109/NSSMIC.2018.8824280 (cit. on p. 58).

[217] C. Schiavi, "ATLAS High-Level Trigger algorithms for Run-2 Data-Taking," ATL-COM-DAQ-2015-053, Tech. Rep., 2015. [Online]. Available: https://cds.cern.ch/record/2016651 (cit. on p. 58).

[218] K. Nagano, A. Collaboration, *et al.*, "Algorithms, performance, development of the ATLAS High-Level trigger," in *Journal of Physics: Conference Series*, IOP Publishing, vol. 513, 2014, p. 012 026. DOI: 10.1088/1742-6596/513/1/012026 (cit. on p. 58).

[219] A. Collaboration *et al.*, "Performance of electron and photon triggers in ATLAS during LHC Run 2," *The European physical journal. C*, vol. 80, no. 1, p. 47, 2020. DOI: 10.1140/epjc/s10052-019-7500-2 (cit. on pp. 58, 136).

[220] G. Aad, "Performance of the ATLAS muon triggers in Run 2," *Journal of Instrumentation*, vol. 15, 2020. DOI: 10.1088/1748-0221/15/09/p09015 (cit. on pp. 58, 136).

[221] V. Lacuesta, "Track and vertex reconstruction in the ATLAS experiment," *Journal of Instrumentation*, vol. 8, no. 02, p. C02035, 2013. DOI: 10.1088/1748-0221/8/02/C02035 (cit. on p. 60).

[222] A. Rosenfeld and J. L. Pfaltz, "Sequential operations in digital picture processing," *Journal of the ACM (JACM)*, vol. 13, no. 4, pp. 471–494, 1966. DOI: 10.1145/321356.321357 (cit. on p. 60).

[223] M. Aaboud, G. Aad, B. Abbott, *et al.*, "Performance of the ATLAS track reconstruction algorithms in dense environments in LHC Run 2," *The European Physical Journal C*, vol. 77, pp. 1–30, 2017. DOI: 10.1140/epjc/s10052-017-5225-7 (cit. on pp. 60–62).

[224] R. Frühwirth, "Application of Kalman filtering to track and vertex fitting," *Nuclear Instruments and Methods in Physics Research Section A: Accelerators, Spectrometers, Detectors and Associated Equipment*, vol. 262, no. 2-3, pp. 444–450, 1987. DOI: 10.1016/0168-9002(87)90887-4 (cit. on p. 60).

[225] P. Billoir and S. Qian, "Simultaneous pattern recognition and track fitting by the Kalman filtering method," *Nuclear Instruments and Methods in Physics Research Section A: Accelerators, Spectrometers, Detectors and Associated Equipment*, vol. 294, no. 1-2, pp. 219–228, 1990. DOI: 10.1016/0168-9002(90)91835-Y (cit. on pp. 60, 62).

[226] R. Mankel, "Pattern recognition and event reconstruction in particle physics experiments," *Reports on Progress in Physics*, vol. 67, no. 4, p. 553, 2004. DOI: 10.1088/0034-4885/67/4/R03 (cit. on p. 60).

[227] A. Collaboration *et al.*, "A neural network clustering algorithm for the ATLAS silicon pixel detector," *Journal of Instrumentation*, vol. 9, no. 09, P09009, 2014. DOI: 10.1088/1748-0221/9/09/P09009 (cit. on p. 60).

[228] T. Cornelissen, M. Elsing, I. Gavrilenko, W. Liebig, E. Moyse, and A. Salzburger, "The new ATLAS track reconstruction (NEWT)," in *Journal of Physics: Conference Series*, IOP Publishing, vol. 119, 2008, p. 032 014. DOI: 10.1088/1742-6596/119/3/032014 (cit. on p. 61).

[229] G. Aad, B. Abbott, J. Abdallah, *et al.*, "Muon reconstruction performance of the ATLAS detector in proton–proton collision data at $\sqrt{s}$ = 13 TeV," *The European Physical Journal C*, vol. 76, pp. 1–30, 2016. DOI: 10.1140/epjc/s10052-016-4120-y (cit. on pp. 61, 69, 71, 99).

[230] W. Lampl, P. Loch, S. Menke, *et al.*, "Calorimeter clustering algorithms: description and performance," Tech. Rep., 2008. [Online]. Available: https://cds.cern.ch/record/1099735?ln=en (cit. on p. 63).

[231] A. Collaboration, "Topological cell clustering in the ATLAS calorimeters and its performance in LHC Run 1," *Eur. Phys. J. C*, vol. 77, p. 490, 2017. DOI: 10.1140/epjc/s10052-017-5004-5 (cit. on p. 63).

[232] G. Aad, B. Abbott, D. C. Abbott, *et al.*, "Jet energy scale and resolution measured in proton–proton collisions at $\sqrt{s}$ = 13 TeV with the ATLAS detector," *The European Physical Journal C*, vol. 81, no. 8, p. 689, 2021. DOI: 10.1140/epjc/s10052-021-09402-3 (cit. on pp. 64, 74, 75).

[233] A. Buckley, C. White, and M. White, *Practical Collider Physics*. IOP Publishing, 2021 (cit. on pp. 64, 88).

[234] M. Aaboud, G. Aad, B. Abbott, *et al.*, "Jet reconstruction and performance using particle flow with the ATLAS Detector," *The European Physical Journal C*, vol. 77, pp. 1–47, 2017. DOI: 10.1140/epjc/s10052-017-5031-2 (cit. on pp. 64, 74).

[235] M. Aaboud, G. Aad, B. Abbott, *et al.*, "Electron reconstruction and identification in the ATLAS experiment using the 2015 and 2016 LHC proton–proton collision data at $\sqrt{s}$ = 13 TeV TeV," *The European Physical Journal C*, vol. 79, pp. 1–40, 2019. DOI: 10.1140/epjc/s10052-019-7140-6 (cit. on pp. 67, 68, 71, 98, 99).

[236] G. Aad, B. Abbott, D. C. Abbott, *et al.*, "Electron and photon performance measurements with the ATLAS detector using the 2015–2017 LHC proton-proton collision data," *Journal of Instrumentation*, vol. 14, no. 12, P12006, Dec. 2019. DOI: 10.1088/1748-0221/14/12/P12006 (cit. on pp. 67, 68).

[237] M. Aaboud, G. Aad, B. Abbott, *et al.*, "Electron and photon energy calibration with the ATLAS detector using 2015–2016 LHC proton-proton collision data," *Journal of Instrumentation*, vol. 14, no. 03, P03017, Mar. 2019. DOI: 10.1088/1748-0221/14/03/P03017 (cit. on p. 68).

[238] G. Aad, B. Abbott, D. C. Abbott, *et al.*, "Muon reconstruction and identification efficiency in ATLAS using the full Run 2 pp collision data set at $\sqrt{s}$ = 13 TeV," *The European Physical Journal C*, vol. 81, no. 7, p. 578, 2021. DOI: 10.1140/epjc/s10052-021-09233-2 (cit. on pp. 69, 70).

[239] R. K. Ellis, W. J. Stirling, and B. R. Webber, *QCD and collider physics*. Cambridge university press, 2003 (cit. on p. 71).

[240] G. Sterman and S. Weinberg, "Jets from quantum chromodynamics," *Physical Review Letters*, vol. 39, no. 23, p. 1436, 1977. DOI: 10.1103/PhysRevLett.39.1436 (cit. on p. 72).

[241] G. C. Blazey, J. R. Dittmann, S. D. Ellis, *et al.*, "Run II jet physics: proceedings of the run II QCD and weak boson physics workshop," 2000. DOI: 10.48550/arXiv.hep-ex/0005012 (cit. on p. 72).

[242] G. P. Salam and G. Soyez, "A practical seedless infrared-safe cone jet algorithm," *Journal of High Energy Physics*, vol. 2007, no. 05, p. 086, 2007. DOI: 10.1088/1126-6708/2007/05/086 (cit. on p. 72).

[243] R. Atkin, "Review of jet reconstruction algorithms," in *Journal of Physics: Conference Series*, IOP Publishing, vol. 645, 2015, p. 012 008. DOI: 10.1088/1742-6596/645/1/012008 (cit. on p. 72).

[244] M. Cacciari, G. P. Salam, and G. Soyez, "FastJet user manual: (for version 3.0. 2)," *The European Physical Journal C*, vol. 72, pp. 1–54, 2012. DOI: 10.1140/epjc/s10052-012-1896-2 (cit. on p. 72).

[245] S. Catani, Y. L. Dokshitzer, M. H. Seymour, and B. R. Webber, "Longitudinally-invariant K_T-clustering algorithms for hadron-hadron collisions," *Nuclear Physics B*, vol. 406, no. 1-2, pp. 187–224, 1993. DOI: 0.1016/0550-3213(93)90166-M (cit. on p. 72).

[246] "A Cambridge-Aachen (C-A) based Jet Algorithm for boosted top-jet tagging," CERN, Geneva, Tech. Rep., 2009. [Online]. Available: https://cds.cern.ch/record/1194489 (cit. on p. 72).

[247] M. Cacciari, G. P. Salam, and G. Soyez, "The anti-K_t jet clustering algorithm," *Journal of High Energy Physics*, vol. 2008, no. 04, p. 063, 2008. DOI: 10.1088/1126-6708/2008/04/063 (cit. on pp. 72, 73).

[248] G. Aad, B. Abbott, J. Abdallah, *et al.*, "Jet energy measurement with the ATLAS detector in proton-proton collisions at $\sqrt{s}$ = 7 TeV," *The European Physical Journal C*, vol. 73, no. 3, p. 2304, 2013. DOI: 10.1140/epjc/s10052-013-2304-2 (cit. on p. 73).

[249] M. Aaboud, G. Aad, B. Abbott, *et al.*, "Determination of jet calibration and energy resolution in proton–proton collisions at $\sqrt{s}$ = 8 TeV using the ATLAS detector," *The European Physical Journal C*, vol. 80, pp. 1–81, 2020. DOI: 10.1140/epjc/s10052-020-08477-8 (cit. on p. 74).

[250] M. Aaboud, G. Aad, B. Abbott, *et al.*, "Jet energy scale measurements and their systematic uncertainties in proton-proton collisions at $\sqrt{s}$ = 13 TeV with the ATLAS detector," *Phys. Rev. D*, vol. 96, p. 072 002, 7 Oct. 2017. DOI: 10.1103/PhysRevD.96.072002 (cit. on pp. 74, 75).

[251] G. Aad, B. Abbott, K. Abeling, *et al.*, "New techniques for jet calibration with the ATLAS detector," *The European Physical Journal C*, vol. 83, no. 8, p. 761, 2023. DOI: 10.1140/epjc/s10052-023-11837-9 (cit. on p. 74).

[252] G. Aad, B. Abbott, J. Abdallah, *et al.*, "Performance of pile-up mitigation techniques for jets in pp collisions at $\sqrt{s}$ = 8 TeV using the ATLAS detector," *The European Physical Journal C*, vol. 76, pp. 1–36, 2016. DOI: 10.1140/epjc/s10052-016-4395-z (cit. on p. 74).

[253] G. Aad, B. Abbott, D. C. Abbott, *et al.*, "ATLAS flavour-tagging algorithms for the LHC Run 2 pp collision dataset," *The European Physical Journal C*, vol. 83, no. 7, p. 681, 2023. DOI: 10.1140/epjc/s10052-023-11699-1 (cit. on pp. 75, 76, 93).

[254] "Optimisation of the ATLAS b-tagging performance for the 2016 LHC Run," CERN, Geneva, Tech. Rep., 2016. [Online]. Available: https://cds.cern.ch/record/2160731 (cit. on p. 75).

[255] "Identification of Jets Containing b-Hadrons with Recurrent Neural Networks at the ATLAS Experiment," CERN, Geneva, Tech. Rep., 2017. [Online]. Available: https://cds.cern.ch/record/2255226 (cit. on p. 75).

[256] S. Heer, "The secondary vertex finding algorithm with the ATLAS detector," CERN, Geneva, Tech. Rep., 2018. DOI: 10.22323/1.314.0762 (cit. on p. 76).

[257] "Topological b-hadron decay reconstruction and identification of b-jets with the JetFitter package in the ATLAS experiment at the LHC," CERN, Geneva, Tech. Rep., 2018. [Online]. Available: https://cds.cern.ch/record/2645405 (cit. on p. 76).

[258] A. Collaboration, "ATLAS b-jet identification performance and efficiency measurement with $t\bar{t}$ events in pp collisions at $\sqrt{s}$ = 13 TeV," *Eur. Phys. J. C*, vol. 79, p. 970, 2019. DOI: 10.1140/epjc/s10052-019-7450-8 (cit. on p. 76).

[259] T. G. Rizzo, *Z′ Phenomenology and the LHC*, 2006. DOI: 10.48550/arXiv.hep-ph/0610104 (cit. on p. 76).

[260] G. Aad, B. Abbott, D. C. Abbott, *et al.*, "ATLAS b-jet identification performance and efficiency measurement with $t\bar{t}$ events in pp collisions at $\sqrt{s}$ = 13 TeV," *The European Physical Journal C*, vol. 79, pp. 1–36, 2019. DOI: 10.1140/epjc/s10052-019-7450-8 (cit. on pp. 77, 163).

[261] M. Aaboud, G. Aad, B. Abbott, *et al.*, "Performance of missing transverse momentum reconstruction with the ATLAS detector using proton–proton collisions at $\sqrt{s}$ = 13TeV," *The European Physical Journal C*, vol. 78, no. 11, pp. 1–46, 2018. DOI: 10.1140/epjc/s10052-018-6288-9 (cit. on pp. 77, 78, 163).

[262] *ATLAS Run-2 Event Displays: Top-Antitop Quark Event*, https://twiki.cern.ch/twiki/bin/view/AtlasPublic/EventDisplayRun2Physics#Top_antiptop_candidate_event_rec, Accessed: 2023-05-16 (cit. on pp. 77, 79).

[263] B. Webber, "Parton shower Monte Carlo event generators," *Scholarpedia*, vol. 6, no. 12, p. 10 662, 2011. [Online]. Available: http://scholarpedia.org/article/Parton_shower_Monte_Carlo_event_generators (cit. on p. 80).

[264] S. Höche, "Introduction to parton-shower event generators," in *Journeys Through the Precision Frontier: Amplitudes for Colliders: TASI 2014 Proceedings of the 2014 Theoretical Advanced Study Institute in Elementary Particle Physics*, World Scientific, 2016, pp. 235–295. DOI: 10.48550/arXiv.1411.4085 (cit. on p. 80).

[265] A. Buckley, J. Butterworth, S. Gieseke, *et al.*, "General-purpose event generators for LHC physics," *Physics Reports*, vol. 504, no. 5, pp. 145–233, 2011. DOI: 10.1016/j.physrep.2011.03.005 (cit. on p. 80).

[266] R. Jansky and on behalf of the ATLAS Collaboration, "The ATLAS fast Monte Carlo production chain project," *Journal of Physics: Conference Series*, vol. 664, no. 7, p. 072 024, Dec. 2015. DOI: 10.1088/1742-6596/664/7/072024 (cit. on p. 82).

[267] C. Bierlich, S. Chakraborty, N. Desai, *et al.*, "A comprehensive guide to the physics and usage of PYTHIA 8.3," *SciPost Physics Codebases*, p. 008, 2022. [Online]. Available: https://arxiv.org/abs/2203.11601 (cit. on p. 83).

[268] R. Kleiss and R. Pittau, "Weight optimization in multichannel Monte Carlo," *Computer Physics Communications*, vol. 83, no. 2-3, pp. 141–146, 1994. DOI: 10.1016/0010-4655(94)90043-4 (cit. on p. 84).

[269] E. Byckling and K. Kajantie, "N-particle phase space in terms of invariant momentum transfers," *Nuclear Physics B*, vol. 9, no. 4, pp. 568–576, 1969. DOI: 10.1016/0550-3213(69)90271-5 (cit. on p. 84).

[270] A. van Hameren and C. G. Papadopoulos, "A hierarchical phase space generator for qcd antenna structures," *The European Physical Journal C - Particles and Fields*, vol. 25, no. 4, pp. 563–574, 2002. DOI: 10.1007/s10052-002-1000-4 (cit. on p. 84).

[271] R. Kleiss, S. Ellis, and W. J. Stirling, "A new Monte Carlo treatment of multiparticle phase space at high energies," *Comput. Phys. Commun.*, vol. 40, no. CERN-TH-4299-85, pp. 359–373, 1985. DOI: 10.1016/0010-4655(86)90119-0 (cit. on p. 84).

[272] S. Catani, S. Devoto, M. Grazzini, S. Kallweit, and J. Mazzitelli, "Top-quark pair hadroproduction at NNLO: differential predictions with the $\overline{\text{MS}}$ mass," *Journal of High Energy Physics*, vol. 2020, no. 8, pp. 1–30, 2020. DOI: 10.1007/JHEP08(2020)027 (cit. on pp. 84, 85).

[273] H. Elvang and Y.-t. Huang, "Scattering amplitudes," 2013. DOI: 10.48550/arXiv.1308.1697 (cit. on p. 84).

[274] K. G. Wilson and J. Kogut, "The renormalization group and the ϵ expansion," *Physics Reports*, vol. 12, no. 2, pp. 75–199, 1974, ISSN: 0370-1573. DOI: https://doi.org/10.1016/0370-1573(74)90023-4 (cit. on p. 84).

[275] W. T. Giele and E. W. N. Glover, "Higher-order corrections to jet cross sections in e^+e^- annihilation," *Phys. Rev. D*, vol. 46, pp. 1980–2010, 5 Sep. 1992. DOI: 10.1103/PhysRevD.46.1980 (cit. on p. 84).

[276] W. T. Giele, E. N. Glover, and D. A. Kosower, "Higher-order corrections to jet cross sections in hadron colliders," *Nuclear Physics B*, vol. 403, no. 3, pp. 633–667, 1993. DOI: 10.1016/0550-3213(93)90365-V (cit. on p. 84).

[277] S. Catani and M. H. Seymour, "A general algorithm for calculating jet cross sections in NLO QCD," *Nuclear Physics B*, vol. 485, no. 1-2, pp. 291–419, 1997. DOI: 10.1016/S0550-3213(96)00589-5 (cit. on p. 84).

[278] S. Catani, S. Dittmaier, M. H. Seymour, and Z. Trocsanyi, "The dipole formalism for next-to-leading order QCD calculations with massive partons," *Nuclear Physics B*, vol. 627, no. 1-2, pp. 189–265, 2002. DOI: 10.1016/S0550-3213(02)00098-6 (cit. on p. 84).

[279] S. Frixione, Z. Kunszt, and A. Signer, "Three-jet cross sections to next-to-leading order," *Nuclear Physics B*, vol. 467, no. 3, pp. 399–442, 1996. DOI: 10.1016/0550-3213(96)00110-1 (cit. on p. 84).

[280] S. Frixione, "A general approach to jet cross sections in QCD," *Nuclear Physics B*, vol. 507, no. 1-2, pp. 295–314, 1997. DOI: 10.1016/S0550-3213(97)00574-9 (cit. on p. 84).

[281] S. Catani and M. Grazzini, "Next-to-next-to-leading-order subtraction formalism in hadron collisions and its application to Higgs-boson production at the Large Hadron Collider," *Physical review letters*, vol. 98, no. 22, p. 222 002, 2007. DOI: 10.1103/PhysRevLett.98.222002 (cit. on p. 84).

[282] M. Czakon, "A novel subtraction scheme for double-real radiation at NNLO," *Physics Letters B*, vol. 693, no. 3, pp. 259–268, 2010. DOI: 10.1016/j.physletb.2010.08.036 (cit. on p. 84).

[283] M. Czakon and D. Heymes, "Four-dimensional formulation of the sector-improved residue subtraction scheme," *Nuclear Physics B*, vol. 890, pp. 152–227, 2015. DOI: 10.1016/j.nuclphysb.2014.11.006 (cit. on p. 84).

[284] M. Grazzini, *Soft gluon resummation vs parton shower simulations*, May 2016. [Online]. Available: https://virgilio.mib.infn.it/~nason/mcws2/Grazzini.pdf (cit. on p. 86).

[285] M. Kollár, "Top-Quark and Top-Squark Production at Hadron Colliders at Electroweak NLO," Ph.D. dissertation, Universität München, 2007. [Online]. Available: https://www.researchgate.net/publication/36418716_Top-Quark_and_Top-Squark_Production_at_Hadron_Colliders_at_Electroweak_NLO (cit. on p. 86).

[286] P. Nason and B. Webber, "Next-to-leading-order event generators," *Annual Review of Nuclear and Particle Science*, vol. 62, pp. 187–213, 2012. DOI: 10.1146/annurev-nucl-102711-094928 (cit. on p. 87).

[287] F. Krauss, *Multijet merging techniques*, Sep. 2010. [Online]. Available: https://indico.cern.ch/event/93790/contributions/1281098/attachments/1103798/1574779/Trento10.pdf (cit. on p. 87).

[288] S. Frixione and B. R. Webber, "Matching NLO QCD computations and parton shower simulations," *Journal of High Energy Physics*, vol. 2002, no. 06, p. 029, 2002. DOI: 10.1088/1126-6708/2002/06/029 (cit. on p. 87).

[289] P. Nason, "A new method for combining NLO QCD with shower Monte Carlo algorithms," *Journal of High Energy Physics*, vol. 2004, no. 11, p. 040, 2004. DOI: 10.1088/1126-6708/2004/11/040 (cit. on p. 87).

[290] S. Frixione, P. Nason, and C. Oleari, "Matching NLO QCD computations with parton shower simulations: the POWHEG method," *Journal of High Energy Physics*, vol. 2007, no. 11, p. 070, 2007. DOI: 10.1088/1126-6708/2007/11/070 (cit. on p. 87).

[291] S. Höche, F. Krauss, S. Schumann, and F. Siegert, "QCD matrix elements and truncated showers," *Journal of High Energy Physics*, vol. 2009, no. 05, p. 053, 2009. DOI: 10.1088/1126-6708/2009/05/053 (cit. on p. 87).

[292] L. Lönnblad, "Correcting the colour-dipole cascade model with fixed order matrix elements," *Journal of High Energy Physics*, vol. 2002, no. 05, p. 046, 2002. DOI: 10.1088/1126-6708/2002/05/046 (cit. on p. 87).

[293] R. Frederix and S. Frixione, "Merging meets matching in MC@NLO," *Journal of High Energy Physics*, vol. 2012, no. 12, pp. 1–41, 2012. DOI: 10.1007/JHEP12%282012%29061 (cit. on p. 87).

[294] N. Lavesson and L. Lönnblad, "Extending CKKW-merging to one-loop matrix elements," *Journal of High Energy Physics*, vol. 2008, no. 12, p. 070, 2008. DOI: 10.1088/1126-6708/2008/12/070 (cit. on p. 87).

[295] L. Lönnblad and S. Prestel, "Merging multi-leg NLO matrix elements with parton showers," *Journal of High Energy Physics*, vol. 2013, no. 3, pp. 1–73, 2013. DOI: 10.1007/JHEP03(2013)166 (cit. on p. 87).

[296] Y. I. Azimov, Y. L. Dokshitzer, V. A. Khoze, and S. Trovan, "Similarity of parton and hadron spectra in QCD jets," *Zeitschrift für Physik C Particles and Fields*, vol. 27, pp. 65–72, 1985. DOI: 10.1007/BF01642482 (cit. on p. 88).

[297] X. Artru and G. Mennessier, "String model and multiproduction," *Nuclear Physics B*, vol. 70, no. 1, pp. 93–115, 1974. DOI: 10.1016/0550-3213(74)90360-5 (cit. on p. 88).

[298] R. Field and R. P. Feynman, "A parametrization of the properties of quark jets," *Nuclear Physics B*, vol. 136, no. 1, pp. 1–76, 1978. DOI: 10.1016/0550-3213(78)90015-9 (cit. on p. 88).

[299] B. Andersson, G. Gustafson, G. Ingelman, and T. Sjöstrand, "Parton fragmentation and string dynamics," *Physics Reports*, vol. 97, no. 2-3, pp. 31–145, 1983. DOI: 10.1016/0370-1573(83)90080-7 (cit. on p. 88).

[300] B. Andersson, *The Lund model*. Cambridge University Press, Jul. 2005, vol. 7, ISBN: 978-0-521-01734-3, 978-0-521-42094-5, 978-0-511-88149-7. DOI: 10.1017/CBO9780511524363 (cit. on p. 88).

[301] J. Jamieson, "Aiming For The Top Corner: Measuring top-quark pair production in association with additional jets in highly boosted events using the ATLAS detector," Presented 28 Feb 2022, 2022. [Online]. Available: https://cds.cern.ch/record/2805713 (cit. on p. 89).

[302] B. R. Webber, "A QCD model for jet fragmentation including soft gluon interference," *Nuclear Physics B*, vol. 238, no. 3, pp. 492–528, 1984. DOI: 10.1016/0550-3213(84)90333-X (cit. on p. 88).

[303] J.-C. Winter, F. Krauss, and G. Soff, "A modified cluster-hadronisation model," *The European Physical Journal C-Particles and Fields*, vol. 36, pp. 381–395, 2004. DOI: 10.1140/epjc/s2004-01960-8 (cit. on p. 88).

[304] D. Amati and G. Veneziano, "Preconfinement as a Property of Perturbative QCD," *Physics Letters B*, vol. 83, no. 1, pp. 87–92, 1979. DOI: 10.1016/0370-2693(79)90896-7 (cit. on p. 88).

[305] J. M. Butterworth, J. R. Forshaw, and M. H. Seymour, "Multiparton interactions in photoproduction at HERA," *Zeitschrift für Physik C: Particles and Fields*, vol. 72, pp. 637–646, 1996. DOI: 10.1007/s002880050286 (cit. on p. 89).

[306] M. Bähr, S. Gieseke, and M. H. Seymour, "Simulation of multiple partonic interactions in Herwig++," *Journal of High Energy Physics*, vol. 2008, no. 07, p. 076, 2008. DOI: 10.1088/1126-6708/2008/07/076 (cit. on p. 89).

[307] M. Aaboud, G. Aad, B. Abbott, *et al.*, "Measurement of charged-particle distributions sensitive to the underlying event in $\sqrt{s}$ = 13TeV proton-proton collisions with the ATLAS detector at the LHC," *Journal of High Energy Physics*, vol. 2017, no. 3, pp. 1–42, 2017. DOI: 10.1007/JHEP03(2017)157 (cit. on pp. 89, 109).

[308] G. Aad, B. Abbott, D. C. Abbott, *et al.*, "Measurement of distributions sensitive to the underlying event in inclusive Z boson production in pp collisions at $\sqrt{s}$ = 13 TeV with the ATLAS detector," *The European Physical Journal C*, vol. 79, pp. 1–31, 2019. DOI: 10.1140/epjc/s10052-014-3195-6 (cit. on p. 89).

[309] "Correlation of Υ meson production with the underlying event in pp collisions measured by the ATLAS experiment," 2022. [Online]. Available: https://inspirehep.net/files/0600aee3b41d0e487378c03a77e862fb (cit. on p. 89).

[310] "Summary of ATLAS Pythia 8 tunes," Aug. 2012. [Online]. Available: https://inspirehep.net/files/4c45668185c8b55053ef8b58a009202d (cit. on p. 89).

[311] Z. Marshall, A. Collaboration, *et al.*, "Simulation of Pile-up in the ATLAS Experiment," in *Journal of Physics: Conference Series*, IOP Publishing, vol. 513, 2014, p. 022 024. DOI: 10.1088/1742-6596/513/2/022024 (cit. on p. 89).

[312] T. Novak, "ATLAS Pile-up and Overlay Simulation," Tech. Rep., 2017. [Online]. Available: https://cds.cern.ch/record/2270396 (cit. on pp. 90, 164).

[313] T. Novak, "New techniques for pile-up simulation in ATLAS," in *EPJ Web of Conferences*, EDP Sciences, vol. 214, 2019, p. 02 044. DOI: 10.1051/epjconf/201921402044 (cit. on p. 90).

[314] D. Collaboration, "Tuning and test of fragmentation models based on identified particles and precision event shape data DELPHI Collaboration," *Zeitschrift für Physik C Particles and Fields*, vol. 73, pp. 11–59, 1997. DOI: 10.1007/s002880050295 (cit. on p. 90).

[315] "ATLAS Pythia 8 tunes to 7 TeV data," CERN, Geneva, Tech. Rep., 2014 (cit. on p. 90).

[316] S. Frixione, E. Laenen, P. Motylinski, and B. R. Webber, "Angular correlations of lepton pairs from vector boson and top quark decays in Monte Carlo simulations," *JHEP*, vol. 04, p. 081, 2007. DOI: 10.1088/1126-6708/2007/04/081 (cit. on p. 91).

[317] P. Artoisenet, R. Frederix, O. Mattelaer, and R. Rietkerk, "Automatic spin-entangled decays of heavy resonances in Monte Carlo simulations," *Journal of High Energy Physics*, vol. 2013, no. 3, p. 15, 2013. DOI: 10.1007/JHEP03(2013)015 (cit. on pp. 91, 111).

[318] N. Mokhov, "Simulation of particle-material interactions," 2020. DOI: 10.48550/arXiv.2006.09866 (cit. on p. 92).

[319] D. Reiter, "The Monte Carlo method for particle transport problems," *Computational many-particle physics*, pp. 141–158, 2008. DOI: 10.1007/978-3-540-74686-7_5 (cit. on p. 93).

[320] S. Agostinelli, J. Allison, K. a. Amako, *et al.*, "GEANT4—a simulation toolkit," *Nuclear instruments and methods in physics research section A: Accelerators, Spectrometers, Detectors and Associated Equipment*, vol. 506, no. 3, pp. 250–303, 2003. DOI: 10.1016/S0168-9002(03)01368-8 (cit. on p. 93).

[321] G. Aad, B. Abbott, J. Abdallah, *et al.*, "The ATLAS simulation infrastructure," *The European Physical Journal C*, vol. 70, no. 3, pp. 823–874, 2010. DOI: 10.1140/epjc/s10052-010-1429-9 (cit. on pp. 93, 94).

[322] E. Richter-Was, D. Froidevaux, and L. Poggioli, "ATLFAST 2.0 a fast simulation package for ATLAS," CERN, Geneva, Tech. Rep., 1998. [Online]. Available: https://cds.cern.ch/record/683751 (cit. on p. 93).

[323] D. Cavalli and S. Resconi, "Comparison between full simulation and fast simulation of ATLAS detector," CERN, Geneva, Tech. Rep., 1997. [Online]. Available: https://cds.cern.ch/record/682483 (cit. on p. 93).

[324] C. ATLAS, M. Beckingham, M. Duehrssen, *et al.*, "The simulation principle and performance of the ATLAS fast calorimeter simulation FastCaloSim," CERN, Geneva, Tech. Rep., 2010. [Online]. Available: https://cds.cern.ch/record/1300517 (cit. on p. 94).

[325] o. b. o. t. A. C. Mechnich Jörg, "FATRAS-The ATLAS fast track simulation project," in *Journal of Physics: Conference Series*, IOP Publishing, vol. 331, 2011, p. 032 046. DOI: 10.1088/1742-6596/331/3/032046 (cit. on p. 94).

[326] G. Aad, B. Abbott, D. Abbott, *et al.*, "AtlFast3: the next generation of fast simulation in ATLAS," *Computing and Software for Big Science*, vol. 6, no. 1, pp. 1–54, 2022. DOI: 10.1007/s41781-021-00079-7 (cit. on p. 94).

[327] A. Ghosh, "Deep generative models for fast shower simulation in ATLAS," CERN, Geneva, Tech. Rep., 2020. DOI: 10.1088/1742-6596/1525/1/012077 (cit. on p. 94).

[328] M. Erdmann, J. Glombitza, and T. Quast, "Precise simulation of electromagnetic calorimeter showers using a Wasserstein Generative Adversarial Network," *Computing and Software for Big Science*, vol. 3, no. 1, pp. 1–13, 2019. DOI: 10.1007/s41781-018-0019-7 (cit. on p. 94).

[329] D. Belayneh, F. Carminati, A. Farbin, *et al.*, "Calorimetry with deep learning: particle simulation and reconstruction for collider physics," *The European Physical Journal C*, vol. 80, no. 7, pp. 1–31, 2020. DOI: 10.1140/epjc/s10052-020-8251-9 (cit. on p. 94).

[330] A. Butter, S. Diefenbacher, G. Kasieczka, B. Nachman, and T. Plehn, "GANplifying event samples," *SciPost Physics*, vol. 10, no. 6, p. 139, 2021. DOI: 10.21468/SciPostPhys.10.6.139 (cit. on p. 94).

[331] J. De Favereau, C. Delaere, P. Demin, *et al.*, "DELPHES 3: a modular framework for fast simulation of a generic collider experiment," *Journal of High Energy Physics*, vol. 2014, no. 2, pp. 1–26, 2014. DOI: 10.1007/JHEP02(2014)057 (cit. on p. 95).

[332] C. Bierlich, A. Buckley, J. M. Butterworth, *et al.*, "Robust independent validation of experiment and theory: Rivet version 3," *SciPost physics*, vol. 8, no. 2, p. 026, 2020. DOI: 10.21468/SciPostPhys.8.2.026 (cit. on p. 95).

[333] A. Buckley, D. Kar, and K. Nordström, "Fast simulation of detector effects in Rivet," *SciPost Physics*, vol. 8, no. 2, p. 025, 2020. DOI: 10.21468/SciPostPhys.8.2.025 (cit. on p. 95).

[334] A. C. Pipkin, *A course on integral equations*. Springer Science & Business Media, 1991 (cit. on p. 97).

[335] V. Blobel, "Unfolding methods in particle physics," 2011. [Online]. Available: https://indico.cern.ch/event/107747/contributions/32645/attachments/24317/35000/blobel.pdf (cit. on p. 97).

[336] G. Cowan, "A survey of unfolding methods for particle physics," M. R. Whalley and L. Lyons, Eds., vol. 0203181, 2002, pp. 248–257. [Online]. Available: https://inspirehep.net/literature/599644 (cit. on p. 97).

[337] R. Brun, F. Rademakers, P. Canal, *et al.*, *Root-project/root: V6.18/02*, version v6-18-02, Aug. 2019. DOI: 10.5281/zenodo.3895860 (cit. on p. 99).

[338] E. L. Simpson, "SwiftSim: An ATLAS Tool for Ultra-Fast Simulation: Qualification Task," CERN, Geneva, Tech. Rep., 2021. [Online]. Available: https://cds.cern.ch/record/2783577 (cit. on p. 99).

[339] Anisha, O. Atkinson, A. Bhardwaj, C. Englert, W. Naskar, and P. Stylianou, "BSM reach of four-top production at the LHC," *Phys. Rev. D*, vol. 108, p. 035 001, 3 Aug. 2023. DOI: 10.1103/PhysRevD.108.035001 (cit. on p. 101).

[340] H. Qu and L. Gouskos, "Jet tagging via particle clouds," *Phys. Rev. D*, vol. 101, p. 056 019, 5 Mar. 2020. DOI: 10.1103/PhysRevD.101.056019 (cit. on p. 101).

[341] C. Biscarat, S. Caillou, C. Rougier, J. Stark, and J. Zahreddine, "Towards a realistic track reconstruction algorithm based on graph neural networks for the HL-LHC," in *EPJ Web of Conferences*, EDP Sciences, vol. 251, 2021, p. 03 047. DOI: 10.1051/epjconf/202125103047 (cit. on p. 101).

[342] D. Guest, K. Cranmer, and D. Whiteson, "Deep learning and its application to LHC physics," *Ann. Rev. Nucl. Part. Sci.*, vol. 68, pp. 161–181, 2018. DOI: 10.1146/annurev-nucl-101917-021019 (cit. on p. 101).

[343] M. D. Schwartz, "Modern machine learning and particle physics," 2021. DOI: 10.1162/99608f92.beeb1183 (cit. on p. 101).

[344] P. Shanahan, K. Terao, and D. Whiteson, "Snowmass 2021 Computational Frontier CompF03 Topical Group Report: Machine Learning," 2022. DOI: 10.48550/arXiv.2209.07559 (cit. on p. 101).

[345] A. Xu, S. Han, X. Ju, and H. Wang, "Generative Machine Learning for Detector Response Modeling with a Conditional Normalizing Flow," 2023 (cit. on pp. 101, 102).

[346] C. Chen, O. Cerri, T. Q. Nguyen, J.-R. Vlimant, and M. Pierini, "Data augmentation at the LHC through analysis-specific fast simulation with deep learning," 2020. DOI: 10.48550/arXiv.2010.01835 (cit. on p. 101).

[347] D. Benjamin, S. Chekanov, W. Hopkins, Y. Li, and J. R. Love, "Automated detector simulation and reconstruction parametrization using machine learning," *Journal of Instrumentation*, vol. 15, no. 05, P05025, 2020. DOI: 10.1088/1748-0221/15/05/P05025 (cit. on p. 101).

[348] D. Darulis, R. Tyson, D. Ireland, D. Glazier, B. McKinnon, and P. Pauli, "Machine Learned Particle Detector Simulations," 2022. DOI: 10.48550/arXiv.2207.11254 (cit. on p. 102).

[349] D. Kriesel, *A Brief Introduction to Neural Networks. dkriesel. com*. 2005. [Online]. Available: dkriesel.com (cit. on p. 103).

[350] L. Huang, J. Qin, Y. Zhou, F. Zhu, L. Liu, and L. Shao, "Normalization Techniques in Training DNNs: Methodology, Analysis and Application," *IEEE Transactions on Pattern Analysis and Machine Intelligence*, vol. 45, no. 8, pp. 10 173–10 196, 2023. DOI: 10.1109/TPAMI.2023.3250241 (cit. on p. 105).

[351] E. Rodrigues *et al.*, "The Scikit HEP Project – overview and prospects," *EPJ Web Conf.*, vol. 245, C. Doglioni, D. Kim, G. A. Stewart, L. Silvestris, P. Jackson, and W. Kamleh, Eds., p. 06 028, 2020. DOI: 10.1051/epjconf/202024506028 (cit. on p. 105).

[352] F. Chollet *et al.*, *Keras*, https://keras.io, 2015 (cit. on p. 105).

[353] Martín Abadi, Ashish Agarwal, Paul Barham, *et al.*, *TensorFlow: Large-Scale Machine Learning on Heterogeneous Systems*, Software available from tensorflow.org, 2015. [Online]. Available: https://www.tensorflow.org/ (cit. on p. 105).

[354] D. P. Kingma and J. Ba, "Adam: A method for stochastic optimization," 2014. DOI: 10.48550/arXiv.1412.6980 (cit. on p. 105).

[355] G. Klambauer, T. Unterthiner, A. Mayr, and S. Hochreiter, "Self-normalizing neural networks," *Advances in neural information processing systems*, vol. 30, 2017. DOI: https://doi.org/10.48550/arXiv.1706.02515 (cit. on p. 106).

[356] J. Shlomi, P. Battaglia, and J.-R. Vlimant, "Graph neural networks in particle physics," *Machine Learning: Science and Technology*, vol. 2, no. 2, p. 021 001, 2020. DOI: 10.1088/2632-2153/abbf9a (cit. on p. 108).

[357] A. Hariri, D. Dyachkova, and S. Gleyzer, "Graph generative models for fast detector simulations in high energy physics," 2021. DOI: 10.48550/arXiv.2104.01725 (cit. on p. 108).

[358] O. Atkinson, A. Bhardwaj, S. Brown, C. Englert, D. J. Miller, and P. Stylianou, "Improved constraints on effective top quark interactions using edge convolution networks," *Journal of High Energy Physics*, vol. 2022, no. 4, p. 137, 2022. DOI: 10.1007/JHEP04(2022)137 (cit. on p. 108).

[359] A. Duperrin, "Flavour tagging with graph neural networks with the ATLAS detector," 2023. DOI: 10.48550/arXiv.2306.04415 (cit. on p. 108).

[360] ATLAS Collaboration, "Measurement of the $t\bar{t}Z$ and $t\bar{t}W$ cross sections in proton-proton collisions at $\sqrt{s}$ = 13 with the ATLAS detector," *Phys. Rev. D*, vol. 99, no. 7, p. 072 009, 2019. DOI: 10.1103/PhysRevD.99.072009 (cit. on pp. 109, 122).

[361] A. Tumasyan, W. Adam, J. W. Andrejkovic, *et al.*, "Measurement of the cross section of top quark-antiquark pair production in association with a W boson in proton-proton collisions at $\sqrt{s}$ = 13 TeV," *Journal of High Energy Physics*, vol. 2023, no. 7, p. 219, 2023. DOI: 10.1007/JHEP07(2023)219 (cit. on p. 109).

[362] A. M. Sirunyan, A. Tumasyan, W. Adam, *et al.*, "Measurement of top quark pair production in association with a Z boson in proton-proton collisions at $\sqrt{s}$ = 13 tev," *Journal of High Energy Physics*, vol. 2020, no. 3, p. 56, 2020. DOI: 10.1007/JHEP03(2020)056 (cit. on pp. 109, 110, 114, 122).

[363] G. Aad, B. Abbott, D. C. Abbott, *et al.*, "Measurements of the inclusive and differential production cross sections of a top-quark–antiquark pair in association with a Z boson at $\sqrt{s}$ = 13 TeV with the ATLAS detector," *The European Physical Journal C*, vol. 81, no. 8, p. 737, 2021. DOI: 10.1140/epjc/s10052-021-09439-4 (cit. on pp. 109, 110, 113, 120).

[364] A. Tumasyan, W. Adam, J. Andrejkovic, *et al.*, "Measurement of the inclusive and differential $t\bar{t}\gamma$ cross sections in the dilepton channel and effective field theory interpretation in proton-proton collisions at $\sqrt{s}$ = 13 TeV," *Journal of High Energy Physics*, vol. 2022, no. 5, pp. 1–59, 2022. DOI: 10.1007/JHEP05(2022)091 (cit. on p. 109).

[365] M. Aaboud, G. Aad, B. Abbott, *et al.*, "Observation of Higgs boson production in association with a top quark pair at the LHC with the ATLAS detector," *Physics Letters B*, vol. 784, pp. 173–191, 2018. DOI: 10.1016/j.physletb.2018.07.035 (cit. on p. 109).

[366] A. M. Sirunyan, A. Tumasyan, W. Adam, *et al.*, "Observation of $t\bar{t}H$ production," *Phys. Rev. Lett.*, vol. 120, p. 231 801, 23 Jun. 2018. DOI: 10.1103/PhysRevLett.120.231801 (cit. on p. 109).

[367] G. Aad, B. Abbott, D. C. Abbott, *et al.*, "Search for leptonic charge asymmetry in $t\bar{t}W$ production in final states with three leptons at $\sqrt{s}$ = 13 TeV," *Journal of High Energy Physics*, vol. 2023, no. 7, p. 33, 2023. DOI: 10.1007/JHEP07(2023)033 (cit. on p. 109).

[368] G. Aad, B. Abbott, D. Abbott, *et al.*, "Measurement of the charge asymmetry in top-quark pair production in association with a photon with the ATLAS experiment," *Physics Letters B*, vol. 843, p. 137 848, 2023. DOI: 10.1016/j.physletb.2023.137848 (cit. on p. 109).

[369] A. Collaboration, "Inclusive and differential cross-section measurements of $t\bar{t}Z$ production in pp collisions at $\sqrt{s}$ = 13 TeV with the ATLAS detector, including EFT and spin-correlation interpretations," 2023. DOI: 10.48550/arXiv.2312.04450 (cit. on pp. 110, 120, 124).

[370] S. Frixione, V. Hirschi, D. Pagani, H. .-. Shao, and M. Zaro, "Electroweak and QCD corrections to top-pair hadroproduction in association with heavy bosons," *Journal of High Energy Physics*, vol. 2015, no. 6, p. 184, 2015. DOI: 10.1007/JHEP06(2015)184 (cit. on p. 110).

[371] A. Broggio, A. Ferroglia, R. Frederix, D. Pagani, B. D. Pecjak, and I. Tsinikos, "Top-quark pair hadroproduction in association with a heavy boson at NLO+ NNLL including EW corrections," *Journal of High Energy Physics*, vol. 2019, no. 8, pp. 1–46, 2019. DOI: 10.1007/JHEP08(2019)039 (cit. on p. 110).

[372] A. Kulesza, L. Motyka, D. Schwartländer, T. Stebel, and V. Theeuwes, "Associated top quark pair production with a heavy boson: differential cross sections at NLO+ NNLL accuracy," *The European Physical Journal C*, vol. 80, no. 5, p. 428, 2020. DOI: 10.1140/epjc/s10052-020-7987-6 (cit. on p. 110).

[373] L. Mince, "Measurements of the associated production of a top quark pair and a Z boson with the ATLAS detector," Ph.D. dissertation, University of Glasgow, 2023. [Online]. Available: https://theses.gla.ac.uk/83578/ (cit. on p. 110).

[374] W. Bernreuther, D. Heisler, and Z.-G. Si, "A set of top quark spin correlation and polarization observables for the LHC: Standard Model predictions and new physics contributions," *JHEP*, vol. 12, p. 026, 2015. DOI: 10.1007/JHEP12(2015)026 (cit. on pp. 111–113).

[375] D. de Florian, C. Grojean, F. Maltoni, *et al.*, *Handbook of LHC Higgs Cross Sections: 4. Deciphering the Nature of the Higgs Sector* (CERN Yellow Reports: Monographs). Geneva: CERN, 2017. DOI: 10.23731/CYRM-2017-002 (cit. on p. 117).

[376] N. Tonon, H. Aarup Petersen, M. Aldaya Martin, *et al.*, "Probing effective field theory operators in the associated production of top quarks with a Z boson in multilepton final states at $\sqrt{s} = 13$ TeV," *Journal of High Energy Physics*, vol. 2021, no. 12, p. 83, 2021. DOI: 10.1007/JHEP12(2021)083 (cit. on p. 120).

[377] D. Barducci *et al.*, "Interpreting top-quark LHC measurements in the Standard-Model Effective Field Theory," DOI: 10.48550/arXiv.1802.07237 (cit. on p. 121).

[378] N. P. Hartland, F. Maltoni, E. R. Nocera, *et al.*, "A Monte Carlo global analysis of the Standard Model Effective Field Theory: the top quark sector," *JHEP*, vol. 04, p. 100, 2019. DOI: 10.1007/JHEP04(2019)100 (cit. on pp. 121, 122).

[379] A. M. Sirunyan, A. Tumasyan, W. Adam, *et al.*, "Search for new physics in top quark production with additional leptons in proton-proton collisions at $\sqrt{s} = 13$ tev using effective field theory," *Journal of High Energy Physics*, vol. 2021, no. 3, p. 95, 2021. DOI: 10.1007/JHEP03(2021)095 (cit. on p. 122).

[380] J. Brehmer, F. Kling, T. Plehn, and T. M. Tait, "Better Higgs-C P tests through information geometry," *Physical Review D*, vol. 97, no. 9, p. 095 017, 2018. DOI: 10.1103/PhysRevD.97.095017 (cit. on p. 122).

[381] J. J. Ethier, G. Magni, F. Maltoni, *et al.*, "Combined SMEFT interpretation of Higgs, diboson, and top quark data from the LHC," *Journal of High Energy Physics*, vol. 2021, no. 11, pp. 1–97, 2021. DOI: 10.48550/arXiv.2105.00006 (cit. on pp. 122, 123).

[382] A. Einstein, B. Podolsky, and N. Rosen, "Can Quantum-Mechanical Description of Physical Reality Be Considered Complete?" *Phys. Rev.*, vol. 47, pp. 777–780, 10 May 1935. DOI: 10.1103/PhysRev.47.777 (cit. on p. 125).

[383] S. Barnett, *Quantum information*. Oxford University Press, 2009, vol. 16 (cit. on p. 125).

[384] C. E. Shannon, "A mathematical theory of communication," *The Bell System Technical Journal*, vol. 27, no. 3, pp. 379–423, 1948. DOI: 10.1002/j.1538-7305.1948.tb01338.x (cit. on p. 125).

[385] M. Hayashi, *Quantum information theory*. Springer, 2016 (cit. on p. 125).

[386] A. Steane, "Quantum computing," *Reports on Progress in Physics*, vol. 61, no. 2, p. 117, 1998. DOI: 10.1088/0034-4885/61/2/002 (cit. on p. 126).

[387] K. L. Brown, W. J. Munro, and V. M. Kendon, "Using quantum computers for quantum simulation," *Entropy*, vol. 12, no. 11, pp. 2268–2307, 2010. DOI: 10.3390/e12112268 (cit. on p. 126).

[388] D. J. Bernstein and T. Lange, "Post-quantum cryptography," *Nature*, vol. 549, no. 7671, pp. 188–194, 2017. DOI: 10.1038/nature23461 (cit. on p. 126).

[389] E. Schrödinger, "Discussion of probability relations between separated systems," in *Mathematical Proceedings of the Cambridge Philosophical Society*, Cambridge University Press, vol. 31, 1935, pp. 555–563. DOI: 10.1017/S0305004100013554 (cit. on p. 126).

[390] N. Brunner, D. Cavalcanti, S. Pironio, V. Scarani, and S. Wehner, "Bell nonlocality," *Rev. Mod. Phys.*, vol. 86, pp. 419–478, 2 Apr. 2014. DOI: 10.1103/RevModPhys.86.419 (cit. on p. 126).

[391] D. M. Greenberger, M. A. Horne, and A. Zeilinger, "Going beyond Bell's theorem," in *Bell's theorem, quantum theory and conceptions of the universe*, Springer, 1989, pp. 69–72 (cit. on p. 126).

[392] N. Gisin, "Bell's inequality holds for all non-product states," *Physics Letters A*, vol. 154, no. 5-6, pp. 201–202, 1991. DOI: 10.1016/0375-9601(91)90805-I (cit. on p. 126).

[393] S. Popescu and D. Rohrlich, "Generic quantum nonlocality," *Physics Letters A*, vol. 166, no. 5-6, pp. 293–297, 1992. DOI: 10.1016/0375-9601(92)90711-T (cit. on p. 126).

[394] C. H. Bennett, G. Brassard, C. Crépeau, R. Jozsa, A. Peres, and W. K. Wootters, "Teleporting an unknown quantum state via dual classical and Einstein-Podolsky-Rosen channels," *Phys. Rev. Lett.*, vol. 70, pp. 1895–1899, 13 Mar. 1993. DOI: 10.1103/PhysRevLett.70.1895 (cit. on p. 126).

[395] P. Shor, "Algorithms for quantum computation: discrete logarithms and factoring," in *Proceedings 35th Annual Symposium on Foundations of Computer Science*, 1994, pp. 124–134. DOI: 10.1109/SFCS.1994.365700 (cit. on p. 126).

[396] A. K. Ekert, "Quantum cryptography based on Bell's theorem," *Phys. Rev. Lett.*, vol. 67, pp. 661–663, 6 Aug. 1991. DOI: 10.1103/PhysRevLett.67.661 (cit. on p. 126).

[397] H.-P. Breuer, F. Petruccione, *et al.*, *The theory of open quantum systems*. Oxford University Press on Demand, 2002 (cit. on p. 126).

[398] S. Gharibian, "Strong np-hardness of the quantum separability problem," *Quantum Inf. Comput.*, vol. 10, no. 3&4, pp. 343–360, 2010. DOI: 10.26421/QIC10.3-4-11 (cit. on p. 127).

[399] L. Gurvits, "Classical deterministic complexity of Edmonds' problem and quantum entanglement," in *Proceedings of the thirty-fifth annual ACM symposium on Theory of computing*, 2003, pp. 10–19. DOI: https://arxiv.org/abs/quant-ph/0303055 (cit. on p. 127).

[400] D. Bruß, "Characterizing entanglement," *Journal of Mathematical Physics*, vol. 43, no. 9, pp. 4237–4251, 2002. DOI: 10.1063/1.1494474 (cit. on p. 127).

[401] R. Horodecki, P. Horodecki, M. Horodecki, and K. Horodecki, "Quantum entanglement," *Rev. Mod. Phys.*, vol. 81, pp. 865–942, 2 Jun. 2009. DOI: 10.1103/RevModPhys.81.865 (cit. on pp. 127, 128, 133).

[402] C. A. Kocher and E. D. Commins, "Polarization Correlation of Photons Emitted in an Atomic Cascade," *Phys. Rev. Lett.*, vol. 18, pp. 575–577, 15 Apr. 1967. DOI: 10.1103/PhysRevLett.18.575 (cit. on p. 127).

[403] S. J. Freedman and J. F. Clauser, "Experimental Test of Local Hidden-Variable Theories," *Phys. Rev. Lett.*, vol. 28, pp. 938–941, 14 Apr. 1972. DOI: 10.1103/PhysRevLett.28.938 (cit. on p. 127).

[404] J.-Å. Larsson, "Loopholes in Bell inequality tests of local realism," *Journal of Physics A: Mathematical and Theoretical*, vol. 47, no. 42, p. 424 003, 2014. DOI: 10.1088/1751-8113/47/42/424003 (cit. on p. 127).

[405] A. Aspect, P. Grangier, and G. Roger, "Experimental Tests of Realistic Local Theories via Bell's Theorem," *Phys. Rev. Lett.*, vol. 47, pp. 460–463, 7 Aug. 1981. DOI: 10.1103/PhysRevLett.47.460 (cit. on p. 127).

[406] A. Aspect, P. Grangier, and G. Roger, "Experimental Realization of Einstein-Podolsky-Rosen-Bohm Gedankenexperiment: A New Violation of Bell's Inequalities," *Phys. Rev. Lett.*, vol. 49, pp. 91–94, 2 Jul. 1982. DOI: 10.1103/PhysRevLett.49.91 (cit. on p. 127).

[407] M. Giustina, M. A. M. Versteegh, S. Wengerowsky, *et al.*, "Significant-Loophole-Free Test of Bell's Theorem with Entangled Photons," *Phys. Rev. Lett.*, vol. 115, p. 250 401, 25 Dec. 2015. DOI: 10.1103/PhysRevLett.115.250401 (cit. on p. 127).

[408] B. Hensen, H. Bernien, A. E. Dréau, *et al.*, "Loophole-free Bell inequality violation using electron spins separated by 1.3 kilometres," *Nature*, vol. 526, no. 7575, pp. 682–686, 2015. DOI: 10.1038/nature15759 (cit. on p. 127).

[409] E. Hagley, X. Maitre, G. Nogues, *et al.*, "Generation of Einstein-Podolsky-Rosen Pairs of Atoms," *Phys. Rev. Lett.*, vol. 79, pp. 1–5, 1 Jul. 1997. DOI: 10.1103/PhysRevLett.79.1 (cit. on p. 127).

[410] A. Go *et al.*, "Measurement of Einstein-Podolsky-Rosen-Type Flavor Entanglement in $\Upsilon(4S) \to B^0\overline{B}^0$ Decays," *Phys. Rev. Lett.*, vol. 99, p. 131 802, 13 Sep. 2007. DOI: 10.1103/PhysRevLett.99.131802 (cit. on p. 127).

[411] J. A. Formaggio, D. I. Kaiser, M. M. Murskyj, and T. E. Weiss, "Violation of the Leggett-Garg Inequality in Neutrino Oscillations," *Phys. Rev. Lett.*, vol. 117, p. 050 402, 5 Jul. 2016. DOI: 10.1103/PhysRevLett.117.050402 (cit. on p. 127).

[412] J. Steinhauer, "Observation of quantum Hawking radiation and its entanglement in an analogue black hole," *Nature Physics*, vol. 12, no. 10, pp. 959–965, 2016. DOI: 10.1038/nphys3863 (cit. on p. 127).

[413] Y. Shi, "Entanglement in relativistic quantum field theory," *Phys. Rev. D*, vol. 70, p. 105 001, 10 Nov. 2004. DOI: 10.1103/PhysRevD.70.105001 (cit. on p. 127).

[414] B. Kayser, J. Kopp, R. G. H. Robertson, and P. Vogel, "Theory of neutrino oscillations with entanglement," *Phys. Rev. D*, vol. 82, p. 093 003, 9 Nov. 2010. DOI: 10.1103/PhysRevD.82.093003 (cit. on p. 127).

[415] A. Cervera-Lierta, J. I. Latorre, J. Rojo, and L. Rottoli, "Maximal Entanglement in High Energy Physics," *SciPost Phys.*, vol. 3, p. 036, 2017. DOI: 10.21468/SciPostPhys.3.5.036 (cit. on p. 127).

[416] A. Peres, "Separability Criterion for Density Matrices," *Phys. Rev. Lett.*, vol. 77, pp. 1413–1415, 8 Aug. 1996. DOI: 10.1103/PhysRevLett.77.1413 (cit. on p. 128).

[417] P. Horodecki, "Separability criterion and inseparable mixed states with positive partial transposition," *Physics Letters A*, vol. 232, no. 5, pp. 333–339, 1997. DOI: 10.1016/S0375-9601%2897%2900416-7 (cit. on p. 128).

[418] W. K. Wootters, "Entanglement of Formation of an Arbitrary State of Two Qubits," *Phys. Rev. Lett.*, vol. 80, pp. 2245–2248, 10 Mar. 1998. DOI: 10.1103/PhysRevLett.80.2245 (cit. on p. 129).

[419] J. Aguilar-Saavedra and J. Casas, "Improved tests of entanglement and Bell inequalities with LHC tops," *The European Physical Journal C*, vol. 82, no. 8, p. 666, 2022. DOI: 10.1140/epjc/s10052-022-10630-4 (cit. on p. 132).

[420] Y. Afik and J. R. M. de Nova, "Quantum information with top quarks in QCD," *Quantum*, vol. 6, p. 820, 2022. DOI: 10.22331/q-2022-09-29-820 (cit. on p. 132).

[421] R. Aoude, E. Madge, F. Maltoni, and L. Mantani, "Quantum SMEFT tomography: Top quark pair production at the LHC," *Phys. Rev. D*, vol. 106, p. 055 007, 5 Sep. 2022. DOI: 10.1103/PhysRevD.106.055007 (cit. on p. 132).

[422] C. Severi and E. Vryonidou, "Quantum entanglement and top spin correlations in SMEFT at higher orders," *Journal of High Energy Physics*, vol. 2023, no. 1, pp. 1–42, 2023. DOI: 10.1007/JHEP01(2023)148 (cit. on p. 132).

[423] M. Fabbrichesi, R. Floreanini, and G. Panizzo, "Testing Bell Inequalities at the LHC with Top-Quark Pairs," *Phys. Rev. Lett.*, vol. 127, p. 161 801, 16 Oct. 2021. DOI: 10.1103/PhysRevLett.127.161801 (cit. on p. 132).

[424] C. Severi, C. D. E. Boschi, F. Maltoni, and M. Sioli, "Quantum tops at the LHC: from entanglement to Bell inequalities," *The European Physical Journal C*, vol. 82, no. 4, p. 285, 2022. DOI: 10.1140/epjc/s10052-022-10245-9 (cit. on p. 132).

[425] Z. Dong, D. Gonçalves, K. Kong, and A. Navarro, "When the Machine Chimes the Bell: Entanglement and Bell Inequalities with Boosted $t\bar{t}$," 2023. DOI: 10.48550/arXiv.2305.07075 (cit. on p. 132).

[426] M. Fabbrichesi, R. Floreanini, E. Gabrielli, and L. Marzola, "Stringent bounds on HWW and HZZ anomalous couplings with quantum tomography at the LHC," 2023. DOI: 10.48550/arXiv.2304.02403 (cit. on p. 132).

[427] A. J. Barr, "Testing Bell inequalities in Higgs boson decays," *Physics Letters B*, vol. 825, p. 136 866, 2022. DOI: 10.1016/j.physletb.2021.136866 (cit. on p. 132).

[428] A. J. Barr, P. Caban, and J. Rembieliński, "Bell-type inequalities for systems of relativistic vector bosons," *Quantum*, vol. 7, p. 1070, 2023. DOI: 10.22331/q-2023-07-27-1070 (cit. on p. 132).

[429] J. Aguilar-Saavedra, "Laboratory-frame tests of quantum entanglement in H→ W W," *Physical Review D*, vol. 107, no. 7, p. 076 016, 2023 (cit. on p. 132).

[430] J. A. Aguilar-Saavedra, "Laboratory-frame tests of quantum entanglement in $H \to WW$," *Phys. Rev. D*, vol. 107, p. 076 016, 7 Apr. 2023. DOI: 10.1103/PhysRevD.107.076016 (cit. on p. 132).

[431] M. M. Altakach, P. Lamba, F. Maltoni, K. Mawatari, and K. Sakurai, "Quantum information and CP measurement in $H \to \tau^+\tau^-$ at future lepton colliders," *Phys. Rev. D*, vol. 107, p. 093 002, 9 May 2023. DOI: 10.1103/PhysRevD.107.093002 (cit. on p. 132).

[432] M. Fabbrichesi, R. Floreanini, and E. Gabrielli, "Constraining new physics in entangled two-qubit systems: top-quark, tau-lepton and photon pairs," *The European Physical Journal C*, vol. 83, no. 2, p. 162, 2023. DOI: 10.1140/epjc/s10052-023-11307-2 (cit. on p. 132).

[433] F. Fabbri, J. Howarth, and T. Maurin, "Isolating semi-leptonic $H \to WW$ decays for Bell inequality tests," 2023. DOI: 10.48550/arXiv.2307.13783 (cit. on p. 133).

[434] M. Plávala, "General probabilistic theories: An introduction," *Physics Reports*, vol. 1033, pp. 1–64, 2023, General probabilistic theories: An introduction, ISSN: 0370-1573. DOI: 10.1016/j.physrep.2023.09.001 (cit. on p. 133).

[435] M. Eckstein and P. Horodecki, "Probing the limits of quantum theory with quantum information at subnuclear scales," *Proceedings of the Royal Society A*, vol. 478, no. 2259, p. 20 210 806, 2022. DOI: 10.1098/rspa.2021.0806 (cit. on p. 133).

[436] A. Go, A. Bay, K. Abe, *et al.*, "Measurement of Einstein-Podolsky-Rosen-Type Flavor Entanglement in $\Upsilon(4S) \to B^0\overline{B}^0$ Decays," *Phys. Rev. Lett.*, vol. 99, p. 131 802, 13 Sep. 2007. DOI: 10.1103/PhysRevLett.99.131802 (cit. on p. 133).

[437] M. Fabbrichesi, R. Floreanini, E. Gabrielli, and L. Marzola, "Bell inequality is violated in $B^0 \to J/\psi K^*(892)^0$ decays," 2023. DOI: 10.48550/arXiv.2305.04982 (cit. on p. 133).

[438] R. Aaij, C. Abellan Beteta, B. Adeva, *et al.*, "Measurement of the polarization amplitudes in $B^0 \to J/\psi K^*(892)^0$ decays," *Phys. Rev. D*, vol. 88, p. 052 002, 5 Sep. 2013. DOI: 10.1103/PhysRevD.88.052002 (cit. on p. 133).

[439] "Luminosity determination in pp collisions at $\sqrt{s} = 13$ TeV using the ATLAS detector at the LHC," Dec. 2022. DOI: 10.48550/arXiv.2212.09379. arXiv: 2212.09379 [hep-ex] (cit. on pp. 136, 163).

[440] R. D. Ball, V. Bertone, S. Carrazza, *et al.*, "Parton distributions for the LHC Run II," *Journal of High Energy Physics*, vol. 2015, no. 4, pp. 1–148, 2015. DOI: 10.1007/JHEP04%282015%29040 (cit. on p. 137).

[441] S. Frixione, P. Nason, and G. Ridolfi, "The POWHEG-hvq manual version 1.0," 2007. DOI: 10.48550/arXiv.0707.3081 (cit. on p. 137).

[442] "ATLAS Pythia 8 tunes to 7 TeV data," 2014. [Online]. Available: https://bib-pubdb1.desy.de/record/193122 (cit. on p. 137).

[443] R. D. Ball, V. Bertone, S. Carrazza, *et al.*, "Parton distributions with LHC data," *Nuclear Physics B*, vol. 867, no. 2, pp. 244–289, 2013. DOI: 10.1016/j.nuclphysb.2012.10.003 (cit. on p. 137).

[444] "Studies on top-quark Monte Carlo modelling for Top2016," CERN, Geneva, Tech. Rep., 2016. [Online]. Available: https://cds.cern.ch/record/2216168 (cit. on pp. 137, 142).

[445] D. J. Lange, "The EvtGen particle decay simulation package," *Nuclear Instruments and Methods in Physics Research Section A: Accelerators, Spectrometers, Detectors and Associated Equipment*, vol. 462, no. 1-2, pp. 152–155, 2001. DOI: 10.1016/S0168-9002(01)00089-4 (cit. on p. 137).

[446] T. Ježo and P. Nason, "On the treatment of resonances in next-to-leading order calculations matched to a parton shower," *Journal of High Energy Physics*, vol. 2015, no. 12, pp. 1–47, 2015. DOI: 10.1007/JHEP12%282015%29065 (cit. on p. 137).

[447] T. Ježo, J. M. Lindert, P. Nason, C. Oleari, and S. Pozzorini, "An NLO+ PS generator for $t\bar{t}$ and Wt production and decay including non-resonant and interference effects," *The European Physical Journal C*, vol. 76, pp. 1–30, 2016. DOI: 10.1140/epjc/s10052-016-4538-2 (cit. on p. 137).

[448] M. Cacciari, G. P. Salam, and G. Soyez, "The catchment area of jets," *Journal of High Energy Physics*, vol. 2008, no. 04, p. 005, 2008. DOI: 10.1088/1126-6708/2008/04/005 (cit. on p. 139).

[449] K. Hagiwara, Y. Sumino, and H. Yokoya, "Bound-state effects on top quark production at hadron colliders," *Physics Letters B*, vol. 666, no. 1, pp. 71–76, 2008. DOI: 10.1016/j.physletb.2008.07.006 (cit. on p. 140).

[450] S. Frixione, E. Laenen, P. Motylinski, C. White, and B. R. Webber, "Single-top hadroproduction in association with a W boson," *Journal of High Energy Physics*, vol. 2008, no. 07, p. 029, 2008. DOI: 10.1088/1126-6708/2008/07/029 (cit. on p. 142).

[451] T. Gleisberg and S. Höche, "Comix, a new matrix element generator," *Journal of High Energy Physics*, vol. 2008, no. 12, p. 039, 2008. DOI: 10.1088/1126-6708/2008/12/039 (cit. on p. 142).

[452] F. Cascioli, P. Maierhöfer, and S. Pozzorini, "Scattering amplitudes with Open Loops," *Physical review letters*, vol. 108, no. 11, p. 111 601, 2012. DOI: 10.1103/PhysRevLett.108.111601 (cit. on p. 142).

[453] F. Buccioni, J.-N. Lang, J. M. Lindert, *et al.*, "OpenLoops 2," *The European Physical Journal C*, vol. 79, pp. 1–56, 2019. DOI: 10.1140/epjc/s10052-019-7306-2 (cit. on p. 142).

[454] C. Anastasiou, L. J. Dixon, K. Melnikov, and F. Petriello, "High precision QCD at hadron colliders: Electroweak gauge boson rapidity distributions at NNLO," *Phys. Rev. D*, vol. 69, p. 094 008, 2004. DOI: 0.1103/PhysRevD.69.094008. arXiv: hep-ph/0312266 (cit. on p. 142).

[455] J. Erdmann, S. Guindon, K. Kroeninger, *et al.*, "A likelihood-based reconstruction algorithm for top-quark pairs and the KLFitter framework," *Nuclear Instruments and Methods in Physics Research Section A: Accelerators, Spectrometers, Detectors and Associated Equipment*, vol. 748, pp. 18–25, 2014. DOI: 10.1016/j.nima.2014.02.029 (cit. on p. 144).

[456] L. Sonnenschein, "Analytical solution of $t\bar{t}$ dilepton equations," *Phys. Rev. D*, vol. 73, p. 054 015, 5 Mar. 2006. DOI: 10.1103/PhysRevD.73.054015 (cit. on p. 145).

[457] B. A. Betchart, R. Demina, and A. Harel, "Analytic solutions for neutrino momenta in decay of top quarks," *Nuclear Instruments and Methods in Physics Research Section A: Accelerators, Spectrometers, Detectors and Associated Equipment*, vol. 736, pp. 169–178, 2014. DOI: 10.1016/j.nima.2013.10.039 (cit. on p. 145).

[458] B. Abbott, M. Abolins, B. Acharya, *et al.*, "Measurement of the top quark mass using dilepton events," *Physical review letters*, vol. 80, no. 10, p. 2063, 1998. DOI: 10.1103/PhysRevLett.80.2063 (cit. on pp. 145, 146).

[459] J. Howarth, "Observation of Spin Correlations in $t\bar{t}$ Events at $\sqrt{s} = 7$ TeV Using the ATLAS Detector," Ph.D. dissertation, The University of Manchester (United Kingdom), 2014. [Online]. Available: https://www.escholar.manchester.ac.uk/item/?pid=uk-ac-man-scw:212598 (cit. on p. 145).

[460] I. Vichou, A. Collaboration, *et al.*, "Performance of missing transverse momentum reconstruction in ATLAS with proton-proton collisions at $\sqrt{s} = 7$ TeV," in *Journal of Physics: Conference Series*, IOP Publishing, vol. 404, 2012, p. 012 011. DOI: 10.1140/epjc/s10052-018-6288-9 (cit. on p. 145).

[461] R. Ferraro and M. Thibeault, "Generic composition of boosts: an elementary derivation of the Wigner rotation," *European journal of physics*, vol. 20, no. 3, p. 143, 1999. [Online]. Available: https://iopscience.iop.org/article/10.1088/0143-0807/20/3/003/meta (cit. on p. 146).

[462] G. D'Agostini, "A multidimensional unfolding method based on Bayes' theorem," *Nuclear Instruments and Methods in Physics Research Section A: Accelerators, Spectrometers, Detectors and Associated Equipment*, vol. 362, no. 2, pp. 487–498, 1995, ISSN: 0168-9002. DOI: 10.1016/0168-9002(95)00274-X (cit. on p. 151).

[463] T. Adye, *Unfolding algorithms and tests using RooUnfold*, 2011. DOI: 10.48550/arXiv.1105.1160 (cit. on p. 151).

[464] A. Buckley and D. Bakshi Gupta, "Powheg-Pythia matching scheme effects in NLO simulation of dijet events," Aug. 2016. [Online]. Available: https://arxiv.org/abs/1608.03577 (cit. on p. 161).

[465] J. Butterworth, S. Carrazza, A. Cooper-Sarkar, *et al.*, "PDF4LHC recommendations for LHC Run II," *Journal of Physics G: Nuclear and Particle Physics*, vol. 43, no. 2, p. 023 001, Jan. 2016. DOI: 10.1088/0954-3899/43/2/023001 (cit. on p. 162).

[466] N. Kidonakis, "Top Quark Production," in *Proceedings, Helmholtz International Summer School on Physics of Heavy Quarks and Hadrons (HQ 2013)*, (JINR, Dubna, Russia, Jul. 15–28, 2013), pp. 139–168. DOI: 10.3204/DESY-PROC-2013-03/Kidonakis. arXiv: 1311.0283 [hep-ph] (cit. on p. 165).

[467] J. A. Raine, M. Leigh, K. Zoch, and T. Golling, "ν^2-Flows: Fast and improved neutrino reconstruction in multi-neutrino final states with conditional normalizing flows," Jul. 2023. DOI: 10.48550/arXiv.2307.02405 (cit. on p. 170).

[468] W.-L. Ju, G. Wang, X. Wang, X. Xu, Y. Xu, and L. L. Yang, "Top quark pair production near threshold: single/double distributions and mass determination," *Journal of High Energy Physics*, vol. 2020, no. 6, p. 158, 2020. DOI: 10.1007/JHEP06(2020)158 (cit. on p. 173).